
Multi-messenger modeling of blazar spectral energy distributions

Dissertation

zur Erlangung des Grades einer
Doktorin der Naturwissenschaften

an der Fakultät für Physik und Astronomie
der Ruhr-Universität Bochum

vorgelegt von

Anastasiia Omeliukh

Bochum 2025

1. Gutachter: Prof. Dr. Anna Franckowiak
 2. Gutachter: Prof. Dr. Julia Tjus
- Datum der Disputation: 10.11.2025

This thesis was typeset using the \LaTeX class `book`. The panel images in Chapters 1–6 and 8, as well as Figures 4.1 and 4.2, were created by the author using the open-source software Inkscape. The panel image for Chapter 6 was created by the author using the open-source software Blender.

Abstract

The origin of the extragalactic neutrino flux detected by the IceCube Neutrino Observatory remains an open question in high-energy astrophysics. Multi-messenger astronomy, which combines observations across different cosmic messengers, offers a promising path toward identifying the sources of these neutrinos. Blazars, a rare subclass of active galactic nuclei with powerful relativistic jets pointed toward Earth, have been proposed to be potential neutrino sources.

In this thesis, blazars are investigated as potential sources of high-energy neutrinos within the framework of multi-messenger modeling. A model developed for the blazar PKS 0735+178 explains its flaring behavior in a multi-messenger context, while also revealing significant degeneracies in hadronic model parameters that complicate reliable constraints on the associated neutrino spectrum. For the blazar VER J0521+211, the day-scale variability observed in TeV gamma rays is modeled using one-zone leptohadronic scenarios, providing a plausible explanation for this unusual behavior. Also, the potential contribution of blazars to the neutrino excess observed near the Seyfert galaxy NGC 4151 is estimated through spectral energy distribution modeling.

The study further explores how parameter degeneracies arise in one-zone models due to limited data coverage and observational uncertainties. Various optimization algorithms are evaluated for their performance in navigating the complex parameter spaces of one-zone leptonic models.

Finally, the thesis investigates fundamental properties of blazars using a large sample, with results cross-validated through an independent method. It is demonstrated that slowly accreting supermassive black holes launch relativistic jets with greater efficiency.

Kurzzusammenfassung

Der Ursprung des extragalaktischen Neutrinoflusses, der vom IceCube Neutrino-Observatorium entdeckt wurde, ist in der Hochenergie-Astrophysik noch nicht geklärt. Die Multimessenger-Astronomie, die Beobachtungen verschiedener kosmischer Boten miteinander kombiniert, bietet eine Möglichkeit, die Herkunft dieser Neutrinos zu erforschen. Blazare, eine seltene Art aktiver Galaxien mit starken, auf die Erde gerichteten Jets, gelten als mögliche Quellen dieser Neutrinos.

In dieser Dissertation werden Blazare mithilfe von Multimessenger-Modellierung als mögliche Quelle hochenergetischer Neutrinos untersucht. Ein entwickeltes Modell für den Blazar PKS 0735+178 erklärt dessen auffälliges Ausbruchsverhalten im Kontext mehrerer kosmischer Boten und zeigt zugleich erhebliche Degeneriertheiten in den Parametern hadronischer Modelle auf, die verlässliche Einschränkungen des zugehörigen Neutrinospektrums erschweren. Für den Blazar VER J0521+211 wird die schnelle Veränderung der TeV-Gammastrahlung im Rahmen eines Ein-Zonen-leptohadronischen Modells untersucht, was eine mögliche Erklärung für dieses ungewöhnliche Verhalten liefert. Außerdem wird abgeschätzt, inwieweit Blazare zum Neutrinoüberschuss in der Nähe der Seyfert-Galaxie NGC 4151 beitragen könnten – auf Basis einer Analyse ihrer spektralen Energieverteilung.

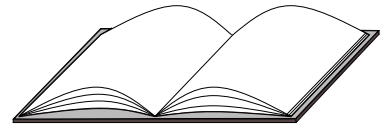
Die Arbeit zeigt auch, wie Unsicherheiten in den Modellparametern bei Ein-Zonen-Modellen durch begrenzte Daten und Messunsicherheiten entstehen. Verschiedene Optimierungsverfahren werden daraufhin überprüft, wie gut sie sich für die Suche in den komplexen Parameterbereichen der Ein-Zonen-leptonischen Modelle eignen.

Zum Schluss werden grundlegende Eigenschaften von Blazaren anhand einer großen Stichprobe untersucht, wobei die Ergebnisse durch eine unabhängige Methode validiert werden. Es wird gezeigt, dass langsam akkretierende supermassereiche Schwarze Löcher relativistische Jets mit höherer Effizienz erzeugen.

Contents

1	Introduction	1
2	Four windows into the universe	3
2.1	Cosmic rays	3
2.2	Photons	6
2.3	Neutrinos	7
2.4	Gravitational waves	9
2.5	Discoveries of the multi-messenger astronomy	10
3	Active galactic nuclei	15
3.1	AGN structure	15
3.2	AGN zoo	18
3.2.1	Radio-quiete AGNs	19
3.2.2	Radio-loud AGNs	19
3.3	Blazars as extreme AGNs	21
4	Numerical modeling of blazar emission	25
4.1	Radiation processes	27
4.1.1	Leptonic processes	27
4.1.2	Hadronic interactions	30
4.2	Blazar radiation models	31
4.2.1	One-zone models	32
4.2.2	Multi-zone models	33
4.3	Numerical approach	34
4.4	Application to blazars	34
4.4.1	Gamma-ray emitters	34
4.4.2	Possible neutrino emitters	35
5	Individual candidates for neutrino emitting blazars	37
5.1	Multiple neutrinos from PKS 0735+178	39
5.1.1	Data collection and data analysis	39
5.1.2	Numerical modeling	42
5.1.3	Results	45
5.1.4	Discussion	51
5.1.5	Summary and conclusions	56
5.2	TeV flaring blazar VER J0521+211	57
5.2.1	Data	57
5.2.2	SED modeling	59

5.2.3	Results	60
5.2.4	Summary and conclusions	64
5.3	Blazar contribution to neutrino neutrino hotspot near NGC 4151	65
5.3.1	Neutrinos from Seyfert galaxies	65
5.3.2	Data	67
5.3.3	Numerical modeling	67
5.3.4	Results	69
5.3.5	Discussion	70
5.3.6	Summary and conclusions	73
6	Parameter spaces of one-zone leptonic models	75
6.1	Leptonic models	77
6.2	Visualization of multi-dimensional spaces	77
6.3	Challenges for parameter fitting	79
6.4	Simulated pseudo-data	80
6.5	Comparison of minimization algorithms on simulated data	81
6.6	Application to blazar data	88
6.7	Discussion	91
6.8	Summary and conclusions	95
7	Extracting accretion physics by modeling large sample of blazars	97
7.1	Leptohadronic modeling of 324 gamma-ray blazars	99
7.1.1	Blazar sample	99
7.1.2	Leptohadronic modeling	99
7.1.3	Results	100
7.1.4	Summary and conclusions	102
7.2	Power of blazar jets	103
7.2.1	Methods of jet power estimation	103
7.2.2	Blazar sample	104
7.2.3	Results	105
7.2.4	Summary and conclusions	109
8	Summary and outlook	111
	Appendices	115
A	Parameter space of leptonic models for PKS 0735+178	115
B	Andrew's plots	119
C	MCMC corner plots	119
	Bibliography	126
	Acknowledgements	141
	Curriculum vitae	143



Chapter 1

Introduction

Like many physics students, I was always captivated by two extremes of the physical world: the physics of the tiniest building blocks of nature – elementary particles – and the violent, energetic phenomena observed in the distant Universe. These seemingly distant realms find common ground in astroparticle physics, where particles such as neutrinos serve as messengers from the most extreme astrophysical environments.

Among all known particles, neutrinos are, in my view, among the most fascinating. These light, neutral fermions are unique in the Standard Model for having only left-handed chirality. Despite their confirmed non-zero mass, both the absolute scale and the mechanism behind their mass generation remain unknown. Neutrino mixing adds further complexity, making them central to several unresolved questions in particle physics. However, this is not what makes neutrinos particularly interesting for astrophysics.

Neutrinos interact only weakly and are hence unlikely to be absorbed. They also cannot be deflected by magnetic fields. These properties make neutrinos unique carriers of information from the distant Universe. Neutrino astronomy, though still a relatively young field, has evolved rapidly. The detection of a diffuse flux of astrophysical neutrinos by the IceCube Neutrino Observatory, together with the first observations of gravitational waves, marked the beginning of multi-messenger astronomy. These discoveries are likely to be remembered as some of the most significant scientific milestones of the 21st century.

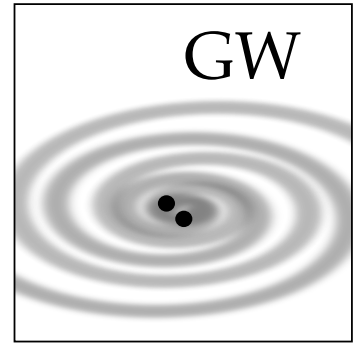
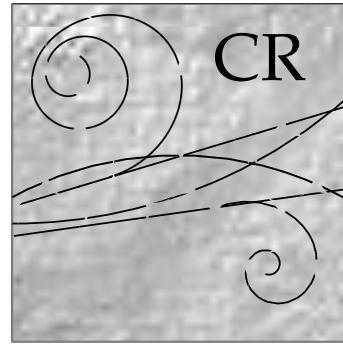
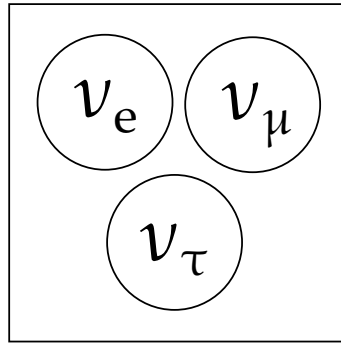
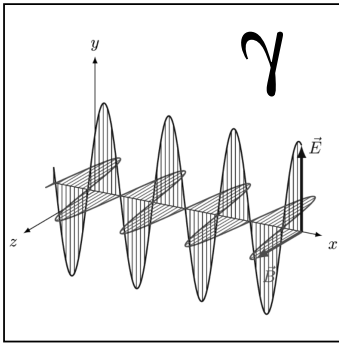
Despite this progress, many fundamental questions remain open. One of the most important is the origin of high-energy astrophysical neutrinos. This thesis investigates some aspects of this question by focusing on a particular class of astrophysical sources: blazars – some of the most powerful objects in the Universe and prospective neutrino emitters.

The goal of this work is not only to examine whether particular blazars

can be neutrino sources, but also to critically reflect on certain aspects of blazar modeling (**Chapter 6** and partially **Chapter 7**), and to gain insights into blazar physics by analyzing a modeled blazar sample. Throughout this thesis, I aim to place individual results within the broader context of blazar phenomenology and multi-messenger astrophysics.

The thesis is structured as follows:

- ▶ **Chapter 2** provides an overview of cosmic rays, photons, neutrinos, and gravitational waves as messengers in multi-messenger astronomy, along with the major recent discoveries in the field.
- ▶ **Chapter 3** gives an introduction to the physics of active galactic nuclei (AGNs) and blazars as their subclass.
- ▶ **Chapter 4** describes radiation processes relevant to blazars and the numerical modeling of their emission.
- ▶ **Chapter 5** discusses PKS0735+178 as a potential neutrino source, VERJ0521+211 with its unusual day-scale variability in TeV gamma rays, and two blazars near NGC 1068 that may contribute to a local neutrino excess.
- ▶ **Chapter 6** discusses the complexity of the parameter spaces involved in modeling and the challenges associated with fitting observational data.
- ▶ **Chapter 7** presents interesting blazar properties identified through blazar sample modeling and verified with an independent method based on radio observations.
- ▶ **Chapter 8** summarizes the key findings and provides an outlook on future research directions.



Chapter 2

Four windows into the universe

Astronomy, one of the oldest sciences, has traditionally relied on visible light to observe natural phenomena for thousands of years. However, over the past century, observational capabilities have expanded significantly with the emergence of radio, infrared, X-ray, and gamma-ray astronomy. These developments have made it possible to investigate highly energetic environments and trace the signatures of relativistic electrons. Notably, even before observations extended beyond the optical spectrum, cosmic rays had already been discovered. Over the past decade, two more windows into the Universe have opened: neutrinos and gravitational waves.

These discoveries have laid the foundation for **multi-messenger astronomy**, which combines information from different messengers to achieve a more comprehensive understanding of astrophysical phenomena.

2.1 Cosmic rays

Cosmic rays (CRs) are highly energetic, charged elementary particles of astrophysical origin. They were first discovered by Victor Hess in 1912 through a balloon experiment, which showed that the rate of ionizing radiation increases with altitude [1].

Since cosmic rays are charged, they are deflected by magnetic fields and can also interact with background photon fields as they travel through the Universe. As a result, their arrival directions provide only limited information about the locations of their sources in the sky.

Primary cosmic rays are protons and nuclei accelerated in astrophysical environments before reaching Earth. Secondary cosmic rays, on the other hand, are produced when primary cosmic rays interact with various targets during their journey through the Universe. For example, lithium, beryllium, and boron nuclei are secondaries [2], as are antiprotons and positrons [3]. Primary cosmic rays consist of approximately 74% protons, and about 70% of the remaining fraction are helium nuclei [4].

Cosmic rays:

- [1]: Hess (1912), Über Beobachtungen der durchdringenden Strahlung bei sieben Freiballonfahrten
- [2]: Vangioni-Flam et al. (2000), Lithium-beryllium-boron: origin and evolution
- [3]: Lipari (2017), Interpretation of the cosmic ray positron and antiproton fluxes
- [4]: Workman and Others (2022), Review of Particle Physics

Energy spectrum

The cosmic ray spectrum spans many orders of magnitude in both energy and flux. **Figure 2.1** shows the all-particle cosmic ray spectrum as a function of energy. To highlight spectral features, the particle flux on the vertical axis is multiplied by $E^{2.6}$. While the overall spectrum follows a power-law distribution, $dN/dE \propto E^{-\gamma}$, the spectral index γ varies with energy. The first notable change in the spectral slope ($\sim E^{-3.1}$) occurs around $3 \cdot 10^{15}$ eV and is referred to as the *knee*, followed by a *second knee* around 10^{17} eV where the spectrum softens further to $E^{-3.3}$. The knee is often interpreted as a transition point from galactic to extragalactic cosmic rays. This energy marks both the upper limit of acceleration capabilities for galactic sources such as supernova remnants [5], and the Larmor radius at which particles begin to escape the galactic plane [6].

Energy spectrum:

[4]: Workman and Others (2022), Review of Particle Physics

[5]: Hillas (2005), Can diffusive shock acceleration in supernova remnants account for high-energy galactic cosmic rays?

[6]: Horandel (2007), "Cosmic rays from the knee to the second knee: 10^4 to 10^{18} eV"

[7]: Greisen (1966), End to the Cosmic-Ray Spectrum?

[8]: Zatsepin and Kuz'min (1966), Upper Limit of the Spectrum of Cosmic Rays

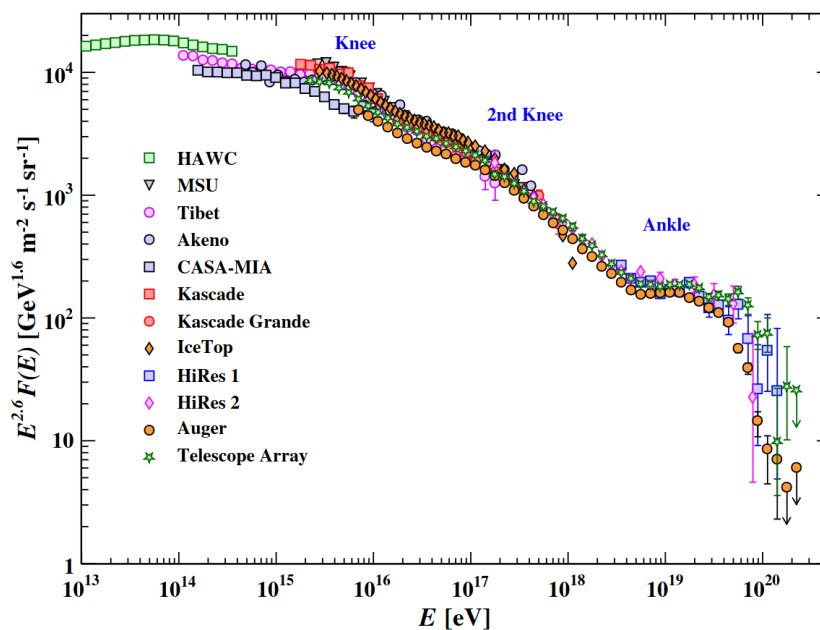


Figure 2.1: The all-particle cosmic-ray spectrum as a function of energy, as measured by various experiments. Reproduced from [4].

At $6 \cdot 10^{18}$ eV, the spectrum flattens again, creating the so-called *ankle* region. At energies above 10^{19} eV, the cosmic-ray flux is expected to drop due to the Greisen–Zatsepin–Kuzmin (GZK) effect [7, 8], also known as the GZK cut-off, caused by photo-hadronic interactions of high-energy cosmic rays with photons of the cosmic microwave background (CMB).

Acceleration:

[9]: Fermi (1954), Galactic Magnetic Fields and the Origin of Cosmic Radiation.

Acceleration mechanisms

Cosmic rays, the most energetic particles in the Universe, gain their energy through acceleration starting from low energies. One of the principal mechanisms responsible for cosmic ray acceleration is the process known as *Fermi acceleration*. In first-order Fermi acceleration, particles gain energy through repeated reflections between two magnetic fields moving toward each other [9]. This mechanism is a key component of many astrophysical acceleration models, particularly in the context of diffusive shock acceleration, which describes first-order Fermi acceleration

occurring in regions dominated by strong shocks and small-scale turbulence. In second-order Fermi acceleration, particles gain energy through stochastic interactions with moving magnetic mirrors [10]. Both mechanisms predict a power-law energy spectrum of the form $E^{-\gamma}$, with the spectral index $\gamma \approx 2$.

Another physical scenario for cosmic ray acceleration is *magnetic reconnection*. In this process, changes in magnetic field topology lead to the rapid release of magnetic energy, part of which can be converted into the energy of accelerated particles. The energy spectrum resulting from magnetic reconnections has a power-law shape $dN/dE \propto E^{-\gamma}$, with γ varying from 4 for non-relativistic reconnections to ≤ 1.5 in the highly relativistic regime [11].

Despite recent observations of several cosmic ray hotspots [12, 13], the exact locations of cosmic ray acceleration sites remain unknown. The extreme energies of cosmic rays require special conditions at their sources, one of which is the Hillas criterion – a confinement requirement that determines whether a given astrophysical environment can accelerate particles to the observed energies [14].

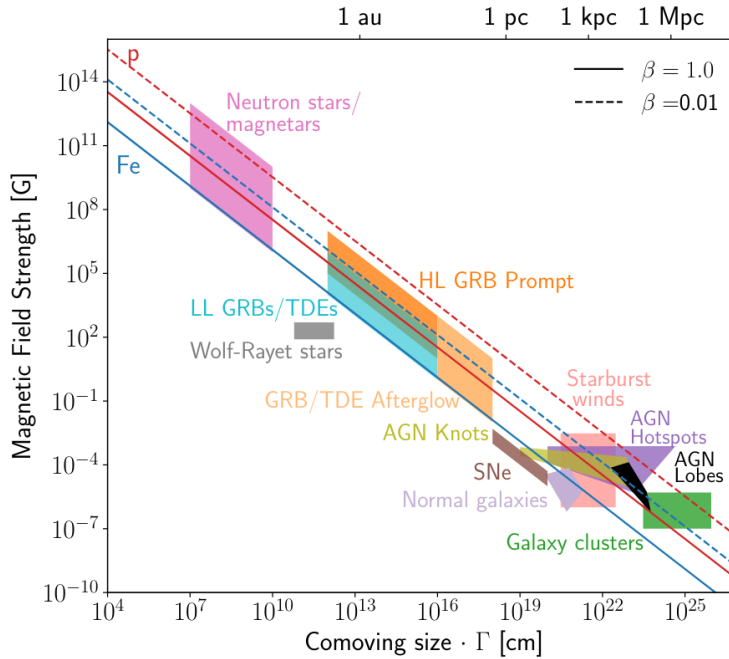


Figure 2.2: Hillas diagram. Classes of astrophysical sources with their typical radial sizes and magnetic field strengths. Diagonal lines show a minimum product $\beta_{\text{sh}}RB$ required to accelerate CR to 10^{20} eV for two values of shock velocity β_{sh} . Classes of objects to the left of the lines do not satisfy the Hillas criterion. Reproduced from [15].

Particles remain within the acceleration region as long as their Larmor radii are smaller than the size of the accelerator. This introduces an upper limit on the particle energy, E_{max} , that can be reached in a source with

Acceleration:

[10]: Fermi (1949), On the Origin of the Cosmic Radiation

[11]: Sironi and Spitkovsky (2014), Relativistic Reconnection: An Efficient Source of Non-thermal Particles

[12]: Abbasi et al. (2014), Indications of Intermediate-scale Anisotropy of Cosmic Rays with Energy Greater Than 57 EeV in the Northern Sky Measured with the Surface Detector of the Telescope Array Experiment

[13]: Aab et al. (2015), Searches for Anisotropies in the Arrival Directions of the Highest Energy Cosmic Rays Detected by the Pierre Auger Observatory

[14]: Hillas (1984), The Origin of Ultra-High-Energy Cosmic Rays

[15]: Alves Batista et al. (2019), Open Questions in Cosmic-Ray Research at Ultrahigh Energies

characteristic size R and magnetic field B :

$$E_{\max} = \beta_{\text{sh}} Z \left(\frac{B}{\mu\text{G}} \right) \left(\frac{R}{\text{kpc}} \right) [\text{EeV}] \quad (2.1)$$

where β_{sh} is the velocity of the shock in units of the speed of light, Z is the charge of the particle, B is the magnetic field strength, and R is a typical size of the acceleration region.

2.2 Photons

Photons are elementary particles that carry the electromagnetic force. Among all astrophysical messengers, photons have the longest history of study, dating back to the earliest civilizations observing the night sky. Photon energies in astronomical studies span over nine orders of magnitude, ranging from below 10^{-6} eV (radio emission) to beyond 10^{15} eV (high-energy gamma rays). The emission of photons at different energies corresponds to different physical processes in astrophysical sources. The fundamental principle of multi-wavelength astronomy is to combine observations across different wavelengths to obtain a more comprehensive understanding of these sources.

Overall, the photon spectra of astrophysical sources can be divided into *thermal* and *non-thermal*. The thermal (or black-body) spectrum is generated by the thermal motion of particles. Its spectral energy density can be calculated using Planck's distribution:

$$u_\nu = \frac{4\pi}{c} \cdot \frac{2h\nu^3}{c^2} (e^{\frac{h\nu}{k_{\text{BT}}}} - 1)^{-1} \quad (2.2)$$

Thermal spectra describe the emission of stars, accretion disks, and even the cosmic microwave background (CMB). Non-thermal emission arises from particle radiative processes and interactions such as synchrotron emission, Compton scattering, and bremsstrahlung. The non-thermal radiation processes, which will be the focus of this thesis, are further discussed in [Section 4.1](#).

Photons, being uncharged particles, do not deflect in magnetic fields during their propagation from the source to the observer. However, high-energy photons from the source can interact with the so-called extragalactic background light (EBL), creating electron-positron pairs and thus being absorbed. [Figure 2.3](#) shows the distance at which photons have a survival probability of approximately 1% as a function of photon energy. PeV photons can be detected only from nearby sources no farther than $\sim 10 - 100$ kpc, which is on the order of the Milky Way's radius. Therefore, at these high energies, photons can no longer carry information about the distant Universe.

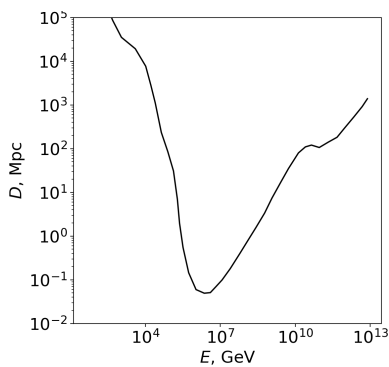


Figure 2.3: Distance at which photons can survive with a probability of $e^{-4.6} \approx 0.01$ as a function of photon energy. Reproduced from [16].

Photons:

[16]: De Angelis et al. (2013), Transparency of the Universe to gamma-rays

2.3 Neutrinos

Neutrinos are neutral elementary particles that have very little mass and interact only weakly. They were first proposed by Wolfgang Pauli as a solution to the problem of energy conservation in nuclear beta decay [17]. The name “neutrino” was introduced by Enrico Fermi, who developed a theory to explain beta decay [18]. Although (electron) neutrinos were first detected in 1952 [19], many of their properties remain largely unknown [20, 21], making them some of the most puzzling particles in the Standard Model.

Neutrino oscillations

Neutrinos come in three flavors: electron neutrinos, muon neutrinos (discovered in 1962 [22]), and tau neutrinos (discovered in 2000 [23]). The process in which a neutrino has a different flavor at the moment of creation and detection, known as *neutrino oscillation*, was theoretically proposed in 1957 by Bruno Pontecorvo [24]. This phenomenon was confirmed by experiments that measured a deficit of solar electron neutrinos [25, 26] due to their oscillations. The flux of detected neutrinos with flavor β is

$$\Phi_{\nu_\beta} \propto \sum_{\alpha=e,\mu,\tau} P_{\alpha\rightarrow\beta} \Phi_{\nu_\alpha} \quad (2.3)$$

where Φ_{ν_α} is the neutrino flux of flavor α at the source, and the neutrino oscillation probability is given by

$$P_{\alpha\rightarrow\beta} \approx \left| \sum_i U_{\alpha i} U_{\beta i}^* \right|^2 \quad (2.4)$$

where U is the so-called PMNS mixing matrix [27]. For neutrino-emitting sources, the neutrino flavor composition on Earth is fully determined by the flavor composition at the source and the parameters of the PMNS matrix.

Sources of neutrinos

Neutrinos can be produced in many different terrestrial and extraterrestrial sources. **Figure 2.4** shows a compilation of all discovered and predicted neutrino spectra. Neutrinos of the lowest energies (up to 0.1 eV) were produced during the Big Bang and big-bang nucleosynthesis (BBN). The keV–MeV energy range is dominated by neutrinos created in nuclear reactions in the Sun. At MeV energies, past supernova explosions produce the so-called diffuse supernova neutrino background (DSNB). Atmospheric neutrinos dominate the GeV–TeV range and are products of cosmic ray interactions with Earth’s atmosphere, which create hadronic cascades. At energies above 100 TeV, the neutrino flux comes from astrophysical neutrino sources. At the highest energies, due to the GZK effect, photo-hadronic interactions of ultra-high-energy cosmic rays (UHECRs) produce so-called cosmogenic neutrinos.

Neutrinos:

[17]: Pauli (1978), Dear radioactive ladies and gentlemen

[18]: Fermi (1934), An attempt of a theory of beta radiation

[19]: Cowan et al. (1956), Detection of the free neutrino: A Confirmation

[20]: Iachello (2018), Open problems in neutrino physics

[21]: Sajjad Athar et al. (2022), Status and perspectives of neutrino physics

Neutrino oscillations:

[22]: Danby et al. (1962), Observation of

High-Energy Neutrino Reactions and the Existence of Two Kinds of Neutrinos

[23]: Kodama et al. (2001), Observation of tau neutrino interactions

[24]: Pontecorvo (1957), Inverse β -processes and non-conservation of lepton charge

[25]: Davis et al. (1968), Search for Neutrinos from the Sun

[26]: Ahmad et al. (2001), Measurement of the Rate of $\nu_e + d \rightarrow p + p + e^-$

Interactions Produced by ^8B Solar Neutrinos at the Sudbury Neutrino Observatory

[27]: Maki et al. (1962), Remarks on the Unified Model of Elementary Particles

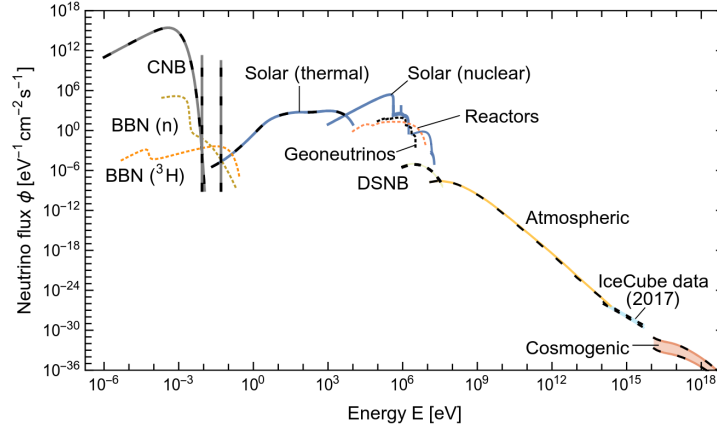


Figure 2.4: All known neutrino spectra. Adapted from [28].

Neutrino sources:

[28]: Vitagliano et al. (2020), Grand unified neutrino spectrum at Earth: Sources and spectral components

[29]: Aartsen et al. (2014), Observation of High-Energy Astrophysical Neutrinos in Three Years of IceCube Data

[30]: Abbasi et al. (2022), Detection of astrophysical tau neutrino candidates in IceCube

[31]: Naab et al. (2023), Measurement of the astrophysical diffuse neutrino flux in a combined fit of IceCube's high energy neutrino data

[32]: Abbasi et al. (2022), Evidence for neutrino emission from the nearby active galaxy NGC 1068

[33]: IceCube Collaboration (2023), Observation of high-energy neutrinos from the Galactic plane

In 2013, the IceCube Neutrino Observatory measured, for the first time, a flux of astrophysical high-energy neutrinos [29] after three years of data collection. The astrophysical component starts to dominate over atmospheric neutrinos at energies around ~ 100 TeV. The IceCube data showed no preferred arrival direction of neutrinos, indicating that the neutrino flux has an extragalactic origin. **Figure 2.5** shows the most recent all-flavor spectrum of astrophysical neutrinos, produced after more than 10 years of data collection. The composition of the astrophysical flux, or flavor ratio, is currently estimated as $(\nu_e : \nu_\mu : \nu_\tau) = (0.20 : 0.39 : 0.42)$ observed at Earth [30].

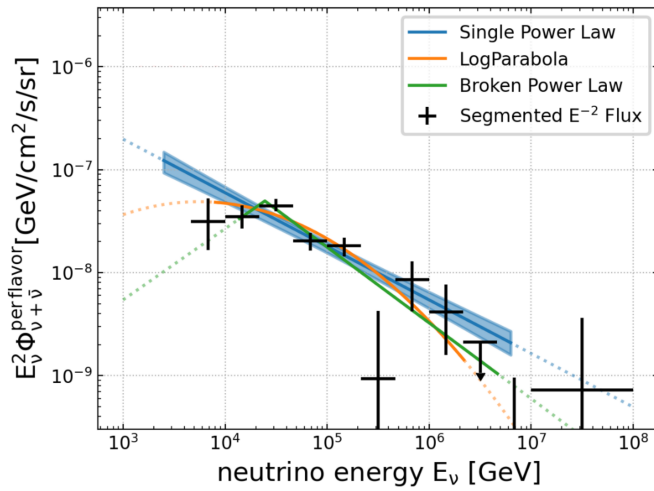


Figure 2.5: IceCube astrophysical neutrino flux based on 10 years of data from multiple neutrino detection channels. Adapted from [31].

The origin of the majority of the IceCube diffuse neutrino flux remains unknown. Additionally, no neutrino source has yet been discovered with a 5σ significance. However, recent detections of neutrino signals from the Seyfert galaxy NGC 1068 (4.2σ significance, [32]) and from the Galactic plane (4.5σ significance, [33]) indicate that discoveries are forthcoming.

Possible neutrino emission from individual blazars and from the blazar population is discussed in the following chapters.

2.4 Gravitational waves

Gravitational waves (GWs) arise as solutions to the Einstein field equations in general relativity, in a way analogous to how electromagnetic waves emerge from Maxwell's equations, although the nature of gravitational waves is fundamentally different. Gravitational waves are ripples in the curvature of space-time that propagate through the Universe at the speed of light and are generated by massive objects with varying quadrupole moments. Their amplitude and frequency depend on the properties of the generating object or system.

While the three previously described messengers are expected to arrive at Earth from numerous sources, gravitational waves are emitted only by objects undergoing asymmetric acceleration, such as binary black holes, binary neutron stars, or highly asymmetric supernova explosions.

The gravitational wave amplitude h decreases with distance as $1/r$. In contrast, photons, neutrinos, and cosmic rays are measured in terms of particle fluxes, which decrease with distance as $1/r^2$. This highlights the importance of gravitational waves as a unique messenger for exploring the distant Universe. The typical GW signal amplitude from binary neutron stars [34] is of the order of

$$h \approx 4 \cdot 10^{-22} \left(\frac{\mu}{M_\odot} \right)^{1/2} \cdot \left(\frac{M}{M_\odot} \right)^{1/3} \cdot \frac{100 \text{ Mpc}}{R} \cdot \left(\frac{100 \text{ Hz}}{f_c} \right)^{1/6} \quad (2.5)$$

where $M = M_1 + M_2$, $\mu = M_1 M_2 / M$ and f_c is frequency of maximum detector sensitivity. If the detector has an arm of 4 km, it must detect a change of

$$\delta l = h \cdot l \approx 10^{-22} \cdot 4 \text{ km} = 4 \cdot 10^{-19} \text{ m} \quad (2.6)$$

which poses a significant technological challenge. The first indirect evidence for gravitational waves was obtained when precise measurements of the orbital period of the binary pulsar PSR J1915+1606 [35] showed a gradual shortening over time. This observation agreed with predictions from general relativity that energy is emitted in the form of gravitational waves [36]. The first direct detection of gravitational waves occurred in 2015 by the laser interferometer LIGO [37], observing the merger of two stellar-mass black holes. More recently, a different detection technique based on pulsar timing arrays has provided evidence of a low-frequency stochastic gravitational wave background [38].

Gravitational waves:

- [34]: Ju et al. (2000), Detection of gravitational waves
- [35]: Hulse and Taylor (1975), Discovery of a pulsar in a binary system.
- [36]: Taylor and Weisberg (1989), Further Experimental Tests of Relativistic Gravity Using the Binary Pulsar PSR 1913+16
- [37]: Abbott et al. (2016), Observation of Gravitational Waves from a Binary Black Hole Merger
- [38]: Agazie et al. (2023), The NANOGrav 15 yr Data Set: Observations and Timing of 68 Millisecond Pulsars

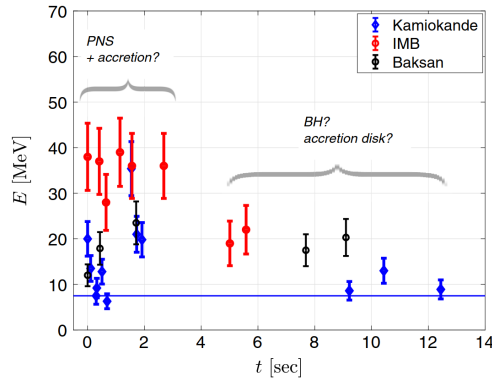


Figure 2.6: Neutrinos from SN1987A. Figure from [39].

SN1987A:

[39]: Bar et al. (2020), Is there a supernova bound on axions?

[40]: Danziger et al. (1987), Optical spectroscopy of SN 1987A.

[41]: Pinto and Woosley (1988), X-Ray and Gamma-Ray Emission from Supernova 1987A

[42]: Hirata et al. (1987), Observation of a neutrino burst from the supernova SN1987A

[43]: Bionta et al. (1987), Observation of a neutrino burst in coincidence with supernova 1987A in the Large Magellanic Cloud

[44]: Alekseev et al. (1987), Detection of the Neutrino Signal from Supernova 1987A Using the INR Baksan Underground Scintillation Telescope

[45]: Fryer et al. (2023), Multimessenger Diagnostics of the Engine behind Core-collapse Supernovae

[46]: Fiorillo et al. (2023), Supernova simulations confront SN 1987A neutrinos

[47]: Chang et al. (2018), Supernova 1987A constraints on sub-GeV dark sectors, millicharged particles, the QCD axion, and an axion-like particle

GW 170817:

[48]: Abbott et al. (2017), Gravitational Waves and Gamma-Rays from a Binary Neutron Star Merger: GW170817 and GRB 170817A

2.5 Discoveries of the multi-messenger astronomy

Currently, no known astrophysical source has been confirmed to emit all four types of messengers. The same is true for the three uncharged messengers (photons, neutrinos, and gravitational waves), which can directly point back to their sources. However, several exciting multi-messenger events combining detections from multiple messengers have been observed. This section provides a brief overview of some of these events.

SN1987A

One of the earliest known multi-messenger events was the explosion of supernova SN1987A in the Large Magellanic Cloud on February 23, 1987. The explosion produced multi-wavelength photon emission, including optical [40], X-rays, and gamma rays [41]. Simultaneously, neutrino emission from the core-collapse supernova generated a ~ 10 -second-long signal detected by Kamiokande II [42], IMB [43], and the Baksan Scintillation Telescope [44], as shown in Figure 2.6. The detected neutrinos were mostly $\bar{\nu}_e$ with energies ranging from 10 to 40 MeV.

Even more than three decades after SN1987A, the multi-messenger data continue to be used for studying the engine of core-collapse supernovae [45], the time evolution of neutrino emission [46], as well as for placing constraints on dark matter models and beyond Standard Model physics [39, 47].

GW 170817/GRB 170814A

On August 17, 2017, the joint observational run of LIGO and Virgo detected the first-ever merger of two neutron stars. Just 1.7 seconds later, the Gamma-ray Burst Monitor onboard Fermi-LAT detected a burst of gamma rays (GRB 170817A), which was spatially and temporally coincident with the gravitational wave signal [48]. The detection of both gravitational waves and electromagnetic signals from this binary neutron star merger triggered a large-scale campaign for broadband observations. Less than 12 hours after the gravitational wave detection, the merger was observed across multiple wavelengths, including X-rays, ultraviolet (UV), optical,

infrared (IR), and radio bands. Observations continued for over a month [49]. This multi-wavelength campaign also revealed a kilonova event that followed the merger.

Although the theory of short gamma-ray bursts (short GRBs) was well developed and supported by numerous indirect pieces of evidence, GW170817/GRB 170817A provided the first direct confirmation that short GRBs are caused by mergers of compact objects. **Figure 2.7** shows the GRB light curve in the 10–50 keV band and the time-frequency map of GW170817. The vertical black line marks the merger time, while the gray line indicates the onset of the GRB. The 1.7-second delay is likely due to the low luminosity of the GRB, which can be explained by an off-axis jet [50].

These multi-messenger observations helped place constraints on the equation of state of dense nuclear matter and provided tests of general relativity [51]. Additionally, the kilonova emission confirmed the production of heavy elements (up to atomic mass $A = 195$) through rapid neutron capture (r -process), establishing neutron star mergers as a major site of rapid neutron capture nucleosynthesis in the Universe [52].

Blazar TXS 0506+056

On September 9, 2017, IceCube detected a 290 TeV neutrino from the direction of the blazar TXS 0506+056 during a period of enhanced gamma-ray flux [53]. The spatial and temporal coincidence of the neutrino and gamma-ray emission suggests a common origin for both messengers. A subsequent search of archival data revealed that 13 ± 5 neutrinos had been emitted from this source in 2015, despite the blazar being in a quiescent gamma-ray state at that time [54]. Most theoretical models predict that neutrino flux should be proportional to gamma-ray flux, making the explanation of the 2015 neutrino signal challenging. Further discussion on neutrino emission from blazars will be presented in **Section 4.4.2**.

TDE AT2019dsg

On October 1, 2019, IceCube detected a ~ 0.2 PeV neutrino from the direction of the tidal disruption event (TDE) AT2019dsg [55]. Tidal disruption events are rare phenomena in which a star passing close to a black hole is torn apart by tidal forces. Part of the

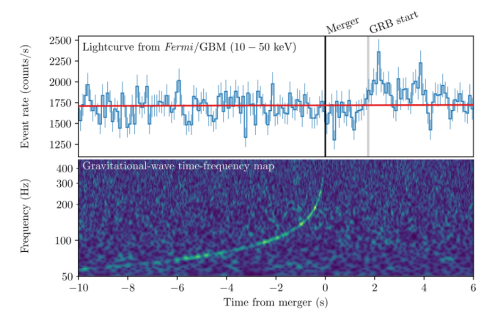


Figure 2.7: Top: Gamma-ray light curve (50 keV) of GRB 170817A. Bottom: Time-frequency map of the gravitational wave event. Figure from [48].

GW 170817:

[49]: Abbott et al. (2017), Multi-messenger Observations of a Binary Neutron Star Merger
 [50]: Troja et al. (2019), A year in the life of GW170817: the rise and fall of a structured jet from a binary neutron star merger
 [51]: Margutti and Chornock (2021), First Multimessenger Observations of a Neutron Star Merger
 [52]: Tanvir et al. (2017), The Emergence of a Lanthanide-rich Kilonova Following the Merger of Two Neutron Stars

TXS 0506+056:

[53]: Aartsen et al. (2018), Neutrino emission from the direction of the blazar TXS 0506+056 prior to the IceCube-170922A alert
 [54]: Aartsen et al. (2018), Neutrino emission from the direction of the blazar TXS 0506+056 prior to the IceCube-170922A alert

AT2019dsg:

[55]: Stein et al. (2021), A tidal disruption event coincident with a high-energy neutrino

AT2019dsg:

[56]: Hayasaki (2021), Neutrinos from tidal disruption events

[57]: Winter and Lunardini (2023), Interpretation of the Observed Neutrino Emission from Three Tidal Disruption Events

[58]: Reusch et al. (2022), Candidate Tidal Disruption Event AT2019fdr Coincident with a High-Energy Neutrino

[59]: van Velzen et al. (2024), Establishing accretion flares from supermassive black holes as a source of high-energy neutrinos

NGC 1068:

[32]: Abbasi et al. (2022), Evidence for neutrino emission from the nearby active galaxy NGC 1068

[60]: Inoue et al. (2020), On the Origin of High-energy Neutrinos from NGC 1068: The Role of Nonthermal Coronal Activity

[61]: Eichmann et al. (2022), Solving the Multimessenger Puzzle of the AGN-starburst Composite Galaxy NGC 1068

[62]: Peretti et al. (2023), Diffusive shock acceleration at EeV and associated multimessenger flux from ultra-fast outflows driven by Active Galactic Nuclei

[63]: Yasuda et al. (2024), Neutrinos and gamma rays from beta decays in an active galactic nucleus NGC 1068 jet

Galactic plane:

[33]: IceCube Collaboration (2023), Observation of high-energy neutrinos from the Galactic plane

stellar material accretes onto the black hole, producing optical, X-ray, infrared (IR), and radio emission. Although many aspects of TDEs remain unknown, multi-messenger observations have driven the development of theoretical models for neutrino production in these events [56, 57]. Following AT2019dsg, neutrinos were also detected from the TDEs AT2019fdr [58] and AT2019aalc [59], both within the same year.

NGC 1068

In 2022, an analysis of nine years of IceCube data revealed the detection of 79^{+22}_{-20} neutrinos with energies of $\sim 1 - 10$ TeV from the Seyfert galaxy NGC 1068, with a significance of 4.2σ [32]. Neutrino and gamma-ray emissions in active galactic nuclei (AGNs) are typically expected to be correlated due to their shared production mechanisms. However, the gamma-ray flux from NGC 1068 was surprisingly low and exhibited an unusual spectral shape. Various scenarios have been proposed to explain neutrino production in AGNs, involving the AGN corona, star-forming regions, or AGN disk winds. Reconciling the multi-messenger observations of NGC 1068 remains a challenge and continues to be an active area of research [60, 61, 62, 63]. Further discussion on neutrino production in AGNs, including Seyfert galaxies, will be presented in the following chapters.

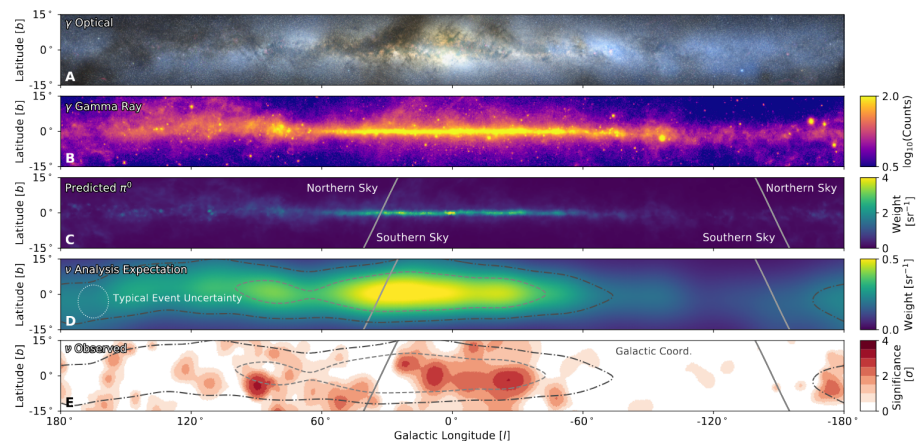
Multi-messenger emission from the galactic plane

Figure 2.8: The plane of the Milky Way galaxy observed in different photon bands and neutrinos. Figure from [33].

In 2023, IceCube reported the discovery of neutrino emission from the Galactic plane, based on ten years of data collection [33]. The multi-messenger view of our Galaxy is illustrated in **Figure 2.8**. Prior to this detection, diffuse high-energy (up to PeV) gamma-ray emission from the Galactic disk had been observed by Tibet-AS γ [64] and LHAASO [65]. A joint analysis of gamma-ray and neutrino data suggests a potentially hadronic origin for the high-energy diffuse gamma-ray emission [66].

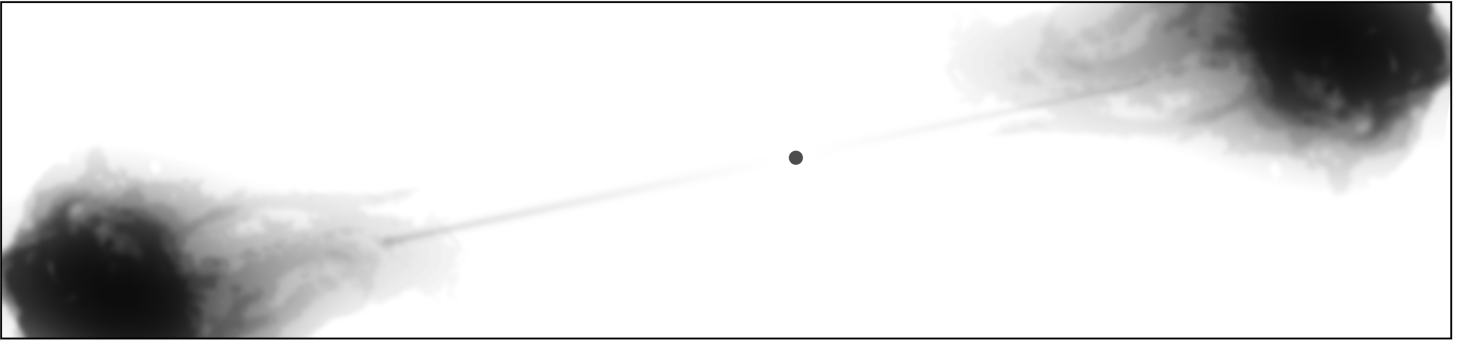
Galactic plane:

[33]: IceCube Collaboration (2023), Observation of high-energy neutrinos from the Galactic plane

[64]: Amenomori et al. (2021), First Detection of sub-PeV Diffuse Gamma Rays from the Galactic Disk: Evidence for Ubiquitous Galactic Cosmic Rays beyond PeV Energies

[65]: Cao et al. (2023), Measurement of Ultra-High-Energy Diffuse Gamma-Ray Emission of the Galactic Plane from 10 TeV to 1 PeV with LHAASO-KM2A

[66]: Fang and Murase (2023), Decomposing the Origin of TeV–PeV Emission from the Galactic Plane: Implications of Multimessenger Observations



Chapter 3

Active galactic nuclei

Most galaxies, if not all, host a supermassive black hole at their center. In 10-15% of galaxies, the emission from the central region can reach $10^2 - 10^3$ times the luminosity of the host galaxy. These regions are known as active galactic nuclei (AGNs). However, the mechanism that triggers this activity remains unknown.

In 1943, Carl Seyfert discovered that some galaxies contain strongly emitting components at their centers, producing high-excitation nuclear emission lines superimposed on a normal star-like spectrum [67]. However, it was not until the development of radio astronomy that these objects attracted significant attention. The groundbreaking idea that AGNs are powered by accretion onto a supermassive black hole was first proposed in 1964 [68, 69]. This chapter provides a brief overview of AGN physics, with a particular focus on a subclass of AGNs – blazars.

AGNs:

[67]: Seyfert (1943), Nuclear Emission in Spiral Nebulae
[68]: Salpeter (1964), Accretion of Interstellar Matter by Massive Objects.
[69]: Zel'dovich and Novikov (1965), Relativistic Astrophysics. I

3.1 AGN structure

Supermassive black hole and accretion disk

A central supermassive black hole (SMBH), shown at the bottom center of **Figure 3.1**, powers the AGN. SMBH have masses ranging from $\sim 10^6$ to $\sim 10^{10}$ Solar masses M_{\odot} . The accretion of matter onto the SMBH releases a significant amount of gravitational potential energy given by:

$$L_{\text{AGN}} = \epsilon \dot{M} c^2 \quad (3.1)$$

where ϵ is the energy conversion efficiency and \dot{M} is the accretion rate.

The size of an SMBH is on the order of $\sim 10^{-3}$ pc. For a stationary, non-charged black hole, this corresponds to the Schwarzschild radius (or gravitational radius):

$$r_g = \frac{2GM}{c^2} \quad (3.2)$$

The accretion disk, composed of hot plasma, extends up to 1 pc (or $\sim 100 r_g$). Its thermal emission is typically observed from the infrared (IR) to ultraviolet (UV) wavelengths. The standard accretion disk model describes it as radiatively efficient, geometrically thin, and optically thick [70].

AGN composition:

[70]: Shakura and Sunyaev (1973), Black holes in binary systems.

Observational appearance [71]: Hickox and Alexander (2018), "Obscured Active Galactic Nuclei"

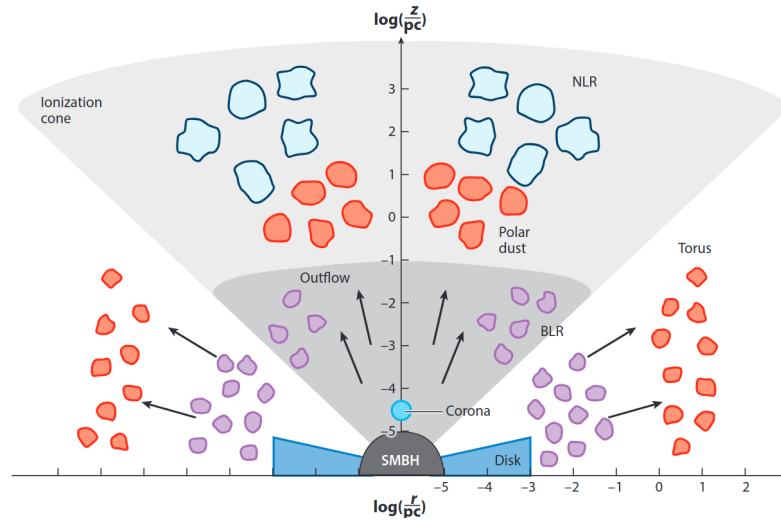


Figure 3.1: Schematic representation of the AGN physical model. Figure from Hickox and Alexander [71].

During accretion, the inner regions of the disk experience increasing radiation pressure due to Thomson scattering in the highly energetic plasma. If the accretion rate becomes too high, this radiation pressure can overcome gravity and expel material from the disk. Consequently, a maximum luminosity is reached when the outward radiation force balances the inward gravitational pull. This threshold is known as the *Eddington luminosity*:

$$L_{\text{Edd}} = \frac{4\pi GM_{\text{BH}}m_p c}{\sigma_T} \approx 1.4 \cdot 10^{46} \left(\frac{M_{\text{BH}}}{10^8 M_{\odot}} \right) [\text{erg/s}] \quad (3.3)$$

Here, M_{BH} is the mass of the SMBH, m_p is the proton mass, c is the speed of light, and σ_T is the Thomson cross-section. Although this limit is derived under the assumption of spherical accretion, it provides a useful

order-of-magnitude estimate and serves as an approximate upper bound for the luminosity of AGNs.

Beyond accretion, a rotating black hole itself can act as an energy source. The *Blandford–Znajek process* describes how the black hole’s rotational energy can be extracted via magnetic fields and converted into Poynting flux [72]. Additionally, angular momentum can be extracted magnetically from the accretion disk through the *Blandford–Payne process* [73]. These two processes are the most widely accepted mechanisms for jet formation.

Corona

The *corona* is a hypothesized region in active galactic nuclei (AGNs), located in the vicinity of the accretion disk and composed of hot plasma. It was proposed as a model to explain the X-ray emission observed in certain classes of AGNs, particularly radio-quiet AGNs (see [Section 3.2.1](#)). In this framework, thermal photons emitted from the accretion disk undergo inverse Compton scattering within the optically thin, high-temperature plasma of the corona. X-ray observations suggest coronal temperatures can reach up to $\sim 10^9$ K [e.g. 74]. For typical AGNs, the characteristic size of the corona is estimated to be $R \lesssim 10 r_g$ [75]. [Figure 3.1](#) illustrates the corona as a compact region located just above the accretion disk. However, the precise geometry of AGN corona remains uncertain, with possible configurations including inner-disk regions or extended structures above the disk, such as conical or spherical geometries. The physical mechanism responsible for coronal heating also remains an open question.

BLR, NLR and dusty torus

Clouds that have been ionized by radiation from the accretion disk orbit the supermassive black hole (SMBH) at various distances. Those located closer to the center (at ~ 0.1 pc) form the *broad-line region (BLR)*. These clouds are denser and move at higher velocities, resulting in Doppler-broadened emission lines. In contrast, clouds situated farther from the SMBH (at ~ 10 – 100 pc) are less dense and move more slowly, producing narrower spectral lines. This area is known as the *narrow-line region (NLR)*.

The *dusty torus* is a structure located at ~ 10 pc from the center and is composed of dust and dust-like molecular gas. It is optically and geometrically thick and opaque to optical radiation. The dusty torus can reprocess optical emission by absorbing it and re-emitting part of the energy as infrared radiation.

Jets

About 10% of all AGNs emit relativistic *jets* of plasma, which are launched perpendicular to the accretion disk. These jets originate from the immediate vicinity of the SMBH and can remain collimated over distances of up to

SMBH:

[72]: Blandford and Znajek (1977), Electromagnetic extraction of energy from Kerr black holes
[73]: Blandford and Payne (1982), Hydromagnetic flows from accretion disks and the production of radio jets.

Corona: [74]: Zdziarski et al. (1994), Physical processes in the X-ray / gamma-ray source of IC 4329A [75]: Kara et al. (2016), A global look at X-ray time lags in Seyfert galaxies

\sim Mpc scales. Radio observations reveal the relativistic motion of plasma structures, known as blobs, propagating outward from the central region. The exact composition of jets remains uncertain, aside from the presence of an electron (or positron) population responsible for radio synchrotron emission. Other possible components include protons, heavier nuclei, and Poynting flux.

3.2 AGN zoo

AGN zoo:

[76]: Urry and Padovani (1995), Unified schemes for radio-loud active galactic nuclei

Since AGNs, unlike stars, do not have spherical symmetry, their observable properties naturally depend on their orientation relative to the observer's line of sight. As a result, AGNs can demonstrate different properties while being physically the same type of objects. Orientation effects are fundamental to the AGN unification scheme [76]. Besides the viewing angle, AGNs are also classified as either radio-loud or radio-quiet, based on the presence or absence of a radio jet.

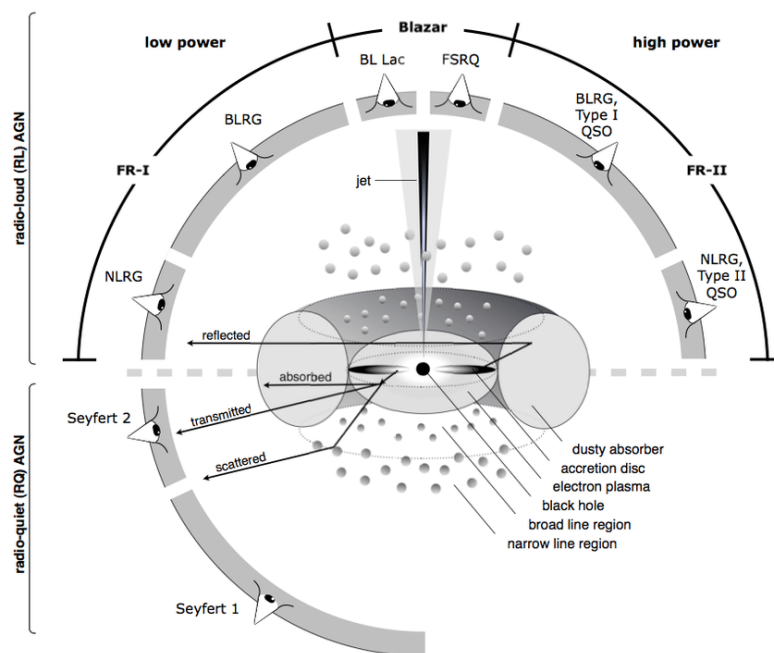


Figure 3.2: AGNs unification scheme. The observed properties of AGN depend on the viewing angle and the presence or absence of a radio jet. Figure from Beckmann and Shrader [77].

AGN zoo:

[77]: Beckmann and Shrader (2012), Active Galactic Nuclei

[78]: Padovani et al. (2017), Active galactic nuclei: what's in a name?

The following sections present some of the most commonly used AGN classifications, many of which were originally established for historical reasons. With advancements in astronomical instrumentation, our understanding of these sources has significantly improved. Today, more than 40 distinct AGN classes can be identified, primarily based on jet power and accretion efficiency [78].

3.2.1 Radio-quiet AGNs

The majority of AGNs (80–90%) do not exhibit radio-detectable jets and are therefore classified as radio-quiet. These can be further divided into Type 1 (including Seyfert 1 and radio-quiet QSOs) and Type 2 objects (such as Seyfert 2).

Seyfert galaxies

This type of AGN is often found in gas- and dust-rich spiral galaxies. Seyfert galaxies are typically located at lower redshifts compared to other AGN classes, mostly at $z < 0.3$ [79]. Seyfert 1 galaxies exhibit both strong broad and narrow emission lines in their spectra, whereas Seyfert 2 galaxies display only narrow emission lines across the near-infrared, optical, and ultraviolet bands. However, since some objects show characteristics of both subclasses, Seyfert galaxies can be assigned fractional classifications based on the relative strength of their broad and narrow lines (e.g., Seyfert 1.9 has weaker broad lines than Seyfert 1.5).

Radio-quiet QSOs

Similar to Seyfert galaxies, radio-quiet quasi-stellar objects (QSOs), or quasars, have no jets. These objects exhibit bright emission from their central regions, often outshining their host galaxies and thus appearing as point sources—hence their historical classification as quasi-stellar objects. QSOs share many characteristics with Seyfert 1 galaxies but are significantly more luminous, possibly due to smaller viewing angles. Unlike Seyfert galaxies, most radio-quiet QSOs reside in giant elliptical galaxies and are typically found at higher redshifts ($z > 1$) [80].

3.2.2 Radio-loud AGNs

The fraction of AGNs that produce jets—and are thus classified as radio-loud—is less than 20% of the total AGN population [81]. Although radio-loud AGNs share similar environments and physical properties with their radio-quiet counterparts, the reason why some AGNs develop jets while others do not remains unclear. Within the framework of the Blandford-Znajek jet

Seyfer galaxies:

[79]: Peña-Herazo et al. (2022), Turin-SyCAT: A multifrequency catalog of Seyfert galaxies

Radio-quiet QSOs:

[80]: Ridgway et al. (2002), "HST NICMOS imaging of $z \sim 2-3$ radio-quiet quasars"

Radio-loud AGNs

[81]: Jiang et al. (2007), The Radio-Loud Fraction of Quasars is a Strong Function of Redshift and Optical Luminosity
[82]: Ghisellini et al. (2014), The power of relativistic jets is larger than the luminosity of their accretion disks

Radio-loud AGNs

[83]: Chiaberge et al. (2015), Radio Loud AGNs are Mergers

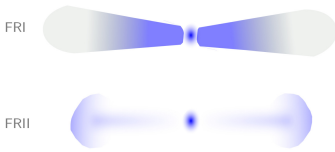


Figure 3.3: Typical radio luminosity distribution of FR I and FR II galaxies. A more intense blue color corresponds to higher luminosity. Figure from [84].

Quasars:

[84]: Ndung'u et al. (2023), Advances on the morphological classification of radio galaxies: A review
[85]: Wang et al. (2021), A luminous quasar at redshift 7.642

Blazars:

[85]: Wang et al. (2021), A luminous quasar at redshift 7.642
[86]: Strittmatter et al. (1972), Compact extragalactic nonthermal sources
[87]: Stein et al. (1976), The BL Lacertae objects

formation mechanism, this distinction may be related to differences in black hole spin, with high-spin black holes more likely to produce jets. Observational evidence supports this hypothesis [82]. Additionally, galaxy mergers may play a significant role in producing rapidly spinning SMBHs, which in turn power jetted AGNs [83].

Radio galaxies

Radio galaxies are jetted AGNs observed at large inclination angles, which often results in the appearance of two-sided jets extending over large distances. When observed at radio frequencies, these galaxies are classified into two categories: low-luminosity Fanaroff–Riley class I (FR I) and high-luminosity Fanaroff–Riley class II (FR II). The primary distinction between these classes lies in the distribution of radio emission across the central region and jets (see Figure 3.3). FR I sources are typically core-dominated, while FR II sources are lobe-dominated, exhibiting prominent edge-brightening.

Radio-loud quasars

Radio-loud quasars are the jetted counterparts of radio-quiet QSOs and are observed at intermediate inclination angles. Their emission lines typically exhibit features from both the broad-line region (BLR) and the narrow-line region (NLR). Owing to their high luminosity, quasars can be detected at redshifts exceeding $z > 7$ [85].

Blazars

Blazars are the most powerful, yet rarest, class of AGNs. Only $\sim 7\%$ of jetted AGNs are blazars [78], accounting for less than 1% of all AGNs. Blazars are characterized by jets that are closely aligned with the observer's line of sight ($\theta_{obs} < \sim 10^\circ$), resulting in significant relativistic boosting of their radiation (see Section 3.3). They are divided into two subclasses: BL Lac objects and flat-spectrum radio quasars (FSRQs).

BL Lac objects are named after the first identified source of this class, BL Lacertae, which was initially misclassified as a variable star. Subsequent studies distinguished BL Lacs from other AGN classes [86, 87] based on the following characteristics:

- (a) the featureless optical spectrum,
- (b) rapid variability in all wavelengths,
- (c) dominance of the non-thermal emission,
- (d) strong and rapidly varying polarization.

The absence of spectral features in BL Lac objects makes it difficult, and in many cases impossible, to determine their redshifts.

The second subclass of blazars, known as flat-spectrum radio quasars (FSRQs), satisfies criteria (b)–(d) but also exhibits broad emission lines in their spectra. Studies of their broadband spectral energy distributions [88]

indicate that FSRQs typically host more massive black holes, have brighter accretion disks, and possess larger broad-line regions (BLRs) that reprocess disk emission. Blazars with $L_{BLR}/L_{Edd} > 5 \times 10^{-4}$ can be classified as FSRQs [88].

3.3 Blazars as extreme AGNs

Special relativity of jets

The relativistic motion of blazar jets plays a crucial role in making them such powerful sources. If an observer is located at angle θ with respect to the jet symmetry axis, a photon emitted in the jet frame is detected in the observer's frame¹ with the energy given by:

$$E' = \frac{\delta_D}{1+z} E \quad (3.4)$$

where E is the photon energy in the jet (comoving) frame, E' is the photon energy in the observer's frame, z is the redshift, and δ_D is the Doppler factor defined as:

$$\delta_D(\theta_{\text{obs}}) = \frac{1}{\Gamma_b(1 - \beta \cos \theta_{\text{obs}})} \quad (3.5)$$

where Γ_b is the bulk Lorentz factor of some region moving along the jet, $\beta = v/c$ is the normalized speed of individual particle and θ_{obs} is the angle between jet symmetry axis and observer's line of sight. For $\cos \theta_{\text{obs}} = \beta$ (also meaning $\sin \theta_{\text{obs}} = 1/\Gamma_b$ or for small angles just $\theta_{\text{obs}} = 1/\Gamma_b$), the Doppler factor simplifies as $\delta_D = \Gamma_b$. The element of the solid angle transforms as follows (for more details see [89, Chapter 3.2.5]):

$$d\Omega = \frac{d\Omega'}{\delta_D^2} \quad (3.6)$$

If we consider the specific intensity – defined as the energy per unit area, per unit time, per unit frequency, per unit solid angle – it transforms between the source and observer frames as:

$$\begin{aligned} I(\nu) &= h\nu \frac{dN}{d\nu dt d\Omega dA} \\ &= \delta h\nu \frac{dN'}{\delta d\nu' (dt'/\delta_D) (d\Omega'/\delta_D) dA'} \\ &= \delta_D^3 I'(\nu') = \delta_D^3 I(\nu/\delta_D) \end{aligned} \quad (3.7)$$

which, after integration over all frequencies, leads to

Blazars:

[88]: Ghisellini et al. (2011), The transition between BL Lac objects and flat spectrum radio quasars

¹Starting from this point and throughout the thesis, quantities measured in the observer's frame will be denoted with a prime, while the corresponding unprimed quantities refer to values in the source frame.

Special relativity of jets:

[89]: Ghisellini (2013), Radiative Processes in High Energy Astrophysics

Variability:

- [90]: Böttcher et al. (2012), Special Relativity of Jets
 [91]: Aharonian et al. (2007), An Exceptional Very High Energy Gamma-Ray Flare of PKS 2155-304
 [92]: Albert et al. (2007), Variable Very High Energy γ -Ray Emission from Markarian 501
 [93]: Marscher and Gear (1985), Models for high-frequency radio outbursts in extragalactic sources, with application to the early 1983 millimeter-to-infrared flare of 3C 273.
 [94]: Virtanen and Vainio (2005), Particle acceleration in thick parallel shocks with high compression ratio
 [95]: Giannios et al. (2009), Fast TeV variability in blazars: jets in a jet
 [96]: Blondin et al. (2008), Time dilation in type Ia supernova spectra at high redshift

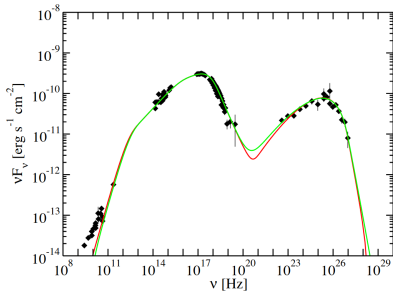


Figure 3.4: The spectral energy distribution of a blazar Mrk 421. Figure from [97].

SED:

- [97]: Abdo et al. (2011), Fermi Large Area Telescope Observations of Markarian 421
 [98]: Alfvén and Herlofson (1950), Cosmic Radiation and Radio Stars

$$I = \delta_D^4 I' \quad (3.8)$$

If an isotropic spherical emitter is located within a relativistically moving source at a luminosity distance d_L , its luminosity is $L = 4\pi d_L^2 F$ where F is the observed flux. $F \propto \int_{\Omega_s} I d\Omega$, therefore F transforms similarly to I . Therefore, the luminosity transforms between the source and observer frames as:

$$L = \delta_D^4 L' \quad (3.9)$$

Variability

Variability is a prominent feature of blazars, observed across all energy bands and over a wide range of timescales. Radio and optical variability typically occurs on timescales of about a day [90, p. 32] and has been recognized since the earliest observations of blazars. More recent observations in the very-high-energy (VHE) gamma-ray regime have revealed minute-scale variability at energies exceeding 100 GeV [91, 92]. The physical origin of this variability remains uncertain, with several mechanisms proposed, including internal shocks propagating along the jet [93], stochastic particle acceleration driven by turbulence [94], and magnetic reconnection events within the jet [95], among others.

Variability imposes an important constraint on the characteristic size of the emission region. Any rapid change in photon flux is limited by the finite speed of light, introducing a delay known as the light-crossing time $\Delta t \sim R/c$. Due to relativistic effects, this timescale is shortened in the observer's frame and transforms as $\Delta t' = \Delta t/\delta_D$. Additionally, the observed timescale is further stretched by a factor of $1/(1+z)$ due to the cosmological expansion of the Universe (see e.g. Appendix A in [96]). Thus, the resulting constraint on the size of the emission region can be written as:

$$R' \leq \frac{c\Delta t'\delta_D}{1+z} \quad (3.10)$$

Broad-band photon emission

The jet emission from blazars is so bright that it typically outshines all other components of the AGN. The characteristic spectral energy distribution (SED) of a blazar displays a distinctive two-bump structure, as shown in **Figure 3.4**. The low-energy emission originates from synchrotron radiation produced by relativistic electrons. Alfvén and Herlofson [98] first suggested that the radio emission from Cygnus A could be interpreted as synchrotron radiation from cosmic-ray electrons gyrating

in a star's magnetic field. A few years later, Shklovsky [99] proposed that both the radio and optical emissions could come from the same population of electrons in the Crab Nebula. The hypothesis of synchrotron radiation was confirmed by the detection of optical linear polarization from the jet in M87 [100]. In most cases, the radio, infrared, optical, and ultraviolet emissions from blazars are of synchrotron origin.

The origin of the high-energy bump remains unknown. The simplest explanation suggests Comptonization of the synchrotron photons by the same electron population that produced the synchrotron emission. Additionally, high-energy emission could originate from hadronic interactions. This will be discussed in detail in the following chapters.

Blazar sequence

In 1998, Fossati et al. [101], based on an analysis of 128 sources, demonstrated that blazars with synchrotron peaks at lower frequencies tend to be brighter gamma-ray emitters. This empirical relationship between the synchrotron peak frequency and gamma-ray luminosity led to the formulation of the blazar sequence, as illustrated in Figure 3.5. With advancements in gamma-ray astronomy and the detection of over 1500 gamma-ray blazars by the *Fermi-LAT* satellite, Ghisellini et al. [102] proposed a revised version of this sequence, known as the *Fermi* blazar sequence.

Blazars can be sub-classified based on the location of their synchrotron peak [103]: sources with a peak frequency below 10^{14} Hz are classified as low-synchrotron-peaked (LSP) blazars, those peaking between 10^{14} Hz and 10^{15} Hz as intermediate-synchrotron-peaked (ISP) blazars, and those with peaks above 10^{15} Hz as high-synchrotron-peaked (HSP) blazars. The majority of observed IBLs and HBLs are low-luminosity BL Lac objects, whereas FSRQs, which exhibit high gamma-ray luminosities, are predominantly classified as LSPs.

SED:

[99]: Shklovsky (1958), Optical emission from the Crab nebula in the continuous spectrum
[100]: Baade (1956), Polarization in the Jet of Messier 87.

Blazar sequence:

[101]: Fossati et al. (1998), A unifying view of the spectral energy distributions of blazars
[102]: Ghisellini et al. (2017), The Fermi blazar sequence
[103]: Abdo et al. (2010), The Spectral Energy Distribution of Fermi Bright Blazars
[104]: Ghisellini (2016), The Blazar Sequence 2.0

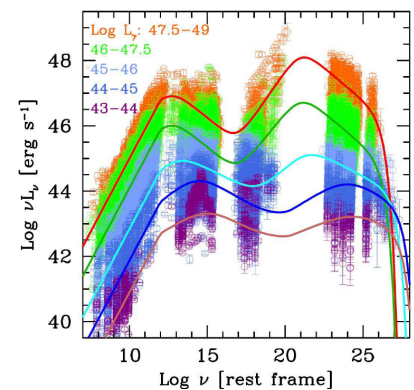
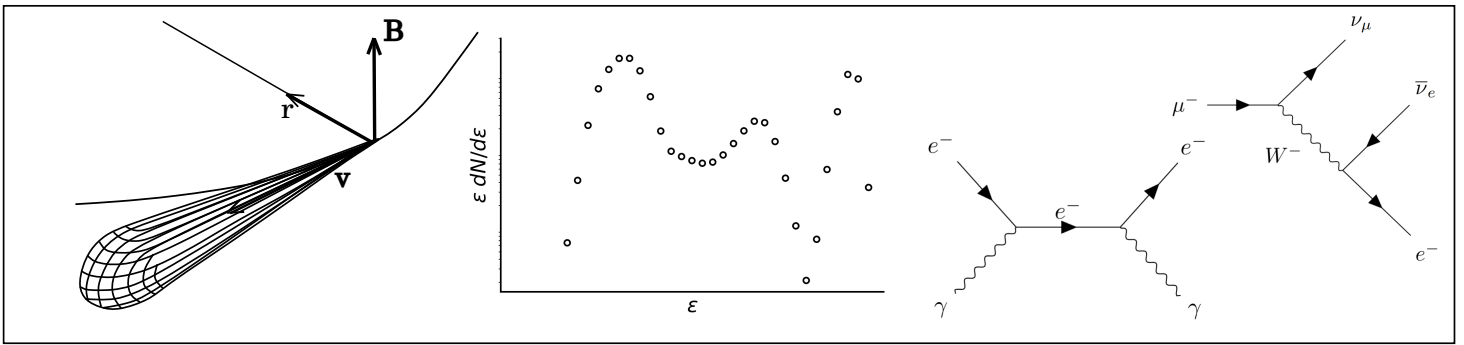


Figure 3.5: Representation of blazar sequence. Figure from [104].



Chapter 4

Numerical modeling of blazar emission

In order to know the truth, it is necessary to imagine a thousand falsehoods.

A card on the door of Sidney Coleman's office, from the letter of R. Socolow

Numerical modeling serves two main purposes: (1) testing theoretical models by comparing their predictions with data, and (2) exploring the nature of observed phenomena, assuming the models accurately reflect reality. For blazar observations, the second purpose is more common. Understanding blazar emission begins with identifying the photon emission mechanisms, characterizing them, and evaluating their relevance. Next, one must determine the source conditions that enable particle interactions producing the observed photon fluxes. These topics are discussed in [Section 4.1](#) and [Section 4.2](#). [Section 4.3](#) introduces the key principles of numerical modeling and common assumptions. The final section briefly reviews studies on gamma-ray-emitting blazars and potential neutrino sources.

4.1 Radiation processes

While many astrophysical sources emit thermal radiation, most of the blazar emission has a non-thermal origin. Non-thermal radiation mechanisms can be broadly divided into two categories: leptonic and hadronic. Leptons are elementary particles with half-integer spin that do not participate in strong interactions, whereas hadrons are composite particles made of quarks, bound together by the strong force. Radiation processes are categorized as leptonic or hadronic based on the type of particles responsible for the emission.

4.1.1 Leptonic processes

Although the term lepton applies to electrons, muons, and taus, the most prevalent leptons in astrophysical environments are electrons (and their antiparticles, positrons). Electrons are naturally abundant in astrophysical plasmas, and as the lightest leptons, they are the easiest to produce through various interactions. Consequently, all subsequent discussions of radiation processes will primarily focus on electrons.

Synchrotron emission

Any charged particle moving with acceleration in a magnetic field emits electromagnetic radiation. If the particle's kinetic energy is smaller than or comparable to its rest energy $m_i c^2$, the emitted radiation is referred to as *cyclotron radiation*. In the case of ultra-relativistic particles (kinetic energy $\gg m_i c^2$), the emitted radiation is called *synchrotron radiation*.

The energy loss via synchrotron radiation can be expressed as

$$-\left(\frac{dE}{dt}\right)_{syn} = \frac{4}{3} \frac{8\pi}{3} \left(\frac{Q^2}{mc^2}\right)^2 c u_B \beta^2 \gamma^2 \quad (4.1)$$

where Q is the particle's charge, γ is the particle's Lorentz factor, and $u_B = B^2/8\pi$ (for more details see [\[105, Chapter 7.2\]](#)). It follows from the

Synchrotron emission:
[\[105\]](#): Dermer and Menon (2009), High Energy Radiation From Black Holes: Gamma Rays, Cosmic Rays, and Neutrinos

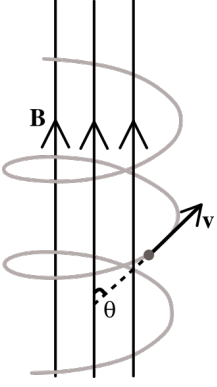


Figure 4.1: Particle gyrating in the magnetic field \mathbf{B} . θ is a pitch angle.

Eq. (4.1) that $-(dE/dt)_{syn} \propto 1/m_i^2$ meaning that heavier particles cool faster.

The power per unit frequency emitted by a single electron with a given Lorentz factor and pitch angle (an angle between the particle velocity and the magnetic field, see **Figure 4.1**) is

$$P_s(\nu, \gamma, \theta) = \frac{\sqrt{3}e^2B \sin \theta}{m_e c^2} \frac{\nu}{v_c} \int_{\nu/v_c}^{\infty} K_{5/3}(y) dy \quad (4.2)$$

with $v_c = \frac{3}{2}v_s \sin \theta$ and $v_s = \gamma^2 \frac{eB}{2\pi m_e c}$. $K_{5/3}(y)$ is the modified Bessel function of order 5/3 which peaks at $\nu \simeq 0.29v_c$. v_c is called the critical frequency. Below the peak, the synchrotron spectrum can be approximated as a power-law with an index 1/3. After the peak, the spectrum decays exponentially, proportionally to $e^{-\nu/v_c}$.

In most cases, however, the photon signal is caused by the emission of multiple electrons, not just one. If the spectrum of the electrons has a power-law shape $N(\gamma) = K\gamma^{-p} = N(E) \frac{dE}{d\gamma}$ for $\gamma_{min} \leq \gamma \leq \gamma_{max}$, the synchrotron power per solid angle can be calculated as

$$\epsilon_s(\nu, \theta) = \frac{1}{4\pi} \int_{\gamma_{min}}^{\gamma_{max}} N(\gamma) P(\nu, \gamma, \theta) d\gamma \quad (4.3)$$

which results into

$$\epsilon_s(\nu, \theta) \propto KB^{(p+1)/2} \nu^{-(p-1)/2} \quad (4.4)$$

Therefore, a population of electrons with energies following a power-law distribution with index p produces a synchrotron spectrum that also follows a power law, with a spectral index $\alpha = (p - 1)/2$. The emitted photon frequencies range from $\nu_{min} = \gamma_{min}^2 v_s$ to $\nu_{max} = \gamma_{max}^2 v_s$ with an exponential cutoff in photon flux occurring beyond ν_{max} .

The counterpart process to synchrotron emission is synchrotron self-absorption. The intensity of the synchrotron self-absorption scales as $I \propto \nu^{5/2} B^{-1/2}$, which changes the shape of the synchrotron spectrum at lower frequencies.

Inverse Compton effect

The Compton effect is a scattering process between an electron and a photon in which part of the photon's energy is transferred to the electron. In astrophysical environments, relativistic electrons often carry significantly more energy than the surrounding photons. When electrons transfer a portion of their energy to incoming photons, the process is known as the *inverse Compton effect* (IC).

Depending on the photon energy in the electron rest frame, we distinguish between the Thomson regime ($\gamma_e h\nu \ll m_e c^2$) and the Klein-Nishina regime ($\gamma_e h\nu \geq m_e c^2$). In the Thomson regime, the electron recoil can be neglected, and the process can be treated as classical elastic scattering. The Klein-Nishina regime, however, requires treatment of electron recoil and accounting for quantum effects.

The energy loss rate of an electron in an isotropic photon field and the Thomson regime can be estimated as

$$-\left(\frac{dE}{dt}\right)_T = \frac{4}{3}c\sigma_T m_e c^2 \gamma^2 \beta^2 u_T \quad (4.5)$$

with $\sigma_T = (8\pi/3)(q^2/m_e c^2)^2$, $u_T = \int_0^{1/\gamma} \epsilon n_{ph}(\epsilon) d\epsilon$ (for more details see [105, Chapter 6.4]). The energy loss in the IC process looks similar to the synchrotron energy loss, except that the magnetic energy density is replaced by the photon energy density. Also, similarly to the synchrotron emission, heavier particles have a higher energy loss rate. In the case of an isotropic photon distribution, the average photon energy after scattering with high-energy electrons ($\gamma_e \gg 1$) is $\epsilon'_f \sim \gamma_e^2 \epsilon'_i$, where the subscripts f and i refer to the final and initial photon energies, respectively.

If relativistic electrons are present in a region with both magnetic and photon fields, they will lose energy through both synchrotron emission and inverse Compton scattering. The ratio of the two luminosities is defined as

$$\frac{L_{syn}}{L_{IC}} = \frac{u_B}{u_T} \quad (4.6)$$

Synchrotron self-absorption and IC scattering in the Klein–Nishina regime may introduce slight deviations from Eq. (4.6).

Photon-photon interactions

In certain dense astrophysical environments, gamma-gamma interactions become significant. The process $\gamma + \gamma \rightarrow e^+ + e^-$ has a threshold of

$$E_{\gamma_1} E_{\gamma_2} (1 - \cos \theta) > 2(m_e c^2)^2 \quad (4.7)$$

where θ is the angle between the colliding photons (as shown in **Figure 4.2**).

The cross section for this process [106] can be expressed as

$$\sigma_{\gamma\gamma} = \frac{3\sigma_T}{16} (1 - \beta^2) \left[2\beta(\beta^2 - 2) + (3 - \beta^4) \ln \frac{1 + \beta}{1 - \beta} \right] \quad (4.8)$$

where $\beta = \sqrt{1 - \frac{2(m_e c^2)^2}{E_{\gamma_1} E_{\gamma_2} (1 - \cos \theta)}}$, also shown in **Figure 4.3** as a function of $E_{\gamma_1} E_{\gamma_2} (1 - \cos \theta) / 2(m_e c^2)^2$. In an isotropic radiation field (averaged over θ), the maximum value of the cross-section is reached at $\sim 4(m_e c^2)^2$ with $\sigma_{\gamma\gamma} \approx 0.25\sigma_T$ before decaying steeply as photon energy increases. Most interactions occur near the threshold, enabling an estimate of the typical energy carried by the electrons. A photon with the dimensionless energy $\epsilon_1 = E_{\gamma_1}/m_e c^2$ interacts predominantly with photons of energy $\epsilon_2 = 1/\epsilon_1$. This results into a total energy (assuming here $E_{\gamma_1} > E_{\gamma_2}$) of $E_{tot} = (\epsilon_1 + 1/\epsilon_1)m_e c^2 \approx E_{\gamma_1}$ implying that each lepton carries energy $E_{\gamma_1}/2$.

IC effect:

[105]: Dermer and Menon (2009), High Energy Radiation From Black Holes: Gamma Rays, Cosmic Rays, and Neutrinos

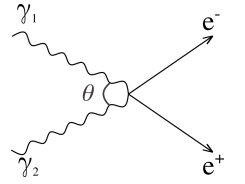


Figure 4.2: Photon-photon pair production.

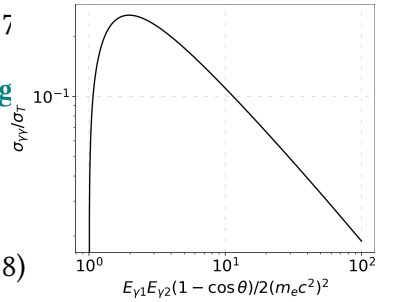


Figure 4.3: Photon-photon cross section (in the units of Thomson cross section) as a function of $E_{\gamma_1} E_{\gamma_2} (1 - \cos \theta) / 2(m_e c^2)^2$.

$\gamma - \gamma$ interactions:

[106]: Dwek and Krennrich (2013), The extragalactic background light and the gamma-ray opacity of the universe

4.1.2 Hadronic interactions

Although the term "hadrons" refers to a variety of composite particles, the most common hadrons in astrophysical environments are protons. Heavier nuclei, which are part of cosmic rays, can also contribute to photon production in hadronic processes. In this section, only interactions between protons and photons are considered.

Many astrophysical environments provide opportunities for proton-proton interactions. However, this is not the case for blazars, where the jet environment is not expected to contain a significant proton target field, in contrast to the (dense) photon fields created by synchrotron emission, the BLR, and thermal photons from the accretion disk. Proton-proton interactions in blazars may occur in extremely rare events, such as a star passing through the jet or during tidal disruption events. Given the low probability of observing signatures of pp interactions in blazar jets, this process will not be considered in any of the following models.

Photon-pion production

Photo-pion production is a process in which a pion π is produced through the interaction of a nucleus N and with photon γ of energy E_γ . Both neutral pions π^0 and charged pions π^\pm can be produced in this process. For simplicity, the following discussion will consider cosmic-ray protons with Lorentz factor γ_p . This process has a threshold of

$$E_{th} = \frac{m_p m_\pi + m_\pi^2}{\epsilon_\gamma} \simeq 1.5 \times 10^{17} \left[\frac{\epsilon_\gamma}{1\text{eV}} \right]^{-1} \text{ eV} \quad (4.9)$$

Figure 4.4 shows the total cross section as a function of photon energy in the proton rest frame $\epsilon_r = \gamma_p E'_\gamma$. The photo-pion production has three main channels:

1. Δ^+ (1232) *resonance production*, followed by its decay into either $p\pi^0$ (in 2/3 of cases) or $n\pi^+$ (in 1/3 of cases), is the dominant channel up to approximately 1 GeV. Its cross-section peaks at $\epsilon_r \approx 0.32$ GeV. Smaller peaks at $\epsilon_r > 0.5$ GeV correspond to the subdominant production of heavier resonances.
2. *Direct production* $p + \gamma \rightarrow n + \pi^+$ dominates at lower energies between the production threshold of ~ 0.15 GeV and ~ 0.25 GeV. It contributes 30% to the total cross-section up to 1 GeV.
3. *Multi-pion production* accounts for the high-energy tail of the cross-section in the energy region $\epsilon_p > 1$ GeV.

The produced pions decay through the following channels:

$$\begin{aligned} \pi^+ &\rightarrow \mu^+ + \nu_\mu \\ \pi^- &\rightarrow \mu^- + \bar{\nu}_\mu \\ \pi^0 &\rightarrow \gamma + \gamma \end{aligned} \quad (4.10)$$

with the subsequent muon decay

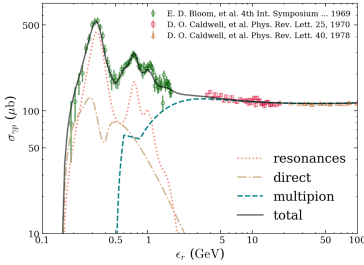
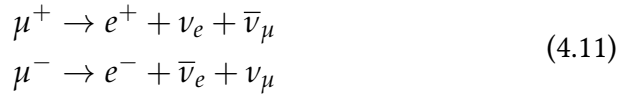


Figure 4.4: Total $p\gamma$ cross section as a function of photon's energy ϵ_r . Figure from [107].

$p - \gamma$ interactions:
[107]: Morejon et al. (2019), Improved photomeson model for interactions of cosmic ray nuclei



In addition, free neutrons decay as



Protons lose $\sim 20\%$ of their energy in $p\gamma$ interactions, meaning that the energy of the secondary particles can be estimated as $\langle E_\gamma \rangle \sim 0.5E_p$, $\langle E_e \rangle \sim 0.1E_p$ and $\langle E_\nu \rangle \sim 0.25E_p \sim 0.05E_p$.

In the Δ^+ (1232) resonance production, photons carry approximately 20% of the proton's energy, which is roughly the same amount of energy carried by the four produced neutrinos (three from pion decay and one from neutron decay). This suggests that the luminosities of high-energy gamma rays and neutrinos are comparable, highlighting an important connection between these two messengers.

Bethe-Heitler pair production

At energies below the threshold for photo-pion production, a photon can produce an electron-positron pair in the electric field of a nucleus, in a process known as Bethe-Heitler pair production. The threshold condition for this process is

$$\gamma_p h\nu > 2m_e c^2 \quad (4.13)$$

where $\gamma_p = E_p/m_p c^2$ is the proton Lorentz factor. The maximum energy of the electron (positron) is given by

$$E_{e,max} = \frac{\gamma_p}{1 + 4\gamma_p h\nu / (m_p c^2)} \left(\sqrt{\gamma_p h\nu} + \sqrt{\gamma_p h\nu - m_e c^2} \right)^2 \quad (4.14)$$

Figure 4.5 shows the energy distributions of electrons and positrons (combined) produced in proton interactions with CMB photons ($T = 2.7$ K). The curves correspond to three different proton energies. The distribution of electrons and positrons produced in the Bethe-Heitler pair creation process is shown with dashed lines. The spectrum has a bell shape with a broad maximum around $\sim 10^{-3}E_p$ [108].

4.2 Blazar radiation models

As briefly described in **Section 3.3**, the SED of a blazar typically exhibits a two-bump structure and originates from non-thermal processes. The radiation processes discussed in **Section 4.1** can explain the nature of blazar emission. However, several different blazar radiation models exist, and this section provides a brief overview of them.

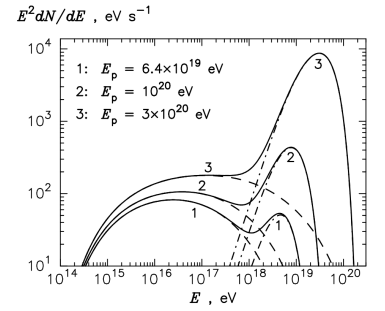


Figure 4.5: The energy distributions of electrons and positrons produced in the interactions of protons of different energies with CMB photons. Dashed lines correspond to the Bethe-Heitler process. Figure from [108].

Bethe-Heitler process: [108]: Kelner and Aharonian (2008), Energy spectra of gamma rays, electrons, and neutrinos produced at interactions of relativistic protons with low energy radiation

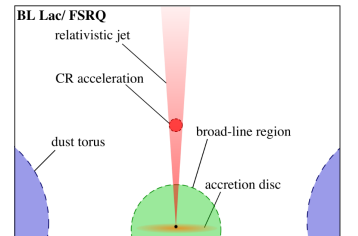


Figure 4.6: The geometry of a typical one-zone model. Figure from [109].

One-zone models: [109]: Rodrigues et al. (2018), Neutrinos and Ultra-high-energy Cosmic-ray Nuclei from Blazars

4.2.1 One-zone models

The assumption that the low-energy emission (infrared, optical, ultraviolet) originates from synchrotron radiation of relativistic electrons is usually consistent with observed data. However, the nature of the high-energy part of the SED remains unclear.

The simplest explanation for the SED suggests that the high-energy emission is produced in the same region as the low-energy emission, with the same population of relativistic electrons responsible for the entire spectrum. The emission region is often approximated by a simple spherical geometry (in the source frame) and is referred to as a “blob”. This blob, with the radius R' , is assumed to propagate along the jet as illustrated in **Figure 4.6** with a bulk Lorentz factor Γ_b . In this basic model, the magnetic field inside the blob is assumed to be isotropic and homogeneous. One-zone models can be categorized based on the particles responsible for gamma-ray production, namely: purely leptonic, purely hadronic, and leptohadronic models.

Leptonic models:

[110]: Maraschi et al. (1992), A Jet Model for the Gamma-Ray-emitting Blazar 3C 279

[111]: Dermer and Schlickeiser (1993), Model for the High-Energy Emission from Blazars

[112]: Sikora et al. (1994), Comptonization of Diffuse Ambient Radiation by a Relativistic Jet: The Source of Gamma Rays from Blazars?

[113]: Bloom and Marscher (1996), An Analysis of the Synchrotron Self-Compton Model for the Multi-Wave Band Spectra of Blazars

[114]: Ghisellini and Tavecchio (2009), Canonical high-power blazars

Hadronic models:

[115]: Böttcher et al. (2009), Implications of the very high energy gamma-ray detection of the quasar 3C279

[116]: Aharonian (2000), TeV gamma rays from BL Lac objects due to synchrotron radiation of extremely high energy protons

[117]: Mücke et al. (2003), BL Lac objects in the synchrotron proton blazar model

[118]: Liodakis and Petropoulou (2020), Proton Synchrotron Gamma-Rays and the Energy Crisis in Blazars

Purely leptonic models

The simplest one-zone model, which requires only a population of accelerated electrons to explain the entire SED, is called the *synchrotron self-Compton* (SSC) model. In this scenario, electrons produce low-energy synchrotron radiation, which then serves as the target photon field for inverse Compton scattering by the same electron population [see e.g. 110, 111, 112, 113].

While SSC models can effectively explain the SEDs of many blazars, some FSRQs with powerful accretion disks require modifications to this model. In FSRQs, the BLR reprocesses radiation from the accretion disk, re-emitting it as both broad lines and a thermal continuum. Additionally, the dusty torus absorbs some of the accretion disk’s emission and thermally re-emits it in the infrared range. In these cases, the BLR and dusty torus can provide additional targets for inverse Compton interactions, contributing to the SED depending on the location of the emission region [e.g. 114]. A model that incorporates these additional target photon fields is called the one-zone *external field model*.

Purely hadronic models

The SEDs of some blazars cannot be accurately reproduced by purely leptonic models (e.g., 3C 279 [115]), highlighting the need for more complex approaches. One such scenario involves a population of high-energy protons coexisting with electrons in the same emission region. Purely hadronic models propose that the dominant source of high-energy photons is proton synchrotron emission [116, 117]. These models are typically characterized by high magnetic field strengths (~ 100 G, compared to the $\sim 10^{-3} - 1$ G range found in leptonic models) and significantly higher jet power.

Lioudakis and Petropoulou [118] studied a sample of 145 Fermi blazars and concluded that a proton synchrotron origin for gamma rays would require a proton luminosity of at least ~ 100 Eddington luminosities for LSP

and ISP sources. Their findings are consistent with earlier results based on a smaller sample of 12 blazars [119]. Both studies suggest that the proton synchrotron component can only be subdominant, or dominate for brief periods such as flares.

Leptohadronic models

Alternatively, both leptonic and hadronic processes may contribute to the gamma-ray emission, with the leptonic component typically dominating. In this scenario, high-energy protons interact with synchrotron photons produced by electrons, leading to the generation of gamma rays and neutrinos. Although the hadronic contribution is generally subdominant, it can become significant during short-lived episodes such as flares. Since this model will be frequently referenced throughout the thesis, a detailed description is provided in [Chapter 5](#).

4.2.2 Multi-zone models

Although one-zone models are the primary focus of this thesis, a brief overview of several proposed multizone models is provided below.

Spine-sheath model

The motivation for the so-called spine-sheath models comes from radio observations of blazar jets, which revealed two key features: first, a difference in polarization angle between the inner and outer regions of the jet (initially observed in the FSRQ PKS B1055+018 [120], and later in other sources), and second, the outer edges of the jet appear brighter than the central region (e.g., [121]). This model has been discussed and applied to selected sources in [122, 123, 124].

Extended jet model

The extended jet model is motivated by observations of large-scale jet structures in some sources, which exhibit inhomogeneities, or “knots”, visible in radio and X-rays, as well as extended gamma-ray emission [125]. This model also incorporates results from relativistic magnetohydrodynamical simulations to more accurately describe the jet geometry, kinetic flow, and magnetic field structure. The first leptonic extended jet model applied to AGNs was presented in [126], while more recent work has discussed leptohadronic extended jet models and their applications [127].

Turbulent extreme multi-zone model

The Turbulent Extreme Multi-Zone (TEMZ) model was motivated by the observed high variability in flux and polarization in blazars. In this model, the jet consists of numerous small turbulent cells, each with a quasi-homogeneous magnetic field [128]. On larger scales, interactions among these turbulent cells can lead to particle acceleration via shocks and magnetic reconnection, while also providing sufficient targets for particle interactions.

Hadronic models:

[119]: Zdziarski and Böttcher (2015), Hadronic models of blazars require a change of the accretion paradigm

Mutli-zone models:

[120]: Attridge et al. (1999), Radio jet-ambient medium interactions on parsec scales in the blazar 1055+018
 [121]: Giroletti and others (2004), Parsec-Scale Properties of Markarian 501
 [122]: Tavecchio and Ghisellini (2015), On the magnetization of BL Lac jets
 [123]: Sikora et al. (2016), A spine-sheath model for strong-line blazars
 [124]: Acciari et al. (2020), Testing two-component models on very high-energy gamma-ray-emitting BL Lac objects
 [125]: Abdalla et al. (2020), Resolving acceleration to very high energies along the jet of Centaurus A
 [126]: Potter and Cotter (2012), Synchrotron and inverse-Compton emission from blazar jets – I. A uniform conical jet model
 [127]: Zacharias et al. (2022), ExHaLe-jet: an extended hadro-leptonic jet model for blazars – I. Code description and initial results
 [128]: Marscher (2013), Turbulent, extreme multi-zone model for simulating flux and polarization variability in blazars

4.3 Numerical approach

Numerical approach:

[129]: Klinger et al. (2024), AM³: An Open-source Tool for Time-dependent Lepto-hadronic Modeling of Astrophysical Sources ; see also <https://am3.readthedocs.io/en/latest/>

State-of-the-art modeling

The research presented in this thesis employs the AM³ code (Astrophysical Multi-Messenger Modeling), a software package designed to efficiently solve the coupled integro-differential equations describing the temporal evolution of particle spectral densities [129]. The kinematics of the various particle species is described by a system of Boltzmann equations, each corresponding to a specific particle type, which are coupled via collision terms.

The equation for evolution of particle density $n_i(E, t) = \frac{\partial^2 N}{\partial E \partial V}$ where i corresponds to different particle species can be written as

$$\partial_t n_i(E, t) = -\partial_E[\dot{E}_i(E, t)n_i(E, t)] - \alpha_i(E, t)n_i(E, t) + Q_i(E, t) \quad (4.15)$$

where α is an escape (sink) term, Q is a source (injection) term, and \dot{E}_i is a cooling term. The indices in α_i, Q_i, \dot{E}_i should be interpreted as sums over all processes j for species i ($\alpha_i = \sum_j \alpha_i^j$). The source term Q_i for interactions of the type $a + b \rightarrow c + d$ is obtained by integrating the corresponding differential cross sections. Details on the treatment of particle interactions and the numerical solver implementation can be found in [129].

Steady-state approximation

AM³ is a time-dependent code and allows tracing the temporal evolution of particle energy densities as well as setting time-dependent model parameters. However, blazar radiation models usually adopt *steady-state approximation* which is defined by

$$\partial_t n_i(E, t) = 0 \quad (4.16)$$

for all particle species i .

The characteristic timescale of the system, also known as the *dynamical timescale*, is often set to the escape timescale $t_{dyn} = R/c$, assuming that particles escape the emission region at the speed of light. The numerical equations are evolved over multiple dynamical timescales to ensure that a steady state is achieved.

4.4 Application to blazars

4.4.1 Gamma-ray emitters

Advancements in gamma-ray astronomy have significantly increased the number of detected sources that produce high-energy radiation, with blazars being the primary contributors to the GeV and TeV emission observed in the gamma-ray sky [130, 131, 132]. Radiation models play a crucial role in understanding the underlying physics of blazars. Many of

Gamma-ray emitters:

[130]: Di Mauro et al. (2014), Fermi-LAT γ -ray anisotropy and intensity explained by unresolved radio-loud active galactic nuclei
[131]: Ajello et al. (2015), The Origin of the Extragalactic Gamma-Ray Background and Implications for Dark Matter Annihilation
[132]: Bose et al. (2022), Galactic and extragalactic sources of very high energy gamma rays

the pioneering studies that developed the concept of SSC models (see [Section 4.2.1](#)) were specifically aimed at explaining the gamma-ray emission from blazars. Since then, one-zone models have been applied to a large number of gamma-ray-active blazars.

Modeling individual blazars provides predictions for the required magnetic field strengths and typical electron energy values in the source. In addition, modeling blazar samples offers valuable insights into the physics of this class of sources. For instance, [133] modeled a sample of 12 blazars from various types within the blazar sequence using both leptonic and hadronic models. The study concluded that protons carry most of the power in both scenarios. In the leptonic case, if jet neutrality is required, cold protons (which do not radiate) still dominate the jet's kinetic power. In hadronic models, the SED could not be explained without invoking high proton luminosities. As another example, one-zone models have been used to demonstrate that the power of relativistic jets in blazars exceeds the luminosity of their accretion disks [134].

4.4.2 Possible neutrino emitters

Blazars were established as potential neutrino emitters much later, following the discovery of the first neutrino source candidate in this class, TXS 0506+056 (already discussed in [Section 2.5](#)). Since then, only a few blazars have been associated with possible neutrino emission. A brief overview of these sources, along with key modeling studies, is provided below.

TXS 0506+056

After the discovery of a high-energy neutrino that was spatially and temporally coincident with the flare of TXS 0506+056, several groups modeled the source [e.g., 135, 136, 137]. Within the framework of one-zone leptohadronic models, they independently concluded that the number of expected neutrino events in IceCube during the six-month flare should not exceed 0.05. Higher neutrino emission would be incompatible with the observed electromagnetic spectrum. A neutrino rate of 0.05 per six months would also require extremely high jet power. For the archival flare of TXS 0506+056 in 2014–2015 [53], most models cannot produce a sufficient neutrino flux that would be compatible with multi-wavelength observations [138, 139].

PKS 1502+106

PKS 1502+106 is a bright gamma-ray-emitting blazar. However, during the detection of a 300 TeV neutrino (IC-190730A), PKS 1502+106 was quiet at gamma-ray energies. The neutrino emission from PKS 1502+106 can be explained if the neutrino- and gamma-ray-emitting region is located close to the SMBH and interacts with photons from the broad-line region [140]. If the emission zone is located further down the jet, a leptohadronic model predicts 0.1 neutrino events in 10 years but lowers the proton power requirements to well below the Eddington luminosity [141].

Gamma-ray emitters:

[133]: Böttcher et al. (2013), Leptonic and hadronic modeling of Fermi-detected blazars

[134]: Ghisellini et al. (2014), The power of relativistic jets is larger than the luminosity of their accretion disks

TXS 0506+056:

[135]: Gao et al. (2018), "Modelling the coincident observation of a high-energy neutrino and a bright blazar flare"

[136]: Cerruti et al. (2018), Leptohadronic single-zone models for the electromagnetic and neutrino emission of TXS 0506+056

[137]: Keivani et al. (2018), A Multimessenger Picture of the Flaring Blazar TXS 0506+056: Implications for High-energy Neutrino Emission and Cosmic-Ray Acceleration

[53]: Aartsen et al. (2018), Neutrino emission from the direction of the blazar TXS 0506+056 prior to the IceCube-170922A alert

[138]: Rodrigues et al. (2019), Leptohadronic Blazar Models Applied to the 2014–2015 Flare of TXS 0506+056

[139]: Petropoulou et al. (2020), Multi-epoch Modeling of TXS 0506+056 and Implications for Long-term High-energy Neutrino Emission

[140]: Rodrigues et al. (2021), Multiwavelength and Neutrino Emission from Blazar PKS 1502 + 106

[141]: Oikonomou et al. (2021), Multi-messenger emission from the parsec-scale jet of the flat-spectrum radio quasar PKS 1502+106 coincident with high-energy neutrino IceCube-190730A

PKS B1424-418:

[142]: Gao et al. (2017), On the Direct Correlation between Gamma-Rays and PeV Neutrinos from Blazars

PKS B1424-418

In 2013, the flare of the blazar PKS B1424-418 was found to be temporarily and spatially coincident with the detection of a ~ 2 PeV cascade neutrino event, IC-35. [142] show that models with a hadronic origin of gamma rays cannot adequately describe the SED of this blazar. A leptohadronic model with a subdominant hadronic contribution is required and predicts 0.3 neutrino events during the burst.

3HSP BZB J0955+3551:

[143]: Petropoulou et al. (2020), Comprehensive Multimessenger Modeling of the Extreme Blazar 3HSP J095507.9+355101 and Predictions for IceCube

3HSP BZB J0955+3551

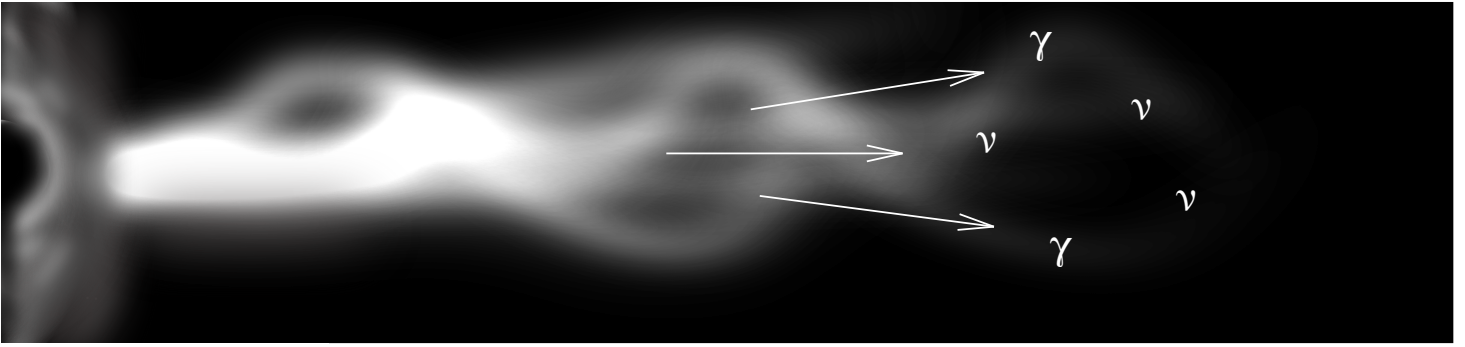
Neutrino IC-200107A arrived from the direction of the blazar 3HSP BZB J0955+3551 during a hard X-ray flare. Leptohadronic modeling [143] revealed a low Poisson probability ($\sim 3\%$) of detecting one neutrino in 10 years of IceCube observations. The most promising scenarios also predict strong intra-source gamma-ray attenuation above 100 GeV.

GB6 J1040+0617:

[144]: Wang and Xue (2021), Hadronuclear interpretation of the possible neutrino emission from PKS B1424-418, GB6 J1040+0617 and PKS 1502+106

GB6 J1040+0617

A high-energy neutrino event, IC-141209A, was associated with the blazar GB6 J1040+0617, as GB6 J1040+0617 was the only gamma-ray source located 0.7° from the best-fit neutrino position. Its gamma-ray flare and strong optical activity coincided with the detection of IC-141209A. The two-zone model by [144], which accounts for both pp and $p\gamma$ interactions, explains the observed SED and predicts a neutrino rate of 0.64 yr^{-1} during the flare.



Chapter 5

Individual candidates for neutrino emitting blazars

All models are wrong, but some are useful.

George E. P. Box

Despite advances in neutrino astronomy, confirmed associations between neutrino detections and specific astrophysical sources remain rare. Detecting neutrinos during a powerful multi-wavelength flare may be considered a fortunate event. The first section of this chapter is dedicated to modeling exactly this kind of source – PKS 0735+178.

The work presented in [Section 5.1](#) is based on Omeliukh et al. [145], for which I am the leading author. I contributed to the data collection, performed the leptonic and leptohadronic modeling, and carried out the analysis of the results.

[145]: Omeliukh et al. (2025), "Multi-epoch leptohadronic modeling of neutrino source candidate blazar PKS 0735+178"

[146]: Abe et al. (2024), Time-dependent modelling of short-term variability in the TeV-blazar VER J0521+211 during the major flare in 2020

[147]: Omeliukh et al. (2025), On the possible contributions of two nearby blazars to the NGC 4151 neutrino hotspot

Unlike PKS 0735+178, the blazar VER J0521+211 has no neutrinos currently associated with it – at least not yet. Nevertheless, this source exhibited flaring activity in TeV gamma rays in February 2020, with flux variations occurring on day-long timescales. Section 5.2 discusses this short-term variability within the framework of one-zone leptohadronic models and explains why this blazar can become a promising target for future neutrino telescopes.

The work presented in [Section 5.2](#) is based on Abe et al. [146], for which I performed leptohadronic modeling, analyzed the results, and contributed to the discussion.

Recent discoveries of neutrino signals from nearby Seyfert galaxies have expanded the list of potential neutrino sources to include other classes of AGNs. In the case of IceCube's second most significant neutrino-emitting Seyfert galaxy, NGC 4151, two gamma-ray active blazars are located nearby and may contribute to the observed signal. The third section of this chapter discusses this possibility.

The work presented in [Section 5.3](#) is based on Omeliukh et al. [147], for which I am the leading author. I contributed to the data collection for constructing the SEDs, performed both leptonic and leptohadronic modeling, and analyzed the results.

5.1 Multiple neutrinos from PKS 0735+178

As mentioned in [Section 4.4.2](#), a temporal and spatial coincidence between a neutrino detection and a gamma-ray flare observed from a blazar suggests a possible physical association between the two events.

In early December 2021, IceCube [\[148\]](#), Baikal-GVD [\[149\]](#), the Baksan Underground Scintillation Telescope [\[150\]](#), and KM3NeT [\[151\]](#) reported multiple neutrino events that were temporally and spatially coincident with the brightest gamma-ray flare ever observed from the blazar PKS 0735+178. In addition to its gamma-ray activity, the blazar was simultaneously active in the optical, infrared, ultraviolet, and X-ray bands. PKS 0735+178 is considered a promising neutrino source, as this marks the first time that multiple neutrino detectors have observed events from the same region of the sky.

5.1.1 Data collection and data analysis

Blazar PKS 0735+178 was one of the first sources identified as a ‘classical BL Lac’ object due to the absence of prominent broad emission lines in its spectrum [\[152\]](#). Therefore, as is common with BL Lac objects (see [Section 3.2.2](#)), estimating the distance to the host galaxy is challenging. In this work, a redshift of $z = 0.45$ is adopted for PKS 0735+178, based on the measurement by Nilsson et al. [\[153\]](#), which is also consistent with the absorption redshift reported by Carswell et al. [\[152\]](#) within uncertainties.

Neutrino emission

On 8 December 2021, the IceCube real-time alert system [\[154\]](#) identified a track-like event, IceCube-211208A, with a 30% probability of being an astrophysical neutrino [\[148\]](#). The reconstructed energy of the neutrino was estimated to be 172 TeV. Approximately four hours later, Baikal-GVD reported the detection of a 43 TeV cascade event with a $\sim 50\%$ probability of astrophysical origin [\[149\]](#). Additionally, four days prior to the IceCube event, the Baksan Underground Scintillation Telescope detected a muon neutrino with energy exceeding 1 GeV [\[150\]](#), consistent with the location of PKS0735+178 and the directions of the neutrinos detected by IceCube and Baikal-GVD.

[Figure 5.1](#) shows the uncertainty contours for the arrival directions of neutrinos detected by the three neutrino observatories. The blazar PKS 0735+178 lies just outside the 90% uncertainty region of IceCube-211208A. Nevertheless, a potential association between the neutrino and the blazar remains plausible, given the possibility of systematic uncertainties in IceCube’s localization and the expectation that approximately 10% of the real counterparts may fall outside this region, as argued by Sahakyan et al. [\[155\]](#).

The KM3NeT neutrino observatory did not detect any neutrinos from the direction of PKS 0735+178 within a one-day window before and after the IceCube event. However, an extended search covering the entire month of December 2021 revealed an 18 TeV neutrino event in ARCA

PKS 0735+178:

[\[148\]](#): IceCube Collaboration (2021), IceCube-211208A - IceCube observation of a high-energy neutrino candidate track-like event
[\[149\]](#): Dzhilkibaev et al. (2021), Baikal-GVD observation of a high-energy neutrino candidate event from the blazar PKS 0735+17 at the day of the IceCube-211208A neutrino alert from the same direction
[\[150\]](#): Petkov et al. (2021), Baksan Underground Scintillation Telescope observation of a GeV neutrino candidate event at the time of a gamma-ray flare of the blazar PKS 0735+17, a possible source of coinciding IceCube and Baikal high-energy neutrinos
[\[151\]](#): Filippini et al. (2022), Search for neutrino counterpart to the blazar PKS0735+178 potentially associated with IceCube-211208A and Baikal-GVD-211208A with the KM3NeT neutrino detectors.
[\[152\]](#): Carswell et al. (1974), Optical Observations of the Radio Source 0735+178
[\[153\]](#): Nilsson et al. (2012), Redshift constraints for RGB 0136+391 and PKS 0735+178 from deep optical imaging
[\[154\]](#): Aartsen et al. (2017), The IceCube realtime alert system
[\[155\]](#): Sahakyan et al. (2022), A multimessenger study of the blazar PKS 0735+178: a new major neutrino source candidate

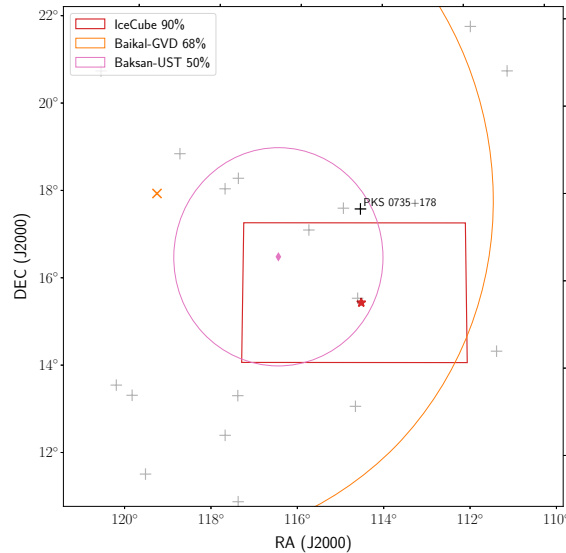


Figure 5.1: Localization of neutrino arrival directions and the position of PKS 0735+178. The gray markers indicate the position of *Fermi*-LAT sources in the 4FGL. Figure from [145].

(high-energy neutrino detection unit) with a weak statistical association (p -value of 0.14). No events were detected in ORCA, the KM3NeT component optimized for low-energy neutrinos [151].

PKS 0735+178:

[145]: Omeliukh et al. (2025), "Multi-epoch leptohadronic modeling of neutrino source candidate blazar PKS 0735+178"
 [151]: Filippini et al. (2022), Search for neutrino counterpart to the blazar PKS0735+178 potentially associated with IceCube-211208A and Baikal-GVD-211208A with the KM3NeT neutrino detectors.

Broad-band light curves

Figure 5.2 presents the multi-wavelength light curves of PKS 0735+178 from 2006 to 2022. In December 2021, the source exhibited its highest gamma-ray activity recorded during the entire *Fermi*-LAT monitoring period. This gamma-ray flare was accompanied by simultaneous flaring across multiple other wavelengths.

Spectral energy distributions

Based on the source's activity in the gamma-ray band, the following blazar activity periods were identified: quiescent state, flare onset (coinciding with the IceCube neutrino arrival), flare peak, and flare decline. The dates corresponding to these periods are listed in **Table 5.1**. The spectral energy distributions (SEDs) were constructed using observations obtained during these time intervals.

Table 5.1: Selected time periods for SED modeling.

Blazar state	Date	MJD
Quiescent	Jan. 23 – Feb. 2, 2010	55219 – 55233
Neutrino arrival	Dec. 8 – 11, 2021	59556 – 59559
Flare peak	Dec. 17 – 19, 2021	59565 – 59567
Post flare	Dec. 25, 2021 – Jan. 6, 2022	59573 – 59600

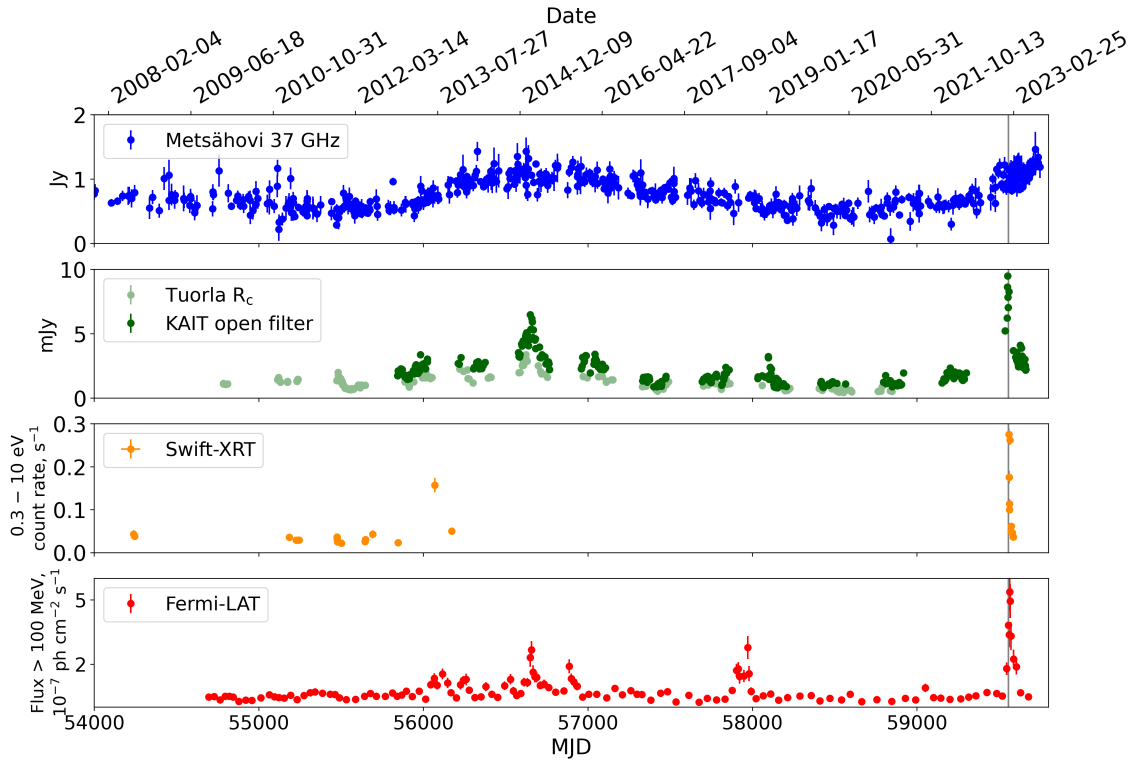


Figure 5.2: Multi-wavelength light curves of PKS 0735+178 from 2006 to 2022. The gray vertical line indicates the time of the IceCube neutrino detection. The light curves show that the source was in an exceptionally high state across all bands at the time of the neutrino’s arrival. Figure reproduced from [145].

Gamma rays

Gamma-ray observations of PKS 0735+178 from the Large Area Telescope (LAT) on board the *Fermi* satellite, collected between August 2008 and May 2022, were analyzed in Garrappa et al. [156], and the results were used for our study. Details of the gamma-ray data analysis are provided in Omeliukh et al. [145]. Additionally, observations by VERITAS and H.E.S.S., conducted shortly after the IceCube neutrino detection, placed constraints on the flux of very-high-energy gamma rays from PKS 0735+178 [157].

X-rays

The X-ray Telescope (XRT) [158] onboard the *Neil Gehrels Swift Observatory* (*Swift*) observed the source 24 times between 20 December 2009 and 6 January 2022. The X-ray integral fluxes between 0.3 and 10 keV from these observations are shown in Figure 5.2. Details on the X-ray data analysis can be found in Omeliukh et al. [145]. Additionally, the X-ray spectrum above 2 keV from the NuSTAR observation on December 11, 2021, as reported by Acharyya et al. [157], was included in the SED data.

PKS 0735+178:

[145]: Omeliukh et al. (2025), "Multi-epoch leptohadronic modeling of neutrino source candidate blazar PKS 0735+178"
 [156]: Garrappa et al. (2024), *Fermi*-LAT follow-up observations in seven years of realtime high-energy neutrino alerts
 [157]: Acharyya et al. (2023), Multiwavelength Observations of the Blazar PKS 0735+178 in Spatial and Temporal Coincidence with an Astrophysical Neutrino Candidate IceCube-211208A
 [158]: Burrows et al. (2004), The Swift X-Ray Telescope

PKS 0735+178:

[159]: Roming et al. (2005), The Swift Ultraviolet/Optical Telescope

[160]: Filippenko et al. (2001), The Lick Observatory Supernova Search with the Katzman Automatic Imaging Telescope

[161]: Li et al. (2003), The Katzman Automatic Imaging Telescope Gamma-Ray Burst Alert System, and Observations of GRB 020813

[162]: Lindfors et al. (2021), Optical and near-infrared observations of PKS 0735+178

[163]: Carrasco et al. (2021), NIR followup of the Blazar PKS 0735+178

[164]: Schlafly and Finkbeiner (2011), Measuring Reddening with Sloan Digital Sky Survey Stellar Spectra and Recalibrating SFD

[165]: Nilsson et al. (2012), Redshift constraints for RGB 0136+391 and PKS 0735+178 from deep optical imaging

[166]: Teräsranta et al. (1998), Fifteen years monitoring of extragalactic radio sources at 22, 37 and 87 GHz

[167]: Lister et al. (2018), MOJAVE. XV. VLBA 15 GHz Total Intensity and Polarization Maps of 437 Parsec-scale AGN Jets from 1996 to 2017

[168]: Domínguez et al. (2011), Extragalactic background light inferred from AEGIS galaxy-SED-type fractions

Ultraviolet and Optical

Simultaneously with the *Swift*-XRT observations, PKS 0735+178 was observed with the UVOT instrument [159] onboard *Swift*. The source was observed in the *W1* band on 31 January 2010, and in the *U*, *B*, *W1*, *M2*, and *W2* bands on 10, 17, 25, and 30 December 2021, as well as 6 January 2022. Additionally, it was observed with the *V* filter on 6 January 2022. PKS 0735+178 has also been monitored in the optical *R* band as part of the Tuorla blazar monitoring program. Measurements taken within the corresponding time frame were used for the quiescent state SED.

The optical light curve is complemented by data obtained with the 76 cm Katzman Automatic Imaging Telescope (KAIT) as part of the Lick Observatory Supernova Search [LOSS; 160] in the *Clear* (open) band, which is close to the *R* band [see 161]. The optical measurement by KAIT on MJD 59559, taken during the neutrino arrival time, was used for the SED modeling.

For the SED modeling of the gamma-ray flare peak, optical and near-infrared (NIR) data were obtained from Lindfors et al. [162]. For the post-flare period, NIR data from Carrasco et al. [163] and optical data from KAIT on MJD 59585 and 59600 were used.

The observed UV, optical, and NIR fluxes were corrected for Galactic extinction using values from Schlafly and Finkbeiner [164]. The contribution of the host-galaxy flux in the UV, optical, and NIR bands is negligible compared to the statistical uncertainties of the flux measurements [165].

Radio

The Metsähovi radio telescope, located in Kirkkonummi, Finland, has been observing the source at 37 GHz for three decades. Details on the instrument and data reduction methods are provided in Teräsranta et al. [166]. The long-term radio light curve is shown in **Figure 5.2**. Additionally, MOJAVE [167] measurements of the 15 GHz radio flux taken two days after the arrival of IceCube-211208A are included in the SED.

5.1.2 Numerical modeling**Simulation framework of one-zone models**

I performed the modeling of PKS 0735+178 within the framework of one-zone models (see **Section 4.2.1**). As typical for these models, radio fluxes cannot originate from the emission zone because it is optically thick to low-frequency radio emission due to synchrotron self-absorption. In addition, the typical size of the emission region obtained from the gamma-ray variability timescales is two to four orders of magnitude smaller than the size of the radio core, which is the dominant emitter of the radio flux. For this reason, the radio fluxes are treated as upper limits.

I utilized the open-source code AM³ (see **Section 4.3**) to model the radiation processes and interactions involving relativistic electrons and protons. The blazar spectra are generated under the steady-state approximation (see **Section 4.3**). Absorption of high-energy gamma rays due to the extragalactic background light (EBL) is included in all models, based on Domínguez et al. [168].

Search for the best solutions

In one-zone models, self-consistent simulations of radiative processes involve a substantial number of free parameters, typically ranging from seven to fourteen. Some of these parameters can be partially constrained by observations. For instance, the gamma-ray variability timescale sets an upper limit on the size of the emission region, while radio observations can help estimate the Lorentz factor of the emitting blob. Nevertheless, the possible parameter values often span wide ranges, making it challenging to determine an optimal set.

I developed a simple and efficient two-step algorithm for identifying best-fit solutions (as demonstrated in [Chapter 6](#)). In the first step, a large number of different SEDs are generated by selecting parameter values that are evenly spaced between their boundary limits. When choosing an equal number of points for each parameter, the total number of models generated is N^m , where m is the number of model parameters (which varies depending on the model) and N is the number of points per parameter (depending on available computational resources). This initial step allows for a coarse identification of the parameter space region containing the best-fit solutions.

In the second step, a local minimization of the goodness of fit is performed within a narrowly defined region of the parameter space. Since all neighboring points around the current best-fit solution are expected to yield lower goodness-of-fit values, their parameter values are used to define new boundaries for the subsequent search. For this local optimization, the `migrad` and `simplex` algorithms from `Minuit` [[169](#), [170](#)] were employed. At this stage, the parameter space is sufficiently constrained, ensuring the convergence of the algorithm.

The advantages of the proposed algorithm include:

1. **Computational efficiency.** Although the initial grid scan requires the generation of a large number of SEDs (in the source frame), these can be reused for other sources. Only the fluxes need to be converted from the source to the observer's frame, and the goodness-of-fit value recomputed – both of which are computationally more efficient than re-simulating the SED. The local minimization must be performed individually for each case, but it typically requires only ~ 200 – 300 SED evaluations.
2. **Simplicity.** The grid scan does not require any decision-making logic to select the next point in parameter space. It is also naturally parallelizable.
3. **Robustness.** The grid scan explores the entire parameter space and can identify multiple viable solutions with comparable goodness-of-fit values.

The primary disadvantage of the method is the computational cost, which increases as a power-law function of the number of model parameters.

Leptonic models

In order to test the simplest assumption, I start the modeling with purely leptonic models. The electrons are assumed to be pre-accelerated

PKS 0735+178:

[[169](#)]: James and Roos (1975), `Minuit` - a system for function minimization and analysis of the parameter errors and correlations

[[170](#)]: Dembinski et al. (2020), `scikit-hep/iminuit`

to a simple power-law spectrum $dN/d\gamma'_e = N_0\gamma'^{-\alpha_e}$ with spectral index α_e , spanning a range of Lorentz factors from γ'_e^{\min} to γ'_e^{\max} . The energy spectrum of the electrons is normalized to the total electron luminosity L'_e with $L'_e = 4/3\pi R_b^3 m_e c^2 \int_{\gamma'_e^{\min}}^{\gamma'_e^{\max}} \gamma'_e dN/d\gamma'_e d\gamma$. These particles are then injected into a single spherical blob of size R'_b (in the comoving frame of the jet) moving along the jet with Lorentz factor Γ_b , where they encounter a homogeneous and isotropic magnetic field of strength B' . As electrons are continuously injected into the radiation zone, they lose energy via synchrotron cooling before leaving the blob, thus, a break in the spectral index of electrons occurs self-consistently. Gamma-ray emission is produced via inverse Compton scattering, with synchrotron photons serving as the target photon field. The jet is assumed to be observed at an angle $\theta_{\text{obs}} = 1/\Gamma_b$ relative to its axis, resulting in a Doppler factor of $\delta_D = \Gamma_b$.

Table 5.2: Boundaries of the parameter space, leptonic models.

Parameter	Value range
R'_{blob} , cm	$[10^{15}, 10^{17.5}]$
B' , gauss	$[0.1, 5]$
Γ_b	$[3.0, 30.0]$
γ_e^{\min}	$[10^{3.0}, 10^4]$
γ_e^{\max}	$[10^4, 10^5]$
α_e	$[0.5, 3.5]$
L'_e / erg s ⁻¹	$[10^{42}, 10^{47}]$

To explore the seven-dimensional parameter space of the leptonic models, I performed a simple grid scan probing 10 points per dimension, resulting in 10^7 simulated models. The parameters of the leptonic models and the boundaries of the parameter space are given in [Table 5.2](#).

I searched for the best-fit parameters in two steps. First, for each of the four SEDs, each corresponding to a different period of blazar activity, I evaluated the reduced χ^2 for a set of 10 million simulated models. The reduced χ^2 is calculated as follows:

$$\chi^2 = \frac{1}{N - N_{\text{par}} + 1} \sum_i \frac{(F_i^{\text{data}} - F_i^{\text{model}})^2}{\sigma_i^2}, \quad (5.1)$$

where N is the number of data points, N_{par} the number of free parameters in the model, F_i^{data} are the observed fluxes, F_i^{model} are the predicted fluxes by the model, σ_i are the observed flux measurement uncertainties, and i is the summation index which corresponds to all observed frequencies. The models that predict higher flux values than *Fermi*-LAT sensitivity-based upper limits are rejected because the model fluxes are expected to significantly decrease in the corresponding energy range.

For the blazar states during the 2021 flare, an additional constraint on the radius of the emission region applies:

$$R'_b \leq \frac{\delta_D c t_{\text{var}}}{1 + z}. \quad (5.2)$$

with a value of $t_{\text{var}} = 14.4$ days for the 2021 flare obtained from the gamma ray data analysis; the values of R'_b and δ_D are free model parameters.

Afterward, a local minimization of the reduced χ^2 is performed, using parameter boundaries defined by the neighboring grid values of the initial best-fit region to obtain the final solution. Models for which the values of R'_b and δ_D do not satisfy [Eq. \(5.2\)](#) are rejected.

Leptohadronic models

In an alternative scenario, both electrons and protons are assumed to be pre-accelerated in the source to power-law spectra $dN/d\gamma'_{e,p} =$

$N_{0,e,p} \gamma'_{e,p}^{-\alpha_{e,p}}$ with spectral indices $\alpha_{e,p}$, spanning a range of Lorentz factors from $\gamma'_{e,p}^{\min}$ to $\gamma'_{e,p}^{\max}$. The energy spectra of the electrons and protons are normalized to the corresponding total electron and proton luminosities, L'_e and L'_p defined as $L'_{e,p} = 4/3\pi R^3 m_{e,p} c^2 \int_{\gamma'_{e,p}^{\min}}^{\gamma'_{e,p}^{\max}} \gamma'_{e,p} dN/d\gamma'_{e,p} d\gamma$. Similarly to the leptonic case, electrons and protons undergo interactions and radiate inside of the spherical blob of size R' with a homogeneous and isotropic magnetic field of strength B' moving along the jet with Lorentz factor Γ_b .

The application of the same two-step algorithm (grid scan followed by local minimization) described above would now require significantly more computational resources, as the number of model parameters has increased from seven to ten. To address this issue, I adopted the approach used by Rodrigues et al. [171], Rodrigues et al. [172], in which the infrared (IR), optical, ultraviolet (UV), and gamma-ray fluxes are first fitted with a purely leptonic model, followed by the selection of hadronic parameters to reproduce the X-ray emission. Most of the optical and GeV gamma-ray emission typically originates from leptons, even in models where protons are included in the emission region, as demonstrated by leptohadronic modeling of several neutrino-candidate blazars [e.g., 173, 140, 155]. I fitted first IR, optical, UV, and gamma rays via the grid scan method (using the same boundaries as in Table 5.2) and locally minimize them using `Minuit`. At this stage, the X-ray fluxes are treated as upper limits. Subsequently, protons are added into the AM^3 simulation. All leptonic parameters are fixed to their previously determined values, while four hadronic parameters are varied over a grid of 10^4 combinations. The parameter boundaries used in the hadronic grid scan are listed in Table 5.3. Including $L_p = 0$ in the grid ensures the possibility of convergence to a purely leptonic solution. As a final step, all ten parameters of the leptohadronic models are refined through local minimization using `Minuit`, allowing for small variations (within boundaries set to $\pm 20\%$ of the previous best-fit values).

5.1.3 Results

Purely leptonic fits

The grid scan results revealed that multiple parameter combinations can yield similarly good fits to the data. To illustrate this parameter degeneracy, two physically distinct solutions were selected for each SED, and the surrounding parameter space was further explored. The number of viable solutions could be even greater if the parameter boundaries were extended beyond the limits considered in this study.

The results of the leptonic modeling are presented in Figure 5.3. The corresponding parameter values are listed in Table 5.4. The figure illustrates two best-fit solutions located in distinct regions of the parameter space, representing physically different scenarios. For each epoch, these solutions are classified as “slow” and “fast” according to their Lorentz factors. The slow solutions have Lorentz factors ranging from 2 to 6, while

Table 5.3: Boundaries of the hadronic parameters

Parameter	Value range
γ_p^{\min}	$[10^1, 10^6]$
γ_p^{\max}	$[10^1, 10^9]$
α_p	$[1.0, 3.0]$
$L'_p / \text{erg s}^{-1}$	$[10^{40}, 10^{48}] \cup \{0\}$

PKS 0735+178:

[171]: Rodrigues et al. (2024), Leptohadronic multi-messenger modeling of 324 gamma-ray blazars
 [172]: Rodrigues et al. (2024), The Spectra of IceCube Neutrino (SIN) candidate sources – V. Modeling and interpretation of multiwavelength and neutrino data
 [173]: Cerruti et al. (2019), Leptohadronic single-zone models for the electromagnetic and neutrino emission of TXS 0506+056
 [140]: Rodrigues et al. (2021), Multiwavelength and Neutrino Emission from Blazar PKS 1502 + 106
 [155]: Sahakyan et al. (2022), A multimessenger study of the blazar PKS 0735+178: a new major neutrino source candidate

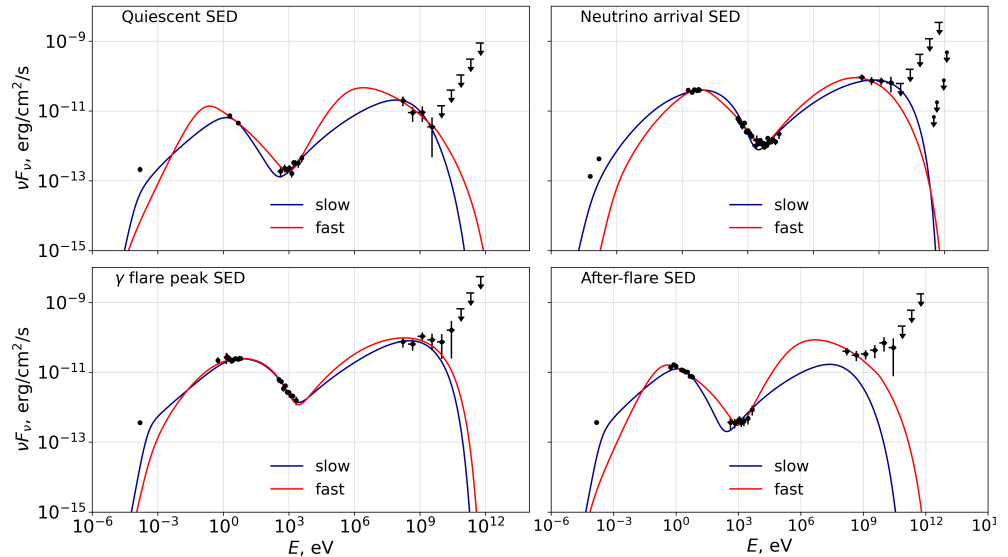


Figure 5.3: Purely leptonic best-fit SEDs of PKS 0735+178 for the selected activity periods. The “slow” and “fast” solutions refer to models with differing Lorentz factors and represent two distinct parameter sets. Model parameters are listed in [Table 5.4](#). Figure from Omeliukh et al. [145].

the fast solutions range from 12 to 18.

For the quiescent state period, variations in magnetic field strength, electron luminosity, and Lorentz factors produce different SED peak shapes. Nevertheless, both models fit the data well, with reduced χ^2 values of 1.4 and 1.1, respectively.

At the time of neutrino arrival, the fast solution features a significantly stronger magnetic field (4 G vs. 0.7 G in the slow model), a softer electron energy spectrum, a smaller emission region, and lower electron luminosity. Despite these differences, both models accurately describe the observed photon fluxes. The larger values of $\chi^2/\text{n.d.f.}$ for all models for this period arise from the five UV data points with $\sim 1\%$ error bars.

A similar distinction between slow and fast solutions is observed at the gamma-ray flare peak. However, in the post-flare phase, neither model successfully reproduces the gamma-ray flux. While both solutions fit optical, UV, and X-ray data well, the slow model underpredicts the gamma-ray flux, whereas the fast model matches the flux level but fails to replicate its spectral shape.

Small variations in certain model parameters can still yield a valid fit. To investigate how changes in each pair of parameters affect the goodness of fit (while keeping the remaining parameters fixed at their best-fit values), I built the contour maps projecting the parameter space. [Figure 5.4](#) shows such a contour map for the fast solution of the neutrino arrival SED, with similar plots for other leptonic models provided in [Appendix A](#). Since the initial grid resolution (ten points per dimension) was insufficient for contour visualization, additional scans were performed by fixing all but two parameters and increasing the resolution to 100 points per di-

Table 5.4: Best-fit leptonic model parameters.

Parameters	Slow solutions				Fast solutions			
	quiescent	neutrino arrival	γ flare peak	post flare	quiescent	neutrino arrival	γ flare peak	post flare
$\log_{10}(R'_b [\text{cm}])$	16.94	16.91	16.67	16.96	15.86	15.22	15.57	15.45
$B' [\text{G}]$	0.79	0.65	2.66	0.60	0.40	4.44	2.27	0.72
Γ_b	2.85	6.21	3.08	5.98	16.08	16.02	12.05	18.49
$\log_{10} \gamma_e^{\text{min}}$	3.90	3.13	3.60	3.30	3.06	3.37	3.00	3.00
$\log_{10} \gamma_e^{\text{max}}$	4.78	4.37	4.38	4.68	5.08	4.50	4.11	4.62
α_e	3.45	0.81	1.23	2.50	3.15	2.72	1.16	2.79
$\log_{10} L'_e [\text{erg/s}]$	44.79	44.15	45.29	43.67	42.62	42.47	43.07	42.51
$\chi^2/\text{n.d.f.}$	1.4	9.6	2.0	3.8	1.1	10.8	2.2	1.4

mension. The color bar indicates reduced χ^2 values, with values above 100 saturated.

The best-fit fast solution for the neutrino arrival period suggests that the synchrotron emission arises from a population of electrons with a soft power-law spectrum, having an index of 2.7. Consequently, the spectrum is dominated by low-energy electrons, leaving the high-energy end poorly constrained, as illustrated in the third row of plots in [Figure 5.4](#). Since the synchrotron peak cannot be reliably determined from the SED (consistent with the findings of Acharyya et al. [157]), the minimum electron energy spans a broad range of possible values. In contrast, the Lorentz factor, magnetic field, and electron luminosity are well constrained, with acceptable fits found only within narrow regions of parameter space around the current solution.

Leptohadronic fits

Given that the leptonic grid scan revealed multiple solutions with similar reduced $\chi^2/\text{n.d.f.}$ values, I modeled the leptohadronic SEDs using the same grid-scan-based approach for both slow and fast solutions.

Before performing local minimization, the models with the lowest reduced χ^2 were selected for each SED and solution type. While the slow and fast leptonic solutions exhibited comparable reduced χ^2 values, the introduction of protons into the emission region led to a notable divergence: the reduced χ^2 values for the slow leptohadronic solutions worsened by more than a factor of two compared to their fast counterparts. Moreover, in the best-fit slow leptohadronic solutions, the hadronic contribution was either negligible or significantly suppressed, favoring the lowest allowed proton energies or luminosities.

The search for leptohadronic solutions was based on the assumption that hadrons primarily contribute to the observed X-ray fluxes, as outlined in [Section 5.1.2](#). Higher Lorentz factors tend to produce a deeper gap in the X-ray spectrum, which can be filled by hadronic emission. As a result, slow solutions naturally favor a leptonic origin of the X-rays, with any hadronic component typically overshooting the observed flux. Consequently, slow leptohadronic models converged toward purely leptonic solutions, with the lowest proton energies or luminosities yielding the best fits. Given the focus on leptohadronic models, all subsequent analysis was restricted to the fast leptohadronic solutions across all selected

PKS 0735+178:

[157]: Acharyya et al. (2023), Multiwavelength Observations of the Blazar PKS 0735+178 in Spatial and Temporal Coincidence with an Astrophysical Neutrino Candidate IceCube-211208A

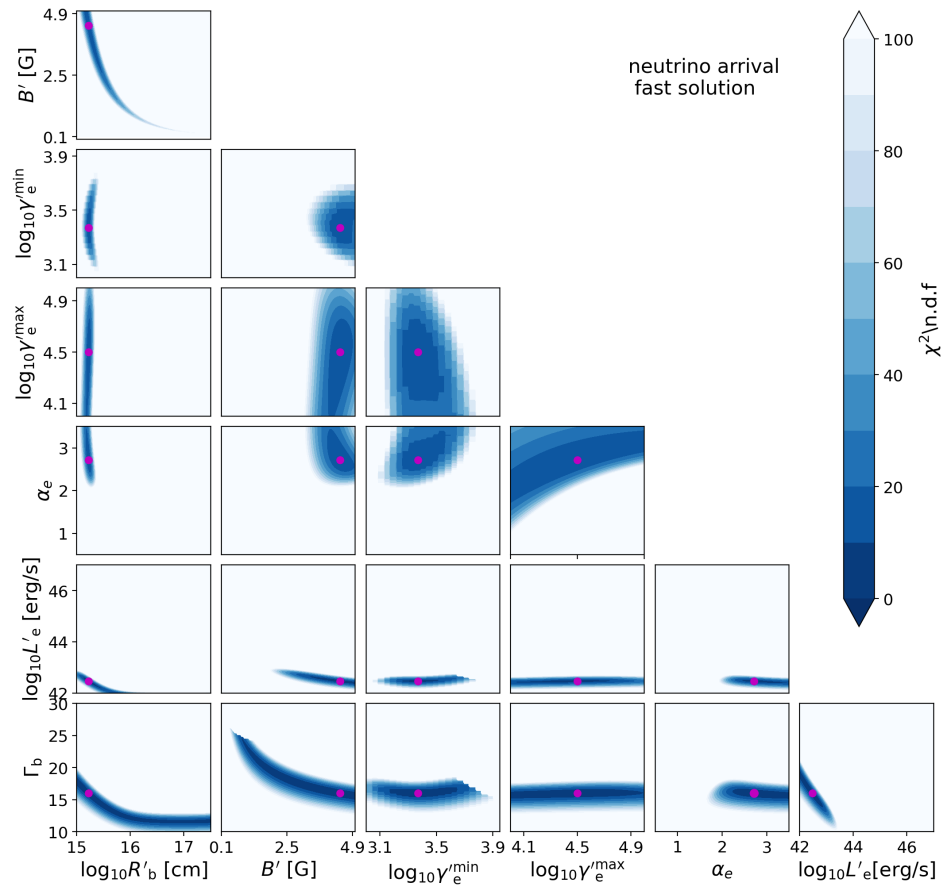


Figure 5.4: Reduced χ^2 values around the best-fit *fast solution* for the *neutrino arrival* SED. Similar plots for other models and SEDs are provided in [Appendix A](#). Figure from Omeliukh et al. [145].

periods of blazar activity.

For the fast leptohadronic solutions, the analysis revealed a degeneracy in the *hadronic* contributions across all models. In addition to the best-fit solution, numerous alternative solutions were identified that shared the same leptonic parameters but differed in their hadronic components. Despite these variations, all solutions yielded nearly identical goodness-of-fit values, with reduced χ^2 differing by less than 2%.

An example of degeneracy in the hadronic contributions is illustrated in **Figure 5.5**. While all the shown leptohadronic models produce comparable photon fluxes that agree with observations, their hadronic components are subdominant and vary in both spectral shape and energy. This variation results in a range of possible neutrino spectra, depicted by the shaded gray region in **Figure 5.5**. The corresponding model parameters are listed in **Table 5.5**.

This degeneracy arises from the fact that the total energy carried by protons can be distributed in multiple ways. For instance, a large number of low-energy protons can produce a similar radiation output as a smaller number of high-energy protons. In **Figure 5.5**, the neutrino spectra for models 1–9 shift toward higher energies as the maximum proton energy increases. Models 2, 3, and 4 share the same minimum and maximum proton energies but differ in their spectral index, leading to a two-order-of-magnitude difference in proton luminosity between models 2 and 4. Models 1–3, characterized by lower proton energies, exhibit high L'_p/L_{Edd} ratios, whereas models 7 and 8 have $L'_p/L_{\text{Edd}} \approx 10^{-4}$. In model 5, hadronic interactions produce a photon spectrum that peaks near the X-ray gap in the SED, which constrains the proton luminosity and results in lower neutrino fluxes compared to the other models.

The collected data for the neutrino arrival SED cover typical observational frequency ranges, including NIR, optical, UV, X-rays, and gamma rays, and effectively constrain the X-ray emission. However, the available data are insufficient to reliably estimate the expected neutrino emission from the source, representing a critical limitation in the modeling's predictive capability. Similar photon energy ranges have been used to study other neutrino-associated blazars, such as TXS 0506+056 and PKS 1502+106. Consistent with those studies, my modeling results indicate that the SED alone does not provide enough constraints to unambiguously predict the neutrino spectrum. A more detailed study of this will be presented in the next chapter.

Among the solutions with different hadronic contributions, I identify the one predicting the highest number of neutrino events in IceCube. This is done by computing the expected number of neutrino events as:

$$N_\nu = \frac{1}{3} T \int \Phi_\nu(E) A_{\text{eff}}(E, \theta) dE, \quad (5.3)$$

where $A_{\text{eff}}(E, \theta)$ is the effective area of the neutrino detector, which depends on the neutrino energy and the source declination, $\Phi_\nu(E)$ is the all-flavor neutrino flux, and T is the exposure time. A factor of 1/3 is included to account for neutrino flavor mixing during propagation, as

PKS 0735+178:

[174]: Aartsen et al. (2017),
All-sky Search for
Time-integrated Neutrino
Emission from
Astrophysical Sources with
7 yr of IceCube Data

only the muon neutrino channel contributes to the detection of track-like events in IceCube. The muon neutrino event rates are computed using IceCube's effective area [174].

The exposure time varies depending on the flare phase: 15 days for the neutrino arrival SED, 8 days for the gamma-ray flare peak, and 27 days for the post-flare period.

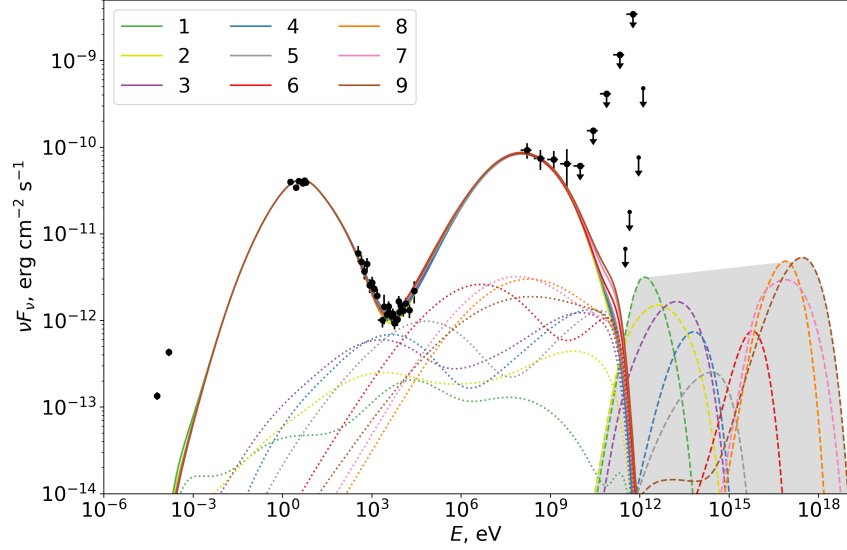


Figure 5.5: Multiple leptohadronic models reproducing the observed photon fluxes during the neutrino arrival period. Solid curves show the total electromagnetic emission, dotted curves indicate the hadronic contribution to the photon flux, and dashed curves represent the predicted all-flavor neutrino spectra. The hadronic parameter values corresponding to each model number in the legend are listed in **Table 5.5**. Figure from Omeliukh et al. [145].

Table 5.5: Parameters of the leptohadronic models shown in **Figure 5.5**. The leptonic parameters in all models are $R'_b = 10^{15.57}$ cm, $B' = 2.2$ G, $\Gamma_b = 15.1$, $\gamma_e^{\min} = 10^{3.46}$, $\gamma_e^{\max} = 10^{4.34}$, $\alpha'_e = 2.42$, $L'_e = 10^{42.65}$ erg s $^{-1}$.

Model number	γ_p^{\min}	γ_p^{\max}	α'_p	$\log_{10} L'_p$	$\chi^2/\text{n.d.f}$
1	3.0	4.0	3.0	48.1	13.33
2	1.0	4.9	2.5	48.82	13.37
3	1.0	4.9	2.0	47.92	13.27
4	1.0	4.9	1.0	46.8	13.21
5	1.5	5.7	1.8	46.4	13.35
6	2.5	6.7	1.5	45.0	13.40
7	7.0	9.0	3.2	44.05	13.24
8	7.0	8.0	2.1	43.88	13.22
9	1.0	9.0	2.5	46.07	13.33

The expected number of neutrino events is calculated for all models satisfying $\delta(\chi^2/\text{n.d.f.}) = \chi_{\text{model}}^2/\text{n.d.f.} - \chi_{\text{best}}^2/\text{n.d.f.} < 1$, corresponding to different hadronic contributions. For each period, the model that yields the highest number of expected neutrino events is selected. These models with the highest neutrino rates are shown in **Figure 5.6** for all analyzed activity phases of PKS 0735+178, with their corresponding parameters listed in **Table 5.6**. Under the assumption of maximizing neutrino fluxes in IceCube, the models predict 0.04 muon neutrino events per year during the quiescent state and 0.1 muon neutrino events during the 50-day 2020–2021 flare.

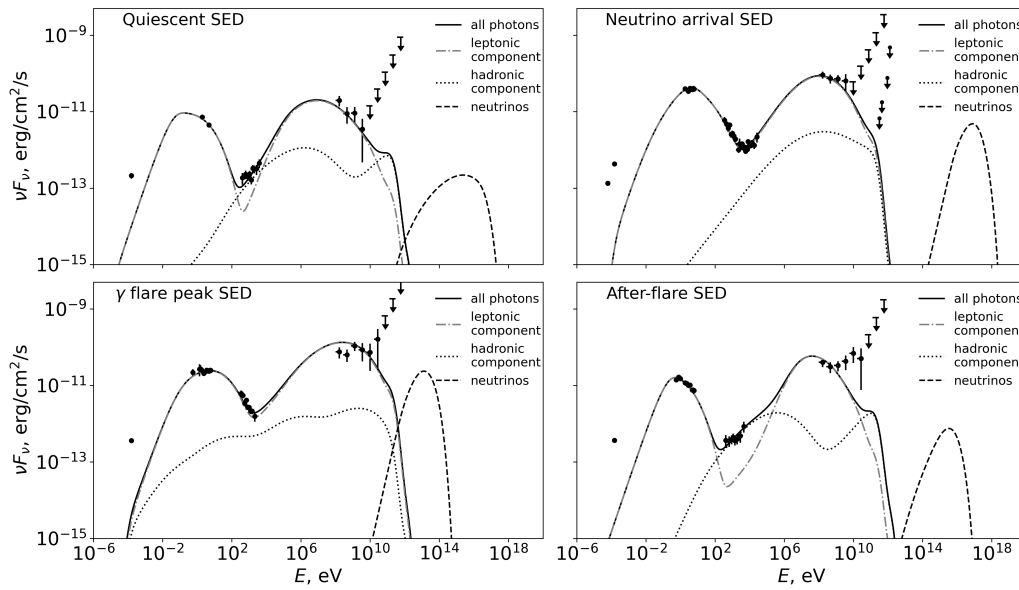


Figure 5.6: Best-fit models for the selected periods of PKS 0735+178 activity under the condition of maximization of neutrino events in IceCube. Figure from Omeliukh et al. [145].

5.1.4 Discussion

Leptonic models successfully reproduce the spectral energy distributions of PKS 0735+178 during both quiescent and active periods. These models assume that an initial population of relativistic electrons emits synchrotron radiation and subsequently upscatters these photons via the synchrotron self-Compton (SSC) process, producing gamma rays. I initially applied this model to all observed SEDs and found good agreement in three out of four activity states, with multiple equally valid solutions for each. However, purely leptonic models cannot account for neutrino emission. While it is possible that neutrinos are produced in a separate region, modeling such a scenario would require additional assumptions regarding geometry, physical conditions, and photon fields, thereby increasing the number of free parameters. To maintain model simplicity, I tested an alternative scenario in which protons are added to the same emission region as the electrons. This addition preserves SSC as the pri-

Table 5.6: Best-fit leptohadronic model parameters with neutrino event rate maximization condition.

Parameters	quiescent	neutrino arrival	γ flare peak	post flare
$\log_{10} R'_b [\text{cm}]$	16.17	15.57	15.54	16.3
$B' [\text{G}]$	0.1	2.28	0.965	0.08
Γ_b	24.0	15.0	17.0	21.0
$\log_{10} \gamma_e^{\text{min}}$	3.0	3.5	3.00	3.44
$\log_{10} \gamma_e^{\text{max}}$	4.17	4.3	4.11	4.21
α_e	2.8	2.42	1.26	2.9
$\log_{10} L'_e [\text{erg/s}]$	42.51	42.65	42.67	42.63
$\log_{10} \gamma_p^{\text{min}}$	2.0	5.0	3.0	3.6
$\log_{10} \gamma_p^{\text{max}}$	7.0	6.0	4.2	6.4
α_p	2.0	1.5	1.25	1.0
$\log_{10} L'_p [\text{erg/s}]$	46.9	46.0	48.33	46.98
$\chi^2/\text{n.d.f.}$	4.4	13.6	4.3	5.3
$N_\nu/\text{time interval}$	0.04/yr	0.03/15d	0.07/8d	0.004/27d

R'_b is the radius of the blob, B' is the magnetic field strength in the emission region, Γ_b is the blob Lorentz factor; $\gamma_{e(p)}^{\text{min}}$ and $\gamma_{e(p)}^{\text{max}}$ are the minimum and maximum Lorentz factor of the electrons (protons) respectively, $\alpha_{e(p)}$ is the spectral index of electrons (protons), $L'_{e(p)}$ is electron (proton) luminosity, $\chi^2/\text{n.d.f.}$ is a value of the reduced χ^2 function, and $N_\nu/\text{(time interval)}$ is a number of expected neutrino events during the selected exposure time (for the flaring state corresponds to the duration of observed state).

primary gamma-ray production mechanism but introduces a hadronic contribution to the X-ray flux and enables neutrino emission. This approach provided good fits for most epochs, avoiding the need for more complex multi-zone models.

Within the one-zone framework, the observed gamma-ray fluxes in the post-flare SED could not be satisfactorily explained. The inability of the algorithm to find any leptonic or leptohadronic model that simultaneously fits both the optical and gamma-ray data suggests the need for an alternative modeling approach. The hard shape of the gamma-ray spectrum, also observed in other sources, might be accounted for by synchrotron self-Compton (SSC) combined with external Compton scattering of photons originating from the BLR [175]. This approach introduces external photon fields emitted by the BLR and adds relatively few free parameters, making it preferable to more complex multi-zone models in cases where leptohadronic models without external fields fail. However, models incorporating external photon fields from the BLR are beyond the scope of this study. Including such fields would introduce at least one additional parameter (e.g., the disk temperature) and significantly increase the complexity of numerical modeling due to added interaction processes, thereby posing computational challenges that will be addressed in future work. If the after-flare SED indeed requires an external photon field for explanation, this may indicate an evolution of the emission region's location. Specifically, during the neutrino arrival and the gamma-ray flare peak, the emission zone could be located between the supermassive black hole (SMBH) and the BLR, whereas during the post-flare period, the emission region might have progressed along the jet to eventually intersect the BLR.

The model for the neutrino arrival SED presented in **Figure 5.6** predicts a slightly higher number of neutrino events compared to the hybrid model by Sahakyan et al. [155], which utilizes a similar physical framework. However, the proton luminosity in our model is four orders of magnitude lower. This difference can be attributed to the fact that our models do not fix the maximum proton energy. Higher-energy protons generate more neutrinos through the process of photo-pion production, and these resulting cascades predominantly contribute to gamma-ray emission rather than being limited by X-ray emission. This effect compensates for the fact that the neutrino peak is shifted toward higher energies relative to IceCube's maximum sensitivity, which is at approximately 100 TeV [176].

In contrast, the best-fit model for the gamma-ray flare peak SED predicts nearly three times more neutrino events in IceCube compared to the external photon field model proposed by [155]. This scenario favors lower proton energies combined with higher proton luminosities, which leads to enhanced neutrino production, particularly in the energy range where IceCube's sensitivity is highest.

It is important to note that the flaring states (neutrino arrival, gamma flare peak, and post-flare SEDs) exhibit higher minimum proton Lorentz factors and harder spectral indices. Such hard spectral indices can be pro-

PKS 0735+178:

[175]: Fichet de Clairfontaine et al. (2023), Hadronic Processes at Work in 5BZB J0630-2406
 [155]: Sahakyan et al. (2022), A multimessenger study of the blazar PKS 0735+178: a new major neutrino source candidate
 [176]: Aartsen et al. (2019), Search for steady point-like sources in the astrophysical muon neutrino flux with 8 years of IceCube data

duced if particles are accelerated in a highly magnetized magnetic reconnection region. Although particle acceleration is not explicitly modeled in this work, it is plausible that particles are pre-accelerated in a magnetic reconnection zone before entering the emission region. Additionally, the highest levels of magnetization in the jet are expected near its base, close to the supermassive black hole (SMBH), gradually dissipating to lower values as particles cool within the expanding emission blob. This is consistent with the earlier hypothesis that the emission region lies between the SMBH and the BLR. In contrast, the softer proton spectral index observed during the quiescent state may indicate that the primary emission zone is located beyond the BLR, or that diffuse shock acceleration dominates the particle acceleration during this period.

For the quiescent-state SED, even when maximizing the predicted neutrino events in IceCube, the best fit yields a maximum of 0.04 neutrino events per year. This result is consistent with Poisson fluctuations and aligns with the observation of 0.0 neutrino events found in the IceCube point-source analysis using 10 years of IceCube data between 2008 and 2018 [177].

Acharyya et al. [157] argue that the SSC model fails to adequately explain the SED of PKS 0735+178. They propose an alternative model that incorporates external photon fields, which results in increased neutrino rates due to a higher number of targets for $p\gamma$ interactions. In contrast, our leptohadronic SSC-based model for the neutrino arrival period successfully accounts for the observed photon fluxes. While it predicts a factor of two fewer neutrino events than the external field model proposed by Acharyya et al. [157], it reduces the required proton power by two orders of magnitude. On the contrary, during the gamma flare peak, our model generates a factor of two more neutrino events compared to the external field model suggested by Acharyya et al. [157].

The predicted neutrino rates should be interpreted as a mean value of Poisson statistics. However, the statistical error associated with the expected neutrino rates is considerably smaller than the uncertainties introduced by the demonstrated degeneracy of hadronic parameters and the Eddington bias [178].

The leptohadronic one-zone models have a long-standing problem of too high proton power requirement to explain the observed neutrino emission [see, e.g., 179, 180]. As mentioned in previous chapters, the fundamental jet power is limited by the Eddington luminosity. The mass of the SMBH in PKS 0735+178 was estimated based on the optical intraday variability timescales [181] as $1.89 \times 10^8 M_\odot$ (corresponding to $L_{\text{Edd}} = 2.5 \times 10^{46} \text{ erg s}^{-1}$) assuming a jet Doppler factor of $\delta \approx 3.5$. If the Doppler factor of the emission zone is higher, which is the case for our leptohadronic models, the corresponding value of the SMBH mass increases by a factor of four, leading to $L_{\text{Edd}} \approx 10^{47} \text{ erg s}^{-1}$. The quiescent and neutrino arrival SEDs are well explained with sub-Eddington proton luminosities, which shortly raise to super-Eddington levels ($L'_p \approx 10 L_{\text{Edd}}$) during the gamma flare peak periods, before returning to sub-Eddington values in the post-flare phase. The blob maintains similar radius values

PKS 0735+178:

[177]: Aartsen et al. (2020), Time-Integrated Neutrino Source Searches with 10 Years of IceCube Data

[157]: Acharyya et al. (2023), Multiwavelength Observations of the Blazar PKS 0735+178 in Spatial and Temporal Coincidence with an Astrophysical Neutrino Candidate IceCube-211208A

[178]: Strotjohann et al. (2019), Eddington bias for cosmic neutrino sources

[179]: Gasparian et al. (2022), Time-dependent lepto-hadronic modelling of the emission from blazar jets with SOPRANO: the case of TXS 0506+ 056, 3HSP J095507. 9+ 355101, and 3C 279

[180]: Petropoulou et al. (2020), Comprehensive Multimessenger Modeling of the Extreme Blazar 3HSP J095507.9+355101 and Predictions for IceCube

[181]: Gupta et al. (2012), Optical intra-day variability timescales and black hole mass of the blazars

during the neutrino arrival and gamma flare peak but expands during the subsequent post-flare phase. Throughout the flare evolution, the magnetic field strength consistently decreases, reaching its maximum value of about 2 G during the neutrino arrival. The proton spectral index is notably harder during periods of high activity compared to the quiescent state, suggesting that the same emission region dominates during the flaring states, consistent with the earlier hypotheses.

However, the values of the blob Lorentz factors vary across the four SEDs, with the highest best-fit value observed in the quiescent state. This variation could result from the independent fitting procedures applied to each state. Considering the existing degeneracies, a similarly acceptable solution with the same Lorentz factor might be achievable. Alternatively, small changes in the viewing angle (approximately $\sim 0.5^\circ$ between consecutive states) could account for this effect. In our modeling, the Doppler factor is approximated as $\delta_D \approx \Gamma_b$, indicating that variations in the viewing angle could explain the variations in both the Doppler factor and the Lorentz factor. Britzen et al. [182] propose that the long-term radio variability observed in PKS 0735+178 may be attributed to jet precession caused by a binary supermassive black hole, which supports the hypothesis of changes in the viewing angle. As another possibility, the differing Lorentz factors could also suggest that the emission originates from different blobs.

In addition to the previously shown inability to constrain $\gamma_{e,p}^{\min}$, $\gamma_{e,p}^{\max}$ and $\alpha_{e,p}$ from the parameter space search, the potential presence of lower-energy particles further complicates the uncertainties of $\gamma_{e,p}^{\min}$ and $\alpha_{e,p}$. Lower values for these parameters suggest that the required luminosities could be higher, potentially surpassing the Eddington luminosity. Sub-Eddington luminosities can be achieved by either increasing the minimum proton energy or hardening the spectral index, resulting in a scenario where the number of protons in the emission zone decreases as they carry more energy, thus conserving energy density.

In the purely leptonic models, the existence of multiple solutions prevents the tracing of the exact evolution of the radiation zone, as the causal relationship between different solutions at any epoch remains unclear. Nevertheless, for any solution, the flare states are characterized by higher values of magnetic field strength and electron luminosity, with their simultaneous increase suggesting energy equipartition. Under the condition of neutrino rate maximization, the different periods during the flare have enhanced magnetic field strength and more compact emission-zone regions. The neutrino flare could be linked to the increase of minimum proton energy and hardening of the proton spectrum leading to increased $p\gamma$ interaction rates.

The properties of the proton spectrum cannot be constrained by the observed photon fluxes, leading to great uncertainty in the subsequent neutrino emission. To break this degeneracy, next-generation neutrino telescopes such as IceCube-Gen2 [183], KM3NeT [184], or P-ONE [185] are needed. Additionally, multi-wavelength polarization can potentially

PKS 0735+178:

- [182]: Britzen et al. (2010), Understanding BL Lacertae objects. Structural and kinematic mode changes in the BL Lac object PKS 0735+178
- [183]: Aartsen et al. (2021), IceCube-Gen2: the window to the extreme Universe
- [184]: Adrián-Martínez et al. (2016), Letter of intent for KM3NeT 2.0
- [185]: Malecki (2024), "Pacific Ocean Neutrino Experiment"

PKS 0735+178:

[186]: Zhang et al. (2024), Revisiting High-energy Polarization from Leptonic and Hadronic Blazar Scenarios

[187]: Zhang et al. (2016), eXTP: Enhanced X-ray Timing and Polarization mission

[188]: Tomsick and others (2019), The Compton Spectrometer and Imager

[189]: Caputo et al. (2022), All-sky Medium Energy Gamma-ray Observatory eXplorer mission concept

[190]: De Angelis et al. (2017), "The e-ASTROGAM mission. Exploring the extreme Universe with gamma rays in the MeV - GeV range"

constrain the hadronic component [186], thus highlighting the importance of future X-ray and MeV polarimeters such as eXTP [187], COSI [188], AMEGO-X [189], and e-ASTROGAM [190].

5.1.5 Summary and conclusions

In this project, I modeled the multi-epoch, multi-messenger emission from PKS 0735+178. The key findings are:

- The grid-scan-based approach clearly revealed degeneracies in both leptonic and lepto-hadronic models.
- Under the assumption of maximizing neutrino detection rates, lepto-hadronic solutions were found for different flare stages, predicting up to 0.1 neutrino events during the 50-day flare—surpassing previous model predictions. During the quiescent state, the maximum neutrino rate is two orders of magnitude lower than during the flare.
- The post-flare SED cannot be reproduced by a simple one-zone lepto-hadronic model and likely requires external photon fields to explain the gamma-ray emission, which may indicate spatial evolution of the emission zone.
- The degeneracy of hadronic parameters in one-zone lepto-hadronic models poses a significant challenge for identifying potential neutrino sources. The proton spectrum characteristics cannot be constrained by observed photon fluxes, leading to substantial uncertainty in neutrino emission predictions. To address this issue, the development of next-generation neutrino telescopes and high-energy polarimeters is crucial.

5.2 TeV flaring blazar VER J0521+211

In February 2020, a BL Lac object VER J0521+211 underwent an extraordinary gamma-ray-flaring state that resulted in the detection of very high energy gamma rays ($E > 200$ GeV). The source was observed with MAGIC telescopes between 26 February 2020 and 2 March 2020. These observations were complemented by an extensive multiwavelength (MWL) campaign, which made it possible to build blazar SEDs and analyze the source's variability on a short time scale.

VER J0521+211 was initially detected in the VHE gamma rays by the VERITAS (Very Energetic Radiation Imaging Telescope Array System) collaboration in 2009. VER J0521+211 is a BL Lac object that is often classified as either an intermediate-frequency synchrotron-peaked BL Lac (IBL) or a high-frequency synchrotron-peaked BL Lac (HBL), depending on whether it is in a quiescent or flaring state.

The optical spectrum of VER J0521+211 is primarily characterized by continuum emission, which is typical of BL Lac-type sources and results in significant uncertainty regarding the blazar's redshift. Current estimates of the source's distance are constrained within $0.18 \lesssim z \lesssim 0.31$, based on lower limits derived from assumptions about the host galaxy's luminosity [191], upper bounds obtained through extrapolations of the HE gamma-ray spectrum to VHE gamma rays [192], and modeling of the observed VHE gamma-ray spectrum [193]. For the SED modeling, the redshift is assumed to be $z = 0.18$.

5.2.1 Data

The MAGIC telescopes observed VER J0521+211 during the six consecutive nights starting 26 February 2020 (MJD 58905 - MJD 58910) in response to an active state in the very high energy (VHE) gamma-ray emission of the source reported by the VERITAS collaboration [194]. The VHE gamma-ray flux ($E > 200$ GeV) was complimented by Fermi-LAT simultaneous measurements of high-energy (HE) gamma-ray flux (0.1 – 300 GeV). The public data of Fermi-LAT [195] were used for data analysis. The two upper panels in **Figure 5.7** show the evolution of VHE and HE gamma-ray fluxes during the flare.

The X-ray data was obtained during the *Swift*-XRT observations (onboard the *Swift* satellite) between 25 February and 1 March 2020 (MJD 58904-58909). Simultaneously with X-ray observations, the Ultraviolet/Optical Telescope (UVOT) onboard the *Swift* satellite conducted five observations of VER J0521+211 between 25 February and 1 March 2020 (MJD 58904-58909). A variety of optical (V, B, U) and UV (W1, W2, W2) filter combinations [196, 197] were used.

Multiple facilities conducted the optical measurements. These include the Tuorla blazar monitoring program [198], the Boston University Blazar Group [199], the Nordic Optical Telescope (NOT), and the Belogradchik Observatory. **Figure 5.7** also shows data from the KAIT Fermi AGN Light-

VER J0521+211:

- [191]: Paiano et al. (2017), On the redshift of TeV BL Lac objects
- [192]: Adams et al. (2022), Multiwavelength Observations of the Blazar VER J0521+211 during an Elevated TeV Gamma-Ray State
- [193]: Sahu et al. (2023), Constraining the redshift of BL Lac VER J0521+211
- [194]: Quinn and VERITAS Collaboration (2020), VERITAS detection of unprecedented gamma-ray flare from the blazar VER J0521+211
- [195]: Abdollahi et al. (2023), The Fermi-LAT Lightcurve Repository
- [196]: Poole et al. (2008), Photometric calibration of the Swift ultraviolet/optical telescope
- [197]: Breeveld et al. (2010), Further calibration of the Swift ultraviolet/optical telescope
- [198]: Takalo et al. (2008), Tuorla Blazar Monitoring Program
- [199]: Jorstad and Marscher (2016), "The VLBA-BU-BLAZAR Multi-Wavelength Monitoring Program"

VER J0521+211:

[200]: MAGIC Collaboration et al. (2020), Testing two-component models on very high-energy gamma-ray-emitting BL Lac objects

Table 5.7: States of VER J0521+211.

State	Epoch
	[MJD]
A	58903.5-58905.5
B	58905.5-58906.5
C	58907.5-58908.5
D	58908.5-58909.5

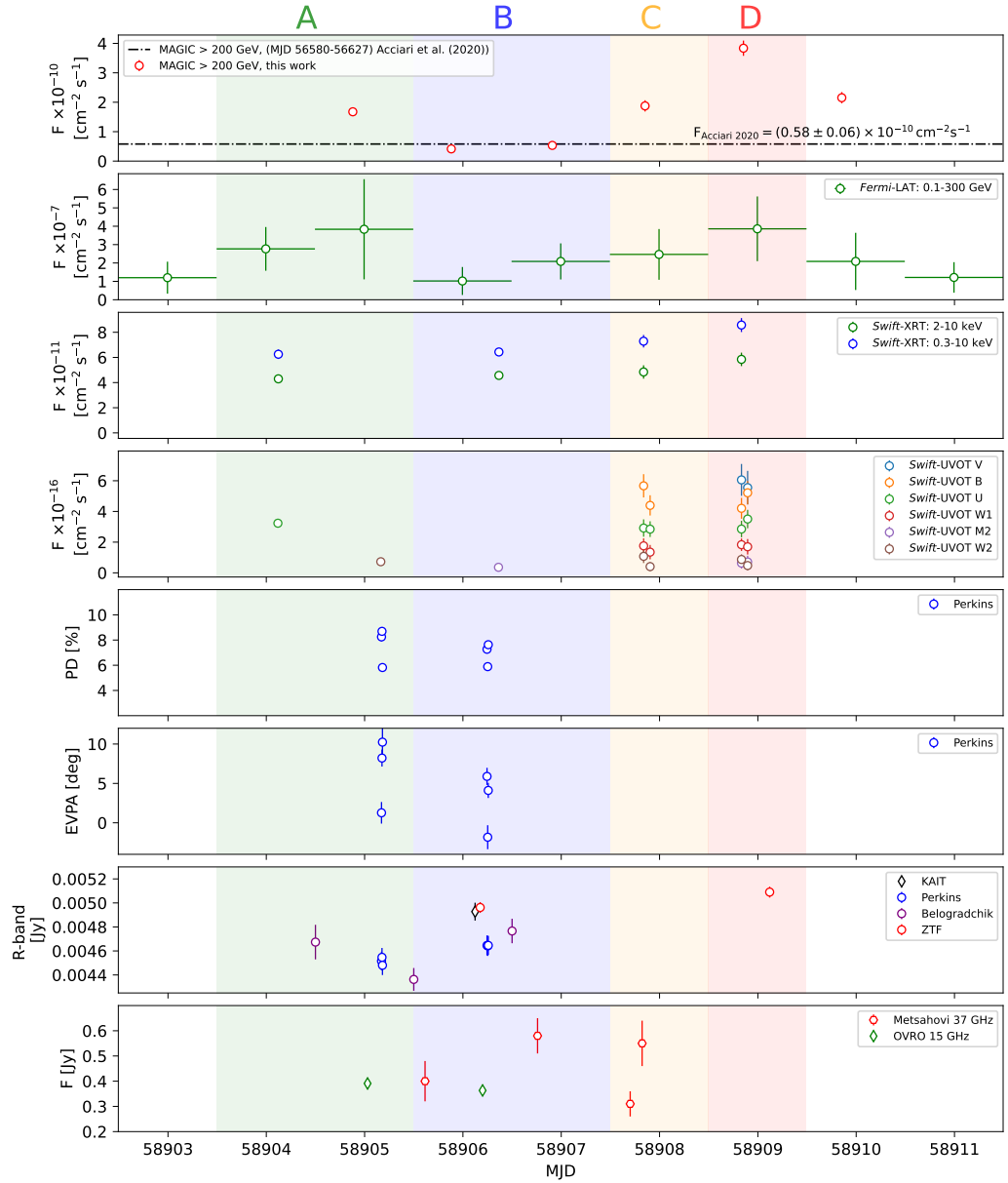


Figure 5.7: Multiwavelength light curve showing the evolution of the flux of VER J0521+211 in different bands and its optical polarization during the 2020 flare. From top to bottom: VHE gamma rays (with a reference value from [200]), HE gamma-ray flux, X-ray flux, UV and optical in various bands, R-band flux from various optical telescopes as well as the evolution of the polarization electric vector polarization angle, and radio flux. Shaded background colors define the states A–D used to build the SED of the source, as described in Table 5.7. Figure from Abe et al. [146].

VER J0521+211 has been monitored in the radio band by the Owens Valley Radio Telescope (OVRO) at 15 GHz. The additional radio data included measurements by 3.7-meter-diameter Metsähovi radio telescope at 37 GHz and the data from Lister et al. [201] observed within the MOJAVE (Monitoring Of Jets in Active galactic nuclei with VLBA Experiments) Project at 15 GHz.

5.2.2 SED modeling

Abe et al. [146] demonstrated that the optical and radio emissions in VER J0521+211 are correlated (with a time lag) indicating a common origin for these energy bands. However, during the 2020 flare, short-term variability was primarily observed at higher energies, including X-rays and beyond. This behavior cannot be explained by a simple one-zone leptonic model. I proposed a leptohadronic model to explain the short-term variability of VER J0521+211, which can account for the observed features of its variability.

To explore the leptohadronic scenario, I utilized the time-dependent code AM³ (see Section 4.3). The one-zone leptohadronic model was explored as an alternative to the two-zone leptonic model, maintaining the same assumption that gamma rays primarily originate from leptonic processes. As mentioned in Section 4.2.1, Zdziarski and Böttcher [119] and Liodakis and Petropoulou [118] showed that for low-frequency and intermediate-frequency BL Lacs, the hadronic contribution to the gamma-ray emission can only be subdominant. Since during the periods of high activity VER J0521+211 is an HBL, a purely hadronic origin of high energy emission during these states is not excluded. Thus, a model where the gamma rays originate from proton synchrotron emission is possible. However, this model will not be considered in this work.

Similarly to the previously described models, the electrons and protons in the jet are assumed to be pre-accelerated with the energies that follow simple power-law spectra, $dN/d\gamma_{e(p)} \propto \gamma_{e(p)}^{-n_{e(p)}}$, with spectral index $n_{e(p)}$, spanning a range of Lorentz factors from $\gamma_{e(p)}^{\min}$ to $\gamma_{e(p)}^{\max}$. Both particle populations are isotropically injected into a single spherical region of size R'_b (in the comoving frame of the jet), where a homogeneous and isotropic magnetic field of strength B exists. Along with electron and proton luminosities, L'_e and L'_p , this defines a ten-parameter space that fully describes the model. The blob Doppler factor is fixed to 15 based on the estimations of the viewing angle from MAGIC Collaboration et al. [200]. For each emission state, the entire multi-wavelength dataset is compared to the model predictions.

I started the modeling from state A, assuming it originates from a steady-state emission. After finding the best-fit solution with a genetic algorithm, I further refined it locally using the `Minuit` package [169]. Given the short time intervals of just one or two days between consecutive observations, each period should not be modeled entirely independently. Instead, the goal was to identify the minimal parameter variations needed

VER J0521+211:

[146]: Abe et al. (2024), Time-dependent modelling of short-term variability in the TeV-blazar VER J0521+211 during the major flare in 2020

[119]: Zdziarski and Böttcher (2015), Hadronic models of blazars require a change of the accretion paradigm

[118]: Liodakis and Petropoulou (2020), Proton Synchrotron Gamma-Rays and the Energy Crisis in Blazars

[201]: Lister et al. (2021), Monitoring Of Jets in Active Galactic Nuclei with VLBA Experiments. XVIII. Kinematics and Inner Jet Evolution of Bright Radio-loud Active Galaxies

[146]: Abe et al. (2024), Time-dependent modelling of short-term variability in the TeV-blazar VER J0521+211 during the major flare in 2020

[202]: Zdziarski and Böttcher (2015), Hadronic models of blazars require a change of the accretion paradigm.

[203]: Liodakis and Petropoulou (2020), Proton Synchrotron Gamma-Rays and the Energy Crisis in Blazars

[200]: MAGIC Collaboration et al. (2020), Testing two-component models on very high-energy gamma-ray-emitting BL Lac objects

[169]: James and Roos (1975), Minuit - a system for function minimization and analysis of the parameter errors and correlations

to explain the observed spectral variations between successive states. The method consisted of fixing in `Minuit` all parameters to a constant value (corresponding to the best fit for state A) except one at a time, and iteratively minimizing the reduced χ^2 function for each parameter. If a satisfactory fit could not be obtained, combinations of two or more parameters were explored by allowing them to vary during the minimization process.

5.2.3 Results

The analysis showed that the transition from state A (steady-state) to state B (enhanced) could be attributed to a 20% increase in electron luminosity and a sixfold decrease in proton luminosity. Likewise, the transition from state B to C was successfully modeled by adjusting only the electron and proton luminosities. Notably, the proton-to-electron luminosity ratio in state C returned to a level comparable to that of state A. However, this gradual progression was disrupted in state D, which could not be explained by changes in just two parameters. A satisfactory fit for state D was only achieved by modifying both the energy spectra and luminosities of protons and electrons.

In this model, both particle species are assumed to be pre-accelerated before being injected into the emission region. Most particle acceleration mechanisms suggest that if electrons and protons are accelerated in the same region, they should experience a similar relative energy gain. In states A, B, and C, the energy spectra of the particles remain unchanged, and variations in particle luminosities can be interpreted as fluctuations in the number of particles entering the emission zone. These fluctuations could be driven by turbulence in the jet's magnetic field. However, state D requires a significant shift in both the particle spectra and luminosities. This could result from a combination of particle cooling from the previous state and the simultaneous injection of a new population of more energetic particles.

The best-fit models for all four states are presented in [Figure 5.8](#), demonstrating a strong overall agreement with the observed data. The parameters of this one-zone model, in which protons and electrons undergo co-acceleration, are listed in [Table 5.8](#). In this model, the majority of the low-energy emission (from radio to optical) is attributed to synchrotron radiation produced by accelerated electrons. Meanwhile, the gamma-ray emission detected by MAGIC primarily originates from hadronic interactions between accelerated protons and low-energy photon fields within the jet. The emission observed by *Fermi*-LAT at GeV energies represents a transition zone, where the dominant contribution shifts from electrons to protons.

The minimum electron Lorentz factors remain consistent across all states, at approximately 10. These low-energy electrons primarily account for the radio emission in this model. However, they do not contribute significantly to the high-energy portion of the SED, as their synchrotron photons can only be upscattered via the inverse Compton effect to the optical and UV bands, which are already dominated by synchrotron

emission from high-energy electrons (see [Figure 5.9](#)). These electrons can be considered a separate population, making them compatible with the electron population from the core in the two-zone model. Notably, if the low-energy electrons coexist with the high-energy electrons in the same emission region, the radio data should be treated as an upper limit, meaning the $\gamma'_{e,min}$ in the best-fit model should be interpreted as a lower limit as well.

Table 5.8: Parameters of the lepto-hadronic one-zone model.

State	R'_{blob} [$\times 10^{16}$ cm]	δ	B [G]	n_e n_p	γ'_e ^{min} γ'_e ^{max}	γ'_p ^{min} γ'_p ^{max}	L'_e [erg/s] L'_p [erg/s]
A	2.3	15.0	0.15	2.0	1.3×10^1	6.31×10^5	1.8×10^{42}
				2.0	6.3×10^5	5.0×10^7	3.0×10^{46}
B	2.3	15.0	0.15	2.0	1.3×10^1	6.31×10^5	2.2×10^{42}
				2.0	6.3×10^5	5.0×10^7	5.0×10^{45}
C	2.3	15.0	0.15	2.0	1.3×10^1	6.31×10^5	1.8×10^{42}
				2.0	6.3×10^5	5.0×10^7	3.8×10^{46}
D	2.3	15.0	0.15	1.6	2.5×10^1	5.0×10^6	1.3×10^{42}
				1.7	2.0×10^5	6.3×10^7	1.8×10^{46}

Columns: (1) State. (2) Epoch. (3) Blob radius. (4) Doppler factor of the blob. (5) Magnetic field strength. (6) Power-law spectral indices for electron and proton distribution. (7) Minimum and maximum energy for electrons. (8) Minimum and maximum energy for protons. (9) Electron and proton luminosity. In bold are parameters that changed compared to state A.

The low-energy emission is explained almost exclusively by the synchrotron emission of the electrons accelerated in the jet. Those electrons also Comptonize their synchrotron radiation, resulting in high-energy contribution (orange dashed line in [Figure 5.9](#)). Another leptonic process that contributes significantly to the GeV – TeV gamma rays is synchrotron emission from pair production $\gamma\gamma \leftrightarrow e^+e^-$. The emission from co-accelerated protons becomes dominant over leptonic emission in the energy range 10 keV – 0.1 GeV. The main contribution in this energy range (blue dashed line in [Figure 5.9](#)) comes from synchrotron emission of electrons created in Bethe-Heitler process $p\gamma \rightarrow pe^+e^-$. At the higher energies (10 GeV – 100 TeV), synchrotron emission of electrons from hadronic cascades in $p\gamma$ interactions ($p\gamma \rightarrow \pi^\pm \rightarrow \mu^\pm \rightarrow e^\pm$) and inverse Compton scattering of synchrotron radiation of Bethe-Heitler electrons have subdominant effect. A separate bump around 10^{17} eV (magenta dashed line in [Figure 5.9](#)) comes from the direct $\pi^0 \rightarrow \gamma\gamma$ decays and thus those photons are produced via a hadronic process. However, this ultra-high-energy component is severely attenuated by photon-photon interactions with CMB photons and is unlikely to be observed.

The model predicted the emission of high-energy neutrinos from interactions between photons and protons, mainly produced during the decay of secondary charged pions (see [Figure 5.9](#) for details on the SED components). The dash-dotted lines in [Figure 5.8](#) show the predicted

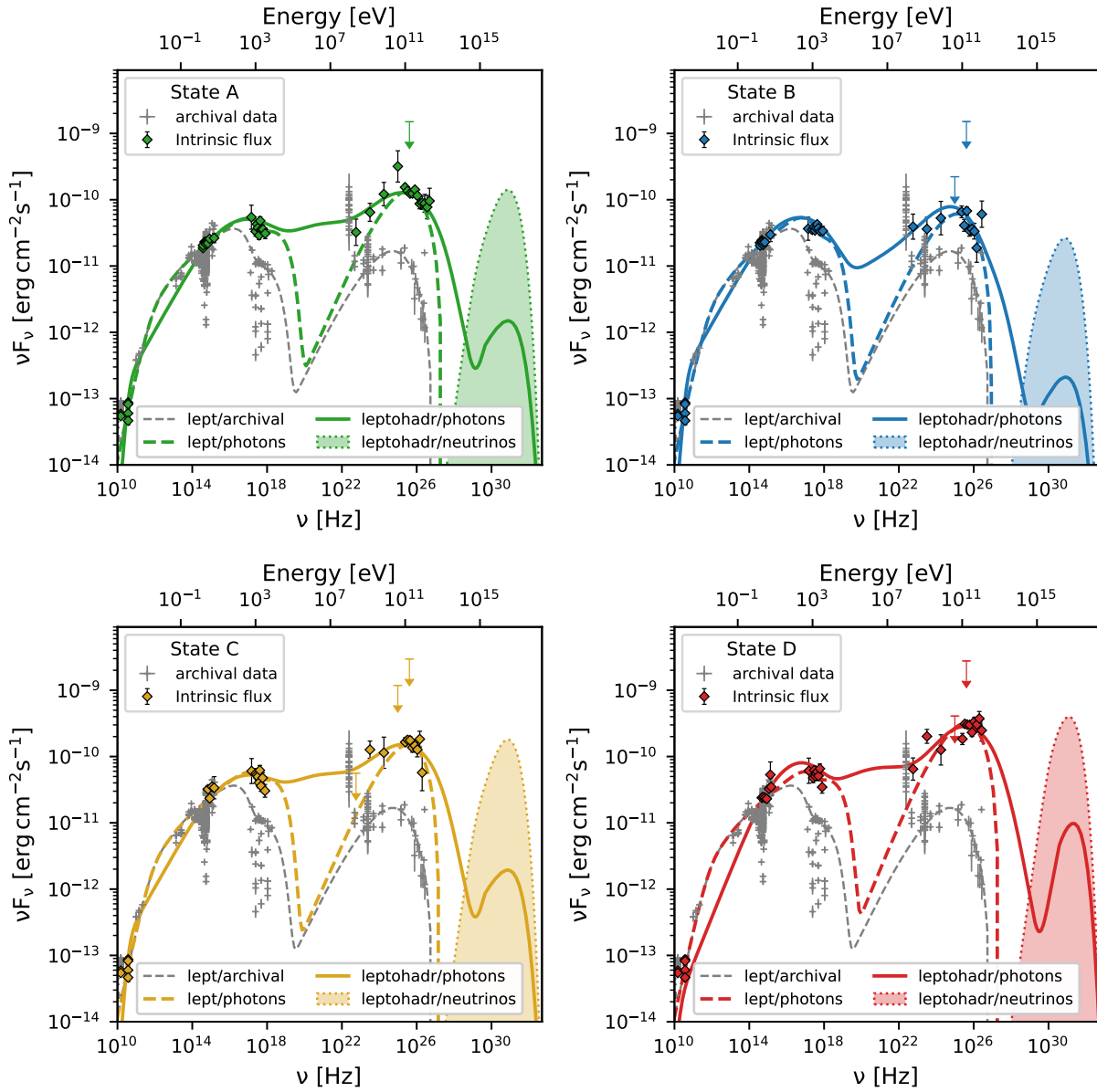


Figure 5.8: Intrinsic broadband SEDs of the four observation epochs listed in [Table 5.7](#). Archival data are shown in grey [200], while the data contemporary to the four epochs are shown in their respective colors. The fluxes predicted by the two-zone leptonic model are shown dashed, while the predictions of the one-zone lepto-hadronic model are shown as solid lines. In both cases, the models are shown to match the intrinsic flux measured by MAGIC, without taking into account γ - γ absorption by extragalactic background light (relevant for TeV photons) and cosmic microwave background (completely absorbing PeV photons). The spectra of emitted neutrinos predicted by the lepto-hadronic model are shown as dash-dotted lines. Figure from Abe et al. [146].

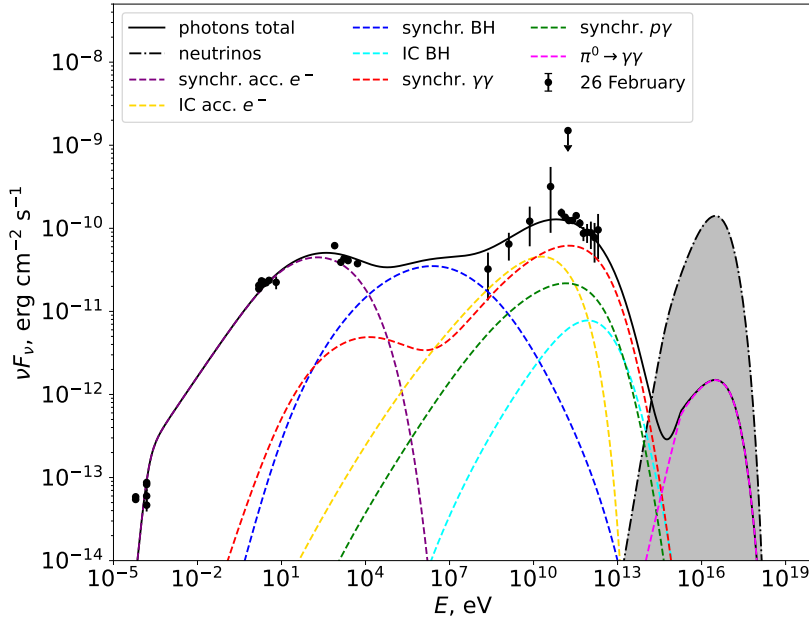


Figure 5.9: Contributions from different radiative processes to the SED of VER J0521+211 (state A). The solid line shows a total radiated photon flux, same as in [Figure 5.8](#) (upper left panel). Dashed lines correspond to the following contributions: purple – synchrotron radiation from electrons accelerated in the jet, blue – synchrotron radiation from pairs created in Bethe-Heitler process, orange – SSC emission, red – synchrotron radiation from $\gamma\gamma$ pair creation, green – synchrotron from electrons created in hadronic cascades following $p\gamma$ interactions, cyan – inverse Compton Bethe-Heitler electrons, and magenta – pion decay to $\gamma\gamma$. Neutrinos are shown with a dash-dotted filled curve. Figure from Abe et al. [146].

neutrino flux that peaks around 400 PeV. To estimate the number of neutrinos the IceCube observatory would detect from the source during each of the four states, I used the [Eq. \(5.3\)](#). The predicted all-flavor neutrino spectra were convolved with the IceCube effective area for the source’s declination band [204], multiplied by the duration of states A, B, C, and D, and, finally, divided by three to account for neutrino mixing and detection via one channel. The calculations predict 0.010, 0.002, 0.013, and 0.016 neutrino events per day during the respective states, resulting in about 0.05 neutrino events over the 6-day total observation period. Considering Poisson statistics, these numbers align with the lack of neutrino detections reported by Aartsen et al. [205]. Therefore, the current upper limits on the neutrino flux from the IceCube experiment do not rule out the lepto-hadronic scenario. However, as the IceCube observatory and future neutrino telescopes continue to monitor the neutrino sky, they might eventually detect a neutrino signal that would support the lepto-hadronic emission scenario, especially if the source is observed again during a flaring state in the VHE gamma-ray range.

Another way to identify hadronic signatures in blazar emission is by exploring new energy ranges in the SED. Instead of the characteristic two-

VER J0521+211:

[204]: Aartsen et al. (2017), All-sky Search for Time-integrated Neutrino Emission from Astrophysical Sources with 7 yr of IceCube Data

[205]: Aartsen et al. (2020), Time-Integrated Neutrino Source Searches with 10 Years of IceCube Data

bump feature, the dip in X-rays almost disappears when adding protons due to synchrotron radiation from Bethe-Heitler pairs. **Figure 5.9** shows the contributions from leptonic and hadronic processes to the total photon fluxes. Observations in the hard X-ray band or the MeV range would be essential for refining the multi-wavelength spectrum and distinguishing between purely leptonic and lepto-hadronic models.

5.2.4 Summary and conclusions

In this project, I modeled the emission from the TeV-flaring blazar VER J0521+211, observed between 26 February 2020 and 2 March 2020 with the MAGIC telescopes.

- I performed lepto-hadronic modeling for each of the four states identified during the flare.
- Given the day-scale variability, only a few model parameters varied between consecutive states. The proposed model successfully reproduced the time-evolving broadband SEDs of VER J0521+211.
- States A, B, and C differ only in terms of electron and proton luminosities, which can be interpreted as fluctuations in the number of particles entering the emission zone. In contrast, state D requires changes in both the particle spectra and luminosities, possibly indicating the injection of a more energetic particle population during this period.
- The observation of neutrinos with future neutrino telescopes could support the validity of this model, particularly during periods of intense TeV activity.
- The detection of hard X-ray or MeV fluxes at the level of $\sim 5 \times 10^{-11}$ erg/cm²/s (compared to $\sim 10^{-13}$ erg/cm²/s in purely leptonic models) would provide a clear observational signature of hadronic processes in the SED.

5.3 Blazar contribution to neutrino neutrino hotspot near NGC 4151

5.3.1 Neutrinos from Seyfert galaxies

As mentioned in [Section 2.3](#), the origin of the diffuse astrophysical neutrino flux discovered by IceCube remains unknown. Up to this point, I have focused on blazars as one of the most promising candidate sources. However, other classes of AGNs, as discussed in [Section 3.2](#), may also contribute to the observed neutrino flux [[206](#), [207](#)]. Recently, the IceCube Collaboration reported a 4.2σ excess in the direction of the nearby Seyfert galaxy NGC 1068 [[208](#), [32](#)].

Blazar jets, which outshine other components of their host galaxies and are considered potential sites for cosmic ray acceleration, are natural candidates for high-energy neutrino production. In contrast, the spectral energy distributions of Seyfert galaxies are more complex, as they include emissions from multiple regions within the AGN.

Interestingly, in the case of NGC 1068, the observed gamma-ray flux is roughly two orders of magnitude lower than the associated neutrino flux. This discrepancy has raised questions about the origin of the neutrinos and sparked an active theoretical discussion.

Inoue et al. [[209](#)] proposes that diffusive shock acceleration occurs in AGN coronae, supported by observations of non-thermal electrons. If protons are accelerated under similar conditions, they can produce neutrinos through $p\gamma$ and pp interactions. In this scenario, the suppressed gamma-ray flux is attributed to $\gamma\gamma$ pair production in the dense coronal environment. Inoue and Khangulyan [[210](#)] extends this model, suggesting that coronal activity is responsible for the neutrino emission, whereas the observed gamma rays originate from a weak jet.

Murase et al. [[211](#)] presents an alternative model in which protons in AGN coronae are stochastically accelerated by plasma turbulence. Neutrinos are produced via $p\gamma$ and pp interactions, while gamma rays peak in the MeV range due to hadronic cascades and Bethe–Heitler cooling.

Fiorillo et al. [[212](#)] investigate proton acceleration via magnetic reconnection. In their model, neutrinos are produced exclusively through $p\gamma$ interactions, and the predicted luminosity in the MeV band is expected to be comparable to the neutrino luminosity.

Eichmann et al. [[61](#)] argue that a single emission region cannot fully account for the observed multi-messenger data. They propose that both the AGN corona and the surrounding starburst regions must be considered to achieve a comprehensive explanation.

Peretti et al. [[62](#)] demonstrate that powerful AGN winds, known as ultra-fast outflows, can accelerate particles to energies up to the EeV scale. In this scenario, neutrinos are produced via both $p\gamma$ and pp interactions. The lack of observed gamma-ray emission is attributed to the absorption of gamma rays through $p\gamma$ and pp processes, with the AGN photon fields serving as the primary targets.

Seyfert galaxies:

[[206](#)]: Stecker et al. (1991), High-energy neutrinos from active galactic nuclei

[[207](#)]: Kalashev et al. (2015), Neutrinos in IceCube from active galactic nuclei

[[208](#)]: Aartsen et al. (2020), Time-Integrated Neutrino Source Searches with 10 Years of IceCube Data

[[32](#)]: Abbasi et al. (2022), Evidence for neutrino emission from the nearby active galaxy NGC 1068

[[209](#)]: Inoue et al. (2019), On High-energy Particles in Accretion Disk Coronae of Supermassive Black Holes: Implications for MeV Gamma-rays and High-energy Neutrinos from AGN Cores

[[210](#)]: Inoue and Khangulyan (2023), Gamma-ray emission in the Seyfert galaxy NGC 4151: Investigating the role of jet and coronal activities

[[211](#)]: Murase et al. (2020), Hidden Cores of Active Galactic Nuclei as the Origin of Medium-Energy Neutrinos: Critical Tests with the MeV Gamma-Ray Connection

[[212](#)]: Fiorillo et al. (2024), TeV Neutrinos and Hard X-Rays from Relativistic Reconnection in the Corona of NGC 1068

[[61](#)]: Eichmann et al. (2022), Solving the Multimessenger Puzzle of the AGN-starburst Composite Galaxy NGC 1068

[[62](#)]: Peretti et al. (2023), Diffusive shock acceleration at EeV and associated multimessenger flux from ultra-fast outflows driven by Active Galactic Nuclei

Seyfert galaxies:

[213]: Abbasi et al. (2024), IceCube Search for Neutrino Emission from X-ray Bright Seyfert Galaxies

[214]: Neronov et al. (2024), Neutrino Signal from a Population of Seyfert Galaxies

[215]: Sommani et al. (2024), Two 100 TeV neutrinos coincident with the Seyfert galaxy NGC 7469

[216]: Abbasi et al. (2024), Search for neutrino emission from hard X-ray AGN with IceCube

[217]: Yuan et al. (2020), The Cepheid Distance to the Seyfert 1 Galaxy NGC 4151

[218]: Buson et al. (2023), Extragalactic neutrino factories

[219]: Murase et al. (2024), Sub-GeV Gamma Rays from Nearby Seyfert Galaxies and Implications for Coronal Neutrino Emission

Apart from the discovery of neutrino flux from NGC 1068, Seyfert galaxies being potential neutrino emitters were supported by additional observational studies [213, 214, 215]. The IceCube Collaboration has recently announced over 2σ evidence for ~ 10 TeV neutrino emission from the direction of another Seyfert galaxy, NGC 4151 [213, 216], located at a distance of $d = 15.8$ Mpc [217].

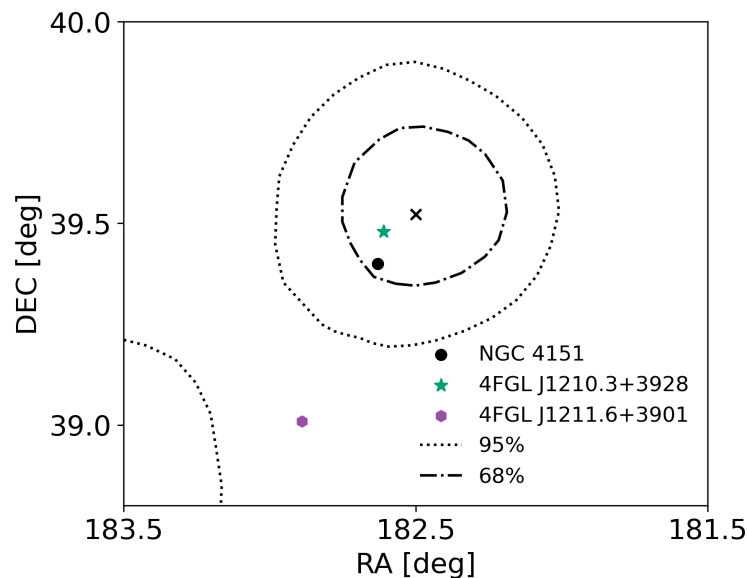


Figure 5.10: The location of 4FGL J1210.3+3928 and 4FGL J1211.6+3901 with respect to NGC 4151. The black cross, dash-dotted, and dotted black lines correspond respectively to the best-fit location of the neutrino source and its 68% and 95% confidence regions [216]. Figure from Omeliukh et al. [147].

However, two gamma-ray loud blazars, 4FGL J1210.3+3928 and 4FGL J1211.6+3901, are located 0.08° and 0.43° from NGC4151, respectively. Notably, 4FGLJ1210.3+3928 lies within the 68% confidence region of the neutrino excess associated with NGC 4151 [216], as shown in **Figure 5.10**, making it a natural candidate for a contributing source. This object has also been linked to a previously reported neutrino hotspot [218]. In contrast, 4FGLJ1211.6+3901 lies outside the 95% confidence contour. However, the extent of this contour depends on the assumed neutrino energy spectrum and can vary with different spectral indices, also due to both statistical and systematic uncertainties [see Fig. 8 in 216]. Given this potential uncertainty in the contour shape and the fact that 4FGLJ1210.3+3928 and 4FGLJ1211.6+3901 are the only nearby gamma-ray loud sources [219], both blazars can be considered candidates for the neutrino-emitting sources.

Since blazars are potential neutrino sources, these two nearby blazars could contribute to the neutrino signal from NGC 4151. I model multi-wavelength emission from J1210.3+3928 and J1211.6+3901 to evaluate their role in the observed neutrino excess.

5.3.2 Data

To build the spectral energy distribution of 4FGL J1210.3+3928 and 4FGL J1211.6+3901, I collect the available multi-wavelength data.

4FGL J1210.3+3928

4FGLJ1210.3+3928 is a BL Lac object located at a redshift of $z = 0.615$ [220]. The gamma-ray data for this source are obtained from the *Fermi*-LAT 14-Year Point Source Catalog [4FGL-DR4; 221, 222]. 4FGLJ1210.3+3928 is detected with a significance of approximately 6σ in gamma rays.

The source has been monitored long-term in the X-ray band due to its proximity to NGC 4151 [223]. Between 2000 and 2022, it was within the field of view of 33 *XMM-Newton* observations. However, usable spectra could only be extracted from 11 of them due to the selected science mode. For this study, a 10-ks observation from December 10, 2012, was selected for two reasons: (1) selecting a high-flux spectrum is consistent with the goal of estimating the source's maximum neutrino emission, and (2) the observation date is close to those of the other multi-wavelength data used. More details on the X-ray data analysis are provided in Omeliukh et al. [147].

For the multi-wavelength dataset, optical data were obtained from the SDSS Photometric Catalogue, Release 9 [224]. Infrared fluxes were measured by the Wide-field Infrared Survey Explorer (WISE) and retrieved from the WISE All-Sky Data Release [225, 226]. The source was also detected at 1.4 GHz in 1993 by the FIRST Survey [227].

4FGL J1211.6+3901

A second blazar, 4FGL J1211.6+3901, is classified as a BL Lac object [228] and has a redshift of $z = 0.89$, based on spectroscopic measurements by Della Ceca et al. [229]. It has been detected in GeV gamma rays by *Fermi*-LAT with a significance of approximately 5.4σ [221, 222].

X-ray data were collected during a 15-ks *XMM-Newton* observation on June 14, 2002. Although the blazar was not the primary target of this observation, it was in an active state at the time. Unfortunately, it was outside the field of view of the Optical Monitor onboard *XMM-Newton*, and therefore no simultaneous UV data point could be obtained. Further details on the X-ray data analysis are provided in Omeliukh et al. [147].

Optical measurements were obtained using OSIRIS/R5000R [229], the Catalina Sky Survey [230], and the SDSS Photometric Catalogue, Release 12 [231]. Infrared emission was measured by the Wide-field Infrared Survey Explorer (WISE), with fluxes retrieved from the WISE All-Sky Data Release [225, 226]. The source was also detected at 1.4 GHz by the FIRST Survey in 1993 [227].

5.3.3 Numerical modeling

The spectral energy distributions (SEDs) of both 4FGLJ1210.3+3928 and 4FGLJ1211.6+3901 exhibit a blackbody-like bump in the eV range,

Blazars near NGC 4151:

[220]: Stocke et al. (1991), The Einstein Observatory Extended Medium-Sensitivity Survey. II. The Optical Identifications
 [221]: Ballet et al. (2024), Fermi Large Area Telescope Fourth Source Catalog Data Release 4 (4FGL-DR4)
 [222]: Abdollahi et al. (2022), Incremental Fermi Large Area Telescope Fourth Source Catalog
 [223]: Maselli et al. (2008), The 26 year-long X-ray light curve and the X-ray spectrum of the BL Lacertae object 1E 1207.9+3945 in its brightest state
 [224]: Ahn et al. (2012), The Ninth Data Release of the Sloan Digital Sky Survey: First Spectroscopic Data from the SDSS-III Baryon Oscillation Spectroscopic Survey
 [225]: Cutri et al. (2012), VizieR Online Data Catalog: WISE All-Sky Data Release (Cutri+ 2012)
 [226]: Cutri et al. (2012), Explanatory Supplement to the WISE All-Sky Data Release Products
 [227]: White (1997), A Catalog of 1.4 GHz Radio Sources from the FIRST Survey
 [228]: Rector et al. (2000), The Properties of the X-Ray-selected EMSS Sample of BL Lacertae Objects
 [229]: Della Ceca et al. (2015), Exploring the active galactic nuclei population with extreme X-ray-to-optical flux ratios ($f_x/f_o > 50$)
 [230]: Drake et al. (2009), First Results from the Catalina Real-Time Transient Survey
 [231]: Alam et al. (2015), The Eleventh and Twelfth Data Releases of the Sloan Digital Sky Survey: Final Data from SDSS-III

which shows no significant variability [225, 226]. This feature may originate from stellar emission in their host galaxies. A similar spectral component can be found in the SED of Mrk 501, a well-known high-synchrotron-peaked BL Lac (HBL) object. **Figure 5.11** presents a comparison of the rest-frame SEDs of these blazars with that of Mrk 501². The similarity in their broadband spectral properties supports the classification of both sources as typical HBLs.

²The Mrk 501 SED data were obtained using the SEDBuilder tool: <https://tools.ssdc.asi.it/SED/>

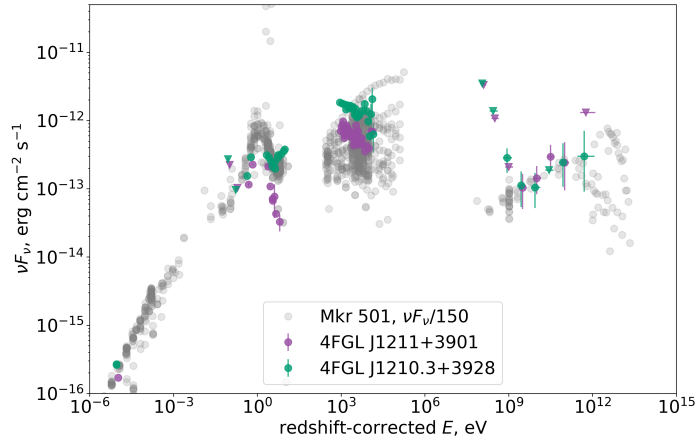


Figure 5.11: Comparison between spectral energy distributions of 4FGL J1210.3+3928, 4FGL J1211.6+3901 and Mrk 501. The grey data points correspond to the archival Mrk 501 SED scaled by 150. The green and purple data points (round – measurements, triangles – upper limits) correspond to 4FGL J1211.6+3901 and 4FGL J1211.6+3901 SEDs correspondingly. Figure from Omeliukh et al. [147].

Blazars near NGC 4151:

[232]: Bruzual and Charlot (2003), Stellar population synthesis at the resolution of 2003

[233]: Itoh et al. (2020), Blazar Radio and Optical Survey (BROS): A catalog of blazar candidates showing flat radio spectrum and their optical identification in Pan-STARRS1 Surveys

The eV bumps in both blazars are well reproduced by an elliptical galaxy spectral template with a stellar mass of $M = 10^{12} M_{\odot}$. For this, the stellar population synthesis model by Bruzual and Charlot [232] was used, assuming the Salpeter initial mass function, instantaneous star formation, age of 10 Gyr, and solar metallicity [see 233, for details].

For each state, I numerically modeled multi-wavelength emission using the AM³. Motivated by the possible neutrino emission, I started with a model where all radiation above ~ 10 eV originates from radiation processes of electrons and protons in the jet. Both electrons and protons are assumed to be accelerated in the source to power-law spectra $dN/d\gamma'_{e,p} \propto \gamma'^{-\alpha_{e,p}}$ with spectral indices $\alpha_{e,p}$, spanning a range of Lorentz factors from $\gamma'_{e,p}^{\min}$ to $\gamma'_{e,p}^{\max}$. The energy spectra of the electrons and protons are normalized to the corresponding total electron and proton luminosities, L'_e and L'_p . These particles are then injected into a single spherical blob of size R'_b moving along the jet with Lorentz factor Γ , where there is a homogeneous and isotropic magnetic field of strength B' . Under the assumption that the jet is observed at an angle $\theta_{\text{obs}} = 1/\Gamma_b$ relative to its axis, the Doppler factor can be approximated as $\delta_D \approx \Gamma_b$. The high-

energy gamma-ray absorption due to EBL is implemented using the model by Domínguez et al. [168]. The best-fit parameter values were found by minimizing the reduced χ^2 with the `Minuit` package. The results of the leptohadronic modeling for 4FGL J1210.3+3928 and 4FGL J1211.6+3901 are shown in [Figure 5.12](#). The values of the model parameters can be found in [Table 5.9](#).

As an alternative scenario, I also considered a case where all radiation originates from purely leptonic processes. In this case, electrons are accelerated to a single power-law spectrum $dN/d\gamma'_e \propto \gamma'^{-\alpha_e}$ with spectral index α_e , spanning a range of Lorentz factors from γ'^{\min}_e to γ'^{\max}_e . The energy spectrum of the electrons is normalized to the total electron luminosity parameter, L'_e . Similarly to the leptohadronic case, electrons undergo interactions and radiate inside of a spherical blob of size R' with a homogeneous and isotropic magnetic field of strength B' moving along the jet with Lorentz factor Γ_b . The obtained best-fit solutions for both sources are shown in [Figure 5.13](#).

5.3.4 Results

The best-fit parameters of the leptohadronic models for both sources are consistent with typical values found in HBLs [171]. The emission region is characterized by a size of 5×10^{16} cm and a magnetic field strength of 0.05 – 0.1 G. To account for the observed optical and X-ray fluxes, both sources require a population of high-energy electrons with Lorentz factors ranging from $\sim 10^4$ to $\sim 10^6$. The presence of highly relativistic protons in the jet is necessary for neutrino production. In these models, the maximum proton energy reaches $\sim 10^{18}$ eV for 4FGL J1210.3+3928, placing it in the ultra-high-energy cosmic ray (UHECR) range, while for 4FGL J1211.6+3901, it is around $\sim 10^{17}$ eV. Comparable maximum proton energies have been predicted for another HBL, Mrk 421, in Dimitrakoudis et al. [234].

The gamma-ray spectrum of 4FGL J1210.3+3928 shows a distinct dip in the GeV range ([Figure 5.12a](#)). This feature is well explained by the leptohadronic model, which combines proton synchrotron emission (\lesssim GeV) with photo-pion production (\gtrsim GeV). In contrast, purely leptonic models struggle to reproduce this spectral feature using inverse Compton emission alone ([Figure 5.13](#)). For 4FGL J1211.6+3901, both leptonic and leptohadronic models provide a good fit to the observed gamma-ray, X-ray, and near-infrared fluxes. The discrepancy in the optical band for both models may be due to non-simultaneous data, highlighting the impact of source variability. However, given the limited optical data, a fully simultaneous SED could not be constructed. There is no clear way to distinguish between purely leptonic and leptohadronic scenarios with the available data.

A key energy range that could help resolve this uncertainty is the MeV gamma-ray band. High-energy photons interacting with protons produce Bethe-Heitler pairs, which subsequently emit synchrotron radiation peaking in the MeV range. This excess of MeV photons could serve as

Blazars near NGC 4151:
[\[171\]](#): Rodrigues et al. (2024), Leptohadronic multi-messenger modeling of 324 gamma-ray blazars
[\[234\]](#): Dimitrakoudis et al. (2014), Self-consistent neutrino and UHE cosmic ray spectra from Mrk 421

Table 5.9: Table of best-fit parameters for leptonic and lepto-hadronic models during the quiescent and flaring states of J1211.6+3901

Parameters	4FGL J1210.3+3928 lepto-hadronic	4FGL J1211.6+3901 lepto-hadronic	4FGL J1210.3+3928 leptonic	4FGL J1211.6+3901 leptonic
R'_b [cm]	5×10^{16}	5×10^{16}	3×10^{16}	3.5×10^{16}
B' [G]	0.1	0.04	0.05	0.04
Γ_b	25	25	25	25
$\gamma'_{e,\min}$	2×10^4	2×10^4	2.5×10^4	1×10^4
$\gamma'_{e,\max}$	1×10^6	1×10^6	1×10^6	1×10^6
α'_e	2.0	2.3	2.3	2.3
L'_e [erg/s]	3×10^{40}	7.5×10^{40}	7×10^{40}	1.4×10^{41}
$\gamma'_{p,\min}$	2×10^3	2×10^3	-	-
$\gamma'_{p,\max}$	1.5×10^9	6×10^7	-	-
α'_p	1.9	1.5	-	-
L'_p [erg/s]	4×10^{45}	1.5×10^{46}	-	-

a hadronic signature, emphasizing the importance of future MeV Compton telescopes such as COSI [188], GRAMS [235], and AMEGO-X [189].

The lepto-hadronic modeling predicts all-flavor neutrino fluxes of $\sim 10^{-12}$ erg cm $^{-2}$ s $^{-1}$ peaking above ~ 10 PeV for both blazars. These predicted fluxes suggest that the contribution of these sources to the neutrino signal observed by IceCube in the direction of NGC 4151 is minor. The data analysis was performed using a high X-ray flux level to estimate the maximum possible neutrino contribution from both blazars. Considering the time-averaged emission state would further decrease the blazar contribution to the NGC 4151 hotspot, strengthening the conclusion that their role is subdominant.

Although the next-generation IceCube-Gen2 observatory will feature enhanced PeV-range sensitivity in its optical array [183], detecting neutrino emission from J1210.3+3928 or J1211.6+3901 remains challenging due to their high energies. Detection of neutrinos at $10^{16} - 10^{17}$ eV, where the emission peaks, would require either the radio array of IceCube-Gen2 or a detector like GRAND [236]. The predicted neutrino flux from 4FGL J1210.3+3928 could be detectable by both facilities, while the flux from 4FGL J1211.6+3901 is near the 10-year sensitivity threshold of GRAND 200k's and slightly above the 10-year sensitivity of IceCube-Gen2's radio array, suggesting a potential detection with IceCube-Gen2. The expected angular resolution is better than 1° for the IceCube-Gen2 radio array [183] and better than 0.5° for GRAND [236]. If multiple neutrinos are detected, the directional accuracy could further improve, potentially allowing for the spatial separation of signals from the two blazars.

5.3.5 Discussion

The lepto-hadronic model of 4FGL J1210.3+3928 successfully reproduces the observed electromagnetic fluxes, including the GeV dip in gamma rays, which cannot be explained by a purely leptonic scenario. For 4FGL J1211.6+3901, both leptonic and lepto-hadronic models provide equally good fits to the observed data. The predicted neutrino flux for both sources

Blazars near NGC 4151:

[188]: Tomsick and others (2019), The Compton Spectrometer and Imager

[235]: Aramaki et al. (2020), Dual MeV gamma-ray and dark matter observatory - GRAMS Project

[189]: Caputo et al. (2022), All-sky Medium Energy Gamma-ray Observatory eXplorer mission concept

[183]: Aartsen et al. (2021), IceCube-Gen2: the window to the extreme Universe

[236]: Álvarez-Muñiz et al. (2020), The Giant Radio Array for Neutrino Detection (GRAND): Science and Design

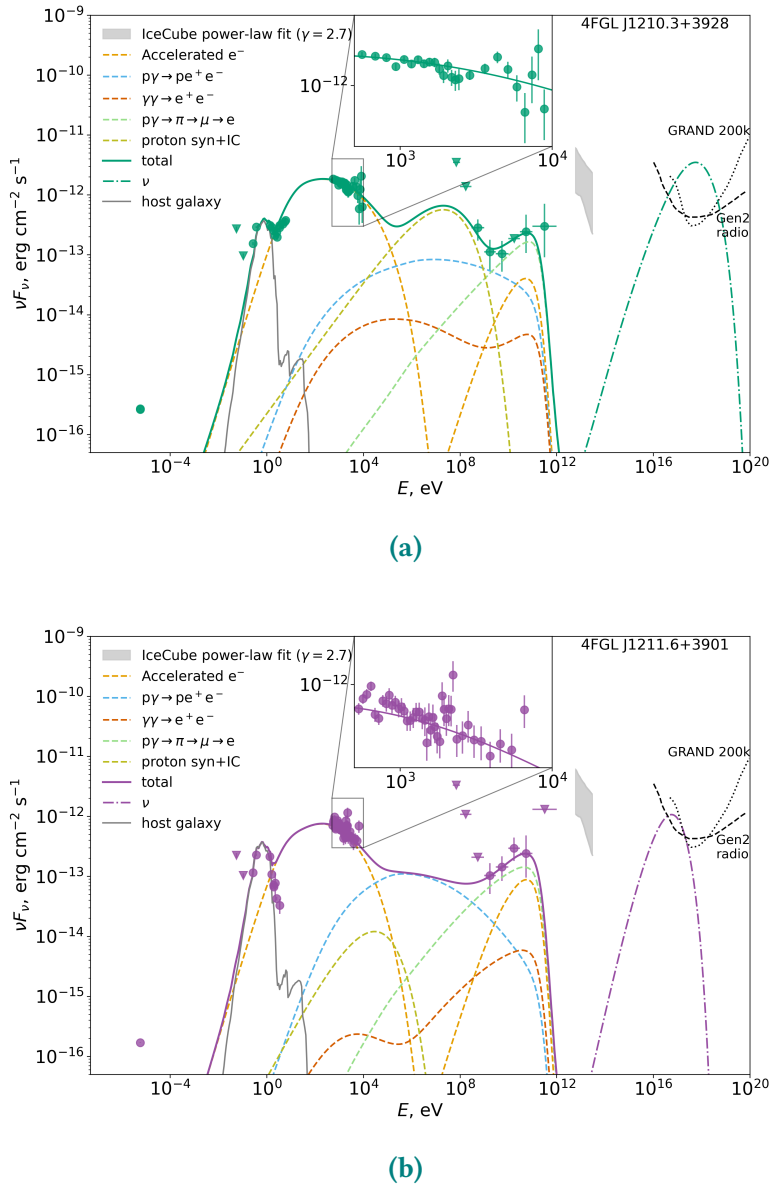


Figure 5.12: Leptohadronic model for (a) 4FGL J1210.3+3928 and (b) 4FGL J1211.6+3901. The green solid line corresponds to the multi-wavelength photon emission. The components are shown with the dashed line. The green dash-dotted line corresponds to the all-flavor neutrino spectrum. The gray shaded area is a neutrino flux from NGC 4151 under the assumption of power-law with spectral index $\gamma = 2.7$ [213]. The black dash-dotted line shows 10 year sensitivity of IceCube-Gen2 optical array [183], black dashed – 10 year all-flavor sensitivity of IceCube-Gen2 radio array [183], black dotted line – 10 year all-flavor sensitivity of GRAND 200k [236]. Figure from Omeliukh et al. [147].

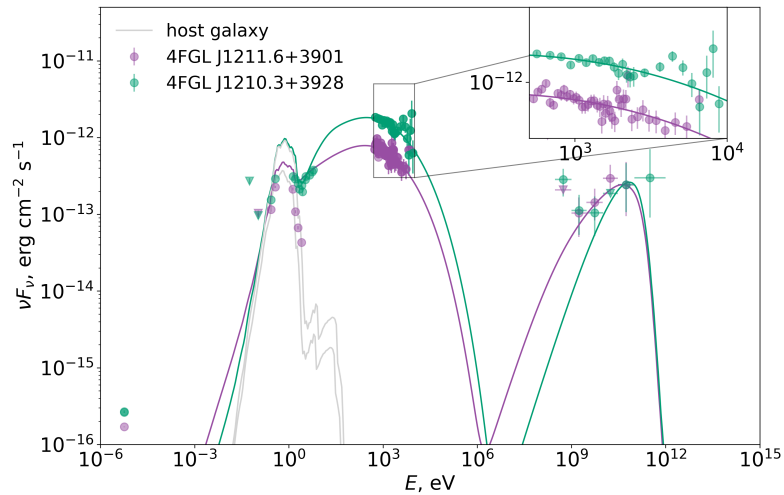


Figure 5.13: Leptonic models for 4FGL J1210.3+3928 (green) and 4FGL J1211.6+3901 (purple). The solid line corresponds to the multi-wavelength photon emission. The solid gray line corresponds to the emission of the host galaxy. Figure from Omeliukh et al. [147].

peaks around 10^{17} eV, with their contribution to the observed TeV neutrino flux expected to be minor.

Both 4FGL J1210.3+3928 and 4FGL J1211.6+3901 have high-energy synchrotron peaks located in the X-ray band, indicating efficient particle acceleration. In the proposed model, the neutrino spectrum peaks at approximately ~ 10 – 100 PeV, due to $p\gamma$ interactions with internal synchrotron photons and the extension of cosmic-ray spectra to EeV energies. Reducing the maximum proton energy could shift the neutrino peak toward TeV energies [237], aligning with IceCube’s detection of neutrinos from the direction of NGC4151. However, such a scenario would require significantly higher proton power and fails to reproduce the observed broadband electromagnetic spectra. The maximum proton Lorentz factor for the leptohadronic model of 4FGL J1211.6+3901 is notably lower than that for 4FGL J1210.3+3928. This difference arises because, at higher proton energies, Bethe-Heitler pair production and proton synchrotron emission become more significant, leading to inconsistencies with the observed X-ray and gamma-ray spectra.

The proton luminosity is fundamentally constrained by the accretion power. Since direct measurements of accretion power are unavailable for these blazars, an order-of-magnitude estimate based on the Eddington luminosity is used. Following the empirical relation between black hole mass and bulk mass [e.g., 238, 239], the fitted galactic profile suggests $M_{\text{bulk}} = 10^{12} M_{\odot}$, corresponding to a black hole mass of $M_{\text{BH}} = 10^9 M_{\odot}$ and an Eddington luminosity of $L_{\text{Edd}} \sim 10^{47}$ erg/s. Even when the maximum proton energy is reduced to 10^{15} – 10^{16} eV and proton luminosity is set to the Eddington limit, the neutrino spectrum is still expected to peak above PeV energies. Consequently, the contribution of these blazars to the

Blazars near NGC 4151:

[237]: Dermer et al. (2014), Photopion production in black-hole jets and flat-spectrum radio quasars as PeV neutrino sources

[238]: Häring and Rix (2004), On the Black Hole Mass-Bulge Mass Relation

[239]: Zhu et al. (2021), The Correlation between Black Hole Mass and Stellar Mass for Classical Bulges and the Cores of Ellipticals

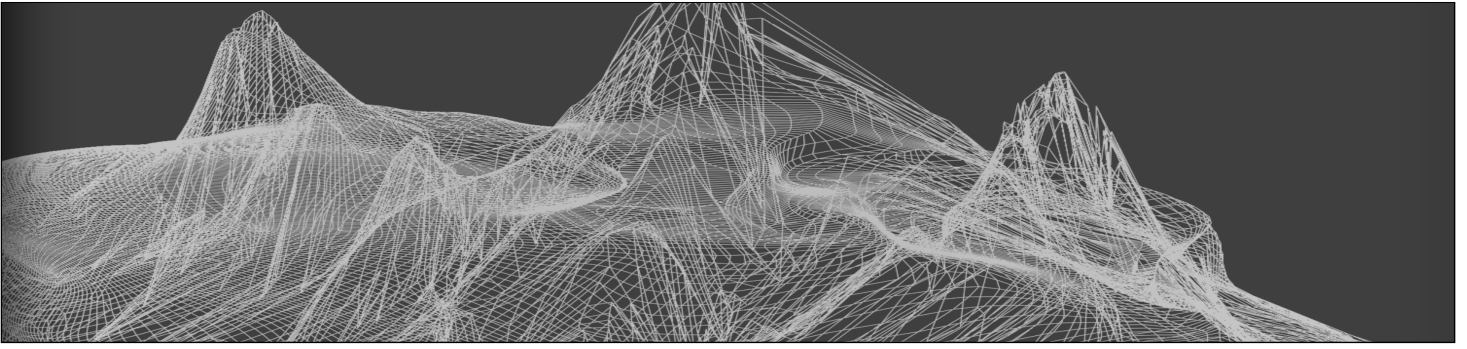
neutrino signal from the region near NGC 4151 can only be subdominant.

Neutrino emission models for the Seyfert galaxy NGC 4151 predict lower-energy neutrinos compared to those for the two nearby blazars. While most models suggest a neutrino spectrum cutoff above 10–100 TeV for Seyfert galaxies, HBLs can generate neutrinos at significantly higher energies. Next-generation neutrino observatories like IceCube-Gen2 and GRAND could help resolve this discrepancy by probing higher energy ranges and potentially distinguishing between two spatially separate hotspots. Additionally, upcoming MeV gamma-ray missions will offer new opportunities to test for signatures of hadronic emission.

5.3.6 Summary and conclusions

The IceCube analysis has identified approximately 30 signal neutrinos from the direction of NGC4151 over ten years of data. However, two gamma-ray bright blazars, 4FGL J1210.3+3928 and 4FGL J1211.6+3901, are located just 0.08° and 0.43° away from NGC4151, respectively. Given that blazars are considered promising neutrino emitters, they may contribute to the observed neutrino hotspot. In this project, I modeled the multi-wavelength spectra of both blazars and obtained the following results:

- The leptohadronic model for 4FGL J1210.3+3928 successfully reproduces the observed electromagnetic fluxes, including a GeV-range dip in the gamma-ray spectrum, which may serve as a hadronic signature. For 4FGL J1211.6+3901, both leptonic and leptohadronic scenarios provide equally good fits to the observational data.
- The predicted neutrino flux from both sources peaks around 10^{17} eV. However, their contribution to the observed TeV-scale neutrino flux is expected to be subdominant.
- Detecting neutrinos from these blazars will likely require radio-based detection techniques and may become feasible with future instruments, such as the radio array of IceCube-Gen2 or GRAND.



Chapter 6

Parameter spaces of one-zone leptonic models

When Dyson met with him in 1953, Fermi welcomed him politely, but he quickly put aside the graphs he was being shown indicating agreement between theory and experiment. His verdict, as Dyson remembered, was “There are two ways of doing calculations in theoretical physics. One way, and this is the way I prefer, is to have a clear physical picture of the process you are calculating. The other way is to have a precise and self-consistent mathematical formalism. You have neither.” When a stunned Dyson tried to counter by emphasizing the agreement between experiment and the calculations, Fermi asked him how many free parameters he had used to obtain the fit. Smiling after being told “Four,” Fermi remarked, “I remember my old friend Johnny von Neumann used to say, with four parameters I can fit an elephant, and with five I can make him wiggle his trunk.” There was little to add.

G. Serge, B.Hoelin, The Pope of Physics: Enrico Fermi and the Birth of the Atomic Age, 2016

Blazars are the primary sources of extragalactic GeV–TeV gamma rays and are also promising candidates for neutrino emission. Understanding their emission mechanisms is essential for advancing both gamma-ray and neutrino astronomy.

As discussed in previous chapters, one-zone models are the simplest way to explain blazar SEDs and have become a common framework for modeling both individual blazars and blazar samples. However, advanced radiation models often involve many free parameters, making it challenging to fit the observed data due to the significant computational efforts required.

One-zone leptonic models are expected to exhibit some degeneracies (as discussed in [Section 6.1](#)). Finding the best-fit solutions in complex parameter spaces can be quite difficult, and different optimization algorithms may yield varying results, affecting the physical interpretation of those solutions.

This chapter focuses on the challenges of data fitting within the complex parameter space of one-zone leptonic models. First, I discuss the data-fitting features that arise from the fundamental concepts of radiation models. Next, I compare the performance of five selected optimization algorithms on simulated pseudo-data with known true parameter values. Finally, I present the fitting results for actual blazar data and discuss the implications, extending the conclusions to models with additional free parameters.

Parameter spaces:

[240]: Apel et al. (2025), Impact of model parameter degeneracy on leptonic radiation models. The case of blazar multi-wavelength spectra

The work presented in this Chapter is based on Apel et al. [240]. I am one of the two first authors of this publication, and my contribution consists of: a proposal of the original idea for this study, contribution to methodology, development and adaption of grid scan, Minuit and MCMC algorithms for coupling with AM³, contribution to the discussion of the obtained results.

6.1 Leptonic models

In a typical one-zone synchrotron self-Compton (SSC) model, the electrons are assumed to be pre-accelerated to a simple power-law spectrum $dN/d\gamma'_e \propto \gamma'^{-\alpha_e}$ with spectral index α_e , spanning a range of Lorentz factors from γ_e^{\min} to γ_e^{\max} . The energy spectrum of the electrons is normalized to the total electron luminosity parameter, L'_e . Then, electrons are injected into a single spherical blob of size R'_b (in the co-moving frame of the jet) moving along the jet with Lorentz factor Γ , where they encounter a homogeneous and isotropic magnetic field of strength B' . The electrons produce low-energy synchrotron emission which becomes a target photon field for inverse Compton scattering with the same electron population. Apart from synchrotron radiation and Compton scattering, the photon-photon pair-production is taken into account. The EBL absorption is modeled using Domínguez et al. [168]. The jet is assumed to be observed at an angle $\theta_{\text{obs}} = 1/\Gamma_b$ relative to its axis, resulting in a Doppler factor of $\delta_D = \Gamma_b$. In this project, the radiation processes are numerically modeled with the AM³ within a steady-state approximation (see Section 4.3).

The parameter space of one-zone leptonic models consists of possible values of seven free parameters ($\theta \in \mathbb{R}^7$) which are summarized in Table 6.1.

Table 6.1: List of one-zone leptonic model parameters.

Parameter	Meaning
R'_{blob} , cm	Radius of the spherical emission zone region
B' , G	Strength of the homogeneous magnetic field
Γ_b	Blob Lorentz factor
γ_e^{\min}	Minimal electron Lorentz factor
γ_e^{\max}	Maximal electron Lorentz factor
α_e	Power-law index of the electron energy distribution
L'_e , erg s ⁻¹	Total electron luminosity

One-zone leptonic models:

[168]: Domínguez et al. (2011), Extragalactic background light inferred from AEGIS galaxy-SED-type fractions

6.2 Visualization of multi-dimensional spaces

A typical data fitting procedure includes assessing the goodness of fit. In this study, the reduced χ^2 function is chosen as the goodness-of-fit measure. It is defined as

$$\chi^2(\theta)/\text{n.d.f.} = \frac{1}{N - N_{\text{par}} + 1} \sum_i \frac{(F_i^{\text{data}} - F_i^{\text{model}}(\theta))^2}{\sigma_i^2}, \quad (6.1)$$

where N is the number of data points, $N_{\text{par}} = 7$ the number of free parameters in the model, F_i^{data} are the observed fluxes, F_i^{model} are the predicted fluxes by the model, and i is the summation index that corresponds

to the observed frequency values, and σ_i are the flux measurement uncertainties. The function input $\theta \in \mathbb{R}^7$ are the model parameters from **Table 6.1**. While in the general case different goodness-of-fit functions are possible, we select the reduced χ^2 function commonly used in physics and astronomy as its values directly indicate a poor fit ($\chi^2(\theta)/\text{n.d.f.} \gg 1$), an overfitting ($\chi^2(\theta)/\text{n.d.f.} \ll 1$) or a good fit ($\chi^2(\theta)/\text{n.d.f.} \approx 1$). The model that produces the minimal value of the reduced χ^2 is defined as the best fit. If the SED contains upper limits on the flux values, they do not contribute to the reduced χ^2 value as long as the model predictions are below their values. In the opposite case, a large value (10^5) is added to the reduced χ^2 so that a model overshooting upper limits is considered highly unfavorable.

Multi-dimensional spaces:

[241]: Aggarwal et al. (2001), "On the Surprising Behavior of Distance Metrics in High Dimensional Space"
 [242]: Van der Maaten and Hinton (2008), Visualizing data using t-SNE.

To meaningfully compare the outcomes of the selected minimization procedures, it is essential to assess the similarity between the resulting multidimensional vectors of model parameters, i.e., to evaluate how closely different solutions lie within the parameter space. While it might seem straightforward to use standard distance metrics, such as the Euclidean distance, these measures often fail to accurately capture the notion of proximity in high-dimensional settings [e.g., 241].

To address this challenge, this work employs a machine learning technique known as *t-distributed stochastic neighbor embedding* (t-SNE) [242], which enables the visualization of high-dimensional data in low-dimensional spaces. This approach facilitates the identification of multiple regions in the parameter space that exhibit similar goodness-of-fit values and allows for a more intuitive comparison of the relative proximity among different best-fit solutions.

t-SNE reduces the dimensionality of data by preserving the similarity relationships between points in both the high-dimensional and low-dimensional spaces. These similarities are expressed as probabilities that are non-linearly related to metric distances, such that points with higher similarity are mapped closer together in the resulting two-dimensional representation. However, it is important to note that t-SNE does not preserve the exact ratios of distances between points from the original space.

A key challenge in using t-SNE lies in distinguishing truly close points from those that appear clustered due to the selected representation. One influential hyperparameter in this context is perplexity, which roughly corresponds to the number of nearest neighbors considered during the embedding. Perplexity plays a critical role in balancing local and global structure in the data and can significantly affect the formation of artificial clusters. More details on hyperparameter tuning for reliable similarity representation can be found in Apel et al. [240].

The parameter spaces in this project are visualized with the t-SNE tool from the `scikit-learn` open-source Python library [243]. To account for the different scales of the model parameters, the parameters R'_{blob} , γ'_{min} , γ'_{max} and L'_e are transformed to a logarithmic scale (decimal base), while the other parameters are kept in a linear scale. The model parameter values are then normalized to a common range between zero and one for each parameter. After this, the t-SNE algorithm is used to create a low-

Multi-dimensional spaces:

[240]: Apel et al. (2025), Impact of model parameter degeneracy on leptonic radiation models. The case of blazar multi-wavelength spectra
 [243]: Pedregosa et al. (2011), Scikit-learn: Machine Learning in Python

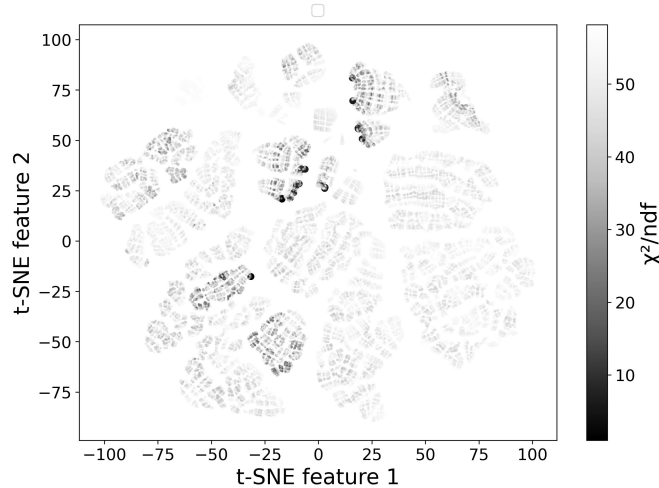


Figure 6.1: Example of the seven-dimensional parameter space mapping with t-SNE (grid scan results for simulated dataset 2 (see [Section 6.4](#) for description)). Each point represents one model consisting of seven parameters. Darker colors correspond to lower $\chi^2/\text{n.d.f.}$ values. The plot shows the first 50 000 points with the lowest $\chi^2/\text{n.d.f.}$ values and the perplexity is set to 30. Figure from Apel et al. [[240](#)].

dimensional representation of the parameter space. The goodness-of-fit value associated with each set of parameters is displayed as a color scale, highlighting areas in the parameter space where better solutions can be found.

Then the low-dimensional map of the parameter space is built using the t-SNE. The goodness-of-fit value which corresponds to each parameter vector is used as a color scale to highlight the regions in the parameter space with the best solutions. [Figure 6.1](#) illustrates a t-SNE plot that represents the parameter space of the leptonic models applied to simulated dataset 1 (description will be given in [Section 6.4](#)). The darker areas in the plot indicate regions where good-fit solutions are located.

Various methods are available for visualizing multidimensional data, including parallel coordinates, principal component analysis, and Andrew’s plots. Given the requirement to represent a large number of points while maintaining clear distinctions between them, t-SNE was selected as one of the most effective techniques for this purpose. Additional details on the representation of grid scan solutions for PKS 0735+178 using Andrew’s plots can be found in [Appendix B](#), while the t-SNE visualization will be used throughout this work.

6.3 Challenges for parameter fitting

Having a large number of free parameters in smooth³ convex⁴ functions typically do not affect the validity of the minimization process. However, the reduced χ^2 (as essentially any goodness-of-fit function) is not a smooth and convex function of model parameters.

³All first derivatives are continuous.

⁴A function $f : \mathbb{R}^n \rightarrow \mathbb{R}$ is convex if for all $0 \leq t \leq 1$ and all $x, y \in \mathbb{R}^n$ $f(tx + (1-t)y) \leq tf(x) + (1-t)f(y)$.

The first reason originates from the intrinsic characteristics of the radiation processes involved. Some processes have energy thresholds (like $\gamma\gamma \rightarrow e^+e^-$) or exhibit markedly different behavior across energy regimes, as seen in the transition from the Thomson to the Klein-Nishina regime in the inverse Compton effect. These features disrupt the smoothness of the goodness-of-fit function, as even minor variations in certain parameters can lead to substantial changes in the resulting spectral shape. Consequently, the function becomes difficult or impossible to differentiate numerically.

The second factor contributing to the expected non-smooth and non-convex nature of the goodness-of-fit function is the limited amount of photon flux measurements. Ideally, for data covering many orders of magnitudes without gaps, the shape of the SED is unambiguously defined by the model parameters. In practice, however, the SED typically contains gaps due to the limited energy coverage of observational instruments. As a result, distinct electron populations can yield similar observed photon fluxes, with meaningful differences appearing only in the unmeasured regions. Different electron populations can produce similar photon-flux levels with differences that could be spotted only in the missing data regions. By varying, for example, the electron maximum Lorentz factor, spectral index, and electron luminosity (which normalizes the spectrum), similar levels of photon fluxes can be achieved for different combinations of these parameters. Moreover, since the observed luminosity follows $L \simeq \delta_D^4 L'$, there exists such a bulk Lorentz factor that the observed luminosity remains unchanged. However, different Doppler factors alter the shape of the SED, which can again be balanced by adjusting the electron spectral parameters. This interplay results in multiple parameter combinations yielding similarly good fits, reinforcing the expectation that the goodness-of-fit function is non-convex. While defining an optimal fit is conceptually straightforward, computing it in practice is considerably more difficult – a challenge that will be addressed in [Section 6.5](#).

6.4 Simulated pseudo-data

To assess the performance of different optimization algorithms, it is essential to compare their best-fit results with the true values of the model parameters. In the case of real blazars, the one-zone model framework remains only an assumption with physical parameters being unknown. For testing purposes, simulated pseudo-data were generated based on a selected AM³-produced SED. To ensure that the SED falls within realistic flux and energy ranges, we adopted the model parameters of the quiescent-state SED of the ISP blazar PKS 0735+178 from Omeliukh et al. [145]. Furthermore, to examine the impact of data coverage and measurement uncertainties on the modeling process, three distinct datasets were generated. For each dataset, to mimic the uncertainty of data measurements, the data points were shifted from their true values by a random value that follows a normal distribution (with zero mean value and the

standard deviation equal to the set error value). After the new flux value was calculated, its uncertainty was introduced as a percentage of the new flux values.

Dataset 1 represents the most optimistic (or close to the ideal) case where the photon flux is measured across the whole photon energy range. The data points are uniformly distributed in logarithmic space. The flux values are shifted by random values that follow a normal distribution with zero mean and 10% standard deviation. The flux uncertainty is set to 10% of the obtained flux.

Dataset 2 represents a more realistic case with selected energy ranges in infrared, optical, ultraviolet, X-ray, MeV gamma rays, and GeV gamma rays. The energy bins correspond to the real typical energy bins of *Swift*-XRT, COMPTEL, and *Fermi*-LAT telescopes. For completeness, the last two points represent *Fermi*-LAT sensitivity-based upper limits. The procedure of adding random noise is similar to that of dataset 1. The uncertainty remained fixed at 10% of fluxes for all energy ranges.

Dataset 3 resembles a blazar SED with the least amount of available data. The data covers only optical, UV, X-rays, and GeV gamma rays. The added noise in this case has a standard deviation of 10% for optical and UV, 30% for X-ray, and 40% for gamma rays. The same percentages of the obtained fluxes are added as error bars. Similarly to dataset 2, the last two points in the SED resemble *Fermi*-LAT sensitivity-based upper limits.

The resulting simulated datasets are shown in [Figure 6.2](#). The dashed line in the plot corresponds to the original SED simulated with AM³. The parameters of the model used for simulation can be found in [Table 6.5](#).

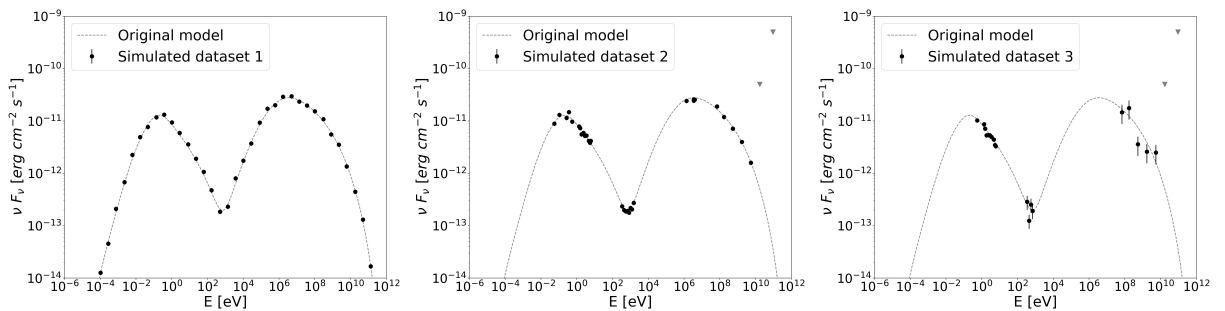


Figure 6.2: The plots show the three simulated datasets in each plot as black dots. The dashed curve shows the original model that was used to generate the data. Figure from Apel et al. [240].

6.5 Comparison of minimization algorithms on simulated data

In a non-smooth and non-convex parameter space, the choice of minimization algorithm can significantly influence the fitting results, impacting the physical interpretation of the models. To examine this effect, five optimization algorithms commonly used in the literature were selected:

Table 6.2: Boundaries of the leptonic model parameters for fitting simulated data.

Parameter	Value range
$\log_{10}(R'_{\text{blob}})$, cm	[15.0, 17.5]
B' , gauss	[0.1, 5]
Γ_b	[3.0, 30.0]
$\log_{10}(\gamma_e^{\text{min}})$	[3.0, 4.0]
$\log_{10}(\gamma_e^{\text{max}})$	[4.0, 5.0]
α_e	[0.5, 3.5]
$\log_{10}(L'_e) / \text{erg s}^{-1}$	[42.0, 47.0]

Minuit:

[244]: James (1998),

MINUIT: function

minimization and error

analysis reference manual

[170]: Dembinski et al.

(2020), scikit-hep/iminuit

[245]: Nelder and Mead

(1965), A simplex method

for function minimization

migrad and simplex (from Minuit), grid scan, two evolutionary algorithms, and Markov Chain Monte Carlo. All algorithms aim to minimize the same reduced χ^2 function, as defined in Eq. (6.1). For the simulated data, the algorithms search for optimal solutions within the same parameter space, constrained by the boundaries listed in Table 6.2.

Minuit

Minuit is a software library for numerical minimization originally developed for applications in high energy physics [244]. For this work, I used the Python interface for Minuit called iminuit [170]. I start the minimization with the Nelder-Mead simplex method [245] due to its robustness and ability to overcome local minima. Given the nature of radiation processes, small variations in model parameters can lead to substantial changes in the reduced χ^2 , making it numerically non-differentiable at certain points. As a gradient-free method, the simplex approach is particularly suitable for complex parameter spaces in leptonic models. After the simplex method, the algorithm proceeds with migrad, a gradient-based optimization technique, to refine the best-fit solution locally in regions where abrupt changes in the reduced χ^2 are not expected.

The initial starting point for the simplex algorithm is an educated guess of what values model parameters can have based on the SED features. In this study, the maximum number of function calls in Minuit was set to 1200. After the initial run, the minimization did not yield a satisfactory value for the reduced χ^2 . Consequently, the current best-fit result was used as a new starting point, and the parameter space boundaries were adjusted to be closer to this best-fit. The minimization procedure was then repeated. During the second run, approximately 300 function calls were required.

Grid scan

Grid scanning is a method in which the goodness-of-fit function is evaluated for every combination of parameter values evenly spaced within defined boundaries (see Table 6.2). This straightforward approach ensures uniform coverage of the entire parameter space and helps identify regions corresponding to low reduced χ^2 values. In this study, ten points were sampled per parameter, resulting in a total of 10^7 points in the parameter space. However, even with 10^7 simulated models, the grid resolution was not sufficient to find an accurate best-fit solution. Therefore, local minimization as a second step was necessary (similarly to the methods in Section 5.1). Since all neighboring points around the current best fit from the grid scan have higher reduced χ^2 values, their parameter values are used as new boundaries to search for an improved best fit. The best result from the grid scan was then locally minimized using Minuit (simplex followed by migrad), initialized at the grid scan best-fit point with the updated boundaries as described above.

Genetic algorithm

The genetic algorithm is an optimization method that belongs to the family of evolutionary algorithms [e.g., 246]. Inspired by the principles of

Table 6.3: Parameters of the genetic algorithm.

Parameter	Values
Number of generations	70 – 80
Number of individuals	10^4
Mutation probability	0.33
Independent probability	1/7
Crossover probability	0.20

Genetic algorithm:

[246]: Kramer and Kramer (2017), Genetic algorithms

biological evolution, it iteratively improves an initial population of candidate solutions to approach an optimal solution by generating new candidates through random “mutations”.

The process begins by randomly initializing a population of candidate solutions, whose fitness is assessed by calculating their reduced χ^2 values. To produce new parameter values, the algorithm uses crossover, analogous to genetic inheritance, where an offspring inherits traits from both parents. In this context, pairs of individuals with higher fitness from the current population are selected to generate offspring with a certain crossover probability. Additionally, random mutations can occur, altering parameter values with a given mutation probability. These mutations are equally likely to affect any of the seven model parameters.

After applying crossover and mutation, the newly generated offspring replace the previous population. This cycle repeats until the population converges to an optimal solution. The genetic algorithm has been successfully applied for SED fitting in [138, 140, 171, 247], utilizing evolutionary functions from the DEAP module in Python [248]. Their values used for this work are given in **Table 6.3**. The standard deviations of the parameter values in the last generation are taken as the uncertainties in the parameter estimation.

CMA-ES

The Covariance Matrix Adaptation Evolution Strategy (CMA-ES) [249, 250] is another type of evolutionary algorithm. It follows a process similar to that of the genetic algorithm but differs primarily in its approach to mutation. In CMA-ES, mutation strength determines how much the offspring differ from the parent population. Unlike genetic algorithms, most evolution strategies, including CMA-ES, adapt the mutation step size based on the success of previous mutations. This adaptive mechanism enables the algorithm to learn the optimal mutation strength as evolution progresses. As a result, evolution strategies generally require less manual parameter tuning compared to genetic algorithms.

In this study, CMA-ES was implemented in Python using the `pycma` package [251]. The initial step size for the first generation must be specified at the start, after which it is automatically adjusted in each subsequent generation. Here, the initial step size was set to $\sigma = 2$.

MCMC

Markov chain Monte Carlo (MCMC) is a sampling technique used to draw samples from probability distributions, helping to estimate the posterior probability distribution of model parameters. This posterior distribution provides insight into the most likely parameter values. Although MCMC is widely used for data fitting, [252] caution that merely exploring the parameter space is not sufficient justification for using MCMC, as its primary purpose is to serve as a sampler. Nonetheless, given its frequent application in blazar modeling [253, 254, 255, 256, 257], we also investigate its performance in this context.

Genetic algorithm:

[138]: Rodrigues et al. (2019), Leptohadronic Blazar Models Applied to the 2014–2015 Flare of TXS 0506+056

[140]: Rodrigues et al. (2021), Multiwavelength and Neutrino Emission from Blazar PKS 1502 + 106

[171]: Rodrigues et al. (2024), Leptohadronic multi-messenger modeling of 324 gamma-ray blazars

[247]: Rodrigues et al. (2024), The Spectra of IceCube Neutrino (SIN) candidate sources: V. Modeling and interpretation of multiwavelength and neutrino data

[248]: Fortin et al. (2012), DEAP: Evolutionary Algorithms Made Easy

CMA-ES:

[249]: Hansen (2016), The CMA Evolution Strategy: A Tutorial

[250]: Hansen and Ostermeier (2001), Completely Derandomized Self-Adaptation in Evolution Strategies

[251]: Hansen et al. (2019), CMA-ES/pycma on Github

MCMC:

[252]: Hogg and Foreman-Mackey (2018), Data Analysis Recipes: Using Markov Chain Monte Carlo

[253]: Yamada et al. (2020), Variations of the physical parameters of the blazar Mrk 421 based on analysis of the spectral energy distributions

[254]: Tramacere (2020), JetSeT: Numerical modeling and SED fitting tool for relativistic jets

[255]: Tzavellas et al. (2023), Application of neural networks to synchro-Compton blazar emission models

[256]: Sciacaluga et al. (2024), Stochastic acceleration in extreme TeV BL Lacs through MCMC

[257]: Hervet et al. (2024), "Bjet_MCMC: A New Tool to Automatically Fit the Broadband Spectral Energy Distributions of Blazars"

MCMC:

[258]: Goodman and Weare (2010), Ensemble samplers with affine invariance

[259]: Foreman-Mackey et al. (2013), emcee: The MCMC Hammer

[252]: Hogg and Foreman-Mackey (2018), Data Analysis Recipes: Using Markov Chain Monte Carlo

In this study, I utilize the Affine Invariant Markov chain Monte Carlo method [258], implemented in Python using the emcee package [259]. The emcee algorithm requires a definition of a probability function to evaluate the quality of the fit. Using this function, the algorithm constructs the posterior probability density function by performing a specified number of steps with a set of walkers and burn-in samples.

Following the recommendation of Hogg and Foreman-Mackey [252] to initialize MCMC runs near (but not exactly at) the optimum, I initialized the walkers close to the best-fit result from Minuit by adding random perturbations drawn from a standard normal distribution.

I used a “flat” (improper) prior for the model parameters, setting the distribution boundaries according to the values in [Table 6.2](#). Initially, the log-likelihood function was defined as $\ln(P) = -\frac{1}{2} \log_{10}(\chi^2)$. This logarithmic scaling was chosen to avoid issues with very low-probability regions that could separate high-probability areas. However, the optimal parameters found in this MCMC run were located in the same local region as the initial point. Possibly, using the logarithmic reduced χ^2 compromised the precision near the best-fit solution. To address this, I performed a second MCMC run using the optimal solution from the first run as the new starting point. In this run, I defined the log-likelihood as $\ln(P) = -\frac{1}{2}\chi^2$ and restricted the parameter space to the high-likelihood region identified in the first run, aiming for a more precise best-fit solution. The set-up of both MCMC runs is summarized in [Table 6.4](#).

Table 6.4: Parameters of MCMC runs

Parameter	MCMC run 1	MCMC run 2
Log-likelihood function	$\ln(P) = -\frac{1}{2} \log_{10}(\chi^2)$	$\ln(P) = -\frac{1}{2}\chi^2$
Log-prior	flat	flat
Number of walkers	50	50
Number of steps	1000	200
Burn-in samples	100	20
Initial point	from Minuit	from run 1

Results

The methods described above were applied to the simulated datasets to evaluate and compare their performance. To visualize the best-fit parameters identified by each optimization algorithm, t-SNE was used to project their positions within the global parameter space, along with the true parameters and the 50,000 grid scan points yielding the lowest reduced χ^2 values. In the t-SNE plots, points within the range $[(\chi^2/\text{ndf})_{\text{min}}, (\chi^2/\text{ndf})_{\text{min}} + 2]$ are shown as darker and larger. The best-fit SEDs and corresponding t-SNE maps are presented in [Figure 6.3](#), [Figure 6.4](#), and [Figure 6.5](#). The best-fit model parameters obtained by each method are summarized in [Table 6.5](#), with the true parameter values listed in the first row for reference.

Four out of the five tested optimization algorithms converged to a single best-fit solution, with the grid scan being the only method that identified multiple solutions. For consistency in comparison, only one grid scan result was selected for direct comparison with the other algorithms. Nevertheless, the t-SNE plots illustrate the positions of all solutions identified by the grid scan within the broader parameter space.

Figure 6.3 presents the results for dataset 1. As shown in the left panel, all algorithms produced solutions that fit the data well. CMA-ES and the genetic algorithm achieved reduced χ^2 values of 1.6 and 1.8, respectively, with best-fit parameters consistent with the true values within uncertainties (see **Table 6.5**). The grid scan, MCMC, and Minuit performed slightly less well, yielding reduced χ^2 values of 2.2, 3.5, and 4.1, respectively, with deviations primarily in the X-ray–MeV and radio bands. The right panel shows the best-fit parameters in parameter space: the solutions from the grid scan, CMA-ES, and the genetic algorithm lie close to the true values, whereas those from MCMC and Minuit fall outside this region. This discrepancy may be due to the initialization or step size settings and could likely be reduced by tuning these parameters. Overall, in this idealized case with small flux uncertainties, all algorithms converged on similar results. As confirmed by the grid scan, the only region with low χ^2 values corresponds to the true solution.

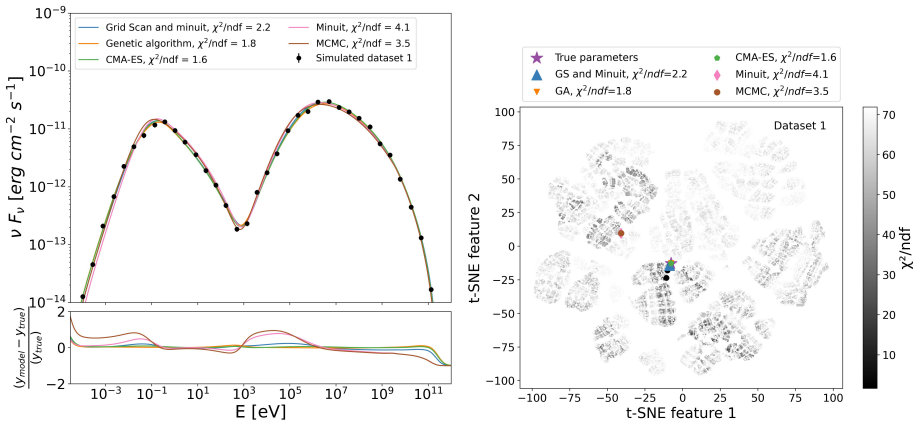


Figure 6.3: Left panel: Best-fit solutions from each of the selected optimization algorithms for the simulated dataset 1. Right panel: t-SNE plot showing the proximities of different solutions. Figure from Apel et al. [240].

Figure 6.4 shows the results for dataset 2. While the best-fit models generally describe the data well, random variations in the IR and optical bands introduced ambiguity in locating the synchrotron peak. As a result, the predictions on low-energy photon fluxes vary across models. The grid scan ($\chi^2/\text{n.d.f.} = 1.6$) and CMA-ES (1.0) produced solutions that differ from those of Minuit (1.4), MCMC (1.3), and the genetic algorithm (1.1) in the keV–MeV energy range. As shown in the right panel, MCMC, Minuit, and the genetic algorithm produced the closest matches to the true model in parameter space, with estimates that align well with the true values within their respective uncertainties.

In contrast, CMA-ES, despite achieving the lowest reduced $\chi^2/\text{n.d.f.}$, yielded parameter values that diverge significantly from the true model. Both CMA-ES and the grid scan underestimated the electron luminosity, compensating with higher Lorentz factors and variations in the blob radius and magnetic field strength. Notably, the grid scan also identified several additional regions in parameter space, marked by large black points, with similarly good fit quality.

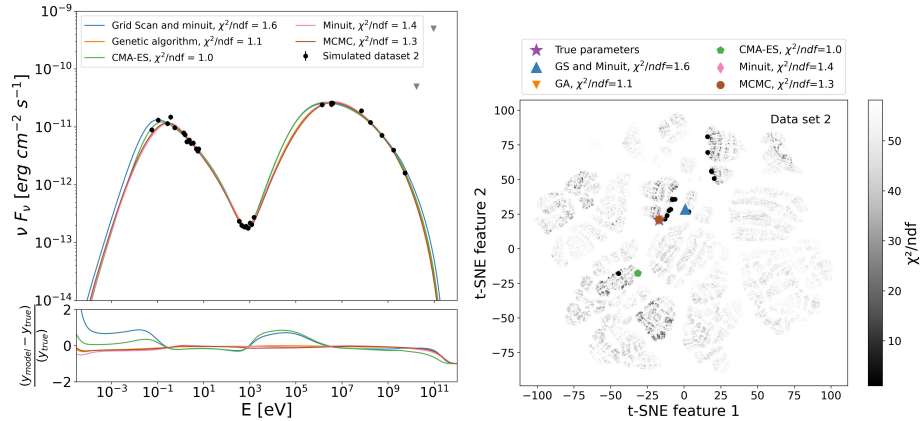


Figure 6.4: Left panel: Best-fit solutions from each of the selected optimization algorithms for the simulated dataset 2. Right panel: t-SNE plot showing the proximities of different solutions. Figure from Apel et al. [240].

Figure 6.5 presents the results for dataset 3. As expected, the reduced number of data points and weaker definition of SED features led to increased parameter degeneracy. Although all algorithms returned similar reduced χ^2 values, the resulting SED shapes varied substantially. As in dataset 2, the largest discrepancies appeared below 0.1 eV and in the MeV range. Additionally, high uncertainties and scatter in the GeV gamma-ray band limited the accuracy in locating the high-energy peak. The t-SNE plot reveals that the best-fit solutions are scattered widely across parameter space, with none located near the true model. The grid scan indicates the presence of multiple alternative regions with comparable fit quality. In this case, both the poorer constraint on the fit minimum and the increased parameter uncertainties (see **Table 6.5**) reflect the reduced quality of the data.

Datasets 2 and 3, which more closely resemble realistic observational scenarios, demonstrate how model degeneracy increases with greater flux uncertainties and fewer data points. In such cases, multiple parameter combinations can produce similarly good fits, and the solutions yielding the lowest reduced χ^2 values do not necessarily correspond to the true model. Only in the idealized case of nearly perfect data (dataset 1) does the choice of optimization method have minimal impact on the results.

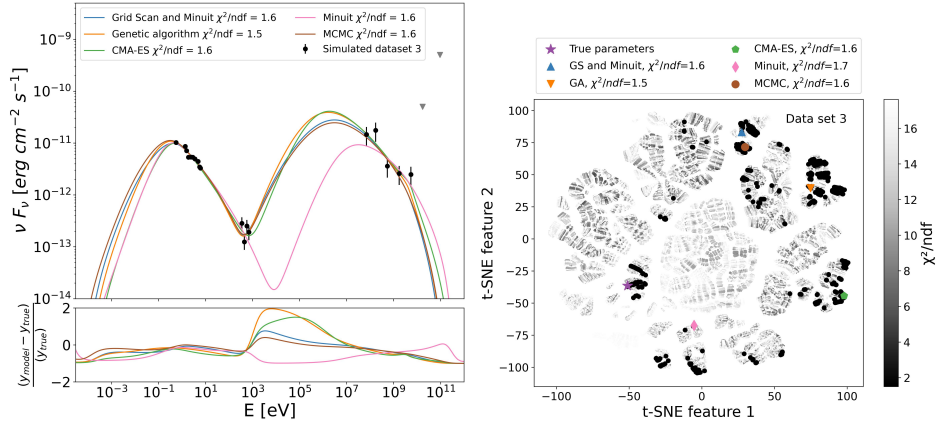


Figure 6.5: Left panel: Best-fit solutions from each of the selected optimization algorithms for the simulated dataset 3. Right panel: t-SNE plot showing the proximities of different solutions. Figure from Apel et al. [240].

Table 6.5: Best-fit model parameters for simulated data.

Dataset	Method	$\lg(R'_{\text{blob}} [\text{cm}])$	$B' [\text{G}]$	$\lg(\gamma'_{\text{min}})$	$\lg(\gamma'_{\text{max}})$	$\lg(L'_e [\text{erg s}^{-1}])$	Γ_b	α	$\chi^2/\text{n.d.f.}$
True		16.58	0.41	3.30	4.88	43.39	7.8	2.82	-
Dataset 1	Grid scan	16.477 ± 0.001	0.42 ± 0.03	3.234 ± 0.001	4.98 ± 0.03	43.202 ± 0.004	9.2 ± 0.1	2.88 ± 0.06	2.2
	GA	$16.60^{+0.07}_{-0.06}$	0.41 ± 0.08	3.30 ± 0.03	4.98 ± 0.04	$43.39^{+0.14}_{-0.22}$	7.8 ± 0.5	2.85 ± 0.07	1.8
	CMA-ES	16.59 ± 0.01	0.39 ± 0.03	3.34 ± 0.01	5.00 ± 0.01	43.365 ± 0.003	8.00 ± 0.02	2.890 ± 0.003	1.6
	Minuit	16.13 ± 0.05	0.51 ± 0.08	3.05 ± 0.53	4.71 ± 0.10	42.79 ± 0.04	12.3 ± 2.83	2.80 ± 0.04	4.1
	MCMC	$16.29^{+0.07}_{-0.08}$	$0.36^{+0.07}_{-0.06}$	$3.04^{+0.04}_{-0.03}$	4.67 ± 0.03	42.84 ± 0.04	$12.37^{+0.13}_{-0.17}$	2.77 ± 0.06	3.5
Dataset 2	Grid scan	16.50 ± 0.67	0.24 ± 0.09	3.07 ± 0.04	4.88 ± 0.50	43.00 ± 0.70	11.5 ± 0.80	2.82 ± 0.45	1.6
	GA	$16.34^{+0.10}_{-0.13}$	0.54 ± 0.12	$3.28^{+0.07}_{-0.08}$	$4.83^{+0.11}_{-0.15}$	$43.20^{+0.15}_{-0.22}$	8.6 ± 0.85	2.82 ± 0.13	1.1
	CMA-ES	16.11 ± 0.01	0.45 ± 0.01	3.00 ± 0.01	4.66 ± 0.01	42.79 ± 0.01	12.40 ± 0.06	2.74 ± 0.01	1.0
	Minuit	16.310 ± 0.003	0.62 ± 0.02	3.3016 ± 0.0004	4.84 ± 0.02	43.21 ± 0.01	8.474 ± 0.001	2.89 ± 0.01	1.4
	MCMC	$16.41^{+0.12}_{-0.14}$	$0.51^{+0.17}_{-0.08}$	$3.31^{+0.03}_{-0.05}$	$4.83^{+0.08}_{-0.09}$	$43.26^{+0.09}_{-0.06}$	$8.21^{+0.29}_{-0.32}$	$2.84^{+0.10}_{-0.13}$	1.3
Dataset 3	Grid scan	15.88 ± 0.06	1.20 ± 0.01	3.21 ± 0.02	4.39 ± 0.31	43.06 ± 0.11	9.0 ± 0.17	2.83 ± 0.25	1.6
	GA	15.47 ± 1.15	1.32 ± 0.33	$3.04^{+0.20}_{-0.38}$	$4.34^{+0.25}_{-0.63}$	42.63 ± 0.92	12.9 ± 2.3	2.91 ± 0.09	1.5
	CMA-ES	15.000 ± 0.006	1.74 ± 0.08	3.000 ± 0.006	4.99 ± 0.02	42.14 ± 0.04	17.8 ± 0.4	3.34 ± 0.15	1.6
	Minuit	16.81 ± 0.13	0.14 ± 0.02	3.58 ± 0.26	5.50 ± 0.80	42.59 ± 0.33	11.3 ± 0.44	3.25 ± 0.07	1.7
	MCMC	$16.21^{+0.22}_{-0.20}$	$0.84^{+0.23}_{-0.21}$	$3.29^{+0.09}_{-0.10}$	$4.55^{+0.25}_{-0.27}$	$43.23^{+0.15}_{-0.17}$	$8.05^{+0.92}_{-1.07}$	$2.84^{+0.18}_{-0.30}$	1.6

Model parameters: R'_b is the radius of the blob, B' is the magnetic field strength in the emission region, Γ_b is the blob Lorentz factor, γ'^{min} and γ'^{max} are the minimum and maximum Lorentz factor of the electrons, α is the spectral index of electrons, L'_e is electron luminosity, $\chi^2/\text{n.d.f.}$ is a value of the reduced χ^2 function.

6.6 Application to blazar data

Following the comparison of algorithm performance on simulated data, two cases of SED fitting for real blazars, PKS 0735+178 and Mrk 501, were tested. The SED of PKS 0735+178 represents a typical case of a source with limited available data, while the SED of Mrk 501, one of the most well-monitored blazars, represents a case of good data coverage.

PKS 0735+178:

[145]: Omeliukh et al. (2025), "Multi-epoch leptohadronic modeling of neutrino source candidate blazar PKS 0735+178"

PKS 0735+178

PKS 0735+178 is an intermediate synchrotron-peaked (ISP) BL Lac object, previously introduced in [Section 5.1](#). The data for its gamma-ray quiescent state is taken from Omeliukh et al. [145]. Since this source served as a prototype for generating simulated pseudo-data, the parameter space boundaries for all algorithms were kept consistent with those in [Table 6.2](#). The results of the SED fitting using different optimization approaches are shown in [Figure 6.6](#).

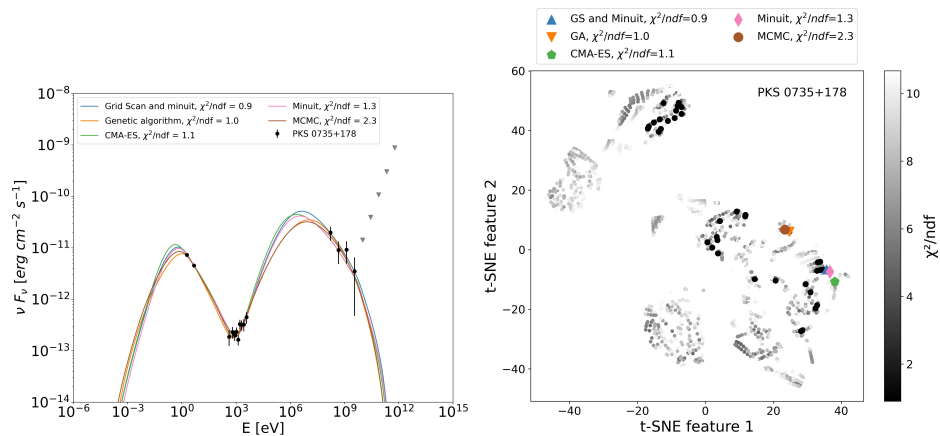


Figure 6.6: Left panel: Best-fit solutions from each of the selected optimization algorithms for the gamma-ray quiescent state of PKS 0735+178. Right panel: t-SNE plot showing the proximities of different solutions for PKS 0735+178. Figure from Apel et al. [240].

The gamma-ray quiescent-state data for PKS 0735+178 represent an intermediate case between simulated datasets 2 and 3. It contains fewer data points than dataset 2 but has smaller error bars than dataset 3. The results of the SED fitting for PKS 0735+178, along with the corresponding t-SNE map showing the locations of the best-fit parameters, are presented in [Figure 6.6](#). The best-fit parameter values from each minimization method are listed in [Table 6.6](#). Although all solutions fit the observed SED data equally well, they exhibit significant differences in regions without observational constraints.

As shown in the lower panel of [Figure 6.6](#), the model parameters are located in different areas of the parameter space. The best solutions from the grid scan (reduced $\chi^2/\text{n.d.f.} = 0.9$), Minuit (1.3), and CMA-ES (1.1) cluster relatively close together, while those from MCMC (2.3) and

Table 6.6: Best-fit model parameters obtained using different optimization methods for the SED of PKS 0735+178.

Method	$\lg(R'_{\text{blob}} [\text{cm}])$	$B' [\text{G}]$	$\lg(\gamma'_{\text{min}})$	$\lg(\gamma'_{\text{max}})$	$\lg(L'_e [\text{erg s}^{-1}])$	Γ_b	α	$\chi^2/\text{n.d.f.}$
Grid scan	15.27 ± 0.04	1.26 ± 0.37	3.221 ± 0.005	5.17 ± 0.27	42.47 ± 0.42	14.9 ± 2.48	3.27 ± 0.54	0.9
GA	$15.54^{+0.06}_{-0.07}$	1.54 ± 0.10	$3.41^{+0.04}_{-0.05}$	$4.96^{+0.05}_{-0.06}$	$42.96^{+0.16}_{-0.27}$	9.65 ± 0.60	3.30 ± 0.08	1.0
CMA-ES	$15.18^{+0.03}_{-0.04}$	1.24 ± 0.29	3.00 ± 0.02	$4.85^{+0.08}_{-0.10}$	$42.21^{+0.03}_{-0.04}$	18.2 ± 0.46	3.17 ± 0.07	1.1
Minuit	15.082 ± 0.004	1.71 ± 0.01	3.09 ± 0.03	5.15 ± 0.36	42.23 ± 0.03	16.6 ± 0.26	3.26 ± 0.06	1.3
MCMC	$15.71^{+0.16}_{-0.12}$	1.22 ± 0.14	3.36 ± 0.05	$4.84^{+0.18}_{-0.15}$	42.92 ± 0.07	$9.65^{+0.47}_{-0.35}$	$3.08^{+0.16}_{-0.13}$	2.3

the genetic algorithm (1.0) fall outside this region. This separation is also visible in the upper panel of **Figure 6.6**, where the MCMC and genetic algorithm solutions diverge from the others, particularly in the radio and MeV bands where no data are available to constrain the models.

The t-SNE map further illustrates that the results from the grid scan, CMA-ES, and Minuit are grouped in regions where the grid scan identifies favorable solutions. Notably, the grid scan also highlights several other regions in parameter space that could yield comparably good fits, underscoring the strong degeneracy of the model for this SED. The quiescent-state SED of PKS 0735+178 is a clear example of a degenerate case: key features such as the positions and fluxes of the synchrotron and high-energy peaks cannot be well constrained, resulting in large uncertainties in many model parameters.

As with simulated dataset 3, most solutions yield similar reduced χ^2 values despite differing parameter estimates. However, the MCMC and genetic algorithm results deviate significantly from the others, suggesting a larger emission region and higher electron luminosity. Additionally, while the other methods infer bulk Lorentz factors of $\Gamma_b > 14$, both the genetic algorithm and MCMC find a lower value of $\Gamma_b = 9.65$.

Mrk 501

Mrk 501 is a well-known BL Lac object located at a redshift of $z = 0.034$ [260]. Between mid-2017 and mid-2019, it was observed in a low X-ray and gamma-ray state. Multi-wavelength SED data for Mrk 501 during this period were collected by Abe et al. [261], who also modeled the source using a one-zone approach. In this study, we use the same dataset as in Abe et al. [261] and apply five selected optimization algorithms to fit the data with a one-zone SSC model. As in Abe et al. [261], the optical and radio data points are treated as upper limits due to the lack of variability in these energy ranges. For consistency with Abe et al. [262], the EBL model from Franceschini et al. [263] is adopted.

Mrk 501 is a typical high-synchrotron-peaked (HSP) BL Lac object. Its model parameters are expected to occupy a distinct region of parameter space compared to those of intermediate-synchrotron-peaked (ISP) BL Lac objects. In particular, the synchrotron peak being shifted toward higher energies implies higher maximum electron Lorentz factors and lower magnetic field strengths. The boundaries of the parameter space selected for modeling Mrk 501 are listed in **Table 6.7**.

The SED fitting results for Mrk 501 are shown in the left panel of **Figure 6.7**, with the corresponding t-SNE map of best-fit parameter locations

Mrk 501:

[260]: Quinn et al. (1996), Detection of Gamma Rays with $E > 300$ GeV from Markarian 501

[261]: Abe et al. (2023), Multimessenger Characterization of Markarian 501 during Historically Low X-Ray and γ -Ray Activity

[262]: Abe et al. (2023), Multimessenger characterization of Markarian 501 during historically low x-ray and gamma-ray activity

[263]: Franceschini et al. (2008), "Extragalactic optical-infrared background radiation, its time evolution and the cosmic photon-photon opacity"

Table 6.7: Boundaries of the parameter space for Mrk 501.

Parameter	Value range
$R'_{\text{blob}}, \text{cm}$	$[10^{15.5}, 10^{18}]$
B', gauss	$[10^{-3}, 0.5]$
Γ_b	$[5.0, 30.0]$
γ_e^{min}	$[10^2, 10^5]$
γ_e^{max}	$[10^5, 10^7]$
α_e	$[1.0, 3.0]$
$L'_e / \text{erg s}^{-1}$	$[10^{39}, 10^{44}]$

in the right panel. Compared to PKS 0735+178, the quiescent-state SED of Mrk 501 contains more data points. However, interpreting the optical and radio measurements as upper limits makes it difficult to constrain the synchrotron peak. In addition, the MeV gap between the low- and high-energy peaks remains unconstrained due to the absence of observational data in this range.

Mrk 501:

[264]: Abdo et al. (2011), Insights into the high-energy gamma-ray emission of Markarian 501 from extensive multifrequency observations in the Fermi era

All solutions reproduce the X-ray data well and match the high-energy gamma-ray fluxes, but fail to capture the shape of the gamma-ray spectrum, resulting in high reduced χ^2 values (> 26). This suggests that a more complex model may be required. In this work, we employed a simple power-law injection with a self-consistent synchrotron cooling break, whereas Abdo et al. [264] achieved better fits by introducing multiple spectral breaks. Alternatively, better-fitting parameters may lie outside the scanned region (see [Table 6.7](#)).

Despite the high reduced χ^2 values, the upper panel of [Figure 6.7](#) shows that different minimization methods produced distinct solutions. While all approaches yield similar X-ray flux shapes, they diverge significantly in the MeV gap region.

The t-SNE plot reveals that the MCMC ($\chi^2/\text{n.d.f.} = 27.7$) and Minuit ($\chi^2/\text{n.d.f.} = 33.9$) solutions are closely clustered, while those from CMA-ES and the grid scan form separate groups. In contrast to PKS 0735+178, where multiple favorable solutions were identified, the grid scan for Mrk 501 points to a single preferred region that overlaps with the MCMC and Minuit solutions. These models are consistent in the X-ray and high-energy gamma-ray ranges but differ in other spectral regions.

Most solutions require a blob radius of approximately 3×10^{15} cm, a magnetic field strength of 0.2–0.3 G, and an electron luminosity of roughly 5×10^{40} erg/s. The CMA-ES solution deviates from this trend, suggesting a larger emission region, a weaker magnetic field, and a higher electron luminosity.

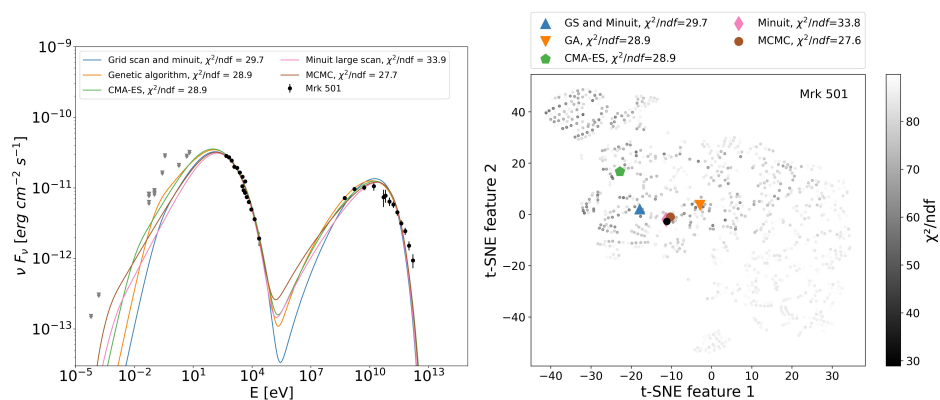


Figure 6.7: Left panel: Best-fit solutions from each of the selected optimization algorithms for the gamma-ray quiescent state of Mrk 501. Right panel: t-SNE plot showing the proximities of different solutions for Mrk 501. Figure from Apel et al. [240].

Table 6.8: Best-fit model parameters obtained using different optimization methods for the SED of Mrk 501.

Method	$\lg(R'_{\text{blob}} [\text{cm}])$	$B' [\text{G}]$	$\lg(\gamma'_{\text{min}})$	$\lg(\gamma'_{\text{max}})$	$\lg(L'_e [\text{erg s}^{-1}])$	Γ_b	α	$\chi^2/\text{n.d.f.}$
Grid scan	15.522 ± 0.007	0.32 ± 0.03	3.22 ± 0.34	5.256 ± 0.0004	40.63 ± 0.02	12.5 ± 0.02	1.97 ± 0.05	29.7
GA	$15.61^{+0.07}_{-0.08}$	0.22 ± 0.03	$3.14^{+0.11}_{-0.15}$	$5.38^{+0.04}_{-0.05}$	$40.65^{+0.10}_{-0.12}$	15.1 ± 0.56	2.26 ± 0.06	28.9
CMA-ES	$16.08^{+0.03}_{-0.04}$	0.15 ± 0.01	$2.79^{+0.15}_{-0.22}$	5.51 ± 0.02	41.13 ± 0.04	10.2 ± 0.3	$2.04^{+0.03}_{-0.12}$	28.9
Minuit	15.485 ± 0.005	0.286 ± 0.004	2.378 ± 0.005	5.231 ± 0.005	40.699 ± 0.003	13.44 ± 0.05	1.959 ± 0.002	33.9
MCMC	15.63 ± 0.05	$0.22^{+0.03}_{-0.02}$	$1.97^{+0.21}_{-0.13}$	5.33 ± 0.03	$40.91^{+0.05}_{-0.06}$	$13.21^{+0.20}_{-0.14}$	$2.05^{+0.03}_{-0.02}$	27.7

6.7 Discussion

Performance

Among all tested methods, the grid scan was the most computationally expensive, using ten probed points per parameter. However, it remains the only approach that guarantees the exploration of multiple physically distinct solutions. Its uniform coverage of the parameter space also enabled visualization via t-SNE. While the one-zone SSC model involved only seven free parameters, applying a grid scan to more complex models would result in a dramatic increase in computational cost. Nonetheless, a key advantage of grid scans is the potential reusability of the results for other sources or datasets. A known limitation is that solutions may lie between predefined grid points. Some studies [e.g., 265] address this by conducting a finer scan following an initial coarse scan, which can result in even greater computational demand. In our setup, this second step was replaced with a local minimization using Minuit.

The evolutionary algorithms demonstrated high accuracy in capturing the true solutions. CMA-ES and the genetic algorithm performed similarly, with CMA-ES converging significantly faster due to its self-adaptation of internal parameters. Both algorithms converged to a single solution. While it is possible to extract additional candidate solutions from intermediate results, evolutionary algorithms inherently narrow the search space with each iteration, resulting in focused but less comprehensive coverage compared to grid scans. Parameter uncertainties, estimated from the final generation, were small due to this tight convergence. However, results are not strictly reproducible because of random initialization and the highly complex parameter space. Repeated runs may yield different outcomes.

For dataset 1 (ideal data with no gaps and small uncertainties), both evolutionary algorithms successfully recovered the true parameters within their uncertainties. The grid scan, followed by local minimization, also produced good fits, though the best-fit parameters were slightly farther from the true values than those obtained by the evolutionary algorithms. A finer grid or broader minimization boundaries with more function calls might have improved these results. In contrast, Minuit and MCMC likely became trapped in a local minimum due to the limited number of probed points relative to the vastness of the parameter space.

Among all methods, Minuit (using the Simplex and Migrad algorithms)

Performance:

[265]: Ahnen et al. (2017), Multiband variability studies and novel broadband SED modeling of Mrk 501 in 2009

Table 6.9: Comparing the performance of the different algorithms

Algorithm	N_{models}	Advantage	Disadvantage
Grid scan + local minimiz.	10^7	Considers more than only one solution, can be reused for other sources, few controllable parameters	Computationally expensive, drastic increase in computing cost with the increase of model parameters
GA	$10^5 - 10^6$	Explores whole parameter space, overcomes local minima	Only one solution, sensitive to setting of algorithm parameters
CMA-ES	10^5	Explores whole parameter space, overcomes local minima, self-adaption of algorithm parameters	Only one solution
Minuit (simplex + migrad)	10^3	Computationally inexpensive, few controllable parameters	May be sensitive to local minima, only one solution, sensitive to the choice of initial point
MCMC (ensemble sampler)	10^5	Provides parameter distributions	Sensitive to the choice of initial point and algorithm parameters

was the fastest, requiring only about 10^3 SED evaluations. It requires only an initial guess and step sizes, but is highly sensitive to the starting point. In the irregular parameter space of one-zone models, reaching the global minimum is not guaranteed. In our studies, Minuit often produced higher reduced χ^2 values (i.e., worse fits) than other methods, although its best-fit parameters were generally close to those obtained by more complex algorithms.

MCMC sampling, configured with 50 walkers and 1,000 steps, required approximately 10^5 SED evaluations. Like Minuit, it is sensitive to the initial starting point, and a preliminary minimization step (e.g., using Minuit) is therefore recommended. It also requires assumptions about prior distributions. A key advantage of MCMC, however, is that it provides posterior probability distributions and two-dimensional parameter correlations. The corresponding figures for all simulated and real datasets are provided in [Appendix B](#).

Performance:

[266]: Bégué et al. (2024), Modeling Blazar Broadband Emission with a Convolutional Neural Network. I. Synchrotron Self-Compton Model

[267]: Sahakyan et al. (2024), Modeling Blazar Broadband Emission with Convolutional Neural Networks. II. External Compton Model

Interestingly, in more degenerate scenarios (datasets 2 and 3), Minuit and MCMC were more successful. In such cases, many regions of parameter space yield acceptable fits, increasing the likelihood of identifying a suitable solution even with limited sampling. For complex likelihood landscapes, nested sampling methods such as MultiNest [266, 267] may offer a more efficient alternative.

A detailed summary of the performance, advantages, disadvantages, and computational cost of all methods is presented in [Table 6.9](#).

Comparison with previous studies

For the observational data, we modeled the radiation of PKS 0735+178 during a quiescent state using each of the five minimization algorithms, resulting in different best-fit solutions. This state was previously modeled by Bharathan et al. [268] and Omeliukh et al. [145]. The latter addressed the issue of multiple viable solutions by performing a grid scan and selecting two physically distinct scenarios (“slow” and “fast” solutions, based on the bulk Lorentz factor). In contrast, our best-fit models from all five algorithms feature magnetic field strengths two to three times higher and significantly smaller emission zone radii than both the slow and fast models reported in Omeliukh et al. [145]. Similarly, compared to the model in Bharathan et al. [268], our solutions exhibit twice the magnetic field strength and a blob radius an order of magnitude smaller. These differences suggest that our five best-fit models are complementary to those found in the literature.

For Mrk 501, our results reproduce the overall flux levels but fail to match the gamma-ray spectral shape. The parameter boundaries were adopted from Abe et al. [262], and we used the same dataset. While Abe et al. [262] fixed the blob size to $R'_{\text{blob}} = 10^{17.06}$ cm, our solutions indicate significantly smaller emission regions. The magnetic field strengths derived from our analysis range between $B' = 0.15\text{--}0.32$ G, whereas their model used a much lower value of $B' = 0.025$ G. The bulk Lorentz factor in their study was fixed at 11, which falls within our inferred range of $\Gamma_b = 10.2\text{--}15.1$. The required electron luminosity in our models was also three orders of magnitude lower. Despite using the same parameter space boundaries as Abe et al. [262], our results differ substantially.

Abdo et al. [264] successfully reproduced the quiescent-state SED of Mrk 501 using a double broken power-law injection spectrum. This may explain why our simpler power-law model (with a naturally occurring cooling break) failed to capture the gamma-ray spectral shape.

Implications for the blazar modeling

Our findings, along with comparisons to other models, highlight the highly degenerate nature of the parameter space in leptonic radiation models. Even the simplest one-zone SSC framework, with only seven free parameters, poses significant challenges in accurately describing blazar emission. More complex models introduce additional parameters, further complicating the parameter space. This underscores the need for cautious interpretation of modeling results. Breaking this degeneracy requires high-quality, quasi-simultaneous multi-wavelength data. In this context, blazar surveys and long-term monitoring programs play a crucial role in constraining the parameter space of one-zone models.

Additionally, exploring new energy ranges, such as MeV or TeV gamma rays, can significantly reduce model degeneracy. For example, including a single MeV data point in our simulated dataset 3 would reduce the number of equally well-fitting models from five to just one or two. Future MeV

Previous studies:

[268]: Bharathan et al. (2024), Multiwavelength spectral modelling of the candidate neutrino blazar PKS 0735+178

[145]: Omeliukh et al. (2025), "Multi-epoch leptohadronic modeling of neutrino source candidate blazar PKS 0735+178"

[262]: Abe et al. (2023), Multimessenger characterization of Markarian 501 during historically low x-ray and gamma-ray activity

[264]: Abdo et al. (2011), Insights into the high-energy gamma-ray emission of Markarian 501 from extensive multifrequency observations in the Fermi era

missions such as COSI [188] and AMEGO-X [189] are therefore expected to play a key role in refining model constraints. Similarly, the addition of TeV gamma-ray flux measurements, especially for HSP sources, will be crucial. The upcoming Cherenkov Telescope Array Observatory [CTAO, 269] is expected to provide high-quality high-energy gamma-ray data that will be essential for constraining these models. For more complex leptohadronic scenarios, multi-wavelength polarization measurements may help disentangle the hadronic component [186].

Implications:

[188]: Tomsick and others (2019), The Compton Spectrometer and Imager

[189]: Caputo et al. (2022), All-sky Medium Energy Gamma-ray Observatory eXplorer mission concept

[269]: Cherenkov Telescope Array Consortium (2019), "Science with the Cherenkov Telescope Array"

[186]: Zhang et al. (2024), Revisiting High-energy Polarization from Leptonic and Hadronic Blazar Scenarios

Apart from the case of a perfect dataset, our analysis of the parameter space in leptonic radiation models suggests that, regardless of the optimization method used, the complex and multimodal nature of the parameter space often prevents algorithms from capturing the true parameter values. This is particularly evident with algorithms that converge to a single solution, which may fail to capture the full range of possible models. As a result, accurately modeling blazar emission becomes highly challenging. The most robust approach is to acknowledge the presence of multiple solutions and employ methods like grid scans, either nested or combined with local minimization, as they provide a more comprehensive view of the parameter space rather than a single best-fit solution.

As demonstrated with the simulated datasets, fitting an SED with broad spectral coverage and small uncertainties yields consistent results across all tested optimization algorithms. In such ideal cases, the grid scan identifies a single well-constrained region containing good solutions. However, when gaps appear in the SED or uncertainties increase, multiple physically distinct yet similarly well-fitting solutions emerge. Under these conditions, all tested optimization algorithms produce divergent results, and none successfully recover the true underlying parameters.

This study employed the simplest framework for modeling the multi-wavelength SED of blazars – the one-zone SSC model. Introducing additional components, such as external photon fields or hadronic processes involving protons in the jet, would increase the number of free parameters and significantly worsen the observed degeneracies. These findings carry important implications for blazar modeling in both gamma-ray and neutrino astronomy. Several strategies may help address model degeneracies:

- Blazar surveys for SED completeness. Blazars are highly variable sources, and their SEDs are often constructed from observations taken months or even years apart. This temporal mismatch can misrepresent the source state at any given time, leading to significant degeneracies in model parameters. Simultaneous or quasi-simultaneous multi-wavelength observations are therefore essential for reliable modeling.
- Measurements in underexplored energy bands, e.g. MeV, are critical for advancing blazar modeling and improving constraints on key model parameters.
- Multi-wavelength polarization measurements can provide complementary information to photon fluxes, offering an additional means of breaking degeneracies in leptonic and hadronic models.

6.8 Summary and conclusions

This study evaluated the performance of five optimization algorithms – grid scan, genetic algorithm, CMA-ES, Minuit, and MCMC – in fitting the spectral energy distributions (SEDs) of blazars using the one-zone synchrotron self-Compton (SSC) model. By applying these algorithms to both simulated pseudo-data and real observations of blazars, we assessed their effectiveness in retrieving best-fit model parameters, their computational efficiency, and their sensitivity to data quality and coverage. The key findings of this study are:

- When data coverage is dense and uncertainties are small, different optimization algorithms yield consistent best-fit solutions. However, as data gaps increase or error bars grow larger, significant parameter degeneracies arise, often resulting in best-fit solutions that deviate substantially from the true values.
- Among the tested methods, the grid scan requires the fewest assumptions and is the only approach capable of identifying multiple physically distinct solutions. However, it is computationally intensive. CMA-ES and the genetic algorithm offered a good balance between computational cost and effective exploration of parameter space. Minuit was the fastest but often converged to local minima due to its strong dependence on initial conditions. MCMC provided detailed insights into parameter correlations and uncertainties but required careful initialization and prior assumptions.
- Even within the simplest SSC one-zone framework, the presence of degeneracies is significant. These degeneracies would only be amplified in more complex models with a higher number of free parameters.
- Addressing these degeneracies requires high-quality, simultaneous multi-wavelength observations, expanded coverage in underexplored energy ranges (e.g., MeV), and the inclusion of multi-wavelength polarization data.



Chapter 7

Extracting accretion physics by modeling large sample of blazars

*Say what you know, do what you must,
come what may.*

Sofia Kovalevskaya

Despite potential links between blazar activity and neutrino emission, the overall contribution of the blazar population to the observed diffuse neutrino flux is estimated to be subdominant. If the neutrino emission from blazars in the *Fermi*-2LAC catalog is assumed to scale with their gamma-ray flux, the 862 studied sources contribute no more than 27% to the total diffuse neutrino flux [270]. Similarly, an analysis of 137 MeV-detected blazars suggests a contribution of no more than 1% [271]. A comparable study using over two thousand blazars from the Fermi-LAT 4LAC-DR2 catalog also finds that fewer than 1% of blazars are likely neutrino emitters [272]. Still, a correlation between gamma-ray and neutrino emission, which is used for source selection and weighting, might not be that simple. In this context, modeling a large sample of blazars could offer valuable insights into the mechanisms of neutrino production and help identify a subpopulation of blazars that can be efficient neutrino emitters.

Blazar sample:

[270]: Aartsen et al. (2017), The contribution of FERMI-2LAC blazars to diffuse TeV–PeV neutrino flux

[271]: Abbasi et al. (2022), Search for Astrophysical Neutrinos from 1FLE Blazars with IceCube

[272]: Abbasi et al. (2023), Search for correlations of high-energy neutrinos detected in IceCube with radio-bright AGN and gamma-ray emission from blazars

[171]: Rodrigues et al. (2024), Leptohadronic multi-messenger modeling of 324 gamma-ray blazars

[82]: Ghisellini et al. (2014), The power of relativistic jets is larger than the luminosity of their accretion disks

[273]: Omeliukh and Inoue (in prep.), "Relativistic Jets from Supermassive Black Holes Thrive on Less Fuel"

Section 7.1 in this Chapter is based on Rodrigues et al. [171]. I am one of the co-authors of this publication and contributed to the dataset preparations, development of methodology, and discussion of the obtained results.

Modeling a large sample of blazars can also provide important insights into the physics of accretion in AGN. For example, Ghisellini et al. [82] showed that jet powers often exceed the radiative power of blazar accretion disks by using purely leptonic models for a sample of gamma-ray-detected blazars. In this study, I apply similar methods to the leptohadronic models presented in Rodrigues et al. [171] to investigate whether the inclusion of high-energy protons in the jet alters these correlations.

Section 7.2 in this Chapter is based on Omeliukh and Inoue [273], for which I am the leading author.

7.1 Leptohadronic modeling of 324 gamma-ray blazars

7.1.1 Blazar sample

The blazar sample consists of 324 sources selected from the Candidate Gamma-ray Blazar Survey (CGRaBS) catalog [274]. The majority are flat-spectrum radio quasars (FSRQs), with 237 sources representing approximately 34% of all 619 FSRQs listed in the fourth *Fermi*-LAT catalog of detected AGNs [4LAC, 275]. The remaining sources include 77 BL Lac objects (most with known redshifts), 3 Seyfert-1 galaxies, and 3 blazar candidates of uncertain type. Multi-wavelength SEDs, covering the infrared, optical/UV, X-rays, and GeV gamma-ray ranges, were constructed for each source by Paliya et al. [276], who modeled them as part of a broader effort to characterize the general physical properties of blazars. As demonstrated in Rodrigues et al. [171], this sample is biased toward blazars with above-average gamma-ray luminosity.

7.1.2 Leptohadronic modeling

Each source in the sample is modeled using a one-zone leptohadronic framework. Pre-accelerated electrons and protons are assumed to be injected into a spherical emission region moving along the jet axis. For FSRQs, the presence of bright accretion disks introduces external radiation fields relative to the emission zone, which are modeled following the approach of Ghisellini and Tavecchio [114].

The broadband optical and GeV gamma-ray features of blazars are typically well reproduced by leptonic models, even when co-acceleration of protons is assumed, as demonstrated in several leptohadronic studies of neutrino source candidates. Therefore, in this work, the optical and gamma-ray fluxes are attributed primarily to leptonic emission processes.

The search for the best-fit parameters was performed in three steps (see Figure 7.1), following the chosen optimization algorithm:

1. In the first step, purely leptonic models are fitted to reproduce the optical and GeV gamma-ray emission. All other spectral data are treated as upper limits during this step.
2. In the second stage, the leptonic parameters are fixed to the best-fit values obtained in the previous step. The hadronic parameter space is then explored using a coarse grid scan to identify viable regions. At this point, the models may still converge to purely leptonic solutions, as the proton luminosity interval includes $L_p = 0$ erg/s.
3. In the final step, all model parameters (both leptonic and hadronic) are simultaneously optimized within narrow intervals around their previously determined values, to ensure that the best value of the goodness of fit is reached.

Blazar sample:

[274]: Healey et al. (2008), CGRaBS: An All-Sky Survey of Gamma-Ray Blazar Candidates

[275]: Abdollahi et al. (2020), Fermi Large Area Telescope Fourth Source Catalog

[276]: Paliya et al. (2017), General Physical Properties of CGRaBS Blazars

[171]: Rodrigues et al. (2024), Leptohadronic multi-messenger modeling of 324 gamma-ray blazars

[114]: Ghisellini and Tavecchio (2009), Canonical high-power blazars

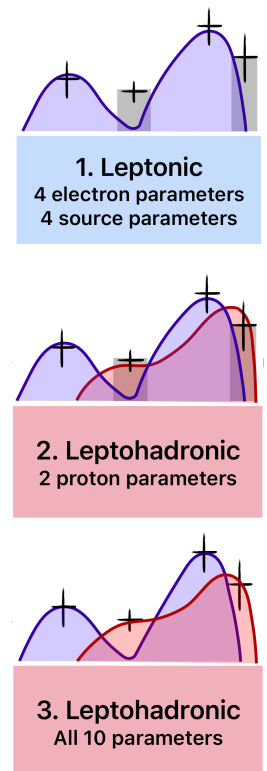


Figure 7.1: Fitting procedure. Figure adapted from Rodrigues et al. [171].

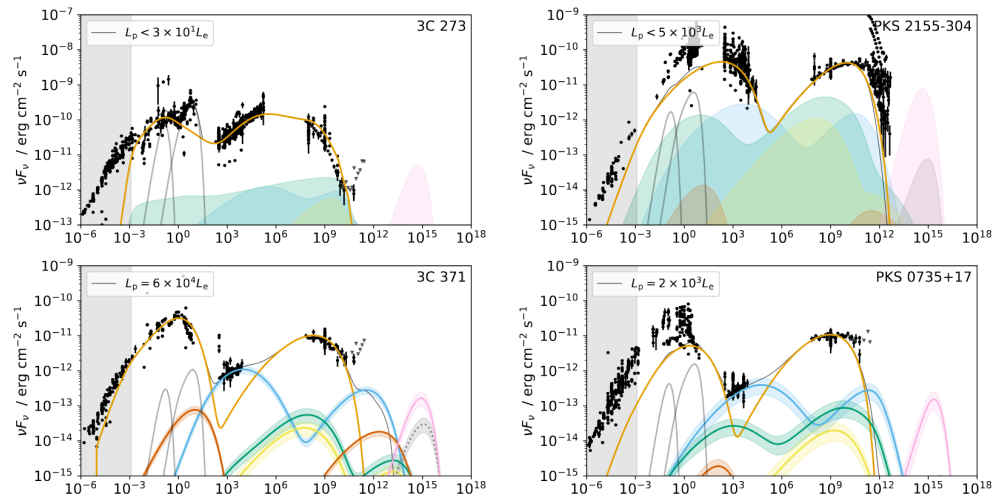


Figure 7.2: Examples of fitted SEDs from the 324 blazar sample. Figure from Rodrigues et al. [171].

7.1.3 Results

Spectral fits

Each source in the sample was modeled using a leptohadronic framework, which allows for convergence to a purely leptonic scenario if fitting better, following the algorithm described above. **Figure 7.2** presents four representative examples of fitted SEDs. The top row shows sources well described by leptonic models. Although a subdominant hadronic component is permitted, it is not required to fit the observed data. The shaded regions in this row represent the maximum allowed hadronic contribution. Of the 324 sources modeled, 216 (66%) were adequately explained by leptonic emission alone.

The bottom row of **Figure 7.2** displays sources for which a hadronic component, primarily from Bethe-Heitler pair production, is necessary to reproduce the X-ray fluxes. In some cases, the hadronic contribution also improves the fit in the gamma-ray band above 100 GeV. A total of 62 sources (20%) required a proton component in the jet to achieve a satisfactory fit.

For the remaining 44 sources (14%), the best-fit models included a proton contribution that matched the data in a limited energy range (mostly above 10 GeV). However, due to the large uncertainties in this region, the fit quality did not significantly deteriorate if the proton component was suppressed. Consequently, the inferred proton luminosities for this subset were excluded from the statistical analysis of the neutrino-emitting blazar population.

Neutrino flux predictions

For the sources where the best-fit models required a hadronic component to explain the data, the corresponding neutrino fluxes were summed to estimate their collective contribution to the observed diffuse astrophysical neutrino flux. The results are shown in **Figure 7.3**. Green lines

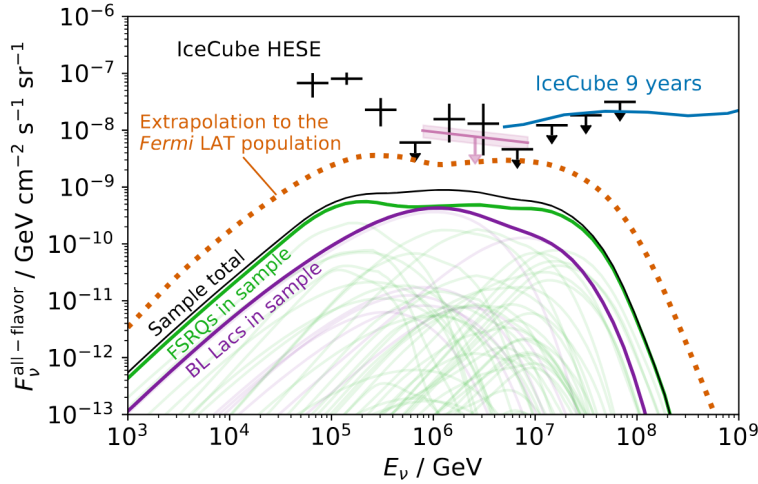


Figure 7.3: Neutrino flux predictions from the studied sample and its extrapolation to the whole blazar population. Figure from Rodrigues et al. [171].

represent the contribution from FSRQs, purple lines – from BL Lac objects, and the solid black line indicates the total emission from the sample. To estimate the contribution from the broader population of gamma-ray-detected blazars, these results were extrapolated using Monte Carlo sampling of gamma-ray luminosity functions, as described in Rodrigues et al. [171]. The outcome of this extrapolation is shown as the dotted orange curve in **Figure 7.3**, suggesting that blazars could account for up to 20% of the IceCube-observed diffuse neutrino flux.

Limitations

The goal of this work was to characterize the time-averaged multi-messenger emission of a sample of 324 gamma-ray-detected blazars. For each source, multi-wavelength SEDs were constructed using all available archival data. However, differences in variability timescales and observational strategies (ranging from long-term monitoring to observations only during flaring states) limit the accuracy of the time-averaged representation. In addition, only a subset of the full parameter space could be explored, and due to inherent degeneracies, the resulting solutions are not unique. The modeling is further constrained by fixed parameters, such as the jet viewing angle ($\theta_{\text{obs}} = 1/\Gamma_b$) and the fixed spectral index of the proton energy spectrum ($\alpha_p = 1$). Moreover, time-dependent effects, spatial evolution, or multiple acceleration zones (e.g., reconnection layers) could significantly alter neutrino and photon outputs, thus limiting the realism of the steady-state model.

7.1.4 Summary and conclusions

- A sample of 324 gamma-ray-detected blazars was modeled based on a source-by-source approach.
- The majority of sources are well described by purely leptonic models. However, in 33% of the sample (106 sources), a hadronic component is either necessary to reproduce the SED or significantly improves the fit.
- A positive correlation was identified between the predicted neutrino luminosity and the observed gamma-ray luminosity.
- Extrapolating the results to the broader population of *Fermi*-detected blazars suggests that blazars could contribute up to 20% of the diffuse astrophysical neutrino flux observed by IceCube, which is consistent with the upper limits from stacking analyses of the *Fermi*-2LAC catalog.

7.2 Power of blazar jets

7.2.1 Methods of jet power estimation

Jet power is a fundamental property of AGN, related to the mechanisms that allow black holes to convert accreted matter into highly collimated outflows. Despite decades of research, these processes remain poorly understood. Moreover, only a limited number of methods are currently available for estimating the power of blazar jets.

Emission of extended radio lobes

The jet power can be estimated as the ratio of the energy content within radio lobes and the age of the AGN. The jet power is correlated with the radio luminosity [e.g., 277, 278]. According to the empirical relation, the time-averaged jet power and extended radio luminosity are connected as follows

$$P_{\text{jet}} = 9.5 \times 10^{46} \left(\frac{f}{10} \right)^{3/2} \left(\frac{L_{151 \text{ MHz}}}{10^{28} \text{ W Hz}^{-1} \text{ sr}^{-1}} \right)^{6/7} \text{ [erg/s]} \quad (7.1)$$

where f is a parameter accounting for systematic error in the model assumptions and includes a variety of unknown factors affecting the normalization of the relation [278]. It typically ranges between 1 and 20. $L_{151 \text{ MHz}}$ is the observed 151 MHz radio luminosity.

SED modeling

The total jet power can be estimated by modeling the blazar SED and combining the power of electrons, protons, and magnetic fields. In addition to this, since there is no physical reason to assume charge asymmetry in the jet, the total charge neutrality in the jet is assumed. In leptonic models, this implies the presence of cold (non-radiating) protons whose number density matches that of the electrons. They carry energy without contributing to the observed emission. In leptohadronic models, which already include a population of relativistic (hot) protons, an additional population of cold protons is introduced to ensure that the combined number density of hot and cold protons equals that of the electrons.

Radio core shift

In the steady-state jet model of [279], the synchrotron spectrum is divided into two regimes: partially optically thick at low energies and optically thin at high energies. The radio “core” is the point where radio emission becomes optically thick. Its apparent position shifts toward the jet base at higher frequencies. Such a core shift’s value from observation can be used for estimation of jet power [280] if one additional assumption or measurement is used (e.g., equipartition between the magnetic and particle energy [281] or using total radio flux measurement in the partially self-absorbed part of the spectrum [282]).

Jet power:

[277]: Willott et al. (1999), The emission line–radio correlation for radio sources using the 7C Redshift Survey

[278]: O’Sullivan et al. (2011), Heating the hot atmospheres of galaxy groups with cavities: the relationship between jet power and low-frequency radio emission

[279]: Blandford and Königl (1979), “Relativistic jets as compact radio sources.”

[280]: Zdziarski et al. (2012), The MeV spectral tail in Cyg X-1 and optically thin emission of jets

[281]: Zamaninasab et al. (2014), “Dynamically important magnetic fields near accreting supermassive black holes”

[282]: Zdziarski et al. (2015), Core shifts, magnetic fields and magnetization of extragalactic jets

Gamma-ray luminosity

A purely phenomenological method for estimating jet power is based on the observed γ -ray luminosity [283]. This approach assumes that the γ -ray emission constitutes a major portion of the bolometric luminosity, and that the total jet power is roughly an order of magnitude higher than the radiative output [82]. Under these assumptions, the jet power can be estimated as:

$$P_{jet} \propto \alpha \frac{L_{\gamma}}{\Gamma^2} \quad (7.2)$$

where L_{γ} is the γ -ray luminosity from a single jet derived from *Fermi*-LAT data, Γ is the bulk Lorentz factor of the emitting region, and the constant α accounts for bolometric corrections and model-specific assumptions, such as external Compton scattering [283].

While this method shares the model dependencies and uncertainties similarly to one-zone SED modeling, it has the advantage of providing a jet power estimate using only a single-instrument γ -ray observation.

7.2.2 Blazar sample

In addition to validating the results of [134] within the framework of leptohadronic modeling, the estimated jet power can be independently cross-checked using one of the methods outlined above. We selected the empirical approach based on extended radio lobe emission, calibrated through studies of X-ray cavities. To reliably compare these two independent jet power estimation methods, a well-defined sample of blazars must satisfy the following criteria:

- a) availability of multi-wavelength data for SED modeling;
- b) measurements of radio flux at 151 MHz;
- c) reliable estimates of black hole mass and accretion disk luminosity.

For condition (a), I used the same sample and corresponding best-fit models described in **Section 7.1**. This sample of 324 blazars was cross-matched with the TGSS catalog, which provides flux measurements at 150 MHz [284], and the NVSS catalog, which offers data at 1.4 GHz [285].

To obtain estimates of disk luminosities and supermassive black hole (SMBH) masses, I cross-matched the sample of 324 blazars with the larger sample of *Fermi*-detected blazars from Paliya et al. [286], where these properties were derived through spectroscopic measurements of broad emission lines. For sources not included in that catalog, estimates were adopted from Paliya et al. [287], provided they were obtained via either spectroscopic methods or modeling of the big blue bump component in the optical–UV SED.

To ensure reliable comparison of jet power estimates, only sources with both radio measurements and disk luminosities were retained. The resulting final sample includes 262 blazars, comprising 226 FSRQs and 34 BL Lac objects.

The empirical jet power relation given in **Eq. (7.1)** requires radio luminosity measured at 151 MHz. To estimate this consistently and to include

Jet power:

[283]: Pjanka et al. (2017), "The power and production efficiency of blazar jets"

[82]: Ghisellini et al. (2014), "The power of relativistic jets is larger than the luminosity of their accretion disks"

Blazar sample:

[284]: Intema et al. (2017), "The GMRT 150 MHz all-sky radio survey. First alternative data release TGSS ADR1"

[285]: Condon et al. (1998), "The NRAO VLA Sky Survey"

[286]: Paliya et al. (2021), "The Central Engines of Fermi Blazars"

[287]: Paliya et al. (2017), "General Physical Properties of CGRaBS Blazars"

sources lacking direct 151 MHz measurements, I derived the radio spectral index α (defined as $F_\nu \propto \nu^{-\alpha}$) using the subset of 160 sources with both 150 MHz (TGSS) and 1.4 GHz (NVSS) flux measurements. The distribution of the resulting spectral indices is shown in **Figure 7.4**. Since the majority of sources in the sample are FSRQs, the spectral indices are clustered around values typical for FSRQs. The average spectral index from this distribution was adopted and used to extrapolate 151 MHz fluxes for the remaining sources in the sample.

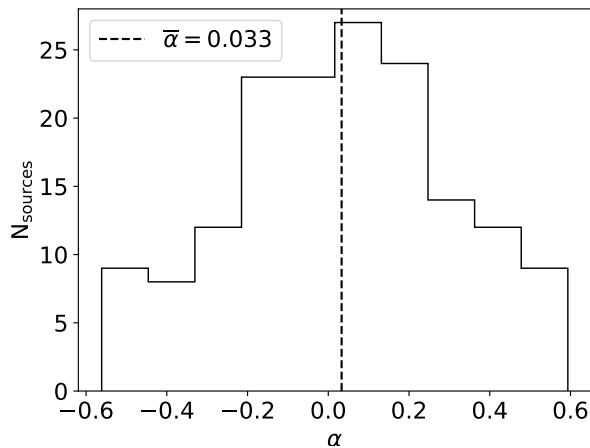


Figure 7.4: The distribution of spectral indices for sources from the sample detected by both TGSS and NVSS surveys. Figure from Omeliukh and Inoue [273].

7.2.3 Results

Figure 7.5 shows the relation between accretion disk luminosity and blazar jet power, with the latter estimated using the radio lobes method. For comparison, a similar analysis for radio galaxies reported a linear correlation between these two quantities, with a best-fit relation of $\log_{10}(P_{\text{jet}}) = 0.96 \log_{10}(L_{\text{disk}}) + 0.79$ [288]. In both Inoue et al. [288] and this study, jet power is calculated in the source frame (i.e., intrinsic to the AGN, unaffected by Doppler boosting or orientation effects). As shown in **Figure 7.5**, nearly all blazars in our sample exhibit systematically higher jet powers compared to radio galaxies at a given disk luminosity. Since the same jet power estimation method was used in both cases, this suggests that blazar jets are intrinsically more powerful than those of radio galaxies, not merely due to observational biases, potentially reflecting differences in black hole spin, magnetic field strength, or accretion disk properties.

Ghisellini et al. [82] studies the same relation for a sample of gamma-ray emitting blazars but with the P_{jet} based on the leptonic SED modeling. The obtained relation $\log_{10}(P_{\text{jet}}) = 0.92 \log_{10}(L_{\text{disk}}) + 4.57$ (see caption to Fig. 2 in Ghisellini et al. [82]; derived using the author's assumption

Results:

[288]: Inoue et al. (2017), "Disk-Jet Connection in Active Supermassive Black Holes in the Standard Accretion Disk Regime"
 [82]: Ghisellini et al. (2014), The power of relativistic jets is larger than the luminosity of their accretion disks

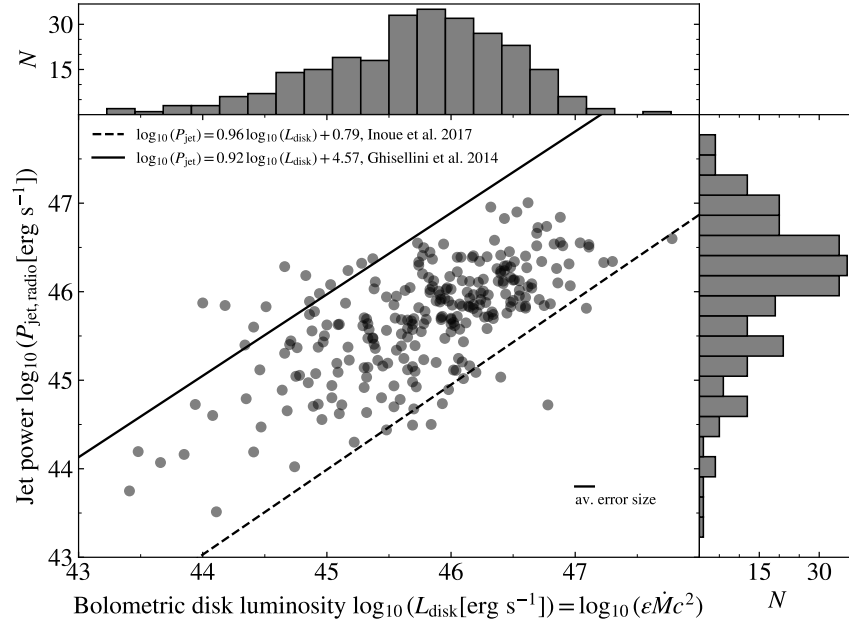


Figure 7.5: Jet power estimated from empirical dependence on radio luminosity vs. the bolometric disk luminosity. The solid line shows the best-fit relation from a blazar sample in Ghisellini et al. [82], where jet power was derived via SED modeling. The dashed line corresponds to the best-fit result for a sample of radio galaxies from Inoue et al. [288], where jet power was estimated using the radio lobes method. Figure from Omeliukh and Inoue [273].

$\eta = 30\%$) predicts jet power higher than its radio-derived value for most of the blazars in our sample.

As the sample modeling in Section 7.1 allowed for accounting proton emission only if it improved the fit, I adopt the results from Section 7.1 following the same division between leptonic and lepto-hadronic best-fit models. Figure 7.6 compares the jet powers derived from radio luminosity with those obtained from SED modeling for our sample. The black solid line indicates the one-to-one correspondence. While jet powers from leptonic models scatter approximately around this equivalence line, lepto-hadronic models tend to predict systematically higher jet powers than those inferred from radio measurements. Figure 7.7 further demonstrates the good agreement between jet power estimates obtained from leptonic SED modeling and those derived using the radio lobes method, whereas models that include proton contributions systematically yield higher jet powers.

Figure 7.8 shows the relation between the jet-to-disk power ratio $P_{\text{jet}}/L_{\text{disk}}$ and disk Eddington ratio $\lambda = L_{\text{disk}}/L_{\text{Edd}}$. To assess potential correlations, I calculate Spearman's rank correlation coefficients and corresponding p-values. The Spearman rank correlation gives $\rho = -0.555$ (with a p-value of $< 10^{-15}$) for radio-estimated jet power, $\rho = -0.462$ (with a p-value of 3.6×10^{-10}) for jet power based on leptonic models,

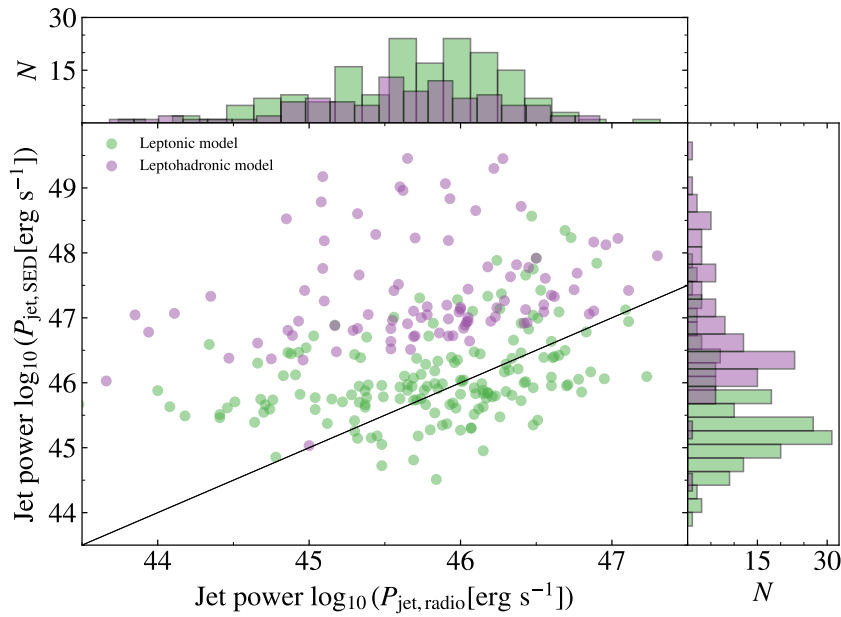


Figure 7.6: The comparison of jet power estimated from SED modeling and the radio luminosity. Green circles correspond to the source in the sample explained by the leptonic models, purple circles correspond to the hadronic models. Figure from Omeliukh and Inoue [273].

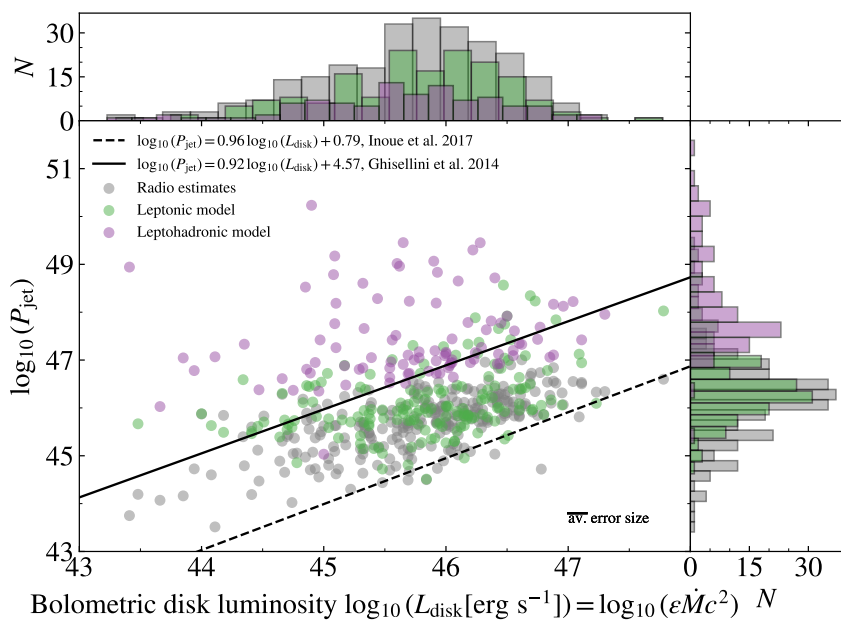


Figure 7.7: Jet power estimated with two independent methods vs. the bolometric disk luminosity. Grey points correspond to the radio lobes method, green and purple correspond to the SED modeling with green being leptonic models and purple leptohadronic models. Figure from Omeliukh and Inoue [273].

and -0.592 (with a p-value of 2.2×10^{-10}) for jet power based on leptohadronic models. Therefore, there is a strong negative correlation between $P_{\text{jet}}/L_{\text{disk}}$ and disk Eddington ratio in blazars. **Figure 7.9** shows the relation between jet production efficiency (assuming accretion efficiency $\epsilon = 10\%$) and disk luminosity, with jet powers estimated using both the radio-lobe method and SED modeling. Similarly, I tested the correlation between these two quantities. The Spearman rank correlation is $\rho = -0.482$ (with a p-value of $< 10^{-15}$) radio-estimated jet power, $\rho = -0.373$ (with a p-value of 7.6×10^{-7}) for jet power based on leptonic models, and $\rho = -0.442$ (with a p-value of 6.2×10^{-6}) for jet power based on leptohadronic models. This correlation suggests that blazars with weaker accretion disks have higher jet production efficiency. The results are summarized in **Table 7.1**.

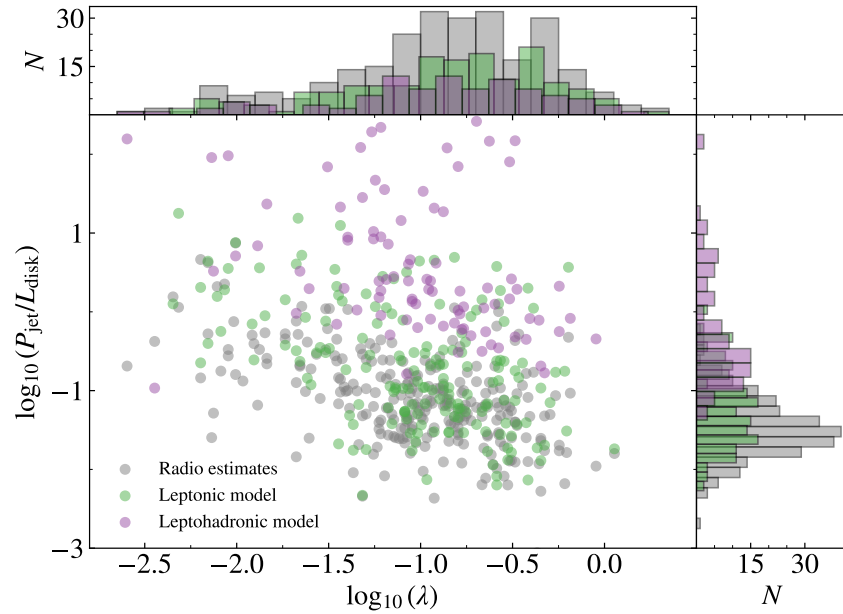


Figure 7.8: Ratio of $P_{\text{jet}}/L_{\text{disk}}$ vs the disk Eddington ratio for different methods of jet power estimation. Figure from Omeliukh and Inoue [273].

Table 7.1: Spearman's rank correlation coefficients

Quantities	Method	ρ^1	p-value
$P_{\text{jet}}/L_{\text{disk}}$ vs λ	radio	-0.483	$< 10^{-15}$
	leptonic SED	-0.424	1.2×10^{-8}
	leptohadronic SED	-0.434	9.5×10^{-6}
$P_{\text{jet}}/\dot{M}c^2$ vs L_{disk}	radio	-0.555	$< 10^{-15}$
	leptonic SED	-0.641	2×10^{-12}
	leptohadronic SED	-0.494	1.3×10^{-11}

¹Spearman's rank correlation coefficient.

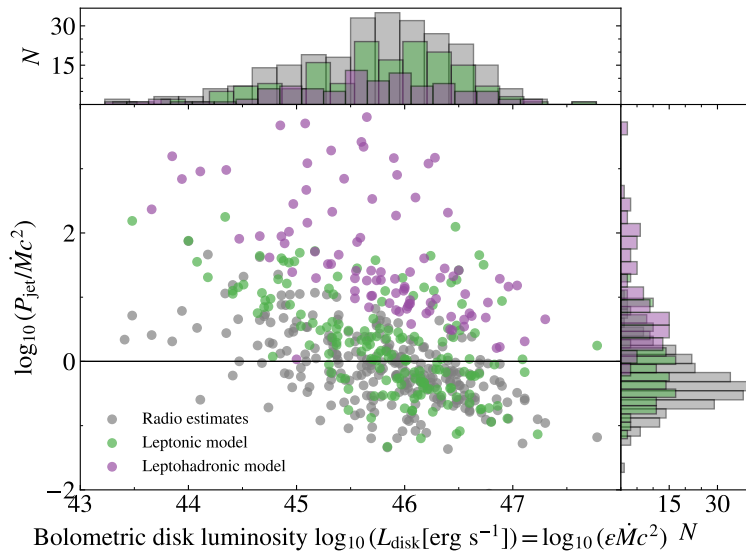


Figure 7.9: Jet production efficiency (assuming accretion efficiency $\epsilon = 10\%$) vs the bolometric disk luminosity. Figure from Omeliukh and Inoue [273].

These observed empirical trends are in strong agreement with theoretical models of magnetically arrested disks (MADs), where strong poloidal magnetic fields threading the black hole's ergosphere allow for efficient energy extraction through the Blandford-Znajek process [289]. In this MAD regime, jets can draw energy directly from the black hole's rotation, resulting in jet powers that surpass the energy supplied by accretion, especially in systems with low Eddington ratios.

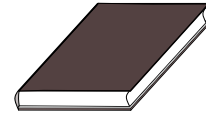
The observed inverse relationship between jet efficiency and accretion rate suggests a physical transition: while systems with high accretion rates are likely magnetically sub-critical, those with low accretion may reach or approach the MAD state. This interpretation links the observational findings with state-of-the-art numerical simulations and offers a coherent framework for understanding jet formation across the blazar population.

7.2.4 Summary and conclusions

- I analyzed a sample of 262 blazars for which the jet power was independently estimated based on the radio lobes method and based on the SED modeling.
- The power of blazar jets in the source frame is higher than that for radio galaxies (using the same jet power estimation method).
- The jet production efficiency is strongly anti-correlated with the disk luminosity, suggesting that slowly accreting black holes produce jets more efficiently.
- These findings provide observational support for theoretical predictions of magnetically arrested disks and the Blandford-Znajek mechanism of jet formation.

Results:

[289]: Tchekhovskoy et al. (2011), "Efficient generation of jets from magnetically arrested accretion on a rapidly spinning black hole"



Chapter 8

Summary and outlook

The origin of the extragalactic neutrino flux detected by the IceCube Neutrino Observatory remains one of the key unsolved problems in high-energy astrophysics. A promising approach to addressing this challenge lies in multi-messenger astronomy, which combines information from different types of cosmic signals—such as electromagnetic radiation, gravitational waves, and neutrinos—to provide a more complete picture of energetic astrophysical phenomena. Among the leading candidates for the sources of these high-energy neutrinos are blazars, a rare and extreme class of active galactic nuclei distinguished by their powerful relativistic jets that are closely aligned with our line of sight.

The spectral energy distribution of blazars typically exhibits a characteristic two-bump structure. The low-energy component, extending from radio wavelengths up to the UV or X-ray band, is produced by synchrotron radiation emitted by relativistic electrons in the jet. The origin of the high-energy component, ranging from X-rays to gamma rays, remains less certain. A commonly adopted approach to explain the SED assumes a single emission region, often referred to as a blob, responsible for the observed radiation. Depending on the types of particles responsible for the high-energy emission, models can be divided into purely leptonic, purely hadronic (proton synchrotron), or leptohadronic. In this thesis, I used the state-of-the-art numerical modeling framework AM^3 to simulate the multi-messenger emission from blazars within the one-zone paradigm.

PKS 0735+178 is the first source where the most powerful multi-wavelength flare ever observed for this source was found to be spatially and temporally coincident with the detection of three neutrinos across three different neutrino observatories. Four distinct emission states of the blazar were analyzed to trace the flare evolution and to identify conditions that could lead to neutrino production. The modeling strategy, presented in [Section 5.1](#), was based on a grid scan technique and revealed substantial degeneracies in both leptonic and hadronic model parameters. Even

with a well-covered multi-wavelength spectrum, constraining the neutrino spectrum remains challenging. Under the assumption of maximizing neutrino detection rates in IceCube, leptohadronic models predict up to 0.1 neutrino events during the 50-day flare, surpassing estimates of other works. The post-flare SED could not be reproduced using a simple one-zone leptohadronic model and likely requires the inclusion of external photon fields to account for the observed gamma-ray emission. This suggests that the emission region may evolve spatially over time. A key challenge in one-zone hadronic modeling is the strong degeneracy among model parameters. Since the proton spectrum cannot be directly constrained by photon data, large uncertainties in neutrino predictions persist. Addressing this issue will require both next-generation neutrino telescopes and high-energy polarimeters to provide more definitive observational signatures.

The blazar VER J0521+211 underwent a flare in TeV gamma rays between 26 February and 2 March 2020, showing significant variability in the very-high-energy (VHE) gamma-ray flux. In [Section 5.2](#), I analyzed the flare using a one-zone leptohadronic model, focusing on four distinct blazar states during the flare. Given the day-long timescale of variability, I adopted a modeling approach that seeks minimal changes in parameters between consecutive states. States A, B, and C differed primarily in electron and proton luminosities, suggesting fluctuations in the number of particles entering the emission zone. State D, in contrast, required changes in both particle spectra and luminosities, possibly indicating the injection of a more energetic particle population. Detection of neutrinos during such flares with future telescopes would provide strong support for this model. Additionally, detecting hard X-ray or MeV emission at levels of approximately 5×10^{-11} erg/cm²/s (compared to $\sim 10^{-13}$ erg/cm²/s in purely leptonic models) would serve as a clear observational signature of hadronic processes.

Recent detections of neutrino signals from nearby Seyfert galaxies have broadened the range of potential astrophysical neutrino sources beyond blazars. In the case of NGC 4151, IceCube's second most significant Seyfert neutrino source, two nearby blazars, 4FGL J1210.3+3928 and 4FGL J1211.6+3901, are located just 0.08° and 0.43° from the galaxy, respectively. Given that blazars are established candidates for neutrino emission, they may contribute to the observed neutrino hotspot. In [Section 5.3](#), I modeled the multi-wavelength SEDs of both blazars using leptonic and leptohadronic scenarios. For 4FGL J1210.3+3928, only the leptohadronic model could reproduce the observed fluxes, including a notable dip in the GeV gamma-ray spectrum, which may represent a hadronic signature. For 4FGL J1211.6+3901, both models provided comparably good fits. In both cases, the predicted neutrino flux peaks around 10^{17} eV, though their contribution to the observed TeV-scale neutrino flux is expected to be minor. Detection of such neutrinos will likely require radio-based techniques and may become feasible with upcoming instruments such as the radio array of IceCube-Gen2 or GRAND.

Chapter 6 explores the performance of five optimization algorithms

– grid scan, genetic algorithm, CMA-ES, Minuit, and MCMC – for fitting blazar SEDs using a one-zone synchrotron self-Compton (SSC) model. By applying these algorithms to both simulated pseudo-data and real observational datasets, we assessed their performance in retrieving best-fit model parameters, their computational efficiency, and their robustness to data quality and coverage. When data coverage is dense and the uncertainties are small, different optimization methods yield consistent results. However, as data gaps widen or uncertainties increase, parameter degeneracies become significant, often leading to best-fit solutions that diverge from the true values. Of the methods tested, the grid scan is the most robust in exploring multiple physically plausible solutions, though it is computationally demanding. CMA-ES and the genetic algorithm offer a balance between performance and computational cost. Minuit is the fastest, but it is prone to converging on local minima due to its sensitivity to initial conditions. MCMC provides detailed information on parameter correlations and uncertainties but requires careful initialization and prior selection. Even within the relatively simple SSC one-zone framework, degeneracies are prevalent and would become even more problematic in more complex models. Addressing these challenges requires high-quality, simultaneous multi-wavelength data, better coverage in poorly explored energy ranges such as MeV, and incorporation of polarization measurements across the spectrum.

In [Chapter 7](#), a large sample of 324 blazars was modeled within a one-zone leptohadronic framework. Out of these, 106 sources required a hadronic component to either reproduce the observed SED or significantly improve the fit quality. When extrapolated to the broader population of Fermi-detected blazars, the results suggest that blazars could account for up to 20% of the diffuse astrophysical neutrino flux detected by IceCube, in agreement with current upper limits from stacking analyses based on the Fermi-2LAC catalog. Using this sample, I also studied the empirical relation between blazar jet power and accretion disk luminosity. To validate the jet power estimates derived from SED modeling, an independent method based on extended radio emission calibrated by X-ray cavities was employed. The observed anti-correlations between the jet-to-disk power ratio ($P_{\text{jet}}/L_{\text{disk}}$) and the Eddington-scaled disk luminosity ($\lambda = L_{\text{disk}}/L_{\text{Edd}}$), as well as between jet production efficiency (assuming 10% accretion efficiency) and disk luminosity, support theoretical predictions that jets are produced more efficiently by black holes with low accretion rates. These findings provide observational evidence in favor of magnetically arrested disk models and the Blandford–Znajek mechanism of jet formation.

As demonstrated throughout this thesis, even state-of-the-art one-zone models, when applied to available multi-messenger blazar data, are unable to unambiguously constrain key physical parameters. Advancements in electromagnetic observations, especially in the poorly explored MeV and TeV ranges, could significantly reduce model uncertainties. Given the rapid variability of blazars, coordinated multi-wavelength monitoring campaigns are essential for capturing time-dependent behavior and

ensuring that the correct emission state is represented, especially during neutrino events. Furthermore, polarization measurements across multiple messengers may help distinguish between leptonic and lepto-hadronic emission scenarios and provide insights into the physical conditions within the emission region. On the neutrino side, next-generation observatories will offer improved sensitivity and broader energy coverage (from PeV to EeV), enabling more precise neutrino spectrum measurements and tighter constraints on the hadronic contribution. These advances may lead to the discovery of new classes of neutrino sources and help uncover the origins of ultra-high-energy cosmic rays.

Appendices

Supplementary material to Chapter 5.1

A Parameter space of leptonic models for PKS 0735+178

Similarly to **Figure 5.4**, **Figure 1** to **Figure 7** show the value of reduced χ^2 for variations of every pair of leptonic model parameters when the remaining parameters are fixed to the best fit. The best-fit value is marked with a pink circle in all plots.

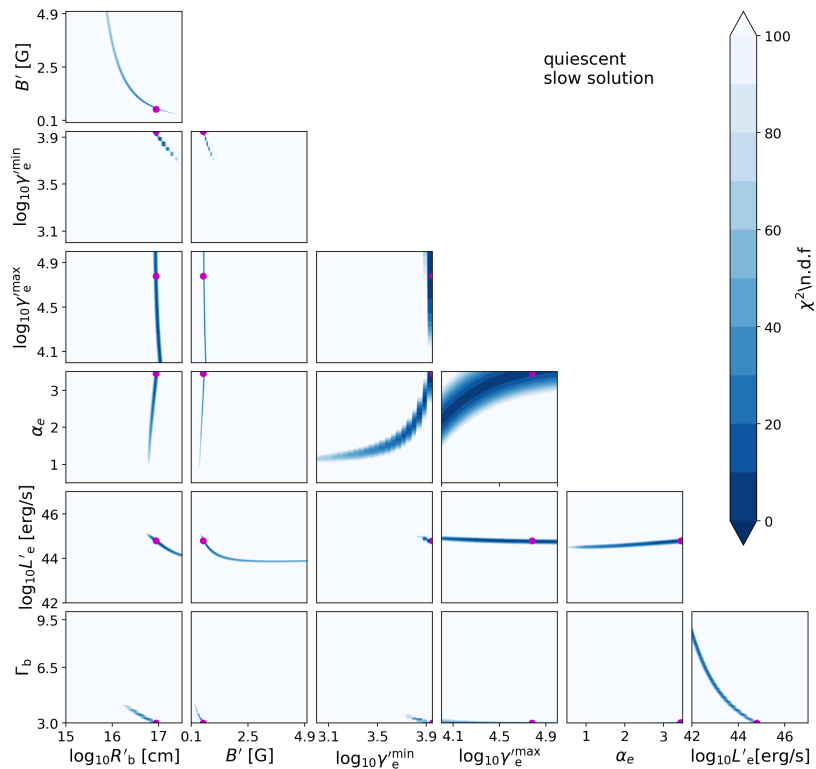


Figure 1: Values of the reduced χ^2 around best-fit slow solution for the quiescent state SED. Figure from Omeliukh et al. [145].

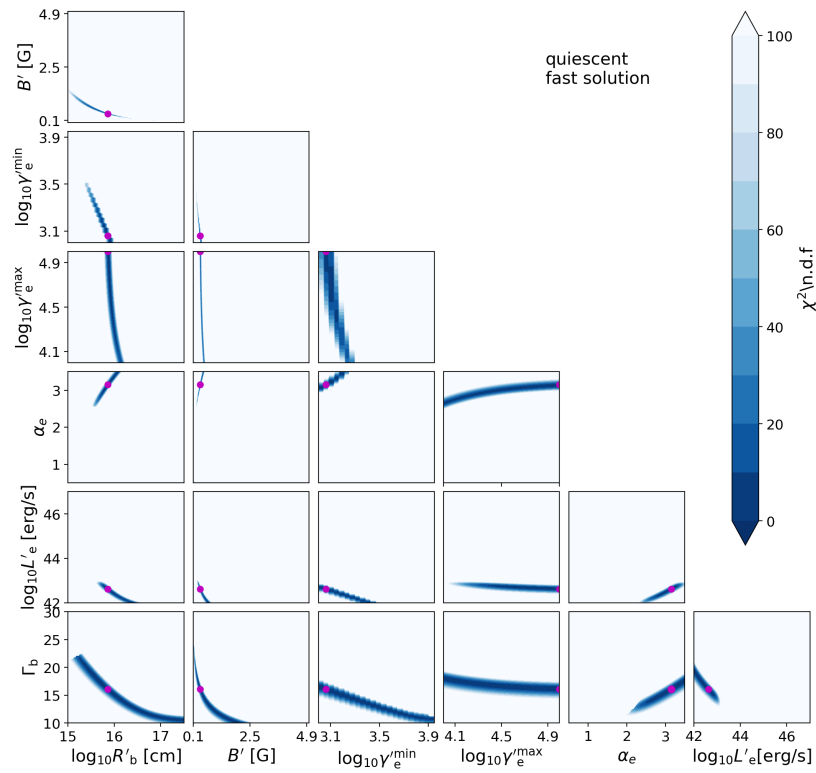


Figure 2: Values of the reduced χ^2 around best-fit fast solution for the quiescent state SED. Figure from Omeliukh et al. [145].

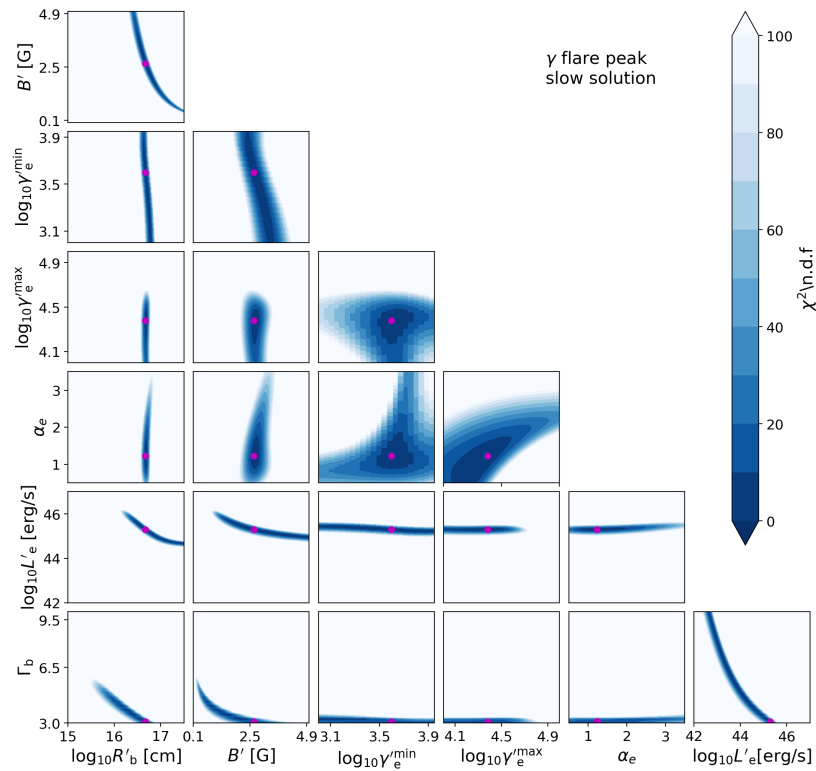


Figure 3: Values of the reduced χ^2 around best-fit slow solution for the γ ray flare peak SED. Figure from Omeliukh et al. [145].

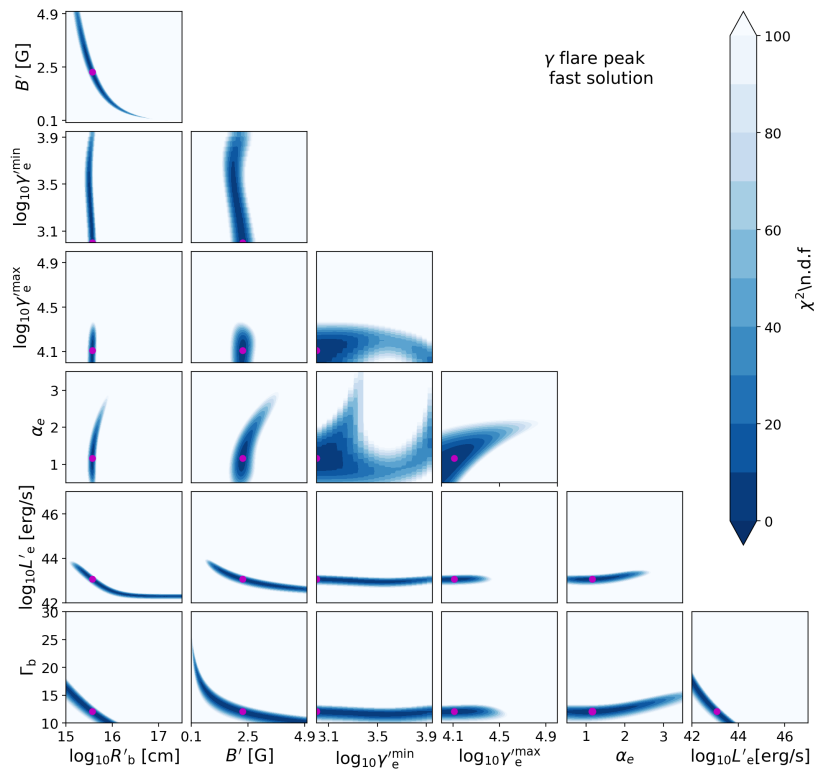


Figure 4: Values of the reduced χ^2 around best-fit fast solution for the γ ray flare peak SED. Figure from Omeliukh et al. [145].

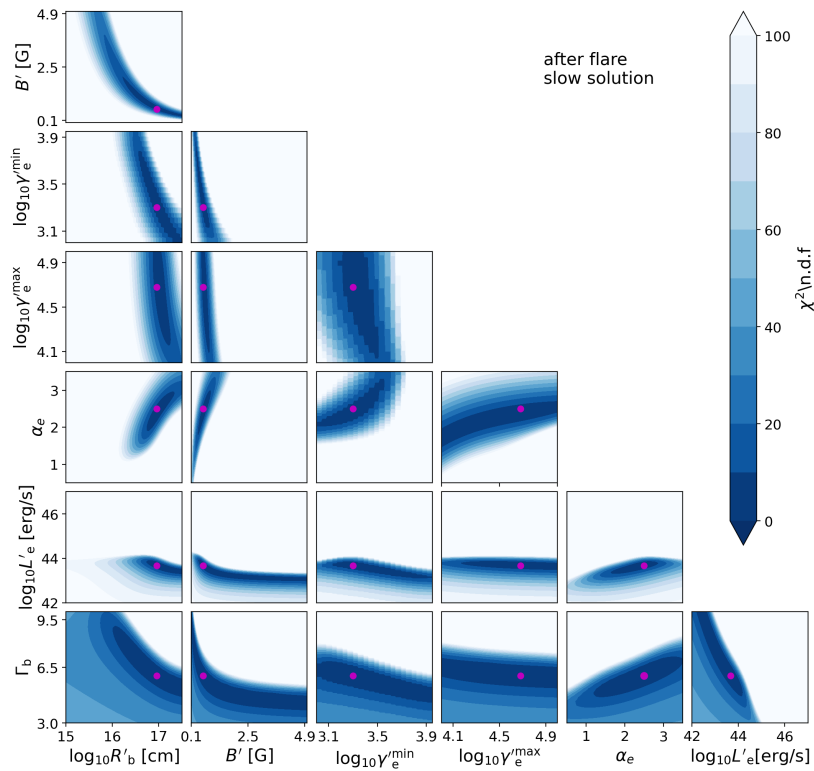


Figure 5: Values of the reduced χ^2 around best-fit slow solution for the after-flare SED. Figure from Omeliukh et al. [145].

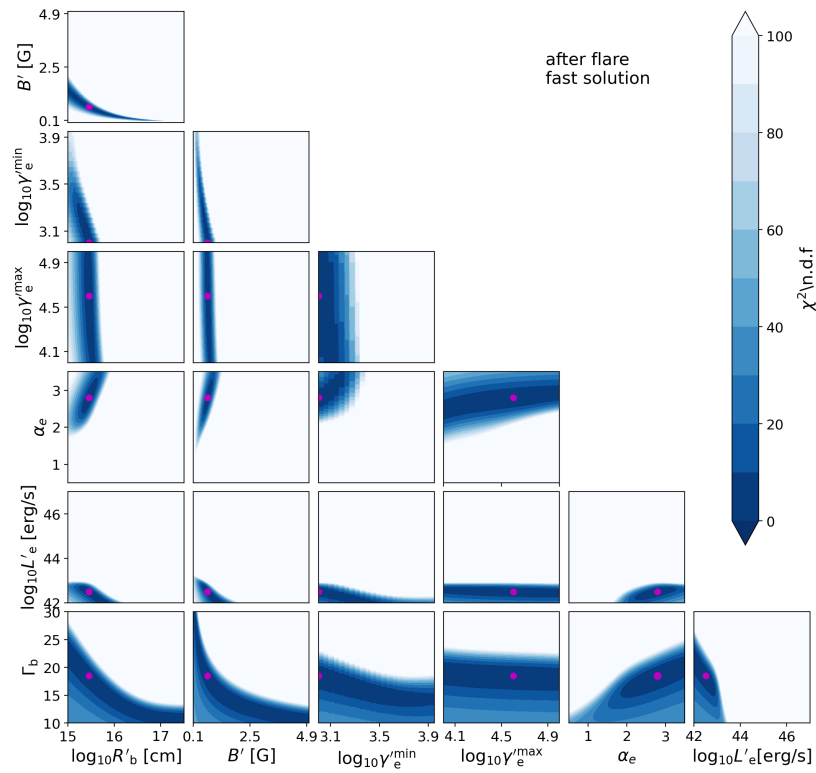


Figure 6: Values of the reduced χ^2 around best-fit fast solution for the after-flare SED. Figure from Omeliukh et al. [145].

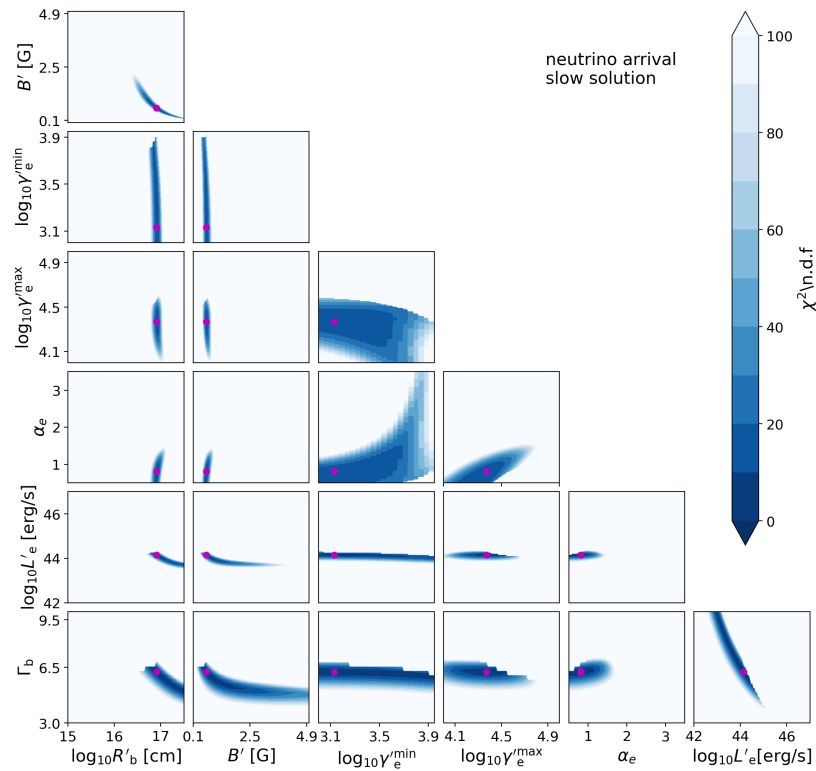


Figure 7: Values of the reduced χ^2 around best-fit slow solution for the neutrino arrival SED. Figure from Omeliukh et al. [145].

Supplementary material to Chapter 6

B Andrew's plots

Andrews plots or Andrews curves is a method proposed in Andrews [290] to visualize high-dimensional data. According to this method, each data point $\bar{x} = (x_1, x_2, \dots, x_n)$ is mapped into a function

$$f_{\bar{x}}(t) = x_1 / \sqrt{2} + x_2 \sin t + x_3 \cos t + x_4 \sin 2t + x_5 \cos 2t + \dots \quad (1)$$

The function is plotted then for $-\pi \leq t \leq \pi$. Thus each data point is represented as a separate curve in the plot. The similarity of the shapes of the curves tells about the close location of the points in high-dimensional space. The components of the data vector differ significantly in both their orders of magnitude (e.g., $R' \sim 10^{16}$ cm and $B' \sim 1$ G) and their respective variances. To ensure that the Andrews function responds equally to variations across all components, I normalized the data as follows:

$$x_i^{norm} = \frac{x_i - \bar{x}_i}{\sigma(x_i)} \quad (2)$$

where \bar{x}_i denotes the mean value of the i -th parameter, and $\sigma(x_i)$ represents its standard deviation.

To illustrate the presence of distinct families of solutions in parameter space, I selected the 15 best-fitting leptonic models for the quiescent-state SED, each with a reduced χ^2 value between 1.6 and 2.7. Models with poorer fits provide little insight into the location of well-fitting regions and tend to obscure meaningful patterns in the Andrews plots by introducing unnecessary noise. **Figure 8** presents the Andrews plots for the selected parameter sets. Each panel corresponds to a different method of assigning colormaps. Every curve represents the full set of seven model parameters. A value of the reduced χ^2 defines the color.

All subfigures in **Figure 8** display the same set of Andrews functions, each representing the seven model parameters. The only variation between subplots lies in the choice of colormap, which influences how the curves are visually grouped. The first two rows of **Figure 8** demonstrate that grouping solutions by parameters such as R'_b , B , L'_e , and Γ_b reveals distinct families of solutions. The similarity in the shapes of the Andrews functions, such as comparable peak positions and amplitudes, indicates that different SED fits yield closely related parameter values. In contrast, the last three subplots, where γ'_{min} , γ'_{max} , and α are used as colormaps, highlight that these parameters cannot be well-constrained.

C MCMC corner plots

Figure 9 to **Figure 13** present the two-dimensional projections of the posterior probability distributions for the model parameters. The MCMC parameter search was conducted in two stages. In the first stage (run 1), the algorithm performed global sampling within predefined parameter boundaries for each SED. These boundaries were then refined based on the results of run 1, and a second sampling (run 2) was carried out. As shown in the run 1 plots for all datasets, the chosen number of walkers and steps was insufficient for the algorithm to converge to a single solution across the global parameter space. However, within the refined and limited region explored in run 2, convergence was achieved, and a well-defined solution was obtained, as evidenced by the corresponding posterior distributions.

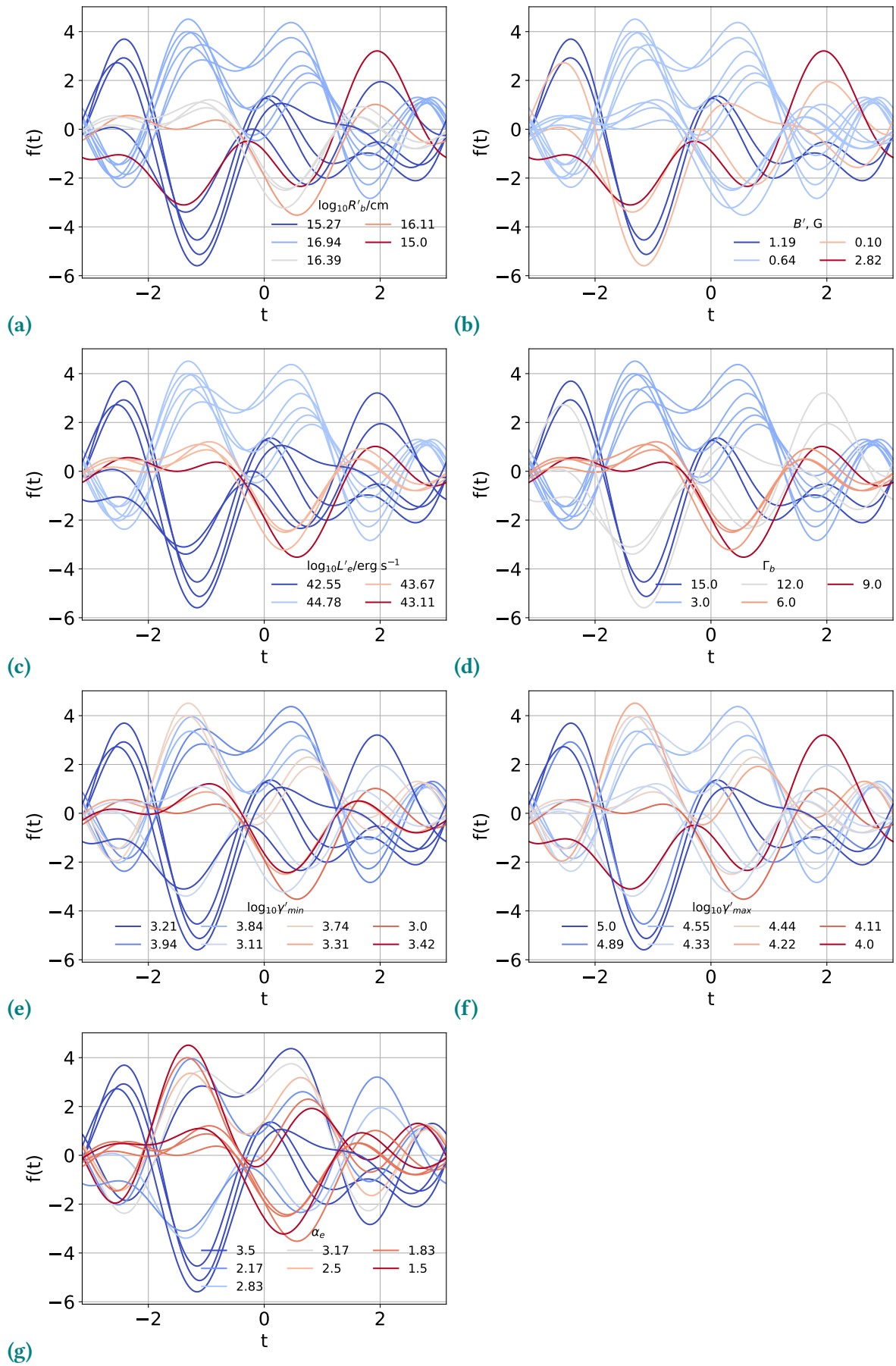
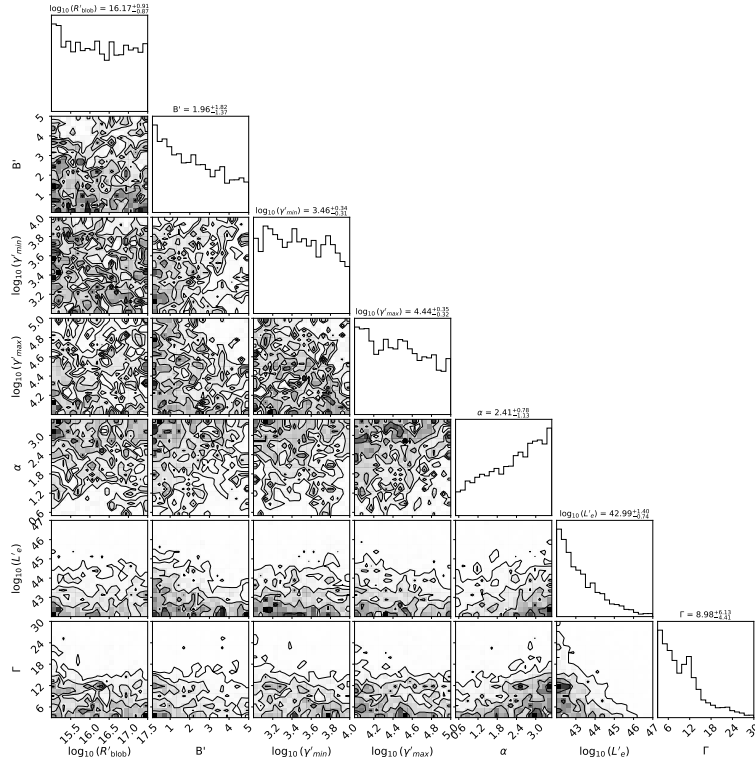
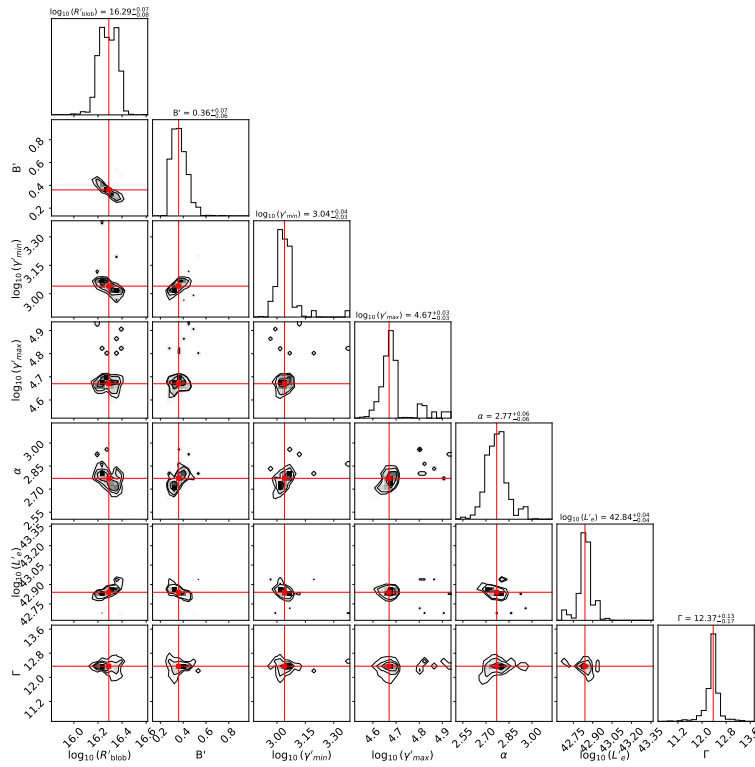


Figure 8: Andrew's plots for the 15 best-fit solution for PKS 0735+178 gamma-ray quiescent SED obtained with grid scan.

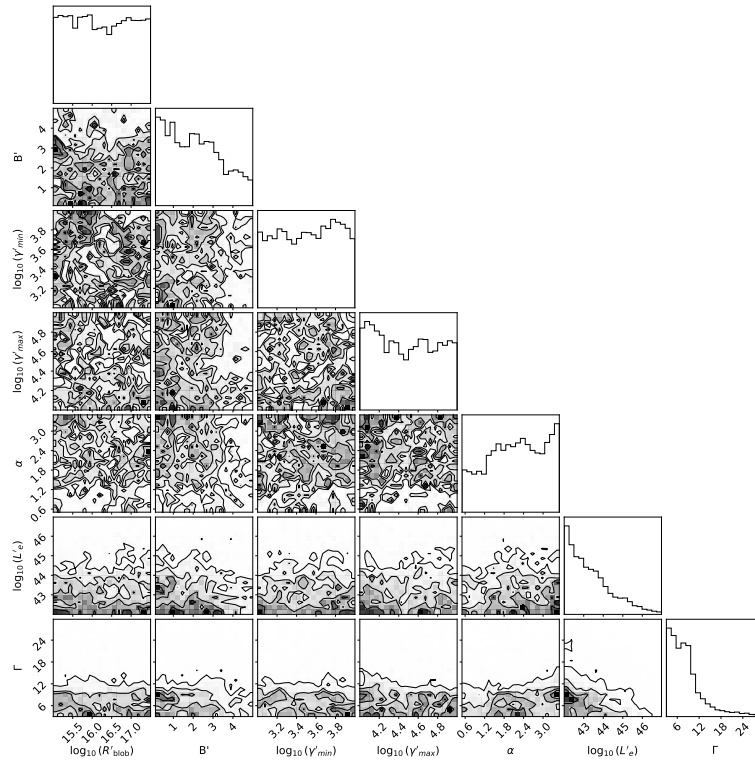


(a) Corner plot for simulated dataset 1. MCMC run 1.

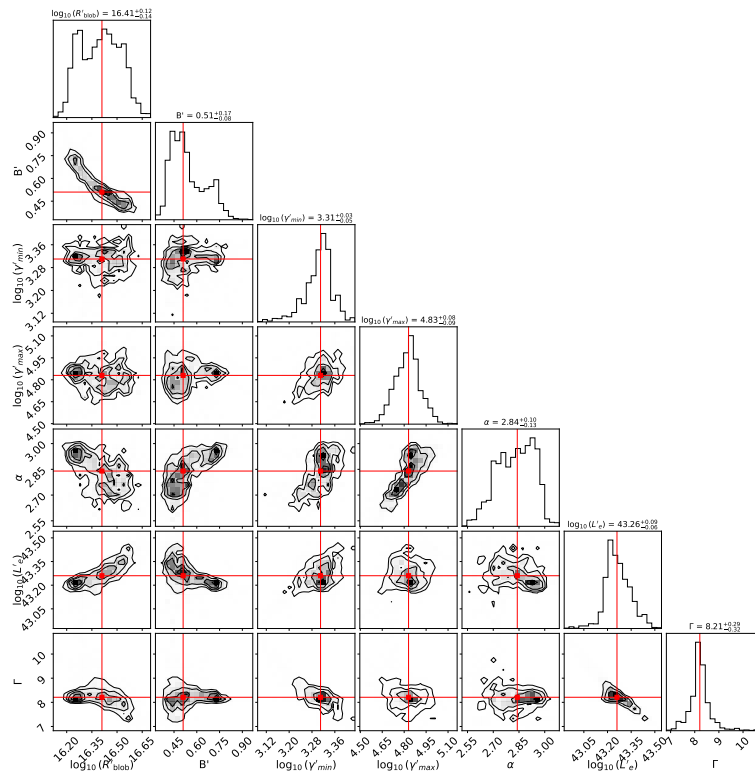


(b) Corner plot for simulated dataset 1. MCMC run 2.

Figure 9: Simulated dataset 1. Figure from Apel et al. [240].

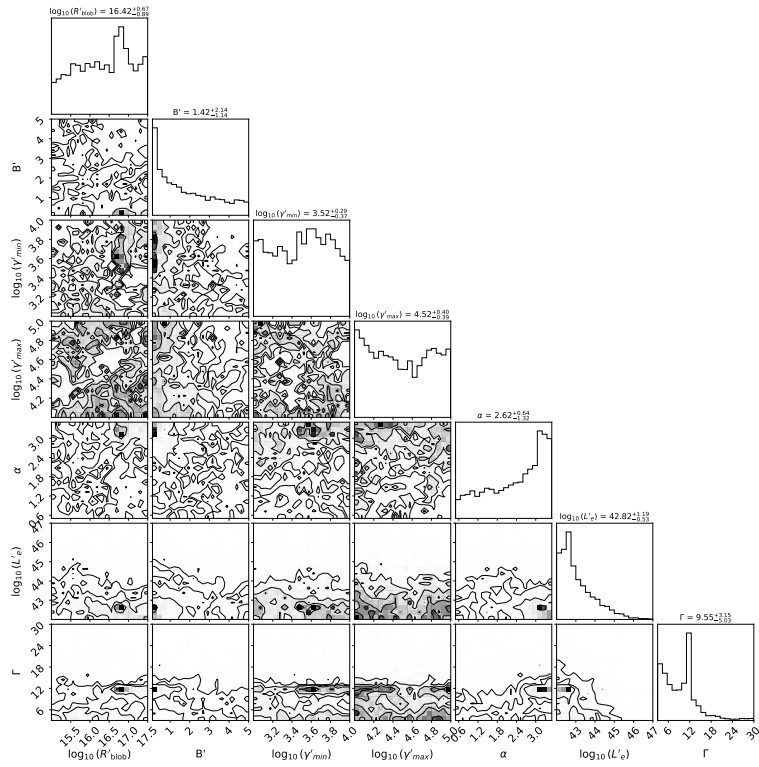


(a) Corner plot for simulated dataset 2. MCMC run 1.

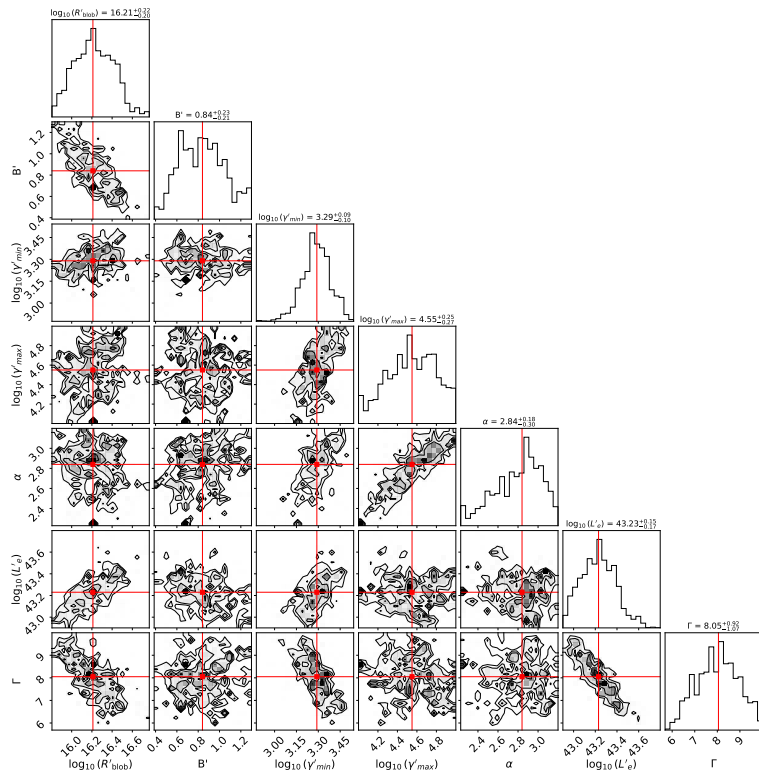


(b) Corner plot for simulated dataset 2. MCMC run 2.

Figure 10: Simulated dataset 2. Figure from Apel et al. [240].

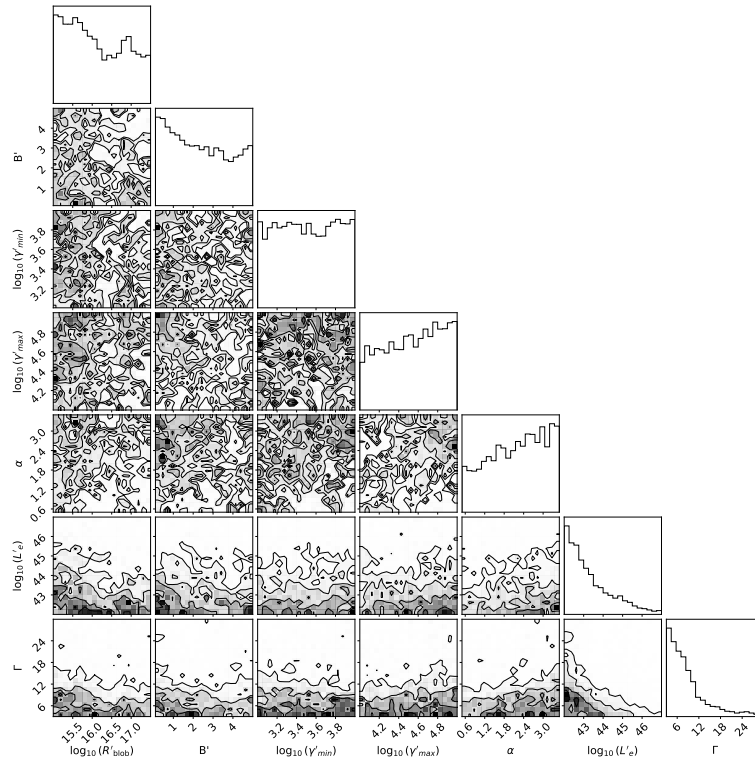


(a) Corner plot for simulated dataset 3. MCMC run 1.

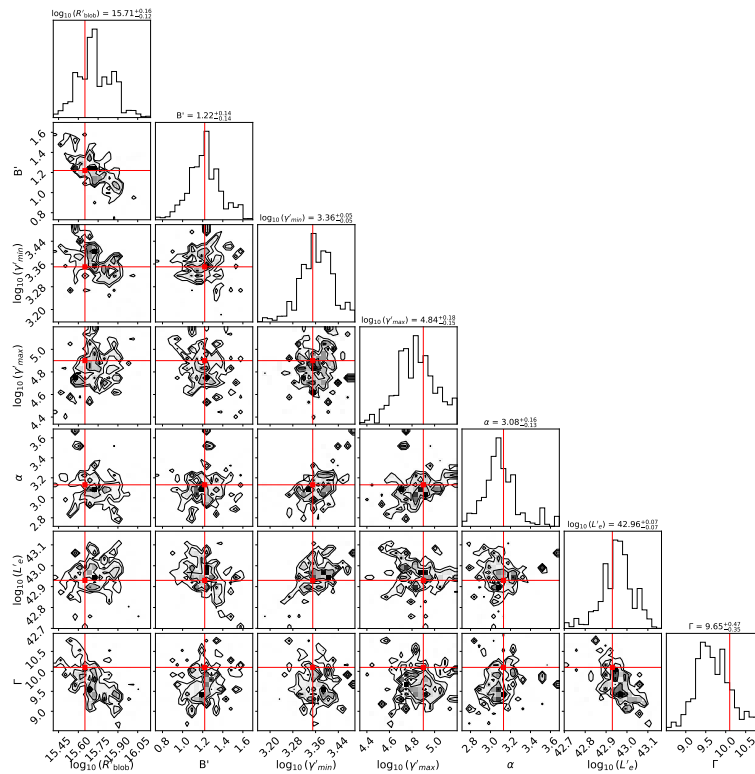


(b) Corner plot for simulated dataset 3. MCMC run 2.

Figure 11: Simulated dataset 3. Figure from Apel et al. [240].

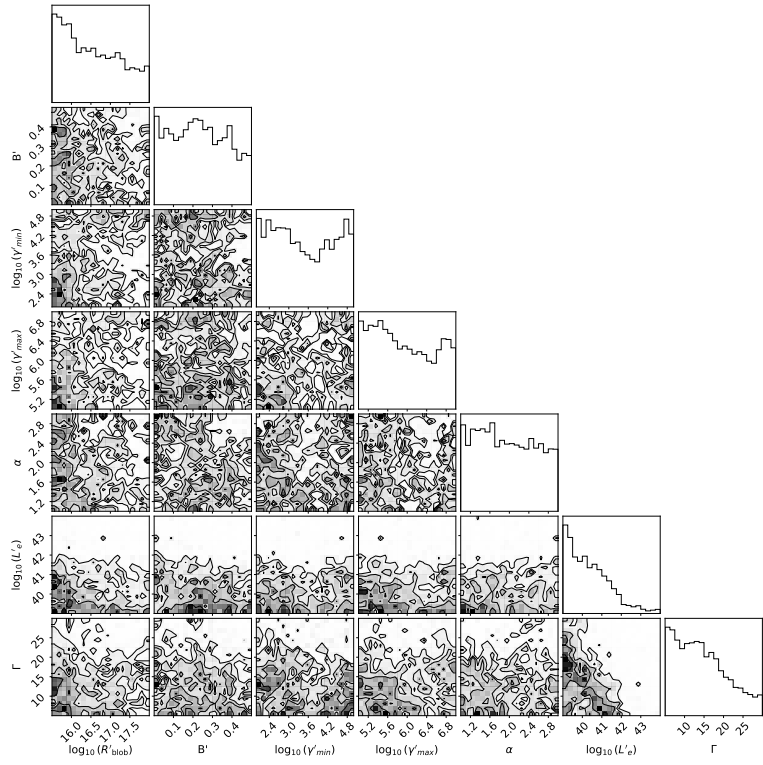


(a) Corner plot for PKS 0735+178. MCMC run 1.

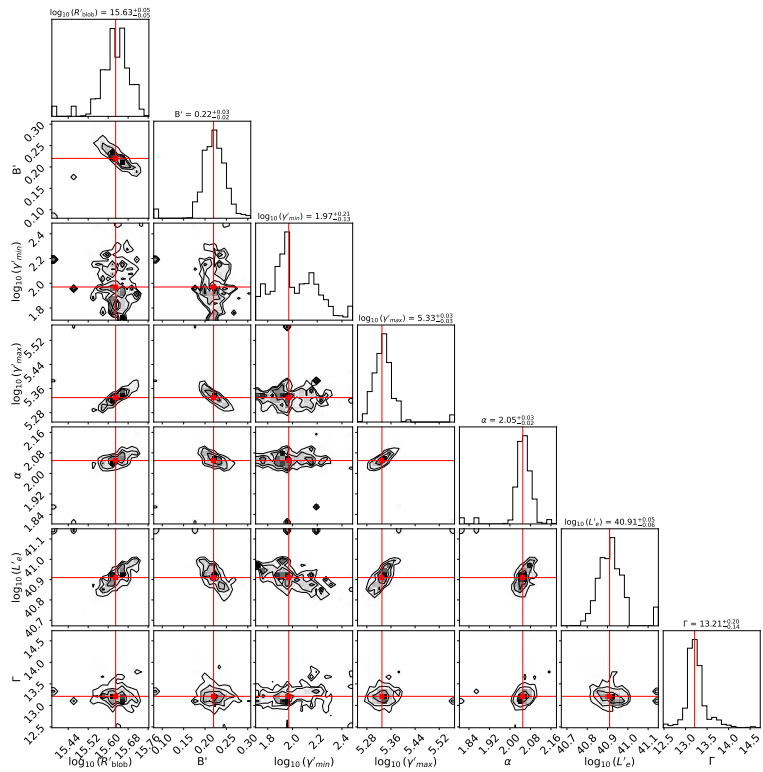


(b) Corner plot for PKS 0735+178. MCMC run 2.

Figure 12: Gamma-ray quiescent state of PKS 0735+178. Figure from Apel et al. [240].



(a) Corner plot for Mrk 501. MCMC run 1.



(b) Corner plot for Mrk 501. MCMC run 2.

Figure 13: Gamma-ray quiescent state of Mrk 501. Figure from Apel et al. [240].

Bibliography

- [1] Victor F. Hess. Über Beobachtungen der durchdringenden Strahlung bei sieben Freiballonfahrten. *Phys. Z.*, 13:1084–1091, 1912.
- [2] E. Vangioni-Flam, M. Cassé, and J. Audouze. Lithium-beryllium-boron: origin and evolution. *Physics Reports*, 333:365–387, August 2000. doi: 10.1016/S0370-1573(00)00030-2.
- [3] P. Lipari. Interpretation of the cosmic ray positron and antiproton fluxes. *Phys. Rev. D*, 95:063009, Mar 2017. doi: 10.1103/PhysRevD.95.063009. URL <https://link.aps.org/doi/10.1103/PhysRevD.95.063009>.
- [4] R. L. Workman and Others. Review of particle physics. *PTEP*, 2022:083C01, 2022. doi: 10.1093/ptep/ptac097.
- [5] A. M. Hillas. Can diffusive shock acceleration in supernova remnants account for high-energy galactic cosmic rays? *Journal of Physics G Nuclear Physics*, 31(5):R95–R131, May 2005. doi: 10.1088/0954-3899/31/5/R02.
- [6] J. R. Horandel. Cosmic rays from the knee to the second knee: 10^4 to 10^{18} ev. *Mod. Phys. Lett. A*, 22:1533–1552, 2007. doi: 10.1142/S0217732307024139.
- [7] K. Greisen. End to the cosmic-ray spectrum? *Phys. Rev. Lett.*, 16:748–750, Apr 1966. doi: 10.1103/PhysRevLett.16.748. URL <https://link.aps.org/doi/10.1103/PhysRevLett.16.748>.
- [8] G. T. Zatsepin and V. A. Kuz'min. Upper limit of the spectrum of cosmic rays. *Soviet Journal of Experimental and Theoretical Physics Letters*, 4:78, August 1966.
- [9] E. Fermi. Galactic magnetic fields and the origin of cosmic radiation. *ApJ*, 119:1, January 1954. doi: 10.1086/145789.
- [10] E. Fermi. On the origin of the cosmic radiation. *Phys. Rev.*, 75:1169–1174, Apr 1949. doi: 10.1103/PhysRev.75.1169. URL <https://link.aps.org/doi/10.1103/PhysRev.75.1169>.
- [11] L. Sironi and A. Spitkovsky. Relativistic reconnection: An efficient source of non-thermal particles. *ApJL*, 783(1):L21, March 2014. doi: 10.1088/2041-8205/783/1/L21.
- [12] R. U. Abbasi et al. Indications of intermediate-scale anisotropy of cosmic rays with energy greater than 57 eev in the northern sky measured with the surface detector of the telescope array experiment. *ApJL*, 790(2):L21, August 2014. doi: 10.1088/2041-8205/790/2/L21.
- [13] A. Aab et al. Searches for anisotropies in the arrival directions of the highest energy cosmic rays detected by the pierre auger observatory. *ApJ*, 804(1):15, May 2015. doi: 10.1088/0004-637X/804/1/15.
- [14] A. M. Hillas. The origin of ultra-high-energy cosmic rays. *ARA&A*, 22:425–444, January 1984. doi: 10.1146/annurev.aa.22.090184.002233.
- [15] R. Alves Batista et al. Open questions in cosmic-ray research at ultrahigh energies. *Frontiers in Astronomy and Space Sciences*, 6:23, June 2019. doi: 10.3389/fspas.2019.00023.
- [16] A. De Angelis, G. Galanti, and M. Roncadelli. Transparency of the universe to gamma-rays. *MNRAS*, 432(4):3245–3249, July 2013. doi: 10.1093/mnras/stt684.
- [17] W. Pauli. Dear radioactive ladies and gentlemen. *Phys. Today*, 31N9:27, 1978.
- [18] E. Fermi. An attempt of a theory of beta radiation. *Z. Phys.*, 88:161–177, 1934. doi: 10.1007/BF01351864.

- [19] C. L. Cowan, F. Reines, F. B. Harrison, H. W. Kruse, and A. D. McGuire. Detection of the free neutrino: A confirmation. *Science*, 124:103–104, 1956. doi: 10.1126/science.124.3212.103.
- [20] F. Iachello. Open problems in neutrino physics. *J. Phys. Conf. Ser.*, 1056(1):012027, 2018. doi: 10.1088/1742-6596/1056/1/012027.
- [21] M. Sajjad Athar et al. Status and perspectives of neutrino physics. *Progress in Particle and Nuclear Physics*, 124:103947, 2022. ISSN 0146-6410. doi: <https://doi.org/10.1016/j.ppnp.2022.103947>. URL <https://www.sciencedirect.com/science/article/pii/S0146641022000084>.
- [22] G. Danby, J.-M. Gaillard, K. Goulianos, L. M. Lederman, N. Mistry, M. Schwartz, and J. Steinberger. Observation of high-energy neutrino reactions and the existence of two kinds of neutrinos. *Phys. Rev. Lett.*, 9:36–44, Jul 1962. doi: 10.1103/PhysRevLett.9.36. URL <https://link.aps.org/doi/10.1103/PhysRevLett.9.36>.
- [23] K. Kodama et al. Observation of tau neutrino interactions. *Physics Letters B*, 504(3):218–224, April 2001. doi: 10.1016/S0370-2693(01)00307-0.
- [24] B. M. Pontecorvo. Inverse β -processes and non-conservation of lepton charge. 7 1957. URL <https://www.osti.gov/biblio/4310840>.
- [25] R. Davis, D. S. Harmer, and K. C. Hoffman. Search for neutrinos from the sun. *Phys. Rev. Lett.*, 20:1205–1209, May 1968. doi: 10.1103/PhysRevLett.20.1205. URL <https://link.aps.org/doi/10.1103/PhysRevLett.20.1205>.
- [26] Q. R. Ahmad et al. Measurement of the rate of $\nu_e + d \rightarrow p + p + e^-$ interactions produced by 8b solar neutrinos at the sudbury neutrino observatory. *Phys. Rev. Lett.*, 87:071301, Jul 2001. doi: 10.1103/PhysRevLett.87.071301. URL <https://link.aps.org/doi/10.1103/PhysRevLett.87.071301>.
- [27] Z. Maki, M. Nakagawa, and S. Sakata. Remarks on the unified model of elementary particles. *Progress of Theoretical Physics*, 28(5):870–880, November 1962. doi: 10.1143/PTP.28.870.
- [28] E. Vitagliano, I. Tamborra, and G. Raffelt. Grand unified neutrino spectrum at earth: Sources and spectral components. *Reviews of Modern Physics*, 92(4):045006, October 2020. doi: 10.1103/RevModPhys.92.045006.
- [29] M. G. Aartsen et al. Observation of high-energy astrophysical neutrinos in three years of icecube data. *Phys. Rev. Lett.*, 113:101101, Sep 2014. doi: 10.1103/PhysRevLett.113.101101. URL <https://link.aps.org/doi/10.1103/PhysRevLett.113.101101>.
- [30] R. Abbasi et al. Detection of astrophysical tau neutrino candidates in icecube. *European Physical Journal C*, 82(11):1031, November 2022. doi: 10.1140/epjc/s10052-022-10795-y.
- [31] R. Naab et al. Measurement of the astrophysical diffuse neutrino flux in a combined fit of icecube’s high energy neutrino data. *PoS, ICRC2023:1064*, 2023. doi: 10.22323/1.444.1064.
- [32] R. Abbasi et al. Evidence for neutrino emission from the nearby active galaxy ngc 1068. *Science*, 378(6619):538–543, November 2022. doi: 10.1126/science.abg3395.
- [33] IceCube Collaboration. Observation of high-energy neutrinos from the galactic plane. *Science*, 380(6652):1338–1343, June 2023. doi: 10.1126/science.adc9818.
- [34] L. Ju, D.G. Blair, and C. Zhao. Detection of gravitational waves. *Reports on Progress in Physics*, 63(9):1317, sep 2000. doi: 10.1088/0034-4885/63/9/201. URL <https://dx.doi.org/10.1088/0034-4885/63/9/201>.
- [35] R. A. Hulse and J. H. Taylor. Discovery of a pulsar in a binary system. *ApJL*, 195:L51–L53, January 1975. doi: 10.1086/181708.
- [36] J. H. Taylor and J. M. Weisberg. Further experimental tests of relativistic gravity using the binary pulsar psr 1913+16. *ApJ*, 345:434, October 1989. doi: 10.1086/167917.
- [37] B. P. Abbott et al. Observation of gravitational waves from a binary black hole merger. *PRL*, 116(6):061102, February 2016. doi: 10.1103/PhysRevLett.116.061102.
- [38] G. Agazie et al. The nanograv 15 yr data set: Observations and timing of 68 millisecond pulsars. *The Astrophysical Journal Letters*, 951(1):L9, jun 2023. doi: 10.3847/2041-8213/acda9a. URL <https://dx.doi.org/10.3847/2041-8213/acda9a>.
- [39] N. Bar, K. Blum, and G. D’Amico. Is there a supernova bound on axions? *Phys. Rev. D*, 101:123025, Jun 2020. doi: 10.1103/PhysRevD.101.123025. URL <https://link.aps.org/doi/10.1103/PhysRevD.101.123025>.
- [40] I. J. Danziger et al. Optical spectroscopy of sn 1987a. *A&A*, 177:L13–L16, May 1987.
- [41] Ph. A. Pinto and S. E. Woosley. X-ray and gamma-ray emission from supernova 1987a. *ApJ*, 329:820, June 1988. doi: 10.1086/166426.
- [42] K. Hirata et al. Observation of a neutrino burst from the supernova sn1987a. *PRL*, 58(14):1490–1493, April 1987. doi: 10.1103/PhysRevLett.58.1490.

- [43] R. M. Bionta et al. Observation of a neutrino burst in coincidence with supernova 1987a in the large magellanic cloud. *PRL*, 58(14):1494–1496, April 1987. doi: 10.1103/PhysRevLett.58.1494.
- [44] E. N. Alekseev et al. Detection of the neutrino signal from supernova 1987a using the inr baksan underground scintillation telescope. In I. J. Danziger, editor, *European Southern Observatory Conference and Workshop Proceedings*, volume 26 of *European Southern Observatory Conference and Workshop Proceedings*, page 237, January 1987.
- [45] Ch.L. Fryer et al. Multimessenger diagnostics of the engine behind core-collapse supernovae. *ApJ*, 956(1):19, October 2023. doi: 10.3847/1538-4357/ace0c3.
- [46] D. F. G. Fiorillo et al. Supernova simulations confront sn 1987a neutrinos. *PRD*, 108(8):083040, October 2023. doi: 10.1103/PhysRevD.108.083040.
- [47] J. H. Chang, R. Essig, and S. D. McDermott. Supernova 1987a constraints on sub-gev dark sectors, millicharged particles, the qcd axion, and an axion-like particle. *Journal of High Energy Physics*, 2018(9):51, September 2018. doi: 10.1007/JHEP09(2018)051.
- [48] B. P. Abbott et al. Gravitational waves and gamma-rays from a binary neutron star merger: Gw170817 and grb 170817a. *The Astrophysical Journal Letters*, 848(2):L13, October 2017. ISSN 2041-8213. doi: 10.3847/2041-8213/aa920c. URL <http://dx.doi.org/10.3847/2041-8213/aa920c>.
- [49] B. P. Abbott et al. Multi-messenger observations of a binary neutron star merger. *The Astrophysical Journal Letters*, 848(2):L12, October 2017. ISSN 2041-8213. doi: 10.3847/2041-8213/aa91c9. URL <http://dx.doi.org/10.3847/2041-8213/aa91c9>.
- [50] E Troja, H van Eerten, G Ryan, R Ricci, J M Burgess, M H Wieringa, L Piro, S B Cenko, and T Sakamoto. A year in the life of gw170817: the rise and fall of a structured jet from a binary neutron star merger. *Monthly Notices of the Royal Astronomical Society*, August 2019. ISSN 1365-2966. doi: 10.1093/mnras/stz2248. URL <http://dx.doi.org/10.1093/mnras/stz2248>.
- [51] R. Margutti and R. Chornock. First multimessenger observations of a neutron star merger. *Annual Review of Astronomy and Astrophysics*, 59(1):155–202, September 2021. ISSN 1545-4282. doi: 10.1146/annurev-astro-112420-030742. URL <http://dx.doi.org/10.1146/annurev-astro-112420-030742>.
- [52] N. R. Tanvir et al. The emergence of a lanthanide-rich kilonova following the merger of two neutron stars. *The Astrophysical Journal Letters*, 848(2):L27, October 2017. ISSN 2041-8213. doi: 10.3847/2041-8213/aa90b6. URL <http://dx.doi.org/10.3847/2041-8213/aa90b6>.
- [53] M. Aartsen et al. Neutrino emission from the direction of the blazar txs 0506+056 prior to the iccube-170922a alert. *Science*, 361(6398):147–151, July 2018. ISSN 1095-9203. doi: 10.1126/science.aat2890. URL <http://dx.doi.org/10.1126/science.aat2890>.
- [54] M. Aartsen et al. Neutrino emission from the direction of the blazar txs 0506+056 prior to the iccube-170922a alert. *Science*, 361(6398):147–151, July 2018. ISSN 1095-9203. doi: 10.1126/science.aat2890. URL <http://dx.doi.org/10.1126/science.aat2890>.
- [55] R. Stein et al. A tidal disruption event coincident with a high-energy neutrino. *Nature Astronomy*, 5(5):510–518, February 2021. ISSN 2397-3366. doi: 10.1038/s41550-020-01295-8. URL <http://dx.doi.org/10.1038/s41550-020-01295-8>.
- [56] K. Hayasaki. Neutrinos from tidal disruption events. *Nature Astronomy*, 5(5):436–437, February 2021. ISSN 2397-3366. doi: 10.1038/s41550-021-01309-z. URL <http://dx.doi.org/10.1038/s41550-021-01309-z>.
- [57] W. Winter and C. Lunardini. Interpretation of the observed neutrino emission from three tidal disruption events. *The Astrophysical Journal*, 948(1):42, May 2023. ISSN 1538-4357. doi: 10.3847/1538-4357/acbe9e. URL <http://dx.doi.org/10.3847/1538-4357/acbe9e>.
- [58] S. Reusch et al. Candidate tidal disruption event at2019fdr coincident with a high-energy neutrino. *Physical Review Letters*, 128(22), June 2022. ISSN 1079-7114. doi: 10.1103/physrevlett.128.221101. URL <http://dx.doi.org/10.1103/PhysRevLett.128.221101>.
- [59] S. van Velzen et al. Establishing accretion flares from supermassive black holes as a source of high-energy neutrinos. *Monthly Notices of the Royal Astronomical Society*, 529(3):2559–2576, February 2024. ISSN 1365-2966. doi: 10.1093/mnras/stae610. URL <http://dx.doi.org/10.1093/mnras/stae610>.
- [60] Y. Inoue, D. Khangulyan, and A. Doi. On the origin of high-energy neutrinos from ngc 1068: The role of nonthermal coronal activity. *Astrophys. J. Lett.*, 891(2):L33, 2020. doi: 10.3847/2041-8213/ab7661.
- [61] B. Eichmann et al. Solving the multimessenger puzzle of the agn-starburst composite galaxy ngc 1068. *Astrophys. J.*, 939(1):43, 2022. doi: 10.3847/1538-4357/ac9588.

- [62] E. Peretti et al. Diffusive shock acceleration at eev and associated multimessenger flux from ultra-fast outflows driven by active galactic nuclei, 2023. URL <https://arxiv.org/abs/2301.13689>.
- [63] K. Yasuda, Y. Inoue, and A. Kusenko. Neutrinos and gamma rays from beta decays in an active galactic nucleus ngc 1068 jet, 2024. URL <https://arxiv.org/abs/2405.05247>.
- [64] M. Amenomori et al. First detection of sub-pev diffuse gamma rays from the galactic disk: Evidence for ubiquitous galactic cosmic rays beyond pev energies. *Phys. Rev. Lett.*, 126:141101, Apr 2021. doi: 10.1103/PhysRevLett.126.141101. URL <https://link.aps.org/doi/10.1103/PhysRevLett.126.141101>.
- [65] Z. Cao et al. Measurement of ultra-high-energy diffuse gamma-ray emission of the galactic plane from 10 tev to 1 pev with lhaaso-km2a. *Phys. Rev. Lett.*, 131:151001, Oct 2023. doi: 10.1103/PhysRevLett.131.151001. URL <https://link.aps.org/doi/10.1103/PhysRevLett.131.151001>.
- [66] K. Fang and K. Murase. Decomposing the origin of tev-pev emission from the galactic plane: Implications of multimessenger observations. *The Astrophysical Journal Letters*, 957(1):L6, October 2023. ISSN 2041-8213. doi: 10.3847/2041-8213/ad012f. URL <http://dx.doi.org/10.3847/2041-8213/ad012f>.
- [67] C. K. Seyfert. Nuclear emission in spiral nebulae. *ApJ*, 97:28, January 1943. doi: 10.1086/144488.
- [68] E. E. Salpeter. Accretion of interstellar matter by massive objects. *ApJ*, 140:796–800, August 1964. doi: 10.1086/147973.
- [69] Ya B Zel'dovich and Igor D Novikov. Relativistic astrophysics. i. *Soviet Physics Uspekhi*, 7(6): 763, jun 1965. doi: 10.1070/PU1965v007n06ABEH003683. URL <https://dx.doi.org/10.1070/PU1965v007n06ABEH003683>.
- [70] N. I. Shakura and R. A. Sunyaev. Black holes in binary systems. observational appearance. *A&A*, 24: 337–355, January 1973.
- [71] Ryan C. Hickox and David M. Alexander. Obscured active galactic nuclei. *Annual Review of Astronomy and Astrophysics*, 56(Volume 56, 2018):625–671, 2018. ISSN 1545-4282. doi: <https://doi.org/10.1146/annurev-astro-081817-051803>. URL <https://www.annualreviews.org/content/journals/10.1146/annurev-astro-081817-051803>.
- [72] R. D. Blandford and R. L. Znajek. Electromagnetic extraction of energy from kerr black holes. *Monthly Notices of the Royal Astronomical Society*, 179(3):433–456, 07 1977. ISSN 0035-8711. doi: 10.1093/mnras/179.3.433. URL <https://doi.org/10.1093/mnras/179.3.433>.
- [73] R. D. Blandford and D. G. Payne. Hydromagnetic flows from accretion disks and the production of radio jets. *MNRAS*, 199:883–903, June 1982. doi: 10.1093/mnras/199.4.883.
- [74] A. A. Zdziarski, A. C. Fabian, K. Nandra, A. Celotti, M. J. Rees, C. Done, P. S. Coppi, and G. M. Madejski. Physical processes in the x-ray / gamma-ray source of ic 4329a. *Monthly Notices of the Royal Astronomical Society*, 269(1):L55–L60, 07 1994. ISSN 0035-8711. doi: 10.1093/mnras/269.1.L55. URL <https://doi.org/10.1093/mnras/269.1.L55>.
- [75] E. Kara, W. N. Alston, A. C. Fabian, E. M. Cackett, P. Uttley, C. S. Reynolds, and A. Zoghbi. A global look at x-ray time lags in seyfert galaxies. *Monthly Notices of the Royal Astronomical Society*, 462(1): 511–531, 07 2016. ISSN 0035-8711. doi: 10.1093/mnras/stw1695. URL <https://doi.org/10.1093/mnras/stw1695>.
- [76] C. Megan Urry and Paolo Padovani. Unified schemes for radio-loud active galactic nuclei. *Publications of the Astronomical Society of the Pacific*, 107(715):803, sep 1995. doi: 10.1086/133630. URL <https://dx.doi.org/10.1086/133630>.
- [77] Volker Beckmann and Chris R. Shrader. *Active Galactic Nuclei*. 2012.
- [78] P. Padovani, D. M. Alexander, R. J. Assef, B. De Marco, P. Giommi, R. C. Hickox, G. T. Richards, V. Smolčić, E. Hatziminaoglou, V. Mainieri, and M. Salvato. Active galactic nuclei: what's in a name? *AAR*, 25(1):2, August 2017. doi: 10.1007/s00159-017-0102-9.
- [79] H. A. Peña-Herazo, F. Massaro, V. Chavushyan, N. Masetti, A. Paggi, and A. Capetti. Turin-sycat: A multifrequency catalog of seyfert galaxies. *A&A*, 659:A32, March 2022. doi: 10.1051/0004-6361/202038752.
- [80] S. Ridgway, T. Heckman, D. Calzetti, and M. Lehnert. "hst nicmos imaging of z~2–3 radio-quiet quasars". *New Astronomy Reviews*, 46(2):175–180, 2002. ISSN 1387-6473. doi: [https://doi.org/10.1016/S1387-6473\(01\)00175-0](https://doi.org/10.1016/S1387-6473(01)00175-0). URL <https://www.sciencedirect.com/science/article/pii/S1387647301001750>. Lifecycles of radio galaxies.
- [81] L. Jiang et al. The radio-loud fraction of quasars is a strong function of redshift and optical luminosity. *ApJ*, 656(2):680–690, February 2007. doi: 10.1086/510831.

- [82] G. Ghisellini, F. Tavecchio, L. Maraschi, A. Celotti, and T. Sbarrato. The power of relativistic jets is larger than the luminosity of their accretion disks. *Nature*, 515(7527):376–378, November 2014. doi: 10.1038/nature13856.
- [83] M. Chiaberge, R. Gilli, J. M. Lotz, and C. Norman. Radio loud agns are mergers. *ApJ*, 806(2):147, June 2015. doi: 10.1088/0004-637X/806/2/147.
- [84] Steven Ndung’u, Trienko Grobler, Stefan J. Wijnholds, Dimka Karastoyanova, and George Azzopardi. Advances on the morphological classification of radio galaxies: A review. *New Astronomy Reviews*, 97: 101685, 2023. ISSN 1387-6473. doi: <https://doi.org/10.1016/j.newar.2023.101685>. URL <https://www.sciencedirect.com/science/article/pii/S1387647323000131>.
- [85] F. Wang et al. A luminous quasar at redshift 7.642. *The Astrophysical Journal Letters*, 907(1):L1, 2021.
- [86] PA Strittmatter, K Serkowski, R Carswell, WA Stein, KM Merrill, and EM Burbidge. Compact extragalactic nonthermal sources. *Astrophysical Journal*, vol. 175, p. L7, 175:L7, 1972.
- [87] WA Stein, SL O’dell, and PA Strittmatter. The bl lacertae objects. In: *Annual review of astronomy and astrophysics. Volume 14.(A76-46826 24-90) Palo Alto, Calif., Annual Reviews, Inc., 1976, p. 173-195.*, 14: 173–195, 1976.
- [88] G. Ghisellini, F. Tavecchio, L. Foschini, and G. Ghirlanda. The transition between bl lac objects and flat spectrum radio quasars. *Monthly Notices of the Royal Astronomical Society*, 414(3):2674–2689, 06 2011. ISSN 0035-8711. doi: 10.1111/j.1365-2966.2011.18578.x. URL <https://doi.org/10.1111/j.1365-2966.2011.18578.x>.
- [89] G. Ghisellini. *Radiative Processes in High Energy Astrophysics*. Springer International Publishing, 2013. ISBN 9783319006123. doi: 10.1007/978-3-319-00612-3. URL <http://dx.doi.org/10.1007/978-3-319-00612-3>.
- [90] M. Böttcher, D. Harris, and H. Krawczynski. *Special Relativity of Jets*, chapter 2, pages 17–38. John Wiley & Sons, Ltd, 2012. ISBN 9783527641741. doi: <https://doi.org/10.1002/9783527641741.ch2>. URL <https://onlinelibrary.wiley.com/doi/abs/10.1002/9783527641741.ch2>.
- [91] Aharonian et al. An exceptional very high energy gamma-ray flare of pks 2155-304. *ApJL*, 664(2): L71–L74, August 2007. doi: 10.1086/520635.
- [92] Albert et al. Variable very high energy γ -ray emission from markarian 501. *ApJ*, 669(2):862–883, November 2007. doi: 10.1086/521382.
- [93] A. P. Marscher and W. K. Gear. Models for high-frequency radio outbursts in extragalactic sources, with application to the early 1983 millimeter-to-infrared flare of 3c 273. *ApJ*, 298:114–127, November 1985. doi: 10.1086/163592.
- [94] J. J. P. Virtanen and R. Vainio. Particle acceleration in thick parallel shocks with high compression ratio. *A&A*, 439(2):461–464, August 2005. doi: 10.1051/0004-6361:20053349.
- [95] Dimitrios Giannios, Dmitri A. Uzdensky, and Mitchell C. Begelman. Fast tev variability in blazars: jets in a jet. *MNRAS*, 395(1):L29–L33, May 2009. doi: 10.1111/j.1745-3933.2009.00635.x.
- [96] Stephanie Blondin, Tamara M Davis, Kevin Krisciunas, Brian P Schmidt, J Sollerman, WM Wood-Vasey, AC Becker, P Challis, A Clocchiatti, G Damke, et al. Time dilation in type ia supernova spectra at high redshift. *The Astrophysical Journal*, 682(2):724, 2008.
- [97] Abdo et al. Fermi large area telescope observations of markarian 421. *ApJ*, 736(2):131, August 2011. doi: 10.1088/0004-637X/736/2/131.
- [98] H. Alfvén and N. Herlofson. Cosmic radiation and radio stars. *Physical Review*, 78(5):616–616, June 1950. doi: 10.1103/PhysRev.78.616.
- [99] I. S. Shklovsky. Optical emission from the crab nebula in the continuous spectrum. *Symposium - International Astronomical Union*, 6:520–528, 1958. doi: 10.1017/S0074180900238102.
- [100] W. Baade. Polarization in the jet of messier 87. *ApJ*, 123:550–551, May 1956. doi: 10.1086/146194.
- [101] G. Fossati, L. Maraschi, A. Celotti, A. Comastri, and G. Ghisellini. A unifying view of the spectral energy distributions of blazars. *MNRAS*, 299(2):433–448, September 1998. doi: 10.1046/j.1365-8711.1998.01828.x.
- [102] G. Ghisellini, C. Righi, L. Costamante, and F. Tavecchio. The fermi blazar sequence. *Monthly Notices of the Royal Astronomical Society*, 469(1):255–266, 04 2017. ISSN 0035-8711. doi: 10.1093/mnras/stx806. URL <https://doi.org/10.1093/mnras/stx806>.
- [103] A. A. Abdo et al. The spectral energy distribution of fermi bright blazars. *ApJ*, 716(1):30–70, June 2010. doi: 10.1088/0004-637X/716/1/30.
- [104] G. Ghisellini. The blazar sequence 2.0. *Galaxies*, 4(4):36, September 2016. doi: 10.3390/galaxies4040036.
- [105] Ch. Dermer and G. Menon. *High Energy Radiation From Black Holes: Gamma Rays, Cosmic Rays, and Neutrinos*. Princeton University Press, 2009.

- [106] Eli Dwek and Frank Krennrich. The extragalactic background light and the gamma-ray opacity of the universe. *Astroparticle Physics*, 43:112–133, March 2013. doi: 10.1016/j.astropartphys.2012.09.003.
- [107] L. Morejon, A. Fedynitch, D. Boncioli, D. Biehl, and W. Winter. Improved photomeson model for interactions of cosmic ray nuclei. *JCAP*, 2019(11):007, November 2019. doi: 10.1088/1475-7516/2019/11/007.
- [108] S. R. Kelner and F. A. Aharonian. Energy spectra of gamma rays, electrons, and neutrinos produced at interactions of relativistic protons with low energy radiation. *PRD*, 78(3):034013, August 2008. doi: 10.1103/PhysRevD.78.034013.
- [109] X. Rodrigues et al. Neutrinos and ultra-high-energy cosmic-ray nuclei from blazars. *ApJ*, 854(1):54, February 2018. doi: 10.3847/1538-4357/aaa7ee.
- [110] L. Maraschi, G. Ghisellini, and A. Celotti. A jet model for the gamma-ray-emitting blazar 3c 279. *ApJL*, 397:L5, September 1992. doi: 10.1086/186531.
- [111] Charles D. Dermer and Reinhard Schlickeiser. Model for the high-energy emission from blazars. *ApJ*, 416:458, October 1993. doi: 10.1086/173251.
- [112] Marek Sikora, Mitchell C. Begelman, and Martin J. Rees. Comptonization of diffuse ambient radiation by a relativistic jet: The source of gamma rays from blazars? *ApJ*, 421:153, January 1994. doi: 10.1086/173633.
- [113] Steven D. Bloom and Alan P. Marscher. An analysis of the synchrotron self-compton model for the multi-wave band spectra of blazars. *ApJ*, 461:657, April 1996. doi: 10.1086/177092.
- [114] G. Ghisellini and F. Tavecchio. Canonical high-power blazars. *Monthly Notices of the Royal Astronomical Society*, 397(2):985–1002, 07 2009. ISSN 0035-8711. doi: 10.1111/j.1365-2966.2009.15007.x. URL <https://doi.org/10.1111/j.1365-2966.2009.15007.x>.
- [115] M. Böttcher, A. Reimer, and A. P. Marscher. Implications of the very high energy gamma-ray detection of the quasar 3c279. *The Astrophysical Journal*, 703(1):1168, sep 2009. doi: 10.1088/0004-637X/703/1/1168. URL <https://dx.doi.org/10.1088/0004-637X/703/1/1168>.
- [116] F.A. Aharonian. Tev gamma rays from bl lac objects due to synchrotron radiation of extremely high energy protons. *New Astronomy*, 5(7):377–395, November 2000. ISSN 1384-1076. doi: 10.1016/S1384-1076(00)00039-7. URL [http://dx.doi.org/10.1016/S1384-1076\(00\)00039-7](http://dx.doi.org/10.1016/S1384-1076(00)00039-7).
- [117] A. Mücke, R.J. Protheroe, R. Engel, J.P. Rachen, and T. Stanev. Bl lac objects in the synchrotron proton blazar model. *Astroparticle Physics*, 18(6):593–613, March 2003. ISSN 0927-6505. doi: 10.1016/S0927-6505(02)00185-8. URL [http://dx.doi.org/10.1016/S0927-6505\(02\)00185-8](http://dx.doi.org/10.1016/S0927-6505(02)00185-8).
- [118] I. Liodakis and M. Petropoulou. Proton synchrotron gamma-rays and the energy crisis in blazars. *The Astrophysical Journal Letters*, 893(1):L20, apr 2020. doi: 10.3847/2041-8213/ab830a. URL <https://dx.doi.org/10.3847/2041-8213/ab830a>.
- [119] A. A. Zdziarski and M. Böttcher. Hadronic models of blazars require a change of the accretion paradigm. *Monthly Notices of the Royal Astronomical Society: Letters*, 450(1):L21–L25, 04 2015. ISSN 1745-3925. doi: 10.1093/mnras/50.1/1. URL <https://doi.org/10.1093/mnras/50.1/1>.
- [120] Joanne M Attridge, David H Roberts, and John FC Wardle. Radio jet-ambient medium interactions on parsec scales in the blazar 1055+018. *The Astrophysical Journal*, 518(2):L87, 1999.
- [121] M. Giroletti and G. others. Parsec-scale properties of markarian 501. *The Astrophysical Journal*, 600(1):127, jan 2004. doi: 10.1086/379663. URL <https://dx.doi.org/10.1086/379663>.
- [122] F. Tavecchio and G. Ghisellini. On the magnetization of bl lac jets. *Monthly Notices of the Royal Astronomical Society*, 456(3):2374–2382, 12 2015. ISSN 0035-8711. doi: 10.1093/mnras/stv2790. URL <https://doi.org/10.1093/mnras/stv2790>.
- [123] Marek Sikora, Mieszko Rutkowski, and Mitchell C. Begelman. A spine-sheath model for strong-line blazars. *Monthly Notices of the Royal Astronomical Society*, 457(2):1352–1358, February 2016. ISSN 1365-2966. doi: 10.1093/mnras/stw107. URL <http://dx.doi.org/10.1093/mnras/stw107>.
- [124] V. A. Acciari et al. Testing two-component models on very high-energy gamma-ray-emitting bl lac objects. *A&A*, 640:A132, August 2020. ISSN 1432-0746. doi: 10.1051/0004-6361/202037811. URL <http://dx.doi.org/10.1051/0004-6361/202037811>.
- [125] H. Abdalla et al. Resolving acceleration to very high energies along the jet of centaurus a. *Nature*, 582(7812):356–359, June 2020. ISSN 1476-4687. doi: 10.1038/s41586-020-2354-1. URL <http://dx.doi.org/10.1038/s41586-020-2354-1>.
- [126] William J. Potter and Garret Cotter. Synchrotron and inverse-compton emission from blazar jets – i. a uniform conical jet model. *Monthly Notices of the Royal Astronomical Society*, 423(1):756–765, 05 2012. ISSN 0035-8711. doi: 10.1111/j.1365-2966.2012.20918.x. URL <https://doi.org/10.1111/j.1365-2966.2012.20918.x>.

- [127] M Zacharias, A Reimer, C Boisson, and A Zech. Exhale-jet: an extended hadro-leptonic jet model for blazars – i. code description and initial results. *Monthly Notices of the Royal Astronomical Society*, 512(3):3948–3971, March 2022. ISSN 1365-2966. doi: 10.1093/mnras/stac754. URL <http://dx.doi.org/10.1093/mnras/stac754>.
- [128] Alan P. Marscher. Turbulent, extreme multi-zone model for simulating flux and polarization variability in blazars. *The Astrophysical Journal*, 780(1):87, December 2013. ISSN 1538-4357. doi: 10.1088/0004-637x/780/1/87. URL <http://dx.doi.org/10.1088/0004-637x/780/1/87>.
- [129] M. Klinger et al. Am³: An open-source tool for time-dependent lepto-hadronic modeling of astrophysical sources. *ApJS*, 275(1):4, November 2024. doi: 10.3847/1538-4365/ad725c.
- [130] Mattia Di Mauro, Alessandro Cuoco, Fiorenza Donato, and Jennifer M. Siegal-Gaskins. Fermi-lat γ -ray anisotropy and intensity explained by unresolved radio-loud active galactic nuclei. *JCAP*, 2014(11):021–021, November 2014. doi: 10.1088/1475-7516/2014/11/021.
- [131] M. Ajello, D. Gasparrini, M. Sánchez-Conde, G. Zaharijas, M. Gustafsson, J. Cohen-Tanugi, C. D. Dermer, Y. Inoue, D. Hartmann, M. Ackermann, K. Bechtol, A. Franckowiak, A. Reimer, R. W. Romani, and A. W. Strong. The origin of the extragalactic gamma-ray background and implications for dark matter annihilation. *ApJL*, 800(2):L27, February 2015. doi: 10.1088/2041-8205/800/2/L27.
- [132] D. Bose, V. R. Chitnis, P. Majumdar, and A. Shukla. Galactic and extragalactic sources of very high energy gamma rays. *European Physical Journal Special Topics*, 231(1):27–66, January 2022. doi: 10.1140/epjs/s11734-022-00434-8.
- [133] M. Böttcher et al. Leptonic and hadronic modeling of fermi-detected blazars. *The Astrophysical Journal*, 768(1):54, apr 2013. doi: 10.1088/0004-637X/768/1/54. URL <https://dx.doi.org/10.1088/0004-637X/768/1/54>.
- [134] G. Ghisellini et al. The power of relativistic jets is larger than the luminosity of their accretion disks. *Nature*, 515(7527):376–378, November 2014. ISSN 1476-4687. doi: 10.1038/nature13856. URL <http://dx.doi.org/10.1038/nature13856>.
- [135] Shan Gao, Anatoli Fedynitch, Walter Winter, and Martin Pohl. "modelling the coincident observation of a high-energy neutrino and a bright blazar flare". *Nature Astronomy*, 3(1):88–92, November 2018. ISSN 2397-3366. doi: 10.1038/s41550-018-0610-1. URL <http://dx.doi.org/10.1038/s41550-018-0610-1>.
- [136] M Cerruti, A Zech, C Boisson, G Emery, S Inoue, and J-P Lenain. Leptohadronic single-zone models for the electromagnetic and neutrino emission of txs 0506+056. *Monthly Notices of the Royal Astronomical Society: Letters*, 483(1):L12–L16, November 2018. ISSN 1745-3933. doi: 10.1093/mnrasl/sly210. URL <http://dx.doi.org/10.1093/mnrasl/sly210>.
- [137] A. Keivani et al. A multimessenger picture of the flaring blazar txs 0506+056: Implications for high-energy neutrino emission and cosmic-ray acceleration. *The Astrophysical Journal*, 864(1):84, August 2018. ISSN 1538-4357. doi: 10.3847/1538-4357/aad59a. URL <http://dx.doi.org/10.3847/1538-4357/aad59a>.
- [138] X. Rodrigues et al. Leptohadronic blazar models applied to the 2014–2015 flare of txs 0506+056. *The Astrophysical Journal*, 874(2):L29, April 2019. ISSN 2041-8213. doi: 10.3847/2041-8213/ab1267. URL <http://dx.doi.org/10.3847/2041-8213/ab1267>.
- [139] M. Petropoulou et al. Multi-epoch modeling of txs 0506+056 and implications for long-term high-energy neutrino emission. *The Astrophysical Journal*, 891(2):115, March 2020. ISSN 1538-4357. doi: 10.3847/1538-4357/ab76d0. URL <http://dx.doi.org/10.3847/1538-4357/ab76d0>.
- [140] X. Rodrigues et al. Multiwavelength and neutrino emission from blazar pks 1502 + 106. *The Astrophysical Journal*, 912(1):54, may 2021. doi: 10.3847/1538-4357/abe87b. URL <https://dx.doi.org/10.3847/1538-4357/abe87b>.
- [141] F. Oikonomou et al. Multi-messenger emission from the parsec-scale jet of the flat-spectrum radio quasar pks 1502+106 coincident with high-energy neutrino icecube-190730a. *Journal of Cosmology and Astroparticle Physics*, 2021(10):082, October 2021. ISSN 1475-7516. doi: 10.1088/1475-7516/2021/10/082. URL <http://dx.doi.org/10.1088/1475-7516/2021/10/082>.
- [142] Sh. Gao, M. Pohl, and W. Winter. On the direct correlation between gamma-rays and pev neutrinos from blazars. *The Astrophysical Journal*, 843(2):109, July 2017. ISSN 1538-4357. doi: 10.3847/1538-4357/aa7754. URL <http://dx.doi.org/10.3847/1538-4357/aa7754>.
- [143] Maria Petropoulou, Foteini Oikonomou, Apostolos Mastichiadis, Kohta Murase, Paolo Padovani, Georgios Vasilopoulos, and Paolo Giommi. Comprehensive multimessenger modeling of the extreme blazar 3hsp j095507.9+355101 and predictions for icecube. *The Astrophysical Journal*, 899(2):113, August 2020.

- ISSN 1538-4357. doi: 10.3847/1538-4357/aba8a0. URL <http://dx.doi.org/10.3847/1538-4357/aba8a0>.
- [144] Ze-Rui Wang and Rui Xue. Hadronuclear interpretation of the possible neutrino emission from pks b1424-418, gb6 j1040+0617 and pks 1502+106. *Res. Astron. Astrophys.*, 21(12):305, 2021. doi: 10.1088/1674-4527/21/12/305.
- [145] A. Omeliukh et al. Multi-epoch leptohadronic modeling of neutrino source candidate blazar PKS 0735+178. *A&A*, 695:A266, March 2025. doi: 10.1051/0004-6361/202452143.
- [146] S. Abe et al. Time-dependent modelling of short-term variability in the tev-blazar ver j0521+211 during the major flare in 2020, 2024. URL <https://arxiv.org/abs/2412.15836>.
- [147] A. Omeliukh, S. Barnier, and Y. Inoue. On the possible contributions of two nearby blazars to the ngc 4151 neutrino hotspot, February 2025.
- [148] IceCube Collaboration. Icecube-211208a - icecube observation of a high-energy neutrino candidate track-like event. *GRB Coordinates Network*, 31191:1, December 2021.
- [149] Zh. A. Dzilkibaev, O. Suvorova, and Baikal-GVD Collaboration. Baikal-gvd observation of a high-energy neutrino candidate event from the blazar pks 0735+17 at the day of the icecube-211208a neutrino alert from the same direction. *The Astronomer's Telegram*, 15112:1, December 2021.
- [150] V. B. Petkov, Yu. F. Novoseltsev, R. V. Novoseltseva, and Baksan Underground Scintillation Telescope Group. Baksan underground scintillation telescope observation of a gev neutrino candidate event at the time of a gamma-ray flare of the blazar pks 0735+17, a possible source of coinciding icecube and baikal high-energy neutrinos. *The Astronomer's Telegram*, 15143:1, December 2021.
- [151] F. Filippini, G. Illuminati, A. Heijboer, C. Gatius, R. Muller, D. Dornic, F. Huang, S. Le Stum, J. Palacios González, S. Celli, A. Zegarelli, R. Coniglione, D. Samtleben, Y. Y. Kovalev, and A. Plavin. Search for neutrino counterpart to the blazar pks0735+178 potentially associated with icecube-211208a and baikal-gvd-211208a with the km3net neutrino detectors. *The Astronomer's Telegram*, 15290:1, March 2022.
- [152] R. F. Carswell, P. A. Strittmatter, R. E. Williams, T. D. Kinman, and K. Serkowski. Optical observations of the radio source 0735+178. *ApJL*, 190:L101, June 1974. doi: 10.1086/181516.
- [153] K. Nilsson, T. Pursimo, C. Villforth, E. Lindfors, L. O. Takalo, and A. Sillanpää. Redshift constraints for RGB 0136+391 and PKS 0735+178 from deep optical imaging. *Astronomy & Astrophysics*, 547:A1, oct 2012. doi: 10.1051/0004-6361/201219848. URL <https://doi.org/10.1051%2F0004-6361%2F201219848>.
- [154] M.G. Aartsen et al. The IceCube realtime alert system. *Astroparticle Physics*, 92:30–41, jun 2017. doi: 10.1016/j.astropartphys.2017.05.002. URL <https://doi.org/10.1016%2Fj.astropartphys.2017.05.002>.
- [155] N. Sahakyan et al. A multimessenger study of the blazar pks 0735+178: a new major neutrino source candidate. *Monthly Notices of the Royal Astronomical Society*, 519(1):1396–1408, 12 2022. ISSN 0035-8711. doi: 10.1093/mnras/stac3607. URL <https://doi.org/10.1093/mnras/stac3607>.
- [156] S. Garrappa, S. Buson, J. Sinapius, A. Franckowiak, I. Liodakis, C. Bartolini, M. Giroletti, C. Nanci, G. Principe, and T. M. Venters. *fermi*-lat follow-up observations in seven years of realtime high-energy neutrino alerts. *arXiv e-prints*, art. arXiv:2401.06666, January 2024. doi: 10.48550/arXiv.2401.06666.
- [157] A. Acharyya et al. Multiwavelength observations of the blazar pks 0735+178 in spatial and temporal coincidence with an astrophysical neutrino candidate icecube-211208a. *ApJ*, 954(1):70, September 2023. doi: 10.3847/1538-4357/ace327.
- [158] D. N. Burrows et al. The swift x-ray telescope. In K. A. Flanagan and O. H. W. Siegmund, editors, *X-Ray and Gamma-Ray Instrumentation for Astronomy XIII*, volume 5165 of *Proc. SPIE Conf.*, pages 201–216, February 2004. doi: 10.1117/12.504868.
- [159] Peter W. A. Roming et al. The swift ultra-violet/optical telescope. *SSR*, 120(3-4):95–142, October 2005. doi: 10.1007/s11214-005-5095-4.
- [160] A. V. Filippenko, W. D. Li, R. R. Treffers, and M. Modjaz. The lick observatory supernova search with the katzman automatic imaging telescope. In Bohdan Paczynski, Wen-Ping Chen, and Claudia Lemme, editors, *IAU Colloq. 183: Small Telescope Astronomy on Global Scales*, volume 246 of *Astronomical Society of the Pacific Conference Series*, page 121, January 2001.
- [161] W. Li, A. V. Filippenko, R. Chornock, and S. Jha. The katzman automatic imaging telescope gamma-ray burst alert system, and observations of grb 020813. *Publications of the Astronomical Society of the Pacific*, 115(809):844, may 2003. doi: 10.1086/376432. URL <https://dx.doi.org/10.1086/376432>.
- [162] E. Lindfors et al. Optical and near-infrared observations of pks 0735+178. *The Astronomer's Telegram*, 15136:1, December 2021.

- [163] L. Carrasco, E. Recillas, G. Escobedo, A. Porras, V. Chavushyan, and Y. D. Mayya. Nir followup of the blazar pks 0735+178. *The Astronomer's Telegram*, 15148:1, December 2021.
- [164] Edward F. Schlafly and Douglas P. Finkbeiner. Measuring reddening with sloan digital sky survey stellar spectra and recalibrating sfd. *ApJ*, 737(2):103, August 2011. doi: 10.1088/0004-637X/737/2/103.
- [165] K. Nilsson, T. Pursimo, C. Villforth, E. Lindfors, L. O. Takalo, and A. Sillanpää. Redshift constraints for rgb 0136+391 and pks 0735+178 from deep optical imaging. *A&A*, 547:A1, November 2012. doi: 10.1051/0004-6361/201219848.
- [166] H. Teräsranta et al. Fifteen years monitoring of extragalactic radio sources at 22, 37 and 87 ghz. *A&A*, 132:305–331, November 1998. doi: 10.1051/aas:1998297.
- [167] M. L. Lister, M. F. Aller, H. D. Aller, M. A. Hodge, D. C. Homan, Y. Y. Kovalev, A. B. Pushkarev, and T. Savolainen. Mojave. xv. vlba 15 ghz total intensity and polarization maps of 437 parsec-scale agn jets from 1996 to 2017. *ApJS*, 234(1):12, January 2018. doi: 10.3847/1538-4365/aa9c44.
- [168] A. Domínguez et al. Extragalactic background light inferred from aegis galaxy-sed-type fractions. *MNRAS*, 410(4):2556–2578, February 2011. doi: 10.1111/j.1365-2966.2010.17631.x.
- [169] F. James and M. Roos. Minuit - a system for function minimization and analysis of the parameter errors and correlations. *Computer Physics Communications*, 10(6):343–367, December 1975. doi: 10.1016/0010-4655(75)90039-9.
- [170] H. Dembinski et al. scikit-hep/iminuit. Dec 2020. doi: 10.5281/zenodo.3949207. URL <https://doi.org/10.5281/zenodo.3949207>.
- [171] X. Rodrigues, V. S. Paliya, S. Garrappa, A. Omeliukh, A. Franckowiak, and W. Winter. Leptohadronic multi-messenger modeling of 324 gamma-ray blazars. *Astronomy & Astrophysics*, 681:A119, January 2024. ISSN 1432-0746. doi: 10.1051/0004-6361/202347540. URL <http://dx.doi.org/10.1051/0004-6361/202347540>.
- [172] X. Rodrigues et al. The spectra of icecube neutrino (sin) candidate sources – v. modeling and interpretation of multiwavelength and neutrino data. *arXiv e-prints*, art. arXiv:2406.06667, June 2024. doi: 10.48550/arXiv.2406.06667.
- [173] M. Cerruti, A. Zech, C. Boisson, G. Emery, S. Inoue, and J. P. Lenain. Leptohadronic single-zone models for the electromagnetic and neutrino emission of txs 0506+056. *MNRAS*, 483(1):L12–L16, February 2019. doi: 10.1093/mnrasl/sly210.
- [174] M. G. Aartsen et al. All-sky search for time-integrated neutrino emission from astrophysical sources with 7 yr of icecube data. *The Astrophysical Journal*, 835(2):151, February 2017. doi: 10.3847/1538-4357/835/2/151.
- [175] G. Fichet de Clairfontaine et al. Hadronic processes at work in 5bzb j0630-2406. *ApJL*, 958(1):L2, November 2023. doi: 10.3847/2041-8213/ad0644.
- [176] M. G. Aartsen et al. Search for steady point-like sources in the astrophysical muon neutrino flux with 8 years of icecube data. *European Physical Journal C*, 79(3):234, March 2019. doi: 10.1140/epjc/s10052-019-6680-0.
- [177] M. G. Aartsen et al. Time-integrated neutrino source searches with 10 years of icecube data. *Phys. Rev. Lett.*, 124:051103, Feb 2020. doi: 10.1103/PhysRevLett.124.051103. URL <https://link.aps.org/doi/10.1103/PhysRevLett.124.051103>.
- [178] N. L. Strotjohann, M. Kowalski, and A. Franckowiak. Eddington bias for cosmic neutrino sources. *A&A*, 622:L9, February 2019. doi: 10.1051/0004-6361/201834750.
- [179] Sargis Gasparyan, Damien Bégué, and Narek Sahakyan. Time-dependent lepto-hadronic modelling of the emission from blazar jets with soprano: the case of txs 0506+ 056, 3hsp j095507.9+ 355101, and 3c 279. *Monthly Notices of the Royal Astronomical Society*, 509(2):2102–2121, 2022.
- [180] M. Petropoulou et al. Comprehensive multimessenger modeling of the extreme blazar 3hsp j095507.9+355101 and predictions for icecube. *ApJ*, 899(2):113, August 2020. doi: 10.3847/1538-4357/aba8a0.
- [181] S.P. Gupta, U.S. Pandey, K. Singh, B. Rani, J. Pan, J.H. Fan, and A.C. Gupta. Optical intra-day variability timescales and black hole mass of the blazars. *New Astronomy*, 17(1):8–17, 2012. ISSN 1384-1076. doi: <https://doi.org/10.1016/j.newast.2011.05.005>. URL <https://www.sciencedirect.com/science/article/pii/S1384107611000571>.
- [182] S. Britzen, A. Witzel, B. P. Gong, J. W. Zhang, Gopal-Krishna, A. Goyal, M. F. Aller, H. D. Aller, and J. A. Zensus. Understanding bl lacertae objects. structural and kinematic mode changes in the bl lac object pks 0735+178. *A&A*, 515:A105, June 2010. doi: 10.1051/0004-6361/200913685.
- [183] M. G. Aartsen et al. Icecube-gen2: the window to the extreme universe. *Journal of Physics G Nuclear Physics*, 48(6):060501, June 2021. doi: 10.1088/1361-6471/abbd48.

- [184] S. Adrián-Martínez et al. Letter of intent for km3net 2.0. *Journal of Physics G Nuclear Physics*, 43(8): 084001, August 2016. doi: 10.1088/0954-3899/43/8/084001.
- [185] Paweł Malecki. "pacific ocean neutrino experiment". *Universe*, 10(2), 2024. ISSN 2218-1997. doi: 10.3390/universe10020053. URL <https://www.mdpi.com/2218-1997/10/2/53>.
- [186] H. Zhang, M. Böttcher, and I. Liodakis. Revisiting high-energy polarization from leptonic and hadronic blazar scenarios. *ApJ*, 967(2):93, June 2024. doi: 10.3847/1538-4357/ad4112.
- [187] S. N. Zhang et al. extp: Enhanced x-ray timing and polarization mission. In Jan-Willem A. den Herder, Tadayuki Takahashi, and Marshall Bautz, editors, *Space Telescopes and Instrumentation 2016: Ultraviolet to Gamma Ray*, volume 9905 of *Society of Photo-Optical Instrumentation Engineers (SPIE) Conference Series*, page 99051Q, July 2016. doi: 10.1117/12.2232034.
- [188] J. Tomsick and others. The Compton Spectrometer and Imager. In *Bulletin of the American Astronomical Society*, volume 51, page 98, September 2019. doi: 10.48550/arXiv.1908.04334.
- [189] Regina Caputo et al. All-sky medium energy gamma-ray observatory explorer mission concept. *Journal of Astronomical Telescopes, Instruments, and Systems*, 8:044003, October 2022. doi: 10.1117/1.JATIS.8.4.044003.
- [190] A. De Angelis et al. The e-ASTROGAM mission. Exploring the extreme Universe with gamma rays in the MeV - GeV range. *Experimental Astronomy*, 44(1):25–82, October 2017. doi: 10.1007/s10686-017-9533-6.
- [191] Simona Paiano, Marco Landoni, Renato Falomo, Aldo Treves, Riccardo Scarpa, and Chiara Righi. On the redshift of tev bl lac objects. *ApJ*, 837(2):144, 2017.
- [192] C. B. Adams et al. Multiwavelength observations of the blazar ver j0521+211 during an elevated tev gamma-ray state. *ApJ*, 932(2):129, June 2022. doi: 10.3847/1538-4357/ac6dd9.
- [193] Sarira Sahu, B. Medina-Carrillo, G. Sánchez-Colón, and Subhash Rajpoot. Constraining the redshift of bl lac ver j0521+211. *MNRAS*, 522(4):5840–5847, July 2023. doi: 10.1093/mnras/stad1324.
- [194] John Quinn and VERITAS Collaboration. Veritas detection of unprecedented gamma-ray flare from the blazar ver j0521+211. *The Astronomer's Telegram*, 13522:1, February 2020.
- [195] S. Abdollahi et al. The fermi-lat lightcurve repository. *ApJS*, 265(2):31, April 2023. doi: 10.3847/1538-4365/acbb6a.
- [196] TS Poole, AA Breeveld, MJ Page, W Landsman, ST Holland, P Roming, NPM Kuin, PJ Brown, C Gronwall, S Hunsberger, et al. Photometric calibration of the swift ultraviolet/optical telescope. *MNRAS*, 383(2):627–645, 2008.
- [197] AA Breeveld, PA Curran, EA Hoversten, S Koch, W Landsman, FE Marshall, MJ Page, TS Poole, P Roming, PJ Smith, et al. Further calibration of the swift ultraviolet/optical telescope. *MNRAS*, 406(3):1687–1700, 2010.
- [198] L. O. Takalo, K. Nilsson, E. Lindfors, A. Sillanpää, A. Berdyugin, and M. Pasanen. Tuorla blazar monitoring program. In Felix A. Aharonian, Werner Hofmann, and Frank Rieger, editors, *American Institute of Physics Conference Series*, volume 1085 of *American Institute of Physics Conference Series*, pages 705–707, December 2008. doi: 10.1063/1.3076774.
- [199] Svetlana Jorstad and Alan Marscher. "the vlba-bu-blazar multi-wavelength monitoring program". *Galaxies*, 4(4), 2016. ISSN 2075-4434. doi: 10.3390/galaxies4040047. URL <https://www.mdpi.com/2075-4434/4/4/47>.
- [200] MAGIC Collaboration et al. Testing two-component models on very high-energy gamma-ray-emitting bl lac objects. *A&A*, 640:A132, August 2020. doi: 10.1051/0004-6361/202037811.
- [201] M. L. Lister, D. C. Homan, K. I. Kellermann, Y. Y. Kovalev, A. B. Pushkarev, E. Ros, and T. Savolainen. Monitoring of jets in active galactic nuclei with vlba experiments. xviii. kinematics and inner jet evolution of bright radio-loud active galaxies. *ApJ*, 923(1):30, December 2021. doi: 10.3847/1538-4357/ac230f.
- [202] A. A. Zdziarski and M. Böttcher. Hadronic models of blazars require a change of the accretion paradigm. *MNRAS*, 450:L21–L25, June 2015. doi: 10.1093/mnras/slv039.
- [203] Ioannis Liodakis and Maria Petropoulou. Proton synchrotron gamma-rays and the energy crisis in blazars. *ApJL*, 893(1):L20, April 2020. doi: 10.3847/2041-8213/ab830a.
- [204] M. G. Aartsen et al. All-sky search for time-integrated neutrino emission from astrophysical sources with 7 yr of icecube data. *The Astrophysical Journal*, 835(2):151, January 2017. ISSN 1538-4357. doi: 10.3847/1538-4357/835/2/151. URL <http://dx.doi.org/10.3847/1538-4357/835/2/151>.
- [205] M. G. Aartsen et al. Time-integrated neutrino source searches with 10 years of icecube data. *Phys. Rev. Lett.*, 124(5):051103, 2020. doi: 10.1103/PhysRevLett.124.051103.

- [206] F. W. Stecker, C. Done, M. H. Salamon, and P. Sommers. High-energy neutrinos from active galactic nuclei. *Phys. Rev. Lett.*, 66:2697–2700, 1991. doi: 10.1103/PhysRevLett.66.2697. [Erratum: *Phys.Rev.Lett.* 69, 2738 (1992)].
- [207] O. Kalashev, D. Semikoz, and I. Tkachev. Neutrinos in icecube from active galactic nuclei. *J. Exp. Theor. Phys.*, 120(3):541–548, 2015. doi: 10.1134/S106377611503022X.
- [208] M. G. Aartsen et al. Time-integrated neutrino source searches with 10 years of icecube data. *PRL*, 124(5):051103, February 2020. doi: 10.1103/PhysRevLett.124.051103.
- [209] Y. Inoue et al. On high-energy particles in accretion disk coronae of supermassive black holes: Implications for mev gamma-rays and high-energy neutrinos from agn cores. *ApJ*, 880(1):40, July 2019. doi: 10.3847/1538-4357/ab2715.
- [210] Y. Inoue and D. Khangulyan. Gamma-ray emission in the seyfert galaxy ngc 4151: Investigating the role of jet and coronal activities. *Publ. Astron. Soc. Jap.*, 75(6):L33–L39–L39, 2023. doi: 10.1093/pasj/psad072.
- [211] K. Murase, Sh. S. Kimura, and P. Meszaros. Hidden cores of active galactic nuclei as the origin of medium-energy neutrinos: Critical tests with the mev gamma-ray connection. *Phys. Rev. Lett.*, 125(1):011101, 2020. doi: 10.1103/PhysRevLett.125.011101.
- [212] D. F. G. Fiorillo et al. Tev neutrinos and hard x-rays from relativistic reconnection in the corona of ngc 1068. *Astrophys. J.*, 961(1):L14, 2024. doi: 10.3847/2041-8213/ad192b.
- [213] R. Abbasi et al. Icecube search for neutrino emission from x-ray bright seyfert galaxies. *arXiv e-prints*, art. arXiv:2406.07601, June 2024. doi: 10.48550/arXiv.2406.07601.
- [214] A. Neronov, D. Savchenko, and D. V. Semikoz. Neutrino signal from a population of seyfert galaxies. *Phys. Rev. Lett.*, 132:101002, Mar 2024. doi: 10.1103/PhysRevLett.132.101002. URL <https://link.aps.org/doi/10.1103/PhysRevLett.132.101002>.
- [215] G. Sommani et al. Two 100 tev neutrinos coincident with the seyfert galaxy ngc 7469, 2024.
- [216] R. Abbasi et al. Search for neutrino emission from hard x-ray agn with icecube. *arXiv e-prints*, art. arXiv:2406.06684, June 2024. doi: 10.48550/arXiv.2406.06684.
- [217] W. Yuan et al. The cepheid distance to the seyfert 1 galaxy ngc 4151. *The Astrophysical Journal*, 902(1):26, oct 2020. doi: 10.3847/1538-4357/abb377. URL <https://dx.doi.org/10.3847/1538-4357/abb377>.
- [218] S. Buson et al. Extragalactic neutrino factories. *arXiv e-prints*, 5 2023.
- [219] K. Murase et al. Sub-gev gamma rays from nearby seyfert galaxies and implications for coronal neutrino emission. *Astrophys. J. Lett.*, 961(2):L34, 2024. doi: 10.3847/2041-8213/ad19c5.
- [220] J. T. Stocke et al. The einstein observatory extended medium-sensitivity survey. ii. the optical identifications. *ApJS*, 76:813, July 1991. doi: 10.1086/191582.
- [221] J. Ballet, P. Bruel, T. H. Burnett, B. Lott, and The Fermi-LAT collaboration. Fermi large area telescope fourth source catalog data release 4 (4fgl-dr4), 2024.
- [222] S. Abdollahi et al. Incremental fermi large area telescope fourth source catalog. *The Astrophysical Journal Supplement Series*, 260(2):53, jun 2022. doi: 10.3847/1538-4365/ac6751. URL <https://dx.doi.org/10.3847/1538-4365/ac6751>.
- [223] A. Maselli et al. The 26 year-long x-ray light curve and the x-ray spectrum of the bl lacertae object 1e 1207.9+3945 in its brightest state. *A&A*, 479(1):35–40, February 2008. doi: 10.1051/0004-6361:20078401.
- [224] Christopher P. Ahn et al. The ninth data release of the sloan digital sky survey: First spectroscopic data from the sdss-iii baryon oscillation spectroscopic survey. *ApJS*, 203(2):21, December 2012. doi: 10.1088/0067-0049/203/2/21.
- [225] R. M. Cutri et al. VizieR online data catalog: Wise all-sky data release (cutri+ 2012). VizieR On-line Data Catalog: II/311., April 2012.
- [226] R. M. Cutri et al. Explanatory supplement to the wise all-sky data release products. Explanatory Supplement to the WISE All-Sky Data Release Products, March 2012.
- [227] Richard L. others White. A catalog of 1.4 ghz radio sources from the first survey. *ApJ*, 475(2):479–493, February 1997. doi: 10.1086/303564.
- [228] T. A. Rector et al. The properties of the x-ray-selected emss sample of bl lacertae objects. *The Astronomical Journal*, 120(4):1626, oct 2000. doi: 10.1086/301587. URL <https://dx.doi.org/10.1086/301587>.
- [229] R. Della Ceca et al. Exploring the active galactic nuclei population with extreme x-ray-to-optical flux ratios ($f_x/f_o > 50$). *Monthly Notices of the Royal Astronomical Society*, 447(4):3227–3242, 01 2015. ISSN 0035-8711. doi: 10.1093/mnras/stu2665. URL <https://doi.org/10.1093/mnras/stu2665>.
- [230] A. J. Drake et al. First results from the catalina real-time transient survey. *ApJ*, 696(1):870–884, May 2009. doi: 10.1088/0004-637X/696/1/870.

- [231] Sh. Alam et al. The eleventh and twelfth data releases of the sloan digital sky survey: Final data from sdss-iii. *ApJS*, 219(1):12, July 2015. doi: 10.1088/0067-0049/219/1/12.
- [232] G. Bruzual and S. Charlot. Stellar population synthesis at the resolution of 2003. *MNRAS*, 344(4): 1000–1028, October 2003. doi: 10.1046/j.1365-8711.2003.06897.x.
- [233] R. Itoh et al. Blazar radio and optical survey (bros): A catalog of blazar candidates showing flat radio spectrum and their optical identification in pan-starrs1 surveys. *Astrophys. J.*, 901(1):3, 2020. doi: 10.3847/1538-4357/abab07.
- [234] S. Dimitrakoudis, M. Petropoulou, and A. Mastichiadis. Self-consistent neutrino and uhe cosmic ray spectra from mrk 421. *Astroparticle Physics*, 54:61–66, February 2014. doi: 10.1016/j.astropartphys.2013.10.005.
- [235] Ts. Aramaki et al. Dual mev gamma-ray and dark matter observatory - grams project. *Astroparticle Physics*, 114:107–114, January 2020. doi: 10.1016/j.astropartphys.2019.07.002.
- [236] J. Álvarez-Muñiz et al. The giant radio array for neutrino detection (grand): Science and design. *Sci. China Phys. Mech. Astron.*, 63(1):219501, 2020. doi: 10.1007/s11433-018-9385-7.
- [237] Ch. D. Dermer, K. Murase, and Y. Inoue. Photopion production in black-hole jets and flat-spectrum radio quasars as pev neutrino sources. *Journal of High Energy Astrophysics*, 3:29–40, September 2014. doi: 10.1016/j.jheap.2014.09.001.
- [238] Nadine Häring and Hans-Walter Rix. On the black hole mass-bulge mass relation. *ApJL*, 604(2):L89–L92, April 2004. doi: 10.1086/383567.
- [239] P. Zhu, L. C. Ho, and H. Gao. The correlation between black hole mass and stellar mass for classical bulges and the cores of ellipticals. *The Astrophysical Journal*, 907(1):6, January 2021. ISSN 1538-4357. doi: 10.3847/1538-4357/abcaa1. URL <http://dx.doi.org/10.3847/1538-4357/abcaa1>.
- [240] F. Apel, A. Omeliukh, A. Franckowiak, and J. Lederer. Impact of model parameter degeneracy on leptonic radiation models. the case of blazar multi-wavelength spectra. 2025. URL <https://arxiv.org/abs/2506.06080>.
- [241] Ch. C. Aggarwal, A. Hinneburg, and D. A. Keim. On the surprising behavior of distance metrics in high dimensional space. In Jan Van den Bussche and Victor Vianu, editors, *Database Theory – ICDT 2001*, pages 420–434, Berlin, Heidelberg, 2001. Springer Berlin Heidelberg. ISBN 978-3-540-44503-6.
- [242] L. Van der Maaten and G. Hinton. Visualizing data using t-sne. *Journal of machine learning research*, 9(11), 2008.
- [243] F. Pedregosa et al. Scikit-learn: Machine learning in Python. 12:2825–2830, 2011.
- [244] F. James. Minuit: function minimization and error analysis reference manual. Technical report, CERN, 1998.
- [245] J. A Nelder and R. Mead. A simplex method for function minimization. *The computer journal*, 7(4): 308–313, 1965.
- [246] O. Kramer and O. Kramer. *Genetic algorithms*. Springer, 2017.
- [247] X. Rodrigues et al. The spectra of icecube neutrino (sin) candidate sources: V. modeling and interpretation of multiwavelength and neutrino data. *A&A*, 689:A147, September 2024. doi: 10.1051/0004-6361/202450592.
- [248] F.-A. Fortin et al. DEAP: Evolutionary algorithms made easy. *Journal of Machine Learning Research*, 13:2171–2175, jul 2012.
- [249] N. Hansen. The cma evolution strategy: A tutorial. *arXiv e-prints*, art. arXiv:1604.00772, April 2016. doi: 10.48550/arXiv.1604.00772.
- [250] N. Hansen and A. Ostermeier. Completely derandomized self-adaptation in evolution strategies. *Evolutionary Computation*, 9(2):159–195, 2001. doi: 10.1162/106365601750190398.
- [251] N. Hansen, Y. Akimoto, and P. Baudis. CMA-ES/pycma on Github. Zenodo, DOI:10.5281/zenodo.2559634, February 2019. URL <https://doi.org/10.5281/zenodo.2559634>.
- [252] D. W. Hogg and D. Foreman-Mackey. Data analysis recipes: Using markov chain monte carlo. *The Astrophysical Journal Supplement Series*, 236(1):11, May 2018. ISSN 1538-4365. doi: 10.3847/1538-4365/aab76e. URL <http://dx.doi.org/10.3847/1538-4365/aab76e>.
- [253] Y. Yamada et al. Variations of the physical parameters of the blazar mrk 421 based on analysis of the spectral energy distributions. *Publications of the Astronomical Society of Japan*, 72(3):42, 05 2020. ISSN 0004-6264. doi: 10.1093/pasj/psaa028. URL <https://doi.org/10.1093/pasj/psaa028>.
- [254] A. Tramacere. Jetset: Numerical modeling and sed fitting tool for relativistic jets. Astrophysics Source Code Library, record ascl:2009.001, September 2020.
- [255] A. Tzavellas et al. Application of neural networks to synchro-compton blazar emission models, 2023. URL <https://arxiv.org/abs/2311.06181>.

- [256] A. Sciacaluga et al. Stochastic acceleration in extreme tev bl lacs through mcmc. *Astronomy & Astrophysics*, 687:A247, July 2024. ISSN 1432-0746. doi: 10.1051/0004-6361/202449870. URL <http://dx.doi.org/10.1051/0004-6361/202449870>.
- [257] O. Hervet, C. A. Johnson, and A. Youngquist. Bjet_mcmc: A new tool to automatically fit the broadband spectral energy distributions of blazars. *The Astrophysical Journal*, 962(2):140, feb 2024. doi: 10.3847/1538-4357/ad09c0. URL <https://dx.doi.org/10.3847/1538-4357/ad09c0>.
- [258] J. Goodman and J. Weare. Ensemble samplers with affine invariance. *Communications in Applied Mathematics and Computational Science*, 5(1):65 – 80, 2010. doi: 10.2140/camcos.2010.5.65. URL <https://doi.org/10.2140/camcos.2010.5.65>.
- [259] D. Foreman-Mackey, D. W. Hogg, D. Lang, and J. Goodman. emcee: The mcmc hammer. *PASP*, 125: 306–312, 2013. doi: 10.1086/670067.
- [260] J. Quinn et al. Detection of gamma rays with $e > 300$ gev from markarian 501. *The Astrophysical Journal*, 456(2):L83, jan 1996. doi: 10.1086/309878. URL <https://dx.doi.org/10.1086/309878>.
- [261] H. Abe et al. Multimessenger characterization of markarian 501 during historically low x-ray and γ -ray activity. *ApJS*, 266(2):37, June 2023. doi: 10.3847/1538-4365/acc181.
- [262] H. Abe et al. Multimessenger characterization of markarian 501 during historically low x-ray and gamma-ray activity. *The Astrophysical Journal Supplement Series*, 266(2):37, jun 2023. doi: 10.3847/1538-4365/acc181. URL <https://dx.doi.org/10.3847/1538-4365/acc181>.
- [263] A. Franceschini, G. Rodighiero, and M. Vaccari. Extragalactic optical-infrared background radiation, its time evolution and the cosmic photon-photon opacity. *A&A*, 487(3):837–852, September 2008. doi: 10.1051/0004-6361:200809691.
- [264] A. A. Abdo et al. Insights into the high-energy gamma-ray emission of markarian 501 from extensive multifrequency observations in the fermi era. *ApJ*, 727(2):129, jan 2011. doi: 10.1088/0004-637X/727/2/129. URL <https://dx.doi.org/10.1088/0004-637X/727/2/129>.
- [265] M. L. Ahnen et al. Multiband variability studies and novel broadband sed modeling of mrk 501 in 2009. *A&A*, 603:A31, 2017. doi: 10.1051/0004-6361/201629540. URL <https://doi.org/10.1051/0004-6361/201629540>.
- [266] D. Bégué et al. Modeling blazar broadband emission with a convolutional neural network. i. synchrotron self-compton model. *ApJ*, 963(1):71, March 2024. doi: 10.3847/1538-4357/ad19cf.
- [267] N. Sahakyan et al. Modeling blazar broadband emission with convolutional neural networks. ii. external compton model. *ApJ*, 971(1):70, August 2024. doi: 10.3847/1538-4357/ad5351.
- [268] Athira M. Bharathan, C. S. Stalin, S. Sahayanathan, Subir Bhattacharyya, and Blesson Mathew. Multiwavelength spectral modelling of the candidate neutrino blazar pks 0735+178. *MNRAS*, 529(4):3503–3510, April 2024. doi: 10.1093/mnras/stae296.
- [269] Cherenkov Telescope Array Consortium. *Science with the Cherenkov Telescope Array*. 2019. doi: 10.1142/10986.
- [270] M. G. Aartsen et al. The contribution of fermi-2lac blazars to diffuse tev–pev neutrino flux. *The Astrophysical Journal*, 835(1):45, jan 2017. doi: 10.3847/1538-4357/835/1/45. URL <https://dx.doi.org/10.3847/1538-4357/835/1/45>.
- [271] R. Abbasi et al. Search for astrophysical neutrinos from 1fle blazars with icecube. *The Astrophysical Journal*, 938(1):38, October 2022. ISSN 1538-4357. doi: 10.3847/1538-4357/ac8de4. URL <http://dx.doi.org/10.3847/1538-4357/ac8de4>.
- [272] R. Abbasi et al. Search for correlations of high-energy neutrinos detected in icecube with radio-bright agn and gamma-ray emission from blazars, 2023. URL <https://arxiv.org/abs/2304.12675>.
- [273] A. Omeliukh and Y. Inoue. Relativistic Jets from Supermassive Black Holes Thrive on Less Fuel. (in prep.).
- [274] S. E. Healey et al. Cgrabs: An all-sky survey of gamma-ray blazar candidates. *The Astrophysical Journal Supplement Series*, 175(1):97, mar 2008. doi: 10.1086/523302. URL <https://dx.doi.org/10.1086/523302>.
- [275] S. Abdollahi et al. Fermi large area telescope fourth source catalog. *ApJS*, 247(1):33, March 2020. doi: 10.3847/1538-4365/ab6bcb.
- [276] V. S. Paliya et al. General physical properties of cgrabs blazars. *The Astrophysical Journal*, 851(1):33, dec 2017. doi: 10.3847/1538-4357/aa98e1. URL <https://dx.doi.org/10.3847/1538-4357/aa98e1>.
- [277] Chris J. Willott et al. The emission line—radio correlation for radio sources using the 7c redshift survey. *Monthly Notices of the Royal Astronomical Society*, 309(4):1017–1033, 11 1999. ISSN 0035-8711. doi: 10.1046/j.1365-8711.1999.02907.x. URL <https://doi.org/10.1046/j.1365-8711.1999.02907.x>.

- [278] E. O'Sullivan et al. Heating the hot atmospheres of galaxy groups with cavities: the relationship between jet power and low-frequency radio emission. *The Astrophysical Journal*, 735(1):11, jun 2011. doi: 10.1088/0004-637X/735/1/11. URL <https://dx.doi.org/10.1088/0004-637X/735/1/11>.
- [279] R. D. Blandford and A. Königl. Relativistic jets as compact radio sources. *ApJ*, 232:34–48, August 1979. doi: 10.1086/157262.
- [280] Andrzej A Zdziarski, Piotr Lubiński, and Marek Sikora. The mev spectral tail in cyg x-1 and optically thin emission of jets. *Monthly Notices of the Royal Astronomical Society*, 423(1):663–675, 2012.
- [281] M. Zamaninasab et al. Dynamically important magnetic fields near accreting supermassive black holes. *Nature*, 510(7503):126–128, June 2014. doi: 10.1038/nature13399.
- [282] Andrzej A. Zdziarski et al. Core shifts, magnetic fields and magnetization of extragalactic jets. *Monthly Notices of the Royal Astronomical Society*, 451(1):927–935, 05 2015. ISSN 0035-8711. doi: 10.1093/mnras/stv986. URL <https://doi.org/10.1093/mnras/stv986>.
- [283] Patryk Pjanka, Andrzej A. Zdziarski, and Marek Sikora. The power and production efficiency of blazar jets. *MNRAS*, 465(3):3506–3514, March 2017. doi: 10.1093/mnras/stw2960.
- [284] H. T. Intema et al. The GMRT 150 MHz all-sky radio survey. First alternative data release TGSS ADR1. *A&A*, 598:A78, February 2017. doi: 10.1051/0004-6361/201628536.
- [285] J. J. Condon et al. The NRAO VLA Sky Survey. *AJ*, 115(5):1693–1716, May 1998. doi: 10.1086/300337.
- [286] V. S. Paliya et al. The Central Engines of Fermi Blazars. *ApJS*, 253(2):46, April 2021. doi: 10.3847/1538-4365/abe135.
- [287] Vaidehi S. Paliya et al. General Physical Properties of CGRaBS Blazars. *ApJ*, 851(1):33, December 2017. doi: 10.3847/1538-4357/aa98e1.
- [288] Y. Inoue et al. Disk-Jet Connection in Active Supermassive Black Holes in the Standard Accretion Disk Regime. *ApJ*, 840(1):46, May 2017. doi: 10.3847/1538-4357/aa6b57.
- [289] A. Tchekhovskoy, R. Narayan, and J. C. McKinney. Efficient generation of jets from magnetically arrested accretion on a rapidly spinning black hole. *MNRAS*, 418(1):L79–L83, November 2011. doi: 10.1111/j.1745-3933.2011.01147.x.
- [290] D. F. Andrews. Plots of high-dimensional data. *Biometrics*, 28(1):125–136, 1972. ISSN 0006341X, 15410420. URL <http://www.jstor.org/stable/2528964>.

Acknowledgments

No matter how uncertain my models were or how strong my frustration with the results became, life over the last four years always had a far more dramatic surprise in store for me – something I could never have imagined before starting my PhD. Fortunately, some of those surprises were positive as well. I am deeply grateful to have had Anna Franckowiak as my supervisor. Her tremendous support helped me overcome all difficulties and is likely the main reason I am able to present the results of my work in the form of this thesis today. Her openness to new ideas and scientific curiosity gave me valuable research freedom and allowed me to explore topics that deviated from the original plan.

A significant part of this thesis would not have been possible without Yoshiyuki Inoue and our collaboration during two research stays in Japan and beyond. I am thankful for your kindness and patience, for our extensive scientific discussions, and for the comforting feeling of being able to ask even naïve questions and still receive amazing answers. I remember my time in Japan as a period of intensive learning, productive work, curiosity, and inspiration. I am convinced that a more talented student than I could become a great scientist under your supervision.

Who knows what would have happened if, a year before starting my PhD, Shan Gao and Xavier Rodrigues had not helped a clueless Master's student with writing a research proposal. I am grateful for your support, it allowed me to get to where I am now. I also cannot imagine the first half of my PhD without the guidance, encouragement, and thoughtful discussions with Xavier Rodrigues. Thank you for your patience and support. Whether it was a well-hidden bug in my code, a hastily written abstract for a conference, or an interesting topic unrelated to physics, you were always there to talk with me and help. I learned a lot from you.

In Ukrainian, we say that to truly learn about someone, you have to eat a pood¹ of salt together. Unfortunately for RUB Mensa, our group surpassed that amount over the course of my PhD. I thank you all for providing a supportive environment, for your expertise in topics that were completely new to me, for the very important distractions from physics during coffee breaks and lunches, and of course, for sharing meals with me. It's hard to estimate the number of poods of salt consumed with my Japanese colleagues due to the high

¹Pood is an old Slavic mass unit approximately equal to 16 kg.

prevalence of soy sauce, but I am equally grateful to Kentaro Nagamine and all the group members for creating such a warm and welcoming atmosphere and for all the wonderful discussions.

I would like to thank the Ettore Majorana Foundation and the Lindau Foundation for reminding me that being a physicist is rooted in a complex cultural and philosophical context. The discussions on science, society, humanism, war, and responsibility had just as much impact on my personal growth as the research presented here.

Most importantly, I am thankful to my family for always being by my side, even in the hardest times.

It takes a village to raise a child. Similarly, many people and funding organizations have provided me with valuable opportunities. I gratefully acknowledge their support:

- DAAD Individual Doctoral Scholarship (57552340)
- RUB Research School Project International funding (in 2023 and in 2024)
- Collaborative Research Center SFB 1491 *Cosmic Interacting Matters - From Source to Signal*
- IAU Travel Grant for IAU Symposium 375
- Wilhelm und Else Heraeus Foundation
- Ettore Majorana Foundation
- The Foundation Lindau Nobel Laureate Meetings

Anastasiia Omeliukh

1

RESEARCH EXPERIENCE

Doctoral candidate, research assistant <i>Ruhr University Bochum, Faculty of Physics and Astronomy, Astronomical Institute</i>	October 2021 – present
Guest researcher <i>Osaka University, Department of Earth and Space Science, Osaka, Japan</i>	June 2023 – June 2024
Visiting Research Intern (Master thesis) <i>DESY Zeuthen, Germany</i>	January 2020 – April 2021
Summer Intern (Mitacs Research Globalink Fellowship) <i>University of Alberta, Edmonton, Canada</i>	May 30 – Aug. 22, 2018

EDUCATION

Ruhr University Bochum <i>Doctoral Candidate</i>	<i>Oct. 2021 – present</i>
Taras Shevchenko National University of Kyiv <i>Master of Science with honours in Physics (specialization – High Energy Physics)</i>	<i>Sept. 2019 – May 2021</i>
National Technical University of Ukraine “Igor Sikorsky Kyiv Polytechnic Institute” <i>Bachelor of Science with honors in Applied Physics</i>	<i>Sept. 2015 – May 2019</i>

GRANTS AND AWARDS

- 2024 - Scholarship from Lindau Foundation and WE-Heraeus-Stiftung for participation in Lindau Nobel Prize Meeting 2024
- 2024 - Research grant from RUB Research School for international projects
- 2023 - Research grant from RUB Research School for international projects
- 2022 - Travel Grant for IAU Symposium 375 “Multi-messenger chakra of blazar jets”, Kathmandu, Nepal
- 2022 - Travel Grant from Ettore Majorana Foundation for 58th Course of the International School of Subnuclear Physics, Erice, Italy and Sidney Coleman Diploma
- 2021 - DAAD Individual Doctoral Scholarship, RUB, Bochum, Germany
- 2020 - DESY Research Internship, Zeuthen, Germany
- 2018 - Travel Grant for SBF-APS São Paulo School of Advanced Science on Experimental Neutrino Physics, Sao Paulo, Brazil
- 2018 - Travel Grant for Perspektywy Women in Tech Summit, Warsaw, Poland
- 2018 - Mitacs Research Globalink Fellowship, Edmonton, Canada

 CONTRIBUTIONS TO CONFERENCES

- International Cosmic Ray Conference 2023** | *Nagoya* July 26 – Aug 3, 2023
- Poster “Interpreting the activity of blazar PKS 0735+178 with particle interactions in the jet”
- IAU Symposium 375 ”Multi-messenger chakra of blazar jets“** | *Kathmandu* December 5 – 9, 2022
- Talk “Interpreting the activity of blazar PKS 0735+178 with particle interactions in the jet”
- 765th WE-Heraeus Seminar “Gravitational Wave and Multimessenger Astronomy”** May 26, 2022
- Poster “Understanding the mutli-wavelength variability of TeV blazar VER J0521+211 with high-energy particle intercatons”
- German Physical Society Spring Meeting** | *online* March 23, 2022
- Talk “ Understanding the multi-wavelength variabilty of TeV blazar VER J0521+211 with high-energy particle interactions”
- International Cosmic Ray Conference 2021** | *online, Berlin* July 12 – 23, 2021
- Poster “Optimization of the optical array geometry for IceCube-Gen2”
- 54th Canadian Undergraduate Physics Conference** | *Edmonton* Aug. 15 – 18, 2018
- Poster Presentation “Simulation of gamma background in the PICO bubble chambers for dark matter search”

 LIST OF PUBLICATIONS

Published:

Omeliukh, A., Garrappa S., Fallah Ramazani V., Franckowiak A., Winter W., Lindfors E., Nilsson K., et al., “Multi-epoch leptohadronic modeling of neutrino source candidate blazar PKS 0735+178”, *Astronomy and Astrophysics*, vol. 695, Art. no. A266, EDP, 2025. doi:10.1051/0004-6361/202452143.

Omeliukh, A., Barnier, S., and Inoue, Y., “Possible contributions of two nearby blazars to the NGC 4151 neutrino hotspot”, *Astronomy and Astrophysics*, vol. 694, Art. no. A203, EDP, 2025. doi:10.1051/0004-6361/202452992.

MAGIC Collaboration, R. Bachev , V. Fallah Ramazani , A. V. Filippenko, T. Hovatta, S. G. Jorstad , S. Kiehlmann, A. Lähteenmäki, I. Liidakis, A. P. Marscher , W. Max-Moerbeck, **A. Omeliukh** , T. Pursimo, A. C. S. Readhead, X. Rodrigues , M. Tornikoski, F. Wierda, and W. Zheng “Time-dependent modelling of short-term variability in the TeV-blazar VER J0521+211 during the major flare in 2020”, *Astronomy and Astrophysics*, vol. 694, Art. no. A308, EDP, 2025. doi:10.1051/0004-6361/202451378.

Rodrigues, X., Paliya, V. S., Garrappa, S., **Omeliukh, A.**, Franckowiak, A., and Winter, W., “Leptohadronic multi-messenger modeling of 324 gamma-ray blazars”, *Astronomy and Astrophysics*, vol. 681, Art. no. A119, EDP, 2024. doi:10.1051/0004-6361/202347540.

In preparation:

Apel, F., **Omeliukh, A.**, Franckowiak, A., and Lederer, J., “Impact of model parameter degeneracy on leptonic radiation models. The case of blazar multi-wavelength spectra”, arXiv e-prints, Art. no. arXiv:2506.06080, 2025. doi:10.48550/arXiv.2506.06080, submitted to *Astronomy and Astrophysics*

A. Omeliukh, Y. Inoue “Relativistic Jets from Supermassive Black Holes Thrive on Less Fuel”, in prep., to be submitted to *Nature Astronomy*